SOCIETÀ ITALIANA DI FISICA

PROCEEDINGS
OF THE
INTERNATIONAL SCHOOL OF PHYSICS
«ENRICO FERMI»

COURSE CLXXV

Radiation and Particle Detectors

SOCIETÀ ITALIANA DI FISICA BOLOGNA-ITALY

SOCIETÀ ITALIANA DI FISICA

RENDICONTI

DELLA

SCUOLA INTERNAZIONALE DI FISICA

"ENRICO FERMI"

CLXXV CORSO

a cura di S. BERTOLUCCI e U. BOTTIGLI

Direttori del Corso

e di

P. OLIVA

VARENNA SUL LAGO DI COMO

VILLA MONASTERO

20 – 25 Luglio 2009

Rivelatori per radiazione e particelle

2010

SOCIETÀ ITALIANA DI FISICA
BOLOGNA-ITALY

ITALIAN PHYSICAL SOCIETY

PROCEEDINGS

OF THE

INTERNATIONAL SCHOOL OF PHYSICS

"ENRICO FERMI"

COURSE CLXXV

edited by S. BERTOLUCCI and U. BOTTIGLI

Directors of the Course

and

P. OLIVA

VARENNA ON LAKE COMO

VILLA MONASTERO

20 – 25 July 2009

Radiation and Particle Detectors

2010

IOS Press

AMSTERDAM, OXFORD, TOKIO, WASHINGTON DC

ISSN 0074-784X (print)
ISSN 1879-8195 (online)

ISBN 978-1-60750-630-0 (print) (IOS)
ISBN 978-1-60750-631-7 (online) (IOS)
ISBN 978-88-7438-058-9 (SIF)

LCCN 2010934193

Production Manager
A. Oleandri

Copy Editor
M. Missiroli

jointly published and distributed by:

IOS PRESS
Nieuwe Hemweg 6B
1013 BG Amsterdam
The Netherlands
fax: +31 20 620 34 19
order@iopress.nl

SOCIETÀ ITALIANA DI FISICA
Via Saragozza 12
40123 Bologna
Italy
fax: +39 051 581340
order@sif.it

Distributor in the UK and Ireland
Gazelle Books Services Ltd.
White Cross Mills
Hightown
Lancaster LA1 4XS
United Kingdom
fax: +44 1524 63232
sales@gazellebooks.co.uk

Distributor in the USA and Canada
IOS Press, Inc.
4502 Rachael Manor Drive
Fairfax, VA 22032
USA
fax: +1 703 323 3668
iosbooks@iospress.com

Proprietà Letteraria Riservata
Printed in Italy

Supported by

Istituto Nazionale di Fisica Nucleare (INFN)

INFN, Sezione di Pisa

This page intentionally left blank

INDICE

Preface

From the 20th to 25th of July 2009 the International School of Physics entitled "Radiation and Particle Detectors" was held in Varenna, which involved the use of detectors for the research in fundamental physics, astro-particle physics, and applied physics. At the school ten teachers and thirty students were present.

In the context of fundamental physics the High Energy Physics (HEP) plays an important role. In general the HEP experiments make use of sophisticated and massive arrays of detectors to analyze the particles which are produced in high-energy scattering events. This aim can be achieved in a large variety of approaches. Some examples are the following:

- Measuring the position and length of ionization trails. Much of the detection depends upon ionization.
- Measuring time of flight permits velocity measurements.
- Measuring radius of curvature after bending the paths of charged particles with magnetic fields permits measurement of momentum.
- Detecting Cherenkov radiation gives some information about energy, mass.
- Measuring the coherent "transition radiation" for particles moving into a different medium.
- Measuring synchrotron radiation for the lighter charged particles when their paths are bent.
- Detecting neutrinos by steps in the decay schemes which are "not there", *i.e.*, using conservation of momentum, etc. to imply the presence of undetected neutrinos.
- Measuring the electromagnetic showers produced by electrons and photons by calorimetric methods.

– Measuring nuclear cascades produced by hadrons in massive steel detectors which use calorimetry to characterize the particles.

– Detecting muons by the fact that they penetrate all the calorimetric detectors.

All these types of detectors are used in the largest accelerator ever built: the Large Hadron Collider (LHC). LHC is a proton-proton (also ions) ring, 27 km long, 100 m underground, with 1232 superconducting dipoles 15 m long at 1.9 K producing a magnetic field of 8.33 T. The figures of merit, for proton-proton operations, are beam-energy 7 TeV ($7\times$ TEVATRON), luminosity $10^{34}\,\mathrm{cm}^{-2}\mathrm{s}^{-1}$ ($>100\times$ TEVATRON), bunch spacing 24.95 ns, particles/bunch $1.1\cdot 10^{11}$, and stored emergy/beam 350 MJ. For ion-ion operations we will have energy/nucleon 2.76 TeV/u, and total initial luminosity of $10^{27}\,\mathrm{cm}^{-2}\mathrm{s}^{-1}$. The main four experiments are two general purpose experiments (ATLAS and CMS), B-physics and CP violation experiment (LHCB), and heavy ions experiment (ALICE).

The international community of physicists hopes that the LHC will help answer many of the most fundamental questions in physics: questions concerning the basic laws governing the interactions and forces among the elementary particles, the deep structure of space and time, especially regarding the intersection of quantum mechanics and cosmology, where current theories and knowledge are unclear or break down altogether. The enormous success of the Standard Model (SM), tested at per mil level with all particles discovered except the Higgs boson, will hopefully be able to build a Cosmology Standard Model.

The issues of LHC physics include, at least:

– Is the Higgs mechanism for generating elementary particles masses via electroweak symmetry breaking indeed realised in nature? It is anticipated that the collider will either demonstrate or rule out the existence of the elusive Higgs boson, completing (or refuting) the SM.

– Is supersymmetry, an extension of the SM and Poincaré symmetry, realised in nature, implying that all known particles have supersimmetric partners?

– Are there extra-dimensions, as predicted by various models inspired by string theory, and can we detect them?

– What is the nature of the Dark Matter which appears to account for 23% of the mass of the universe?

Other questions are:

– Are electromagnetism, the strong force, and the weak interaction just different manifestations of a single unified force, as predicted by various Grand Unification Theories (GUTs)?

– Why is gravity so many orders of magnitude weaker than the other three fundamental interctions (Hierarchy Problem)? For all proposed solutions: new particles should appear at TeV scale or below.

– Are there additional sources of quark flavours, beyond those already predicted within the Standard Model?

– Why are there apparent violations of the symmetry between matter and antimatter (CP violation)?

– What was the nature of the quark-gluon plasma in the early universe (ALICE experiment)?

Obviously, for the construction of a Standard Cosmology Model, the astro-particle experiments are crucial with direct or indirect dark matter measurements. In particular, the Payload for Antimatter Matter Exploration and Light-nuclei Astrophysics (PAMELA) experiment, which went into space on a Russian satellite launched from the Baikonur cosmodrome in June 2006, uses a spectrometer —based on a permanent magnet coupled to a calorimeter— to determine the energy spectra of cosmic electrons, positrons, antiprotons and light nuclei. The experiment is a collaboration between several Italian institutes with additional participation from Germany, Russia and Sweden. PAMELA represents a state of the art of the investigation of the cosmic radiation, addressing the most compelling issues facing astrophysics and cosmology: the nature of the dark matter that pervades the universe, the apparent absence of cosmological antimatter, the origin and evolution of matter in the Galaxy. PAMELA, a powerful particle identifier using a permanent magnet spectrometer with a variety of specialized detectors, is an instrument of extraordinary scientific potential that is measuring with unprecedented precision and sensitivity the abundance and energy spectra of cosmic rays electrons, positrons, antiprotons and light nuclei over a very large range of energy from 50 MeV to hundreds GeV, depending on the species. These measurements, together with the complementary electromagnetic radiation observation that will be carried out by AGILE and GLAST space missions, will help to unravel the mysteries of the most energetic processes known in the universe. Recently published results from the PAMELA experiment have shown conclusive evidence of a cosmic-positron abundance in the 1.5–100 GeV range. This high-energy excess, which they identify with statistics that are better than previous observations, could arise from nearby pulsars or dark matter annihilation. Such a signal is generally expected from dark matter annihilations. However, the hard positron spectrum and large amplitude are difficult to achieve in most conventional WIMP models. The absence of any associated excess in antiprotons is highly constraining on any model with hadronic annihilation modes. The light boson naturally provides a mechanism by which large cross-sections can be achieved through the Sommerfeld enhancement, as was recently proposed. Depending on the mass of the WIMP, the rise may continue above 300 GeV, the extent of PAMELA's ability to discriminate electrons and positrons. The data presented include more than a thousand million triggers collected between July 2006 and February 2008. Fine tuning of the particle identification allowed the team to reject 99.9% of the protons, while selecting more than 95% of the electrons and positrons. The resulting spectrum of the positron abundance relative to the sum of electrons and positrons represents the highest statistics to date. Below 5 GeV, the obtained spectrum

is significantly lower than previously measured. This discrepancy is believed to arise from modulation of the cosmic rays induced by the strength of the solar wind, which changes periodically through the solar cycle. At higher energies the new data unambiguously confirm the rising trend of the positron fraction, which was suggested by previous measurements. This appears highly incompatible with the usual scenario in which positrons are produced by cosmic-ray nuclei interacting with atoms in the interstellar medium. The additional source of positrons dominating at the higher energies could be the signature of dark matter decay or annihilation. In this case, PAMELA has already shown that dark matter would have a preference for leptonic final states. They suggest that the alternative origin of the positron excess at high energies is particle acceleration in the magnetosphere of nearby pulsars producing electromagnetic cascades. The members of the collaboration state that the PAMELA results presented here are insufficient to distinguish between the two possibilities. They seem, however, confident that various positron production scenarios will soon be testable. This will be possible once additional PAMELA results on electrons, protons and light nuclei are published in the near future, together with the extension of the positron spectrum up to 300 GeV thanks to ongoing data acquisition.

S. Bertolucci, U. Bottigli and P. Oliva

This page intentionally left blank

Società Italiana di Fisica

SCUOLA INTERNAZIONALE DI FISICA «E. FERMI»

CLXXV CORSO - VARENNA SUL LAGO DI COMO

VILLA MONASTERO 20 - 25 Luglio 2009

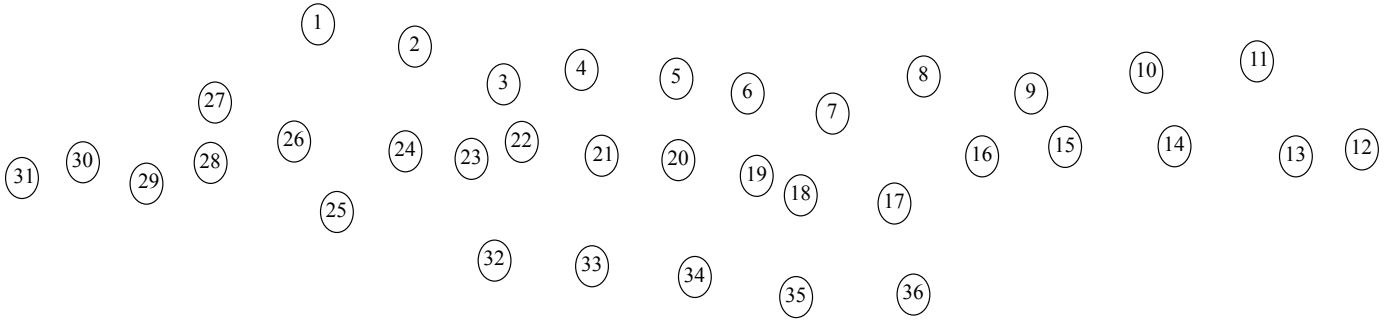

1) A. Agostinelli
2) D. Caffarri
3) A. Junkes
4) F. Bellini
5) B. Guerzoni
6) V. Cavaliere
7) L. Caforio
8) A. Silenzi
9) M. Siciliano
10) D. Fasanella
11) M. Nocente
12) M. Bettuzzi
13) P. Allegrini
14) P. Bennati
15) A. Di Canto
16) F. Sforza
17) M. V. Siciliano
18) F. Albertin
19) P. Garosi
20) G. Volpe
21) L. Velardi
22) J. Lange
23) D. Lattanzi
24) L. Soung Yee
25) E. Gurpinar
26) G. Sabatino
27) M. Endrizzi
28) S. Tangaro
29) B. Alzani
30) R. Brigatti
31) L. Strolin
32) P. Oliva
33) J. Marque
34) M. Mulders
35) U. Bottigli
36) G. Riccobene

This page intentionally left blank

Detectors for medical physics

Notes from the lecture of Maria Giuseppina Bisogni

Università di Pisa, Dipartimento di Fisica "E. Fermi"
and INFN Sezione di Pisa - Pisa, Italy

A straightforward application of detection technologies developed in high-energy physics is medical imaging.

Two main fields of medical imaging have to be covered by these detectors: morphological imaging and functional imaging. And the most used radiation type are X-rays or gamma rays.

Since the beginning of morphological imaging the most used detector has been the screen-film system. However, in the recent years digital detectors have become more and more important. Digital imaging has several advantages with respect to conventional imaging: the images can be displayed, stored and processed by a computer and can be easily transferred from one site to another. Moreover digital detectors have a wider dynamic range so the exposure is a less critical factor.

Digital detection can be performed in a direct on in an indirect way: in the first case the radiation interacts directly with the detector, while in the second case it interacts with a scintillator and the light produced in it is then detected by the digital detector.

A first example of digital detectors for medical imaging are Charge Coupled Devices (CCD). They are based on the technology Metal Oxide Semiconductor (MOS). The charge produced is stored in a potential well. The potential changes to make the charges shift from one pixel to the next in a given column and there is a serial read-out with a clock.

CCDs are generally coupled to scintillators CsI(Tl) to improve efficiency, so they are indirect digital detectors.

Widely used indirect digital detectors are a-Si Flat Panels. They are made of a-Si:H photodiodes (low dark current, high sensitivity to green light), coupled to CsI phosphors. In order to improve efficiency by keeping spatial resolution high, the scintillator is made of CsI:Tl needle crystals: their thickness is about $550\,\mu$m, which allows a good X-ray absorption. The needles act as light guides, leading to a sharp point spread function. Moreover CsI:Tl emits green light.

Examples of direct digital detection are a-Se Flat Panels. They are made of alloyed a-Se with % As and with ppm Cl and the detection system is a TFT.

A challenging application of these detectors is digital mammography. In mammography the details of interest are very low contrast ones (like tumor masses) or very small details (like microcalcifications). So mammography is a demanding task for both efficiency and spatial resolution.

A widely used indirect detection system is the GE Senographe 2000D that uses a Flat Panel Digital Detector Si +CsI(Tl).

The total area covered by the detector is $18 \times 24\,\mathrm{cm}^2$ and the pixel is $100 \times 100\,\mu\mathrm{m}^2$.

Nowadays also direct digital detectors are available (a-Se based flat panels) like SeleniaTM, LORAD-Hologic, Mammomat NovationDR Siemens.

A promising alternative to conventional integrating detectors are Single Photon Counting (SPC) Systems. They allow efficient noise suppression, leading to a higher SNR or lower dose, so they are particularly suited for low-event-rate applications.

They are linear whit exposure and have wider dynamic range (with respect to integration detectors), limited only by counter saturation.

They can allow an energy discrimination rejecting Compton events or X-ray fluorescences.

Also "energy weighting" (low-energy photons weight less than high-energy ones in integrating systems) is suppressed because in SPC systems all photons have the same weight.

Sectra MicroDose is the First SPC commercial mammographic system.

The SYRMEP Project (INFN GV, early '90s) also developed an SPC detector. It is an Edge-on Si strip detector. A silicon microstrip detector is used in the so-called "edge-on" geometry matching the laminar geometry of the beam. The absorption length seen by the impinging radiation is given by the strip length ($\sim 100\%$ in 1 cm of silicon for 20 keV photons). There is almost complete scattering rejection. The pixel size is determined by the strip pitch (H) times the detector thickness (V). A drawback is that the dead volume in front of the strip reduces the efficiency of the detector.

The Integrated Mammographic Imaging Project (IMI) is a collaboration between national universities, INFN and Industry which developed a mammography system demonstrator based on GaAs pixel detectors. Photoelectric interaction probability is about 100% in the mammographic energy range (10–30 keV) for a 200 μm thick GaAs crystal.

So the detector is made of 200 μm thick GaAs bump-bonded to a Photon Counting Chip (PCC). The detection unit presents a $18 \times 24\,\mathrm{cm}^2$ exposure field. A 1D scanning is performed by 9×2 assemblies in 26 exposures and the image is "off-line" reconstructed.

Another application of growing interest in medical imaging is the Computed Tomography (CT). This imaging modality is intrinsically related to digital detector, since slice images have to be reconstructed from actually acquired projection images by a specific algorithm.

Current CTs are spiral CT, that acquire the whole volume of interest in a single exposure by rotating continuously both the source and the detectors while the patient is moving along his axial direction. By using multiple arrays of detectors it is now possible to acquire more than one slice simultaneously. Modern systems can acquire up to 256

different slices at the same time. The future of CT is the cone beam CT with a full area detector, which will allow acquisition of large areas in a very small time.

Micro Computed Tomography is a technique for small fields of measurement (typically 5–50 mm). It is characterized by very-low-power X-ray sources (typically 5–50 W) and long scan times (typically 5–30 minutes). It is devoted to the imaging of a specific organ (bone, teeth, vessels, cancer) or to the imaging of samples (biopsies, excised materials) or small animals (rats/mice) *in vivo*, *ex vivo* or *in vitro*.

Functional imaging is dedicated to the *in vitro* or *in vivo* measure of the intensity of functional/metabolic processes occurring within a living body. Nuclear medicine uses molecules or drugs marked with radioisotopes (radiotracer) for this kind of imaging.

The principle of radiotracer applications is that changing an atom in a molecule for its radioisotope will not change its chemical and biological behavior significantly. As a consequence, the movement, distribution, concentration of the molecule can be measured by radiation detectors.

The two main imaging modalities used in nuclear medicine are SPECT (Single Photon Emission CT) and PET (Positron Emission Tomography).

In SPECT the radiotracer emits one photon (for example ^{99m}Tc, while in PET two anticollinear photons are emitted by positron annihilation.

The main detector used in SPECT is the Gamma Camera, that is made of a Pb collimator (that encodes the spatial information), a NaI (Tl) scintillation crystal and an array of PMTs connected to amplifiers and positional logic circuits.

The principle is that many photomultiplier tubes "see" the same large scintillation crystal; an electronic circuit decodes the coordinates of each event.

γ-rays (typically: 140 keV from ^{99m}Tc) are emitted in all directions hence collimators are required to determine the line of response. To perform a CT, in SPECT scanners rotate around the patient.

In PET a tracer containing a β^+ emitting isotope is used. The emitted positron annihilates in a short range (~ 1 mm) emitting two antiparallel photons of 511 keV.

The signal detection is based on the coincidence detection at 180°, leading to a higher sensitivity and a better signal/noise ratio than SPECT.

Detectors are usually scintillators coupled to a read-out device (typically a photomultiplier, PMT), which can be arranged in a ring geometry or in a parallel-plate geometry.

Detectors are usually scintillators: the most often used is BGO (bismuth germanate, $Bi_4Ge_3O_{12}$) and more recently LSO (lutetium oxi-orto silicate, LuSiO).

In a block detector conventionally used in PET, a 2D array of crystals is attached to 4 PMTs. Usually the array will be cut from a single crystal and the cuts filled with light-reflecting material. When a photon is incident on one of the crystals, the resultant light is shared by all 4 PMTs. Information on the position of the detecting crystal may be obtained from the PMT outputs comparing them to pre-set values.

For more than 80 years, the PMT is the photodetector of choice to convert scintillation photons into electrical signals in most of the applications related to the radiation detection. This is due to its high gain, low noise and fast response. Research is now

moving to solid-state photodetectors that show the following advantages with respect to PMTs:

- Compactness
- High quantum efficiency (to provide an energy resolution comparable to PMTs)
- Insensitivity to magnetic fields (PET/MRI)

TOF-PET (Time-of-Flight PET) systems exploit the time difference between the two emitted photons to better locate the annihilation position. The limit in the annihilation point location is mainly due to the error in the time difference measurement, namely the time resolution Δt of the coincidence system. Time resolution is used by the reconstruction algorithm to locate the annihilation point Δx ($\Delta x = c\Delta t/2$).

Extensive work on TOF PET was done in the '80s and several TOF PET cameras were built and most of the advantages described here were experimentally verified.

But the scintillator materials used in the '80s (BaF_2 and CsF) had drawbacks (*e.g.*, low density, low photofraction) which required other performance compromises, so BGO dominated PET. Nowadays new scintillating materials like LSO (~ 200 ps) and $LaBr_3$ (< 100 ps) can provide outstanding timing resolution without other performance compromises, so TOF PET is experiencing a rebirth.

Simultaneous PET-CT systems are now available. PET needs CT data to anatomically locate the tumor and to correct for the attenuation in order to provide a correct quantification. Present systems exploit multislice CT top quality systems, where the number of slices can reach 128 with rotation time of the order of 300 ms. Being the attenuation coefficients (μ) energy dependent, the CT scanning at an average energy of 70 keV must be rescaled (voxel by voxel) to the gamma rays by using a bi-linear scaling function.

Synchronization of PET-CT acquisitions with breath cycle minimizes motion effects but limits the data statistics thus ultimately increasing the noise in the final image. The use of non-rigid registrations (NRR) among gated-PET images leads to high-quality, low-noise motion-free PET images.

An interesting alternative to PET-CT systems are PET-MR (PET and Magnetic Resonance) systems which allow to combine function (PET) and anatomy and function (MR). However there are technical challenges in realizing PET/MR systems. There is interference on PET photomultiplier and electronics due to the static magnetic field and to the RF and the gradient fields. There are also interferences on MR homogeneity and gradients due to electromagnetic radiation from PET electronics, in maintaining magnetic-field homogeneity. Moreover PET attenuation correction via MR data is a challenge.

Regarding the optimal detection system for PET in PET-MR systems, two different approaches are under investigation: scintillating crystals plus photomultiplier tubes (PMT) or scintillating crystals plus solid-state light detectors. PMTs are well understood, have stable electronics and high gain (10^6). However, Position Sensitive PMT

(PSPMT) operate in magnetic fields of 1 mT. A combination of distance (light guide) and iron shield (1–2 mm of soft iron can further reduce 30 mT $\rightarrow$ 1 mT) is used to allow PSPMT to operate in 1 mT. 1 mT has minimal effect on PSPMT performance. However long light guides reduce the energy resolution from 17 to 27%, but this should not have too big an impact upon performance. Simultaneous and isocentric MR/PET measurements can be performed. However, this system presents a small axial field of view (FOV).

The alternative to PMTs are solid-state devices, like Avalanche Photodiodes (gain ~ 150), Silicon Photomultiplier (gain $\sim 10^6$). They are less well established than PET detectors, but can operate in high static field greater than 7 T. However, there is still the need to shield devices from both gradients and RF.

P. Oliva

This page intentionally left blank

Proceedings of the International School of Physics "Enrico Fermi"
Course CLXXV "Radiation and Particle Detectors", edited by S. Bertolucci, U. Bottigli and P. Oliva
(IOS, Amsterdam; SIF, Bologna)
DOI 10.3254/978-1-60750-630-0-1

Detectors for hadrontherapy

G. A. P. Cirrone, G. Cuttone, F. Di Rosa, P. Lojacono, V. Mongelli, S. Pittera and L. M. Valastro

INFN, Laboratori Nazionali dei Sud - Catania, Italy

S. Lo Nigro

Dipartimento di Fisica ed Astronomia, Università di Catania - Catania, Italy

L. Raffaele and V. Salamone

A.O.U. Policlinico, Università di Catania - Catania, Italy

M. G. Sabini

A.O. Cannizzaro - Catania, Italy

R. Cirio and F. Marchetto

Università di Torino e INFN, Sezione di Torino - Torino, Italy

Summary. — Proton therapy represents the most promising radiotherapy technique for external tumor treatments. At Laboratori Nazionali del Sud of the Istituto Nazionale di Fisica Nucleare (INFN-LNS), Catania, Italy, a proton therapy facility is active since March 2002 and 200 patients, mainly affected by choroidal and iris melanoma, have been successfully treated. Proton beams are characterized by higher dose gradients and linear energy transfer with respect to the conventional photon and electron beams, commonly used in medical centers for radiotherapy. In this paper, we report the experience gained in the characterization of different dosimetric systems, studied and/or developed during the last ten years in our proton therapy facility.

1. – Introduction

Proton therapy represents, today, the most promising radiotherapy technique for external tumor treatments. It exploits the physical and radiobiological properties of charged ions to deliver selectively the dose to the tumor sparing the neighboring healthy tissues. The proton therapy facility developed at INFN-LNS, in collaboration with the Radiological Institute of Catania University is active since March 2002 and 200 patients have been treated. Nowadays, about twelve proton therapy centers are active around the world and more the 9000 patient have been already treated in total. Nevertheless, radiation therapy with protons still represents a pioneering technique and improvements are required in treatment clinical protocols as well as in dosimetry procedures. Proton beams are characterized by higher dose gradients and linear energy transfer with respect to the conventional photon and electron beams, commonly used in medical center for radiotherapy. For these reasons, detectors and new materials are continually tested to find better solutions for relative and absolute proton dosimetry. In this paper, we report the experience gained in the characterization of different dosimetric systems, studied and/or developed during the last ten years in our proton therapy facility. Particular attention to the parallel-plate ionization chamber with the anode segmented in strips, and on the relative dosimetry with natural and CVD diamonds, TLD MOSFET dosimeters is paid.

2. – Irradiation configuration

A proton beam is suitable for radiation treatment purposes if its spatial distribution permits the irradiation of the whole tumors volume sparing the healthy tissues surrounding the lesion. It must be spread both in the longitudinal and transversal directions using energy modulators and scattering systems, respectively. A proton beam longitudinally spread is obtained using the modulator wheel and is called Spread Out Bragg Peak (SOBP). Dosimetry of a clinical proton beam implies determination of absorbed dose at the isocenter and reconstruction of dose distributions in a tissue-equivalent phantom. The choice of the dosimeter will depend on several factors, such as the accuracy, sensitivity and size of the detector's sensitive area with respect to beam spot size, as well as dose gradients involved. In the case of the absorbed dose determination the use of an "absolute" calibrated dosimeter is required.

2˙1. *Absolute dose determination: beam calibration.* – An extensive description of the CATANA proton therapy facility and its related main clinical results can be found in [1] and [2]. The absolute proton beam dosimetry is performed using a plane-parallel *Advanced* PTW 34045 Markus Ionization Chamber. The Markus chamber has an electrode spacing of 1 mm, a sensitive air volume of $0.02\,\mathrm{cm}^3$ and a collector electrode diameter of 5.4 mm. The dose measurements are performed in a water phantom, according to the International Atomic Energy Agency Technical Report Series (IAEA TRS) 398 Code of practice [3]. The absorbed dose to water per monitor unit (cGy/M.U.) is measured at the isocenter, at the middle of SOBP, using the reference circular collimator (diameter $\phi = 25\,\mathrm{mm}$), for each combination of modulator and range shifter used for treatment [3].

2˙2. *Depth dose distribution.* – Depth dose curves both for full energy and modulated proton beams should be acquired in water as recommended by the International Protocols [3].

2˙3. *Lateral dose distribution.* – Also transversal dose measurements should be performed in water or in a water-equivalent phantom with a detector having high spatial resolution in the scan direction. Silicon diodes, radiographic films and small ionization chambers may be used for reconstruction of lateral dose distributions [1].

3. – Detectors for relative dosimetry

As in conventional radiotherapy, clinical proton dosimetry requires the measurements of central-axis depth dose distributions, transverse beam profiles and output factors.

3˙1. *Depth dose reference detectors.* – Central-axis depth dose measurements for unmodulated and modulated proton beams are performed with a PTW parallel-plate *Advanced* Markus chamber in a water phantom. It is a perturbation-free version of the classic Markus chamber, because of the wide guard ring and the smaller electrode spacing (1 mm) and, for the relative measurements, it is positioned at the center of a circular field 25 mm in diameter with the phantom surface located at the isocentre. The high electric field strength ($4000\,\mathrm{V\,cm^{-1}}$) provides a complete ion collection for dose rate up to $100\,\mathrm{Gy\,min^{-1}}$ in the continuous beam of the Superconducting Cyclotron.

3˙2. *Reference detectors for transversal dose.* – Transverse and diagonal dose profiles of the modulated proton beams are measured, in the middle of the SOBP, with radiochromic films oriented normal to the beam axis. They assure high-resolution two-dimensional dosimetry in radiation fields with high dose gradients, such as clinical proton beams. The new *Gafchromic*$^{\mathrm{TM}}$ EBT (ISP Corporation New Jersey) radiochromic film was adopted from 2005 because of the higher sensitivity than HS and MD552, the latter extensively used in the last years for radiotherapy applications. The EBT films are scanned with the Epson Expression 1680 Pro$^{\mathrm{TM}}$ RGB flatbed scanner in transmission mode, using the *FilmScan* and *FilmCal* modules of the MePHYSTO mc^2 PTW software; all EBT films are scanned in the 48-bit RGB mode, resolution of 127 dpi (0.2 mm), but only the red color channel image is used and saved in TIFF file format. The *FilmAnalysis* module of the MePHYSTO mc^2 PTW software was used for dosimetric evaluation of the EBT images. The film uniformity, evaluated according to AAPM report n. 63 [4], resulted to be smaller than 1.5% for the $5 \times 5\,\mathrm{cm^2}$ square EBT sheets, used for dose profile measurements in small eye protontherapy beams. The dose response curve (pixel value *vs.* dose) in the normal orientation for the reference collimator measured in a solid water phantom at the deph of the middle of the SOBP, is well represented in the range 0.25–7 Gy by a third-order polynomial fit; the film response resulted to be independent of the residual ranges at the irradiation deph in the range of 6 (25 MeV) to 15 mm (40 MeV); corresponding to residual ranges associated to the SOBP of the eye protontherapy. As a consequence, only one calibration file is needed to evaluate films exposed at different

Table I. – *Transverse performance of a proton beam profile with EBT Gafchromic™ films.*

	EBT*X*	EBT*Y*
P (mm)	1.01	1.08
H	0.92	0.92
S_T (%)	103.0	102.31
$W_{95\%}$ (mm)	22.0	21.81

depths. In table I beam penumbra (P), uniformity (H), symmetry (S_T (%)) and the useful treatment field ($W_{95\%}$ (mm)) (defined as the field width between the 95% points for 25 mm diameter collimator) are shown.

4. – Relative detectors

4˙1. *Natural and CVD diamond.* – The properties of natural and synthetic diamond CVD (Chemical Vapor Deposition) as radiation detectors are now known. These materials are tissue equivalent, non-toxic, resistant to radiation damage; they also show a high sensitivity, low leakage current and a good time resolution [5]. In particular, synthetic CVD diamond presents the additional advantage that can be manufactured with a controlled amount of impurities at relative low cost. Our studies were focused on the dosimetric behaviour of natural and CVD diamonds. They confirmed the favorable properties of these detectors, not only for high-energy photons and electrons therapy beams but also for a 62 MeV therapeutical proton beam. In particular, after a pre-irradiation, diamond detectors have an excellent time stabitity of sensibility. All the results obtained in our study are reported in the bibliography [6, 7].

4˙2. *Termoluminescence detectors (TLD).* – The TLD are widely used in conventional radiation therapy, their use in the field of proton therapy is relatively new and thanks to our experience we obtained good results. In fact we believe TLDs could provide an effective solution when dosimetry of small fields is required with negligible perturbation of the irradiation beam. These can be the case in the dose mapping and absolute dose measurements for the eye treatment with protons beams. Following our experience we decided to use a group of TLD-100 microcubes ($1 \times 1 \times 1\,\mathrm{mm}^3$) and ribbons ($3 \times 3 \times 0.4\,\mathrm{mm}^3$) of LiF: Mg, Ti produced by Harshaw Company. Annealing of the TLD material before the irradiation of the dosimeters has been done using the following standard procedure: 1 h heating in an oven at 400 °C; cooling at room temperature; 2 h heating in an oven at 100 °C; cooling at room temperature. A sensitivity factor has been attributed to each detector by irradiating all the dosimeters in the same geometrical set-up with a dose of 1 Gy [8]. Dosimeters were analyzed with a Harshaw 3500 reader. In these years of CATANA activity we applied TLD for different purposes: calibration at different quality beams (photons, protons, carbon ions), dose profiles, depth doses, Bragg peak

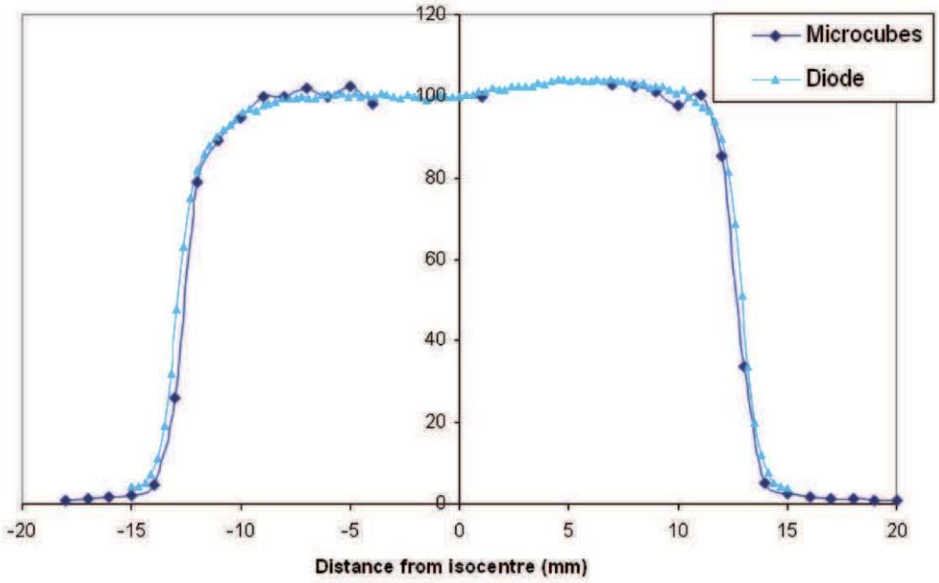

Fig. 1. – Transverse dose distribution obtained with TLD detectors and compared with the output of silicon diode. The y-axis represents the detectors responde in terms of normalized absorbed dose.

either unmodulated and modulated, output factors. We demonstrated that the same calibration curve used for photons can be also used in proton beams [9].

In fig. 1 the possibility to use TLD for transverse dose measurements is well demonstrated. The optimal agreement with silicon diode has been noted. The TLD may be used also for the reconstruction of the Bragg peak, but there is a large dependence from the radiation LET, as shown in fig. 2 [10]. On the other hand, a good agreement can be found for the reconstruction of a typical clinical Spread Out Bragg Peak, as shown in fig. 3.

Finally, a study on the radiation damage caused by high let particles as proton beams has been carried out. It demonstrated the need of a periodical TLD calibration to take into account the change in sensitivity due to radiation damage [11].

4˙3. *MOSFET dosimetry.* – Metal oxide semiconductor field effect transistor (MOSFET) detectors were proposed as a clinical radiation dosimetry, [12, 13] and the use of a dual bias dual MOSFET showed a better linearity, reproducibility and stability with respect to single MOSFET detector [14]. They are emerging as a versatile tool in various medical applications, particularly in patient dose verification [15] and in modern radiation oncology and diagnostic modality [16, 17]. The advantages of the MOSFET dosimeters include small size, immediate readout and reuse, facility of use, compactness, permanent dose storage. They are isotropic, dose rate and temperature independent. The details of the working principle of the MOSFET have been reported earlier [18,19].

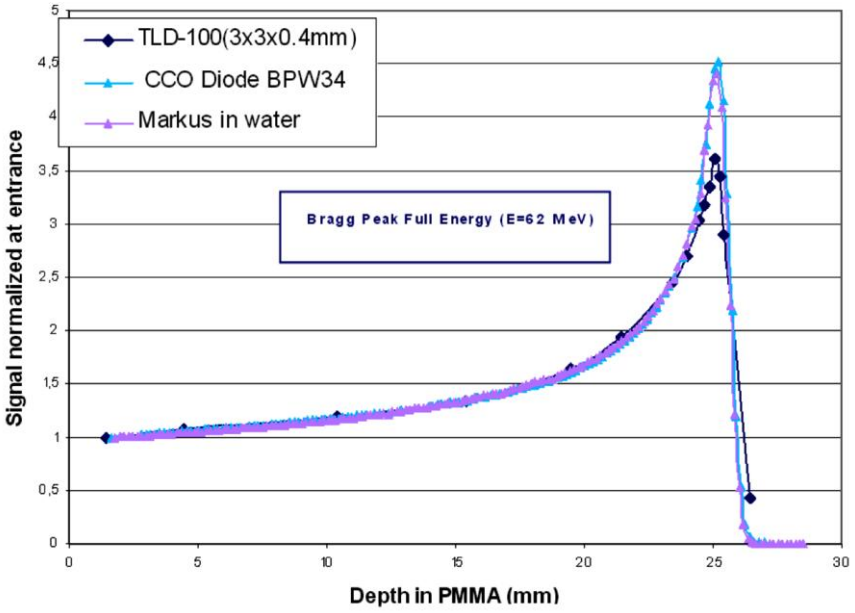

Fig. 2. – Proton Bragg peak reconstructed with TLD detectors and compared with the Markus ionization chamber and a silicon diode response.

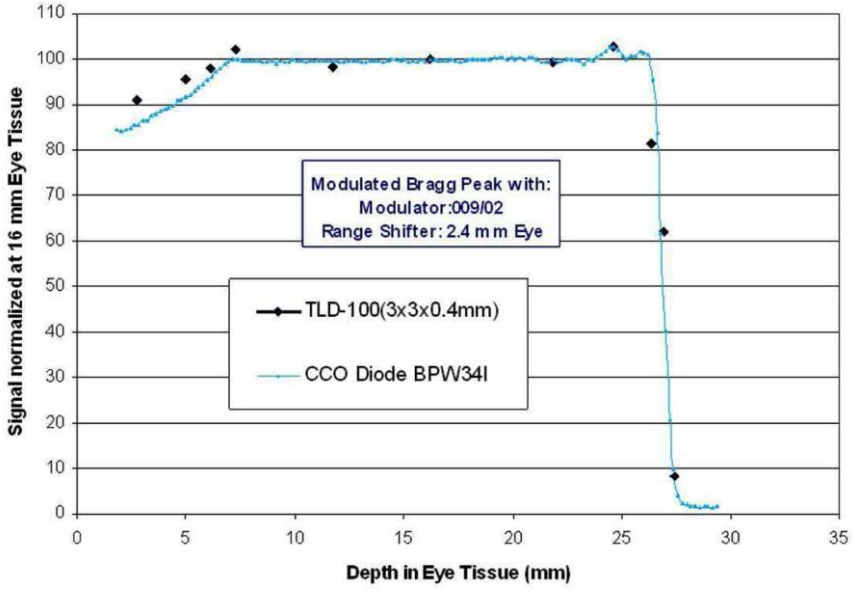

Fig. 3. – Spread Out Bragg Peak (SOBP) reconstructed with TLD detectors and compared with a silicon diode response.

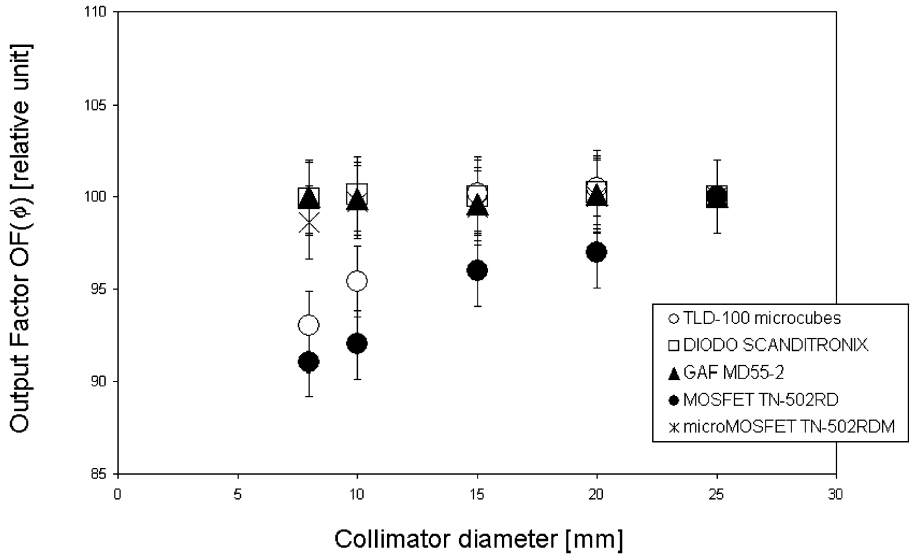

Fig. 4. – Output factors for MOSFET, microMOSFET and other detectors used in the proton-therapy routine.

Considering this favorable dosimetric characteristics of the MOSFET dosimetry, a preliminary study (linearity, reproducibility, sensitivity, energy dependence) on the use of the MOSFET dosimeters, using 62 MeV proton beams is performed. In particular, in this work, the MOSFET and microMOSFET Output Factor (OF) for small radiation fields in proton therapy are presented. Their results are compared with those obtained with other detectors chosen for the same dosimetric test. The investigated devices are the commercially available MOSFET (TN-502RD) and microMOSFET (TN-502RDM), manufactured by Best Medical Canada Ltd, (Ottawa, Canada). The microMOSFET is a commercial name for the MOSFET dosimeter with a small physical size of 1 mm × 1 mm and 1.5 mm thick. This physical size is about half the size of the standard MOSFET dosimeter. In order to verify the possibility to use the MOSFET and microMOSFET as dosimeters for small radiation fields in proton therapy, measurements of Output Factor OF(φ), defined as $L(\varphi)/L(\varphi_0)$, where $L(\varphi)$ and $L(\varphi_0)$ are the detector responses for clinical shaped collimator and for reference collimator, respectively. The irradiation setup was the following: the MOSFET, or the microMOSFET dosimeter, was positioned at the centre depth of a SOBP and irradiated with a fixed dose of 200 cGy. The measurements were carried out with five different collimator diameters: 8, 10, 15, 20 and 25 mm. The results were compared with those obtained with TLD-100 microcubes, Scanditronix silicon diode (PFD) and radiochromic film MD55-2.

The results obtained with MOSFET and microMOSFET are reported in fig. 4, normalized to the reference collimator ($\varphi_0 = 25$ mm), and compared with the OF(φ) measured with TLD-100 microcubes, silicon diode and radiochromic film. As shown in

fig. 4, the MOSFET OF(φ) are, in every case, lower than the corresponding OF silicon diode, radiochromic film and TLD microcubes.

The maximum difference found is about 9% with respect to radiochromic film, for 8 mm diameter collimator. The microMOSFET OF(φ) are close to the results of the diode and the radiochromic film. The maximum difference found is about 1.4% with respect to radiochromic film and silicon diode, for 8 mm diameter collimator. This percentage difference is comparable with the experimental uncertainty in the measurement of the Output Factor. The results of MOSFET OF(φ) show the possibility to use the MOSFET dosimeter for field diameter from 15 to 25 mm. Instead, the microMOSFET results show that they can represent an alternative to the use of the silicon diode, currently used in dose measurements of the small radiation field, involved in proton therapy of uveal melanoma.

4˙4. *MOPI.* – Inside the CATANA facility particular care is devoted to the control of beam shape and symmetry during the patient irradiation. For these purposes, in collaboration with the INFN Section of Torino (Italy), a special transmission detector was developed [20]. The detector is composed of two strips ionization chambers, ortogonally disposed, and located along the beam axis. The detector consists of two contiguous gas cells, each cell being externally limited by an anode plane and having the cathode in common. The anode is made by a kapton foil 35 μm thick covered with a 15 μm thick aluminium layer. This layer has been engraved with a standard printed circuit board technique to obtain 256 conductive strips 400 μm wide interspaced with 100 μm of electrically isolated kapton. The detector sensitive area is $12.8 \times 12.8\,\mathrm{cm}^2$ and is sourronded on three sides by a guard ring which is set to same voltage of the strips. On the fourth side the strips are narrowed and bent to reach the connector. The electric field is generated by polarizing the cathode to -500 V, while the other end of the field is provided by the strip polarization which is at $+2$ V (the same voltage as the input front-end). The described detector permits us the on-line control of the beam shape and symmetry during the irradiation. We defined a specific parameter, mathematically defined as skewness [20]. It contains the desired information on beam quality. The skewness monitoring during the irradiation represents a fundamental method to ensure the quality of proton treatment and provide an high level check of the beam.

5. – Conclusions

Ten years of proton therapy activity has permitted the test of various detectors and materials. Many national and international collaborations have been established and a large amount of scientific papers has been published. These results allow us to affirm that our facility represents an ideal workbench for the test of dosimetric system in proton therapy and give unique possibility in Italy for the improvement of the proton therapy technique.

REFERENCES

[1] Cirrone G. A. P., Cuttone G., Lojacono P. A., Lo Nigro S., Mongelli V., Patti V. I., Privitera G., Raffaele L., Rifuggiato D., Sabini M. G., Salamone V., Spatola C. and Valastro L. M., *IEEE Trans. Nucl. Sci.*, **51** (2004) 860.

[2] Spatola C., Privitera G., Raffaele L., Salamone V., Cuttone G. M., Cirrone G. A. P. and Sabini M. G., *Tumori*, **89** (2003) 502.

[3] *Absorbed Dose Determination in External Beam Radiotherapy: An International Code of Practice for Dosimetry based on Standards of Absorbed Dose to Water*, IAEA Technical Report Series-398 (2000).

[4] *Radiochromic Film Dosimetry, Recommendations of AAPM Radiation Therapy Committee Task Group No. 55*, AAPM Report No. 63 (1998).

[5] Vatnitsky S. M *et al.*, *Radiat. Prot. Dosim.*, **47** (1993) 515.

[6] Cirrone G. A. P., Cuttone G. M., Lo Nigro S., Mongelli V., Raffaele L., Sabini M. G., Valastro L., Bucciolini M. and Onori S., *Nucl. Instrum. Methods Phys. Res. A*, **552** (2005) 197.

[7] Cirrone G. A. P., Cuttone G. M., Lo Nigro S. *et al.*, *Nucl. Phys. B (Proc. Suppl.)*, **150** (2006) 330.

[8] Bucciolini M., Cuttone G., Egger E., Sabini M. G., Raffaele L., Cirrone G. A. P., Lo Nigro S. and Valastro L., *Radiat. Prot. Dosim.*, **101** (2002) 453.

[9] Bucciolini M., Cuttone G., Egger E., Mazzocchi S., Guasti A., Raffaele L. and Sabini M. G., *Physica Medica*, **XV** (1999) 71.

[10] Bucciolini M., Cuttone G., Guasti E. *et al.*, *Physica Medica*, **XVI** (2000) 131.

[11] Sabini M. G., Bucciolini M., Cuttone G. *et al.*, *Nucl. Instrum. Methods Phys. Res. A*, **476** (2002) 779.

[12] Butson M., Rozenfeld A., Mathur J. N., Carolan M., Wong T. P. Y. and Metcalfe J., *Med. Phys.*, **23** (1996) 655.

[13] Ramani R., Russell S. *et al.*, *Int. J. Radiat. Oncol. Biol. Phys.*, **37** (1997) 959.

[14] Soubra M., Cygler J., Mackay G. *et al.*, *Med. Phys.*, **21** (1994) 567.

[15] Scalchi P. and Francescon P., *Int. J. Radiat. Oncol. Biol. Phys.*, **40** (1998) 987.

[16] Chuang C. F., Verhey L. J. and Xia P., *Med. Phys.*, **29** (2002) 1109.

[17] Rosenfeld A. B., *Radiat. Prot. Dosim.*, **101** (2002) 393.

[18] Holmes-Siedle A., *Nucl. Instrum. Methods Phys. Res. A*, **121** (1974) 169.

[19] Cirrone G. A. P., Cuttone G. M. *et al.*, *Physica Medica*, **XXII** (2006) 78.

[20] Givenchi N., Marchetto f. *et al.*, *Nucl. Instrum. Methods Phys. Res. A*, **572** (2007) 1094.

This page intentionally left blank

Proceedings of the International School of Physics "Enrico Fermi"
Course CLXXV "Radiation and Particle Detectors", edited by S. Bertolucci, U. Bottigli and P. Oliva
(IOS, Amsterdam; SIF, Bologna)
DOI 10.3254/978-1-60750-630-0-11

Detection setups in applications of accelerator-based techniques to the analysis of Cultural Heritage

P. A. Mandò

Dipartimento di Fisica e Astronomia, Università di Firenze
and INFN, Sezione di Firenze - Firenze, Italy

Summary. — This paper has been written following the two lectures given by the author on the same subject at the CLXXV Course *Radiation and Particle Detectors*, of the International "E. Fermi" School in Varenna, but should not be considered in itself a comprehensive text on the subject. The basic principles of Ion Beam Analysis (used to deduce the composition of a target material) and of Accelerator Mass Spectrometry (used to deduce the concentration of rare isotopes in a sample) are recalled, and the solutions implemented for their application in the field of Cultural Heritage are described. In particular, the specific requirements for the detectors and for some beam control systems along the lines of the accelerator are discussed in some detail.

Introduction: Why Science for Cultural Heritage?

The "objective" aspects of the manufacts (age, composition, structure, techniques employed to produce them) are worth studying for a number of reasons, *e.g.*,

– attribution and authentication

– understanding the technological skills in the past

– learning about materials used in a given period and production area: the detection of materials known to be locally unavailable can, *e.g.*, prove the existence of trade exchanges from distant areas, which in ancient times is far from being obvious

– detecting deterioration processes of the work

– deciding on an informed basis the most appropriate techniques and materials to be used for a restoration.

As a consequence of the acknowledged importance of such motivations, the impact of scientific investigations on Cultural Heritage (CH) has greatly increased in recent years.

In general, the characteristics required to the techniques used for analysis in this field are minimum destructivity or, better, non-destructivity at all; minimum invasiveness, *i.e.* minimum sampling or no sampling at all; in the latter case, when the works are directly analysed without picking up samples, no damage must arise; the analytical response should be as "complete" as possible, quantitative and characterised by the highest possible accuracy and precision.

Although probably not so well known to many, accelerator-based nuclear techniques can fulfil these requirements, so that they are frequently used in applications to problems concerning works of art, or of historical and archaeological importance.

Two nuclear techniques play an especially important role in this field: Accelerator Mass Spectrometry (AMS), which is nowadays the fundamental tool for radiocarbon dating, and Ion Beam Analysis (IBA), which can provide elemental composition of materials in paintings, drawings, sculptures, and any other manufact. Both AMS and IBA require detection systems for charged particles, X-rays, gamma-rays. The detectors themselves are usually (although not always) relatively standard, but the skill of the experimenter is anyway required to create detection setups that can optimize their performance when the particular constraints in applications to CH are kept into account: for instance, the requirement of ultra-low currents for the ion beam analysis of manufacts of great value (to ensure no damage to the precious works) implies that detection efficiencies must be higher than those still acceptable for other applications of the same techniques.

These lectures will briefly describe examples of specific setups devised with just this kind of requirement in mind.

Ion Beam Analysis (IBA)

Ion Beam Analysis provides the composition of a material, by using it as a target for beam particle bombardment (typically proton or alpha beams at some MeV energy). The detection of the beam-induced emitted radiation (X- or gamma-rays, light, particles, etc.) allows us to infer the composition of the material, because the energies of the emitted radiation are characteristic of the target atoms, or nuclei. The main IBA techniques are classified according to which kind of interaction between beam particle and atom (or nucleus) is exploited:

– PIXE (Particle-Induced X-ray Emission) is a consequence of interactions of beam particles with atomic electrons: when inner shell ionizations are produced, the consequent prompt electronic transitions, from outer shells to the hole created, lead to emissions of X rays at energies characteristic of the atomic species.

– PIGE (Particle-Induced Gamma-ray Emission) is a consequence of inelastic interactions of beam particles with nuclei; these are excited and de-excite through prompt emission of gamma rays with energies characteristic of the specific nucleus.

– PESA (Particle Elastic Scattering Analysis) exploits elastic interactions with nuclei; the particle scattered at a given angle has an energy that depends on the mass of the target nucleus. The rather well known technique of RBS (Rutherford Backscattering Analysis) is the most common among PESA techniques.

In general, the features of IBA, and PIXE in particular, are such that they are very well suited for CH studies. The main feature ensuring no damage is the possibility to use very low beam currents, thanks to the high cross-section values of the processes exploited by IBA. A sort of "must" for these applications is the use of *external beams*, so as to keep the "target" in its natural atmospheric environment. When using external beams there is no need to pick up samples (non-invasiveness) regardless of the size of the work to be analysed. Besides, handling and moving the "target" is much easier. Keeping the works in atmosphere during the measurements also helps to avoid damage (*e.g.* certain materials might deteriorate owing to dehydration in vacuum). With external beam IBA the time for each analysis can be very short because of the high yields and also thanks to the ease of handling the works in the external setup. Thus, many runs are possible in order to obtain statistically more representative results. Since they are non-destructive, the measurements can be repeated (with the same or other techniques) for further checks. Finally, by varying beam energy, intensity and size one can easily find optimum experimental conditions for any given specific problem, and complementary information can be gained "free" when different "signals" (X-rays, gamma rays, particles) are simultaneously recorded.

With an external beam you can easily investigate in a non-destructive way the material composition of really many kinds of artworks (paintings, drawings, paperwork, glassware, ceramics, metal manufacts, etc.). External beam setups imply some peculiar considerations regarding their required detection setups, which will be discussed below.

Among IBA techniques, PIXE has the widest range of simultaneously detectable elements, and is characterised by very high cross-sections (fig. 1). It is therefore the "most important" IBA technique for CH.

Since —as can be seen from fig. 1 (log scale!)— cross-sections strongly decrease for higher-Z elements, to implement sensitive analysis from the lowest- to the highest-Z elements, one must exploit for the latter their L X-rays. From this consideration and from the K and L X-ray energies of the different elements (displayed in fig. 2) one can thus infer that, in order to be sensitive to elements from Na to the highest-Z through either K or L X-rays, a good detection efficiency is required over an energy range from

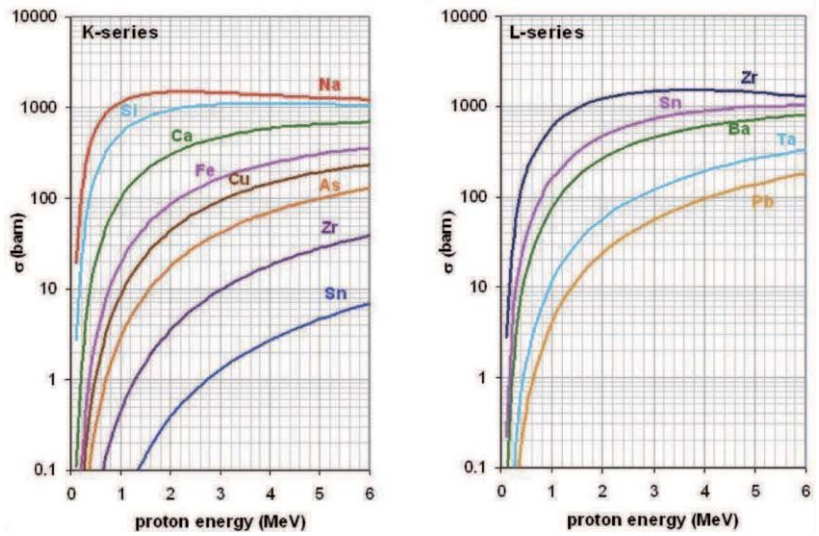

Fig. 1. – X-ray production cross-sections (left: for K series, right: for L series) by proton bombardment, *versus* beam energy. Examples are shown for some different elements.

about 1 keV to about 30 keV. This is not straightforward to be achieved and requires some special arrangements to be devised for the detection systems.

To understand why, some considerations are preliminarily needed concerning quantitative PIXE analysis.

Quantitative PIXE. – In the following, we will assume the standard detection geometry with the X-ray detector placed backwards with respect to the incoming beam

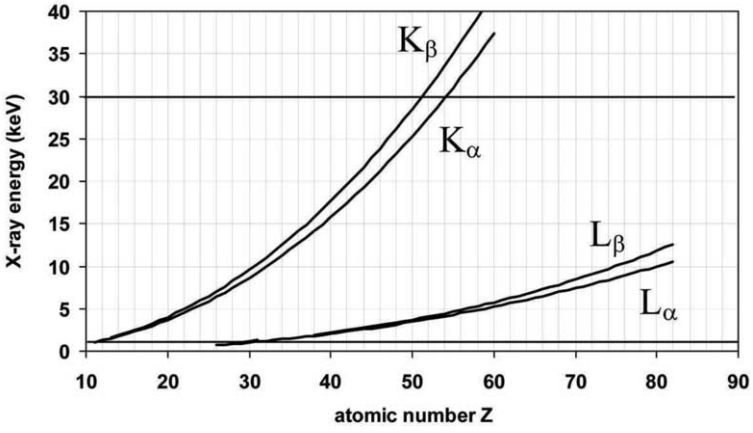

Fig. 2. – Energies of the main X-ray lines as a function of element Z.

direction (*i.e.* on the same side of the target surface). This is required in particular for thick targets, in order to allow for X-ray transmission to the detector without absorption in the target (as would happen with a detector placed behind the target, *i.e.* in a forward geometry). For the sake of simplicity, let us first consider the X-ray yield obtained by bombarding a thin target. Here, "thin" means that: 1) the beam energy loss in traversing the target can be neglected (*i.e.* all beam interactions can be assumed to occur at the same energy); 2) X-rays produced by the beam within the target —at any depth from the surface— can escape towards the detector with negligible absorption probability (no "self-absorption" effect). Both 1) and 2) depend on the target matrix composition. Self-absorption, however, is also strongly dependent on the X-ray energy (lower-energy X-rays are much more severely absorbed) and therefore on the atomic number Z of the element to be detected: the lower the Z, the lower the X-ray energy, and therefore the more stringent the requirement of small thickness for a target to be considered "thin" with respect to the detection of that element. As a matter of fact, one can easily see that, under typical PIXE measuring conditions, a target of up to, let us say, few tens of $\mu\mathrm{g\,cm^{-2}}$, can still reasonably be considered thin for the detection of all elements down to Na. The beam energy loss is negligible (in terms of its effect on X-ray production cross-section) for a typical proton beam of 2–3 MeV energy, and also negligible is the X-ray self-absorption in the target, even for X-rays down to 1 keV, *i.e.* Na K X-rays.

In the hypothesis of a thin target, the yield of detected X-rays (Y_z) from a given element of atomic number Z in the target is simply given by the product of

- X-ray production cross-section σ_{X} at the beam incident energy,
- number of atoms of the element Z per unit target area, $\frac{N_{\mathrm{Avog}}}{A_Z}\rho_Z\, t$, with t the target thickness,
- number of incident beam particles (can be expressed as $\frac{Q}{e}$, with Q the beam charge fluence during the run and e the elementary charge),
- detection efficiency, which, in turn, is the product of:
  - geometric efficiency (solid angle $\Omega/4\pi$)
  - intrinsic detector efficiency $\varepsilon_{\mathrm{det}}$
  - transmission α_Z through the absorbers possibly present between X-ray emission point and detector.

In summary, one has

$$Y_Z = \sigma_{\mathrm{X}} \left(\frac{N_{\mathrm{Avog}}}{A_Z}\, \rho_Z\, t \right) \frac{Q}{e} \left(\frac{\Omega}{4\pi} \right) \varepsilon_{\mathrm{det}} \alpha_Z. \tag{1}$$

We have seen in fig. 1 which are the X-ray production cross-sections. Let us now discuss the other parameters affecting the X-ray yield. Figures 3 and 4 show the calculated values of the transmission coefficient α_Z through various media, as a function of X-ray

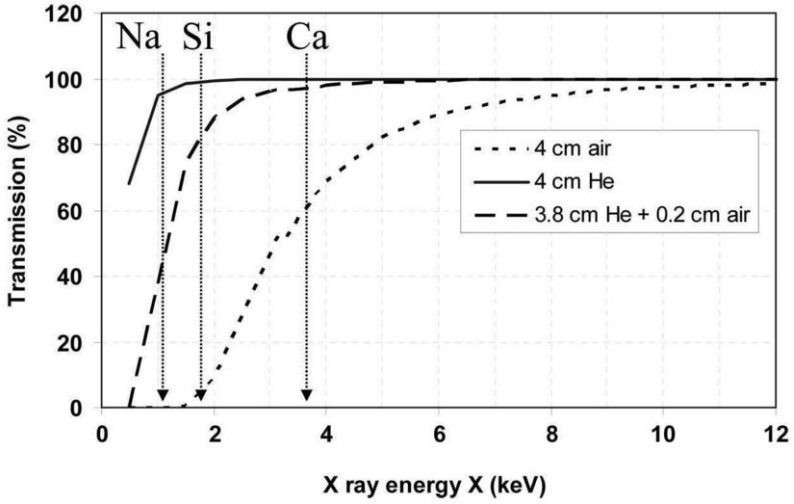

Fig. 3. – Transmission *vs.* X-ray energy through different gaseous media.

energy. Figure 3 refers to a gas medium and clearly shows that even a few centimeters of air strongly attenuate X-rays of low energy. If, instead of air, the path from the X-ray origin (the impact point of the beam on the target) to the detector is flooded with helium, the transmission of even the 1 keV X-rays of Na is again almost 100%. However, even a small amount of residual air, as can be seen, is critical at such low energies. Figure 4 instead shows the effect on transmission of a Mylar absorber: it can be seen that even through a thin layer (the example in the figure refers to 425 μm thickness) X-rays of low-Z elements are not transmitted at all, and those of medium-Z elements are still remarkably affected. These considerations are useful to design an appropriate detection setup; the topic will be discussed below.

Figure 5 shows the intrinsic detection efficiency $\varepsilon_{\mathrm{det}}$ of commercial Si(Li) detectors for X-rays. Intrinsic detection efficiency is the fraction of X-rays that after reaching the detector surface produce a full energy signal from the detector (photoelectric absorption within the detector's active volume). As one can see, the efficiency is substantially 100% in a range of X-ray energies from a few keV to about 15 keV. The efficiency drop at low energies is due to the effect of the detector entrance window (the three curves refer indeed to three different Be window thickness values); the drop at high energy depends on the limited thickness of the detector-sensitive volume (the two curves refer to active volume thickness values of 3 and 5 mm, with that corresponding to 5 mm extending indeed with higher efficiency towards higher X-ray energies).

In summary, the intrinsic efficiencies of these commercial detectors can be reasonably high (above 40%) within a range of X-ray energies from 1 keV to 30–35 keV.

Recently, Silicon Drift Detectors (SDD) [2] are increasingly used for X-ray detection instead of Si(Li) detectors. SDDs are characterized by a much smaller active thickness (500 μm maximum), and therefore a lower intrinsic efficiency at the high-energy end of

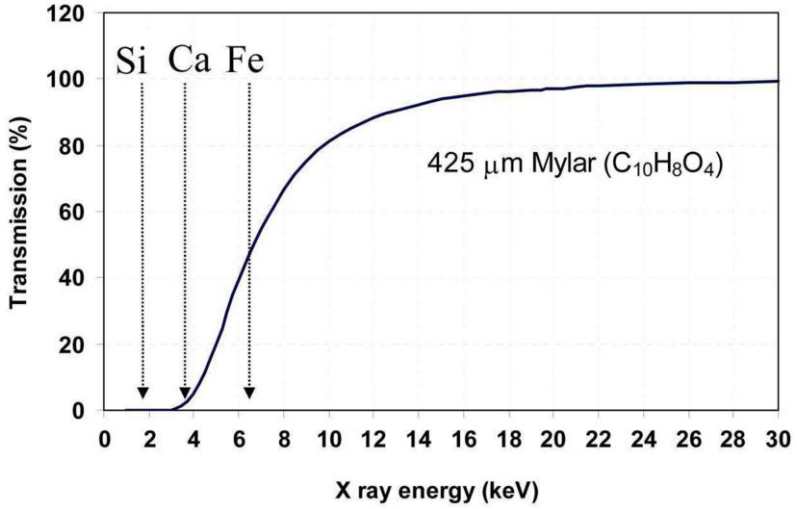

Fig. 4. – Transmission *vs.* X-ray energy through a Mylar absorber of 425 μm thickness.

the desired range of detection. Figure 6 shows the trend of intrinsic efficiency of SDDs of 300 and 500 μm thickness in the X-ray energy region 10–100 keV, compared to the one of a 3 mm thick Si(Li) detector.

The lower efficiency in the higher-energy region is a drawback for the use of SDDs for the detection of higher-Z elements. Apart from this drawback, in all other respects

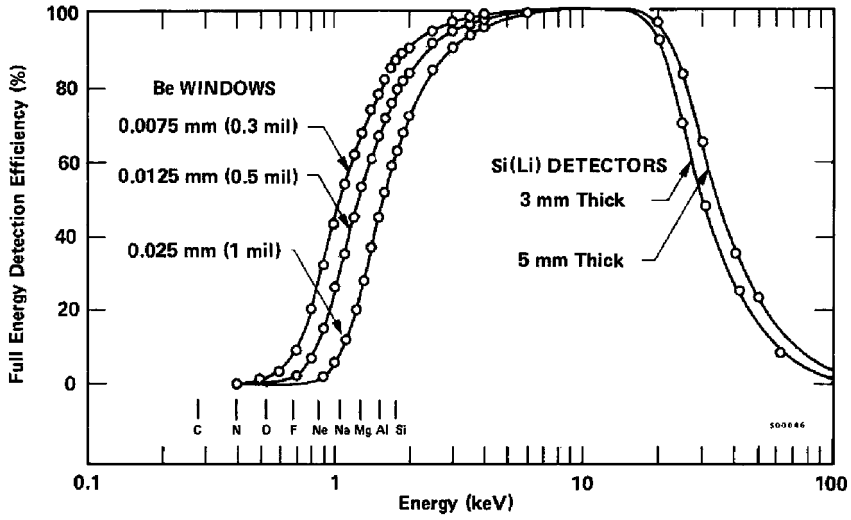

Fig. 5. – Intrinsic detection efficiency $\varepsilon_{\mathrm{det}}$ of commercial Si(Li) detectors for X-rays (from ref. [1]).

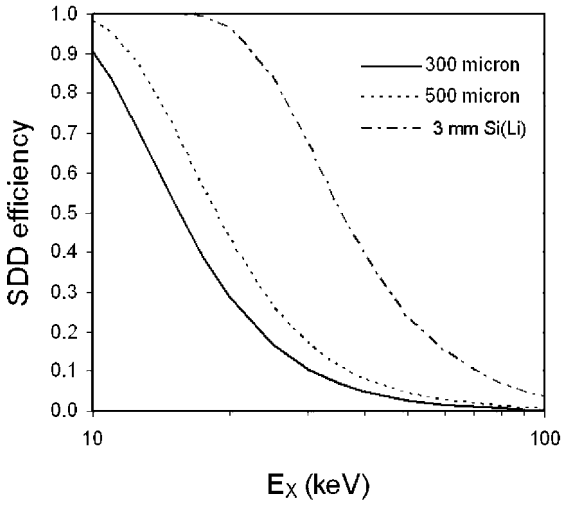

Fig. 6. – Intrinsic efficiency of SDD detectors of 300 and 500 μm thickness, compared to a 3 mm Si(Li), in the energy region 10–100 keV.

last-generation SDDs are preferable to Si(Li) detectors because, first, they can operate at near-room temperature, thus only requiring very simple Peltier cooling; second and most important, thanks to the much smaller effective capacitance due to their peculiar "architecture", their signals can be formed with much shorter shaping times ($\approx 1\,\mu$s *vs.* 10–20 μs of the Si(Li) detectors) still keeping low noise; thus, they work well at much higher count rates, and they have comparable or better energy resolution (even < 130 eV FWHM at 5.9 keV). Therefore, at lower X-ray energies they are surely preferable, also considering that these X-rays are produced with higher cross-sections and therefore give rise to higher count rates.

In connection with the matter of energy resolution (which, needless to say, is an important issue to discriminate in the spectra closely lying X-ray energy peaks from different elements) it may be worthwhile to open a parenthesis.

Table I shows some relevant numbers for silicon detectors. Using a value of 3.65 eV for the energy required to create an electron-hole pair in silicon, and a Fano factor 0.12, in table I the total FWHM is calculated for different X-ray energies in the hypothesis of two cases of electronic noise FWHM, 63 and 106 eV (the statistical FWHM is then added quadratically to calculate the total FWHM).

The same information is given in a visual way in fig. 7.

It is apparent that a lower electronic noise, such as often granted by SDDs with respect to Si(Li)s, is a remarkable advantage in the low-energy region (corresponding to lower-Z elements) where SDDs also display good intrinsic efficiency because their lower thickness is not a problem there. Also considering that lower-Z elements' X-rays are produced with higher count rates (and SDDs have a much higher count rate

TABLE I. – *Total FWHM resolution of silicon detectors at different X-ray energies, keeping into account the statistical FWHM and under two different hypotheses of electronic noise FWHM. All numerical values are given in eV. Calculations assume a Fano factor value of* 0.12*, and an energy required to create an electron-hole pair in silicon equal to* 3.65 eV.

	X-ray energy	$FWHM_{stat}$	FWHM tot	
			$FWHM_{el}$ 63 eV	$FWHM_{el}$ 106 eV
Na-K	1040	50	80	118
Si-K	1740	65	90	125
Mn-K	5900	119	135	160
Fe-K	6400	124	139	164
Cu-K	8040	139	153	175
	10000	156	168	188
	20000	220	229	244
	30000	269	277	290

capability, see above), it can be understood why these detectors are increasingly used in PIXE for the low-energy X-rays detection. For the higher-energy X-rays, instead, the advantage in terms of energy resolution is not relevant because the statistical FWHM is dominant, and also the better performance at higher count rate is in general unexploited because production cross-sections of higher-energy X-rays are much lower. Therefore, no

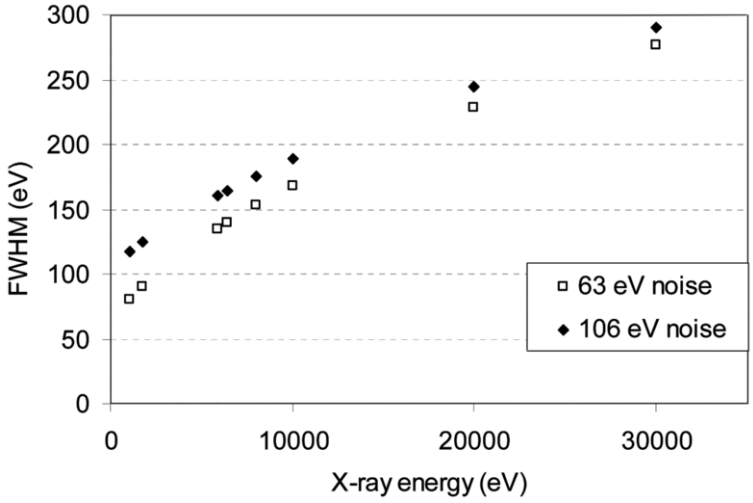

Fig. 7. – Total FWHM resolution of silicon detectors at different X-ray energies, under two different hypotheses of electronic noise FWHM.

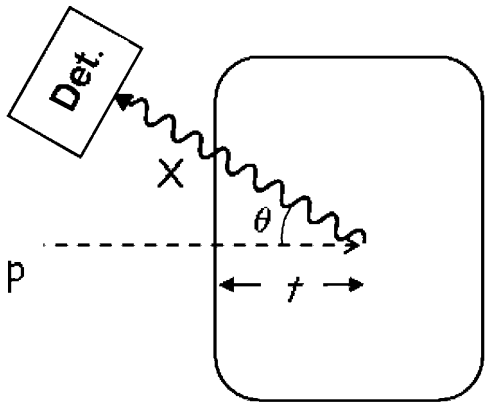

Fig. 8. – Sketch of a thick-target detection geometry (see text).

advantage "compensates" the fall in intrinsic efficiency of SDDs with respect to Si(Li)s, and the latter detectors are still preferred for the PIXE detection of medium or high-Z elements (either through K X-rays for medium-Z elements, or through L X-rays, for the highest Z).

The case of the quantitative analysis of a thick target is not difficult, provided the composition is homogeneous throughout the depth investigated. One has to consider that two "matrix effects" take place: 1) the beam energy decreases while penetrating into the target (thus affecting the X-ray production cross-section at different depths); 2) X-rays produced at different depths are absorbed within the target itself while traveling towards the detector.

With reference to fig. 8, eq. (1) becomes:

$$Y_Z = \left(\frac{N_{\mathrm{Avog}}}{A_Z}\,\rho_Z\right)\frac{Q}{e}\left(\frac{\Omega}{4\pi}\right)\varepsilon_{\mathrm{det}}\alpha_Z\int_0^T \sigma_{\mathrm{X}}\,\mathrm{d}t\,e^{-\mu\frac{t}{\cos\vartheta}}, \tag{2}$$

where t is the depth coordinate and T is the target thickness (or the beam range if the target is thicker than the range), and θ is the angle backwards of the detector with respect to the incoming beam direction (the target is here assumed to be perpendicular to the beam).

Equation (2) can be rewritten with the integral over beam energy rather than over depth in the target, by using the beam stopping power $S(E) = \frac{\mathrm{d}E}{\rho\mathrm{d}t}$. If, in addition, the composition is homogeneous throughout the whole depth, ρ is constant and one has

$$Y_Z = \left(\frac{N_{\mathrm{Avog}}}{A_Z}\right)\frac{Q}{e}\left(\frac{\Omega}{4\pi}\right)\varepsilon_{\mathrm{det}}\alpha_Z\frac{\rho_Z}{\rho}\int_{E_0}^{E_0-\Delta E}\sigma_{\mathrm{X}}(E)\,\frac{\mathrm{d}E}{S(E)}\,e^{-\mu\frac{t(E)}{\cos\vartheta}},$$

with ΔE the beam energy loss through the target thickness T. Often the case is the one of an "infinitely thick" target (*i.e.* the beam range is smaller than the target thickness),

so that the relationship becomes

$$Y_Z = \left(\frac{N_{\mathrm{Avog}}}{A_Z}\right)\frac{Q}{e}\left(\frac{\Omega}{4\pi}\right)\varepsilon_{\mathrm{det}}\alpha_Z\frac{\rho_Z}{\rho}\int_{E_0}^{0}\sigma_{\mathrm{X}}(E)\frac{\mathrm{d}E}{S(E)}\,e^{-\mu\frac{t(E)}{\cos\vartheta}}. \tag{3}$$

If the integral can be calculated, this equation relates the obtained yield and the delivered beam charge (both measurable) with the unknown concentration of element Z in the target (*i.e.* $\frac{\rho_Z}{\rho}$), all the other terms being either constants or depending on the known characteristics of the detection setup.

To calculate the integral, one has to know the target matrix composition, which is needed to evaluate $S(E)$ and μ (and $t(E)$ as the inverse function of $E(t)$, obtained in turn from S). The composition however can be *a priori* unknown (it is often just the goal of the measurements!). Nevertheless, an iterative procedure can be performed: in the first step, one neglects matrix effects, using therefore eq. (1) for thin targets to obtain a first approximation of composition (from the yields of the various elements); this composition is then used to compute $S(E)$ and the μ values in the matrix for the various detected X-rays. The integral in eq (3) is now calculated using these values, and a second approximation of composition is obtained, and so on until the procedure converges (although conceptually equivalent, in practice a different procedure is adopted by the most common software codes for thick-target analysis [3, 4]). It is to be noted that the procedure is anyway correct only for homogeneous targets throughout the target depth (the target density ρ has been carried out of the integral). In the case of non-homogeneous targets, the situation is more complicated and the quantitative analysis becomes more difficult. However, it be can be somehow tackled *e.g.* by repeating PIXE runs with different beam energies (so-called differential PIXE), deducing information about depth inhomogeneities from the comparison of results at different energies.

PIXE external beam setups. – Let us go back to the design of a sensible PIXE detection setup using an external beam and effectively covering the widest possible range of elements. It is first of all clear that it is impossible to be sensitive to elements below Na, because (fig. 3) already at a small distance from the target the absorption of their X-rays in the atmosphere becomes prohibitive (even in case a light gas like He is flooded in front of the detector, a very small residual air would anyway drastically reduce transmission). In addition, even the thinnest available detector entrance windows would severely absorb X-rays below 1 keV (fig. 5). Apart from this, there would seem to be no other limitations from the point of view of the detectors, because the upper energy limit for a good intrinsic detector efficiency covers well the range of K X-rays of medium-Z elements and L X-rays of high-Z ones, while the absorption in air is not a problem at their corresponding energies. However, detector efficiency and X-ray transmission are not all the business. In order to have a "balanced" yield at different Z, one must also keep the different cross-sections into account. And although using L X-rays rather than K X-rays for high-Z elements can help, the balance is not well achieved. Let us make a numeric example exploiting eq. (1).

Take, *e.g.*, a 0.1 μm foil of Si_3N_4 ($\rho = 3.4\,\mathrm{g/cm^3} \rightarrow \rho t = 34\,\mu\mathrm{g\,cm^{-2}}$) $\rightarrow 14.6\,\mu\mathrm{g\,cm^{-2}}$ of Si.
With 100 pA of protons for 100 s $\rightarrow Q = 10^{-8}$ C;
with a detector of 0.1 $\mathrm{cm^2}$ at 5 cm $\rightarrow \Omega/4\pi = 3.2 \cdot 10^{-4}$;
for 3 MeV protons, $\sigma_X(\mathrm{Si}) \approx 1000\,\mathrm{barn} = 10^{-21}\,\mathrm{cm^2}$;
at $E_X = 1.74$ keV (energy of Si X-rays) $\varepsilon_{\mathrm{det}} \approx 1$, $\alpha_Z \approx 1$ in He.

From eq. (1) one obtains: $Y_Z = 10^{-21} \cdot \frac{6 \cdot 10^{23}}{28} \cdot 14.6 \cdot 10^{-6} \cdot \frac{10^{-8}}{1.6 \cdot 10^{-19}} \cdot 3.2 \cdot 10^{-4} = \approx 6000$ Si X-ray counts, which is good statistics for such a short measuring time with such a weak beam current and thin layer.

However, if you take the same thickness of silver, *i.e.* a 0.1 μm layer of Ag ($\rho = 10.5\,\mathrm{g/cm^3} \rightarrow \rho t = 105\,\mu\mathrm{g\,cm^{-2}}$ of Ag), considering that $\sigma_{X,K}(\mathrm{Ag}) \approx 2.3\,\mathrm{barn} = 2.3 \cdot 10^{-24}\,\mathrm{cm^2}$, and still (reasonably) assuming $\varepsilon_{\mathrm{det}} = 1$, $\alpha_Z = 1$, the corresponding calculation gives only ≈ 25 Ag X-ray counts.

If you now have a target where both light elements (X-rays produced with high cross-sections) and heavier elements (lower cross-sections) are present, it is a problem to have a balanced count rate for both, especially if you have (as is often the case) a light matrix (abundance of low-Z elements) and you are also interested in detecting the heavier elements in the target. To increase the count rate of X-rays from these heavier elements, you cannot increase the current because, apart from the problems of the possible damage to the target, your detector would start to be in trouble owing to the light elements in the target producing too high a count rate. Nor can you increase the solid angle, for the same reason. The solution is then to use two different detectors, playing with the solid angles covered and the absorptions in front of each.

One of the detectors covers the largest possible solid angle and can thus collect enough statistics also of X-rays from the higher-Z elements (the large solid angle compensates the low cross-sections). Si(Li) detectors of about 1 $\mathrm{cm^2}$ surface and 5 mm thickness are available, and in typical geometries you can place them as close as at 3 cm distance from the target ($\Omega/4\pi = 8.8 \cdot 10^{-3}$). To avoid being overwhelmed by the large count rate due to the low-energy X-rays from lower-Z elements, this detector can be shielded by a proper absorber (say, a few hundred micron Mylar) which absorbs the largest fraction of these X-rays but affects much less, if not at all, the higher-energy X-rays (absorption strongly depends on X-ray energy!).

Owing to the absorber, the detector is not sensitive to the light elements. Another detector is then used for these elements; for this second detector, X-ray absorption is minimized, *e.g.* by flooding with He the volume from target to detector, and the acceptance solid angle is kept smaller to reduce count rate (it can, *e.g.*, be collimated). The small solid angle implies very low statistics for higher-energy X-rays on this detector (but you have the first detector for them!).

In summary, the count rate can be made comparable for X-rays from both low-Z and high-Z elements, but on two different detectors. Depending on the specific target, this balance can be optimized by properly changing collimation on the smaller solid angle detector, and absorber thickness and material in front of the larger solid angle detector.

Figure 9 shows a sketch of a two-X-ray-detector system.

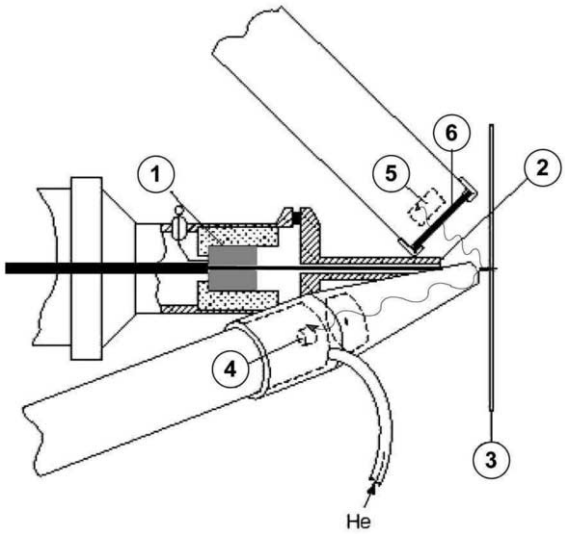

Fig. 9. – Sketch of the Florence external beam PIXE setup using two detectors. 1) Beam collimator in vacuum; 2) beam exit window; 3) target; 4) silicon detector with small solid angle and minimum absorption; 5) silicon detector with large solid angle; 6) absorber.

The solution of simultaneously using two X-ray detectors with different solid angles —the smaller with absorption minimized thanks to He flow and the larger with an explicit absorber of appropriate thickness and material— was first introduced as a routine setup by our group in Florence [5], and has now become a standard whenever the analytical goal is the one of a quantitative analysis covering the largest possible range of elements. Figures 10 and 11 show the number of counts per unit charge delivered and per unit areal density of a given element in the target, collected by the two simultaneously used detectors in a typical external beam setup, using 3 MeV protons. It is apparent that for all elements with $Z > 10$, *i.e.* from Na included, high statistics can be collected in short measuring times and with low beam currents, exploiting either one or the other of the detectors, and either K X-rays or L X-rays.

There is another issue to take into account for the detector with helium flow in front of it. Appropriate systems are required to avoid that backscattered particles be also transmitted to the detector. Indeed, they would release in the detector active volume an extremely higher energy per pulse than the X-rays, for which the front-end electronics is designed, and this would give rise to serious problems in signal handling.

The problems can be solved either via "hardware" tricks or via electronic handling of the signals.

A possible hardware solution is to magnetically deflect the backscattered particles: small permanent magnets produce sufficiently intense magnetic fields to deflect the particles along their path from target to detector (the X-rays are obviously unaffected). Alternatively, the use of a polycapillary X-ray lens has been proposed and tested [6, 7].

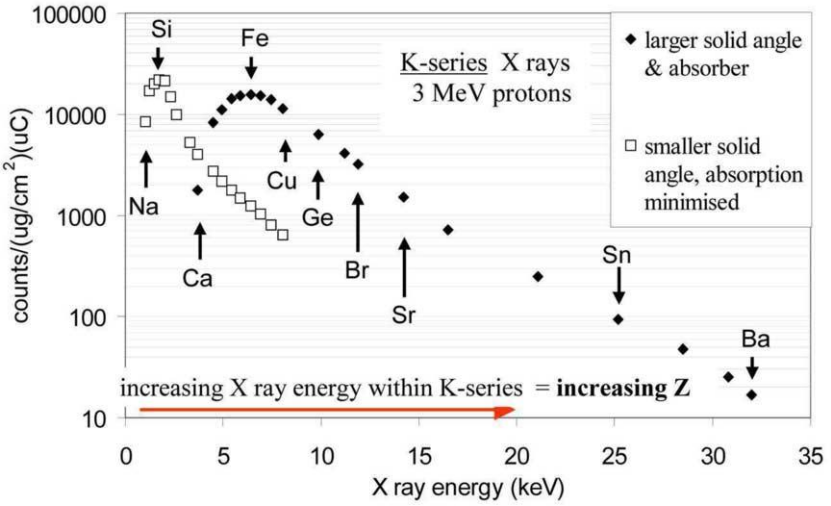

Fig. 10. – Number of counts of K X-rays per μCoulomb of beam charge delivered, and per μg/cm^2 of element in the target, collected by the two simultaneously used detectors in a typical external beam setup (experimental data using thin standards of known areal densities, and a beam of 3 MeV protons).

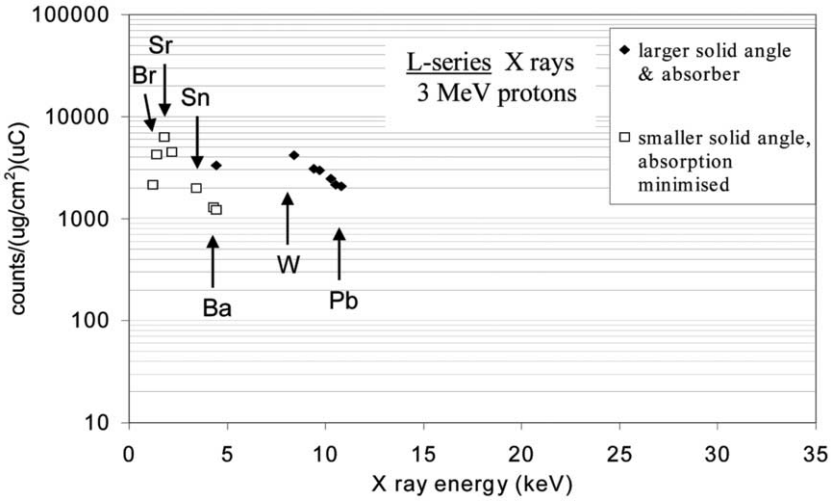

Fig. 11. – Same as fig. 10, but for L X-rays.

It is placed in front of the X-ray detector, and "drives" X-rays to the detector surface, which is much farther away (the capillaries must also be kept in vacuum within the cryostat, to avoid absorption of soft X-rays). The effective acceptance solid angle for X-rays —which is set by the distance from target to lens front, quite close to the target— is thus much larger than the one for particles, which depends on the effective detector distance.

The electronic solution consists instead in acknowledging large pulses just at their start (*e.g.* based on their different leading edge slope in the front-end electronics) and somehow suppressing them by forcing baseline restoration, thus avoiding deep saturations at the subsequent amplifying stages [8].

External scanning microbeams. – Another issue to be mentioned in connection with the peculiar setups that find applications also in Cultural Heritage problems is the use of external scanning microbeams. Indeed, when a beam of very small size is needed (let us say below 200–300 μm) because a selective analysis of very small details is desired, the technique of simply collimating the beam is not appropriate to achieve the desired size. As a matter of fact, scattering on the collimator's edges creates undesired lateral tails in the beam intensity distribution, thus producing an effective beam size larger than the "ideal" one that would be expected from the collimator dimensions. Strong focusing of the beam is then necessary in these cases. In our laboratory, using a quadrupole doublet at the end of a dedicated beamline, the beam is strongly focused to a size that for protons can be as small as 8 μm *on target* (in atmosphere) [9]. To minimise scattering effects that would spoil space resolution, the beam exit windows are ultrathin Si_3N_4 films (the thinnest are 0.1 μm thick) and the target is placed very close to the window, about 3 mm. The standard detection system, as in the setup with external collimated beam shown in fig. 9, includes two detectors for X-rays; one can also use a detector for gamma-rays, and one for backscattered particles —the latter still keeps very good energy resolution (around 15 keV) in spite of the external setup causing some energy straggling of the scattered particles. A picture of the overall detection setup at the external microbeam line is shown in fig. 13.

Beam scanning is magnetic, thanks to coils placed immediately before the quadrupole doublet, and is coupled to a multiple-input list-mode acquisition; the inputs of the acquisition system are the signals from the various detectors and the beam x-y coordinates on the target (obtained by the values of the coils currents). The acquisition system associates to each detection event the x-y position of the beam at the instant of detection. So, one can reconstruct distribution maps of X- and gamma-rays, or of signals from other detectors, over the scanned area.

The system is typically used with 3 MeV protons, but we have worked with external microbeams of protons from 1 to 5 MeV and with heavier ions, too. Proton microbeam current on target can be up to some nA (at maximum focusing) but can be easily tuned to much lower intensities when needed (*e.g.* to avoid damage). The facility is providing a unique tool for analysis also in Cultural Heritage problems (besides geology, electronics, chemistry, biology). An example was its use for the analysis of a portrait by Antonello

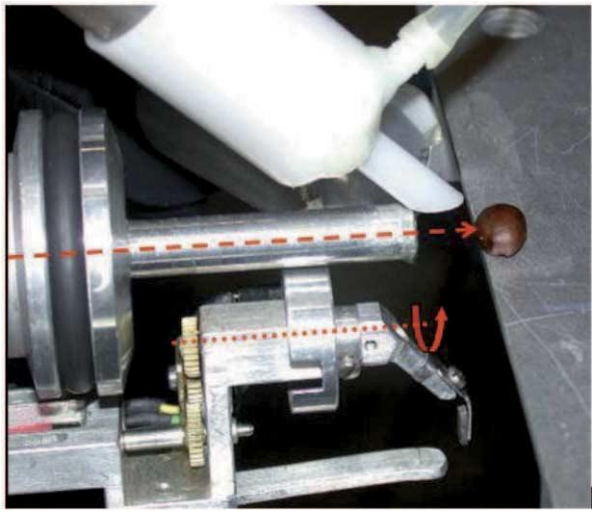

Fig. 12. – The rotating-arm device for indirect beam current measurements (in the displayed picture, the target was a coffee seed).

da Messina, the great Italian Renaissance master: external microbeam scanning on some areas of the painting was very effective in answering questions raised by the restorers in view of their intervention. For instance, it was found that to render the folds of the portrayed gentleman's mantel, Antonello had made a peculiar use of a dark red lacquer irregularly distributed on top of a cinnabar bright red layer [10].

Measurement of beam current. – Another instrumental implementation is necessary to allow for quantitative analysis with IBA: systems are needed to indirectly measure the ultralow beam currents used for CH problems (often few pA), which is not easy especially in external beam setups. Besides being necessary to extract quantitative data from the spectra, monitoring the current is also important prior to and during the measurement to choose and maintain the appropriate beam intensities to avoid damage to a precious target such as is the case in CH problems.

The targets are almost invariably thick, *i.e.* not traversed by the beam. Therefore some device to measure the current before the target is needed. Several solutions have been adopted in different labs. In our laboratory, depending on the circumstances, two indirect current-measuring systems are employed.

In one of them (normally used with the collimated beam setup), a small arm continuously rotates in front of the beam exit window, just before the target (the target is typically at about 1 cm from exit window, so there is enough, although not large, clearance left to allow for the rotation of the arm). The arm intercepts the beam approximately once per second. It is made of graphite, on which some metal, such as nickel, is deposited. Each time the arm intercepts the beam, Ni X-rays are produced and detected, the number of them being proportional to the beam charge integrated during the transit

of the arm in front of the beam. At the end of the measurement, the total number of collected Ni X-rays will therefore be proportional to the beam charge delivered to the target (provided a sufficiently large number of "samplings", *i.e.* beam transits in front of the beam, has taken place in order to average over possible beam intensity fluctuations). The proportionality constant between Ni counts and beam charge can be measured for a given geometry, placing *e.g.* a Faraday cup in the place of the target. Figure 12 shows the rotating-arm device during the analysis of a coffee seed (not exactly a Cultural Heritage item indeed; but Ion Beam Analysis is a very general technique!).

Another beam charge measuring system is adopted when the available space between exit window and target is too little to permit a safe use of the rotating arm. This is the case of the external microbeam setup. As mentioned above, here we use a Si_3N_4 exit window. The beam exit nozzle is shaped in such a way that a dedicated X-ray detector can see and detect only Si X-rays from the window, while remaining shielded from those produced in the target. Thus, the number of Si X-rays on this detector will be proportional to the overall charge traversing the window, *i.e.* the one delivered to the target. Here, too, the system can be calibrated against actual charge delivered. Figure 13 shows the setup.

Accelerator Mass Spectrometry (AMS)

We will not describe here in detail how and why AMS effectively works as an ultra-sensitive rare isotope detection system, in particular for the measurement of ^{14}C concentration for dating purposes (a recent survey on this subject is given, *e.g.*, in [11]).

Let us only recall the main principles. In AMS a beam is produced in the ion source out of the material which has to be analysed in its mass composition; after acceleration, ions of different mass in the beam are separated by a number of selective elements (magnets, electrostatic analysers), and the rare isotope searched for is quantified just by measuring the number of counts on an ion detector, which in principle (if all the filtering processes have worked properly) should only be reached by the ions of the searched isotope. So, here again as in IBA, all depends on some appropriate detector working properly. In this case, "working properly" means that detectors should provide unambiguous information allowing the experimenter to discriminate "good" counts from spurious ones deriving from residual unwanted ions of other isotopes reaching the detector.

The big "enemy" in any mass spectrometry analysis is the presence of isobars. In AMS, most of the work, indeed, is already done by the mass-charge-energy filters along the beam trajectory prior to the detector; the latter, to a very good approximation, is indeed reached only by the "good" ions (in the case of archaeological dating, for instance, ^{14}C ions, which have been separated from ^{12}C and ^{13}C and transmitted to the detector).

Concerning ^{14}C isobars, ^{14}N is eliminated already at the source level, since the ion sources of Tandem accelerators produce negative ions, and nitrogen does not form stable negative ions while carbon does. However, negative ions of *molecular* isobars are also produced ($^{12}CH_2$ and ^{13}CH) in the source, in a much larger number than ^{14}C. Thus, they must be eliminated. This is what happens in AMS, using a Tandem accelera-

Fig. 13. – Final part of the external microbeam setup [9] at LABEC-INFN in Florence, showing in particular the system used for beam current monitoring. This includes a third X-ray detector (the one below the beamline), which detects Si X-rays from the exit window, made of an ultrathin Si_3N_4 layer. The exit nozzle is shaped with the inclined exit window and an "appendix" below (vacuum-sealed by a thin Upilex window on the rear side —not visible therefore in the picture). This exit nozzle geometry allows the dedicated detector to see only X-rays from the window; instead, those produced on the target, which is usually placed two or three mm downstream, cannot reach the dedicated detector because they are out of its unshielded sight. Also visible in the picture are the two X-ray detectors of our standard X-ray detection setup, the larger cryostat of a gamma-ray detector (on the left), a viewing camera and, above the exit nozzle, a cone containing a particle detector for backscattering measurements.

tor: after the first stage of acceleration, during the negative-to-positive charge exchange through stripping at the high-voltage terminal, the molecular isobars dissociate so that, ideally, after the second stage of acceleration only ^{14}C ions should have the appropriate charge-energy-mass combination to be transmitted by the subsequent magnetic analysis. In practice, however, some residual spurious ions can pass the magnetic filter, owing to some charge exchange processes taking place along the accelerator tube during the second stage of acceleration, caused by interactions with residual gas molecules. Some of these processes can produce ions other than ^{14}C, but having such a combination of mass-energy-charge as to give them the same magnetic rigidity of the "good" ^{14}C ions. Thus, they follow the same trajectory in the magnetic field. An electrostatic analyser is then placed downstream along the trajectory to kill these unwanted ions that have "deceived" the magnet (obviously, ions with two different mass-energy-charge combinations cannot follow the same trajectory in *both* a magnetic field *and* an electric field). After these steps, therefore, the final detector might in principle be just a counter with no discriminating capability, because only good ions should reach it. But ... you never know ... even "wrong" ions that should be nominally discarded in the magnetic analysis

and/or in the electrostatic one might indeed be still transmitted along slightly different trajectories, owing, *e.g.*, to forward scattering on the beamline walls. This is why the final detection setups are often provided with further discrimination capabilities, such as time of flight, or $\Delta E - E$.

They still remain, however, rather standard detection systems. The final particle counting is usually performed by ionization chambers (alternatively, by solid-state particle detectors), implying no special arrangements.

What can be, instead, a challenge is the implementation of ultrasensitive beam profile monitors (BPM) for the rare isotope beam along its trajectory. One way to discriminate against the (few) residual spurious particles is in fact to acknowledge their different trajectories; accelerator parameters can then be finely tuned in order to avoid these parasitic particles, thus minimizing the residual background. A beam profile monitor is the appropriate tool to perform this job, but the residual beams after the main filters are typically made of only few tens of particles per second, at most. So, commercial BPMs, with a sensitivity of hundreds of pA at their best, are of no use. The solution we adopted [12] was to place a retractable x-y multiwire proportional chamber just after the final main filter (in our case, the high-energy electrostatic analyser). The device can be inserted along the beam trajectory while tuning, and the impact points are acquired particle by particle, with a dedicated hardware acquisition system and appropriate software reconstructing in real time the x and y profiles of the "few-particles" beam. Particles on "anomalous" trajectories are immediately acknowledged by their off-axis impact points on the multiwire chamber, and the various accelerator parameters (steerers, focusing elements, apertures positions) tuned until the anomalies have been eliminated. Once the accelerator is properly adjusted, the multiwire chamber is retracted from the beam axis and the measurement can safely start.

This device has been only recently implemented and provided "cleaner" measuring conditions, improving the accuracy of ^{14}C dating for old samples, *i.e.* when the concentration of radiocarbon is smaller, approaching the sensitivity limit around 10^{-15}. It is another good example of how the experience gained in basic nuclear physics can be profitably applied to the solutions of problems in quite different fields.

REFERENCES

[1] `http://www.ortec-online.com`, Ortec catalogue, Chapter: Categories of photon detectors, p. 5.
[2] Lechner P. *et al.*, *Nucl. Instrum. Methods Phys. Res. A*, **458** (2001) 281.
[3] Maxwell J. A., Campbell J. L. and Teesdale W. J., *Nucl. Instrum. Methods Phys. Res. B*, **43** (1989) 218.
[4] Maxwell J. A., Teesdale W. J. and Campbell J. L., *Nucl. Instrum. Methods Phys. Res. B*, **95** (1995) 407.
[5] Del Carmine P., Lucarelli F., Mandò P. A. and Pecchioli A., *Nucl. Instrum. Methods Phys. Res. B*, **75** (1993) 480.
[6] Alberti R., Bjeoumikhov A., Grassi N., Guazzoni C., Klatka T., Longoni A. and Quattrone A., *Nucl. Instrum. Methods Phys. Res. B*, **266** (2008) 2296.

[7] Grassi N., Guazzoni C., Alberti R., Klatka T. and Bjeoumikhov A., *Nucl. Instrum. Methods Phys. Res. B*, **268** (2010) 1945.
[8] Alberti R., Grassi N., Guazzoni C. and Klatka T., *Nucl. Instrum. Methods Phys. Res. A*, **607** (2009) 458.
[9] Giuntini L., Massi M. and Calusi S., *Nucl. Instrum. Methods Phys. Res. A*, **576** (2007) 266.
[10] Grassi N., *Nucl. Instrum. Methods Phys. Res. B*, **267** (2009) 825.
[11] Fedi M. E., *Accelerator Mass Spectrometry for* ^{14}C *dating*, in *Organic Mass Spectrometry in Art and Archaeology*, edited by Colombini M. P. and Moudugno F. (Wiley, Chichester) 2009, p. 459.
[12] Taccetti F., Carraresi L., Fedi M. E., Manetti M., Mariani P., Tobia G. and Mandò P. A., *Radiocarbon* **52**, issue 2-3, 2010 (in press).

Proceedings of the International School of Physics "Enrico Fermi"
Course CLXXV "Radiation and Particle Detectors", edited by S. Bertolucci, U. Bottigli and P. Oliva
(IOS, Amsterdam; SIF, Bologna)
DOI 10.3254/978-1-60750-630-0-31

The art of calorimetry

G. Gaudio

Istituto Nazionale di Fisica Nucleare, Sezione di Pavia - via Bassi 6, 27100 Pavia, Italy

M. Livan

Dipartimento di Fisica Nucleare e Teorica, Università di Pavia - via Bassi 6, 27100 Pavia, Italy

R. Wigmans

Department of Physics, Texas Tech University - Lubbock, TX 79409-1051, USA

Summary. — This paper is intended as an introduction to and overview of calorimetric particle detection in high-energy physics experiments. First, the physics that plays a role when high-energy particles are absorbed in dense matter is described, with emphasis on issues that are important for the properties of calorimeters. Next, all aspects of the calorimeter response function are discussed: Mean value, shape, width, and the factors that determine these characteristics. Then, we elaborate on some practical issues that are important for those working with calorimeters: calibration and simulation. Finally, a brief overview of modern developments in this rapidly evolving field is given.

1. – Introduction

Calorimeters were originally developed as crude, cheap instruments for some specialized applications in particle physics experiments, such as detection of neutrino interactions. However, in the past 25 years, their role has changed considerably. In modern

colliders, calorimeters form the heart and the soul of the experiments. They fulfill a number of crucial tasks, ranging from event selection and triggering to precision measurements of the four vectors of individual particles and jets and of the energy flow in the events (missing energy, etc.). This development has benefitted in no small part from the improved understanding of the working of these, in many respects somewhat mysterious, instruments.

The contribution of calorimeter information to the data analysis focuses in many experiments primarily on particle identification (electrons, γ's, muons) and on the energy measurement of particles that develop electromagnetic (em) showers (e, γ, π^0). In ep and $p\bar{p}$ experiments, and especially in experiments at a future linear e^+e^- collider, calorimetric energy measurement of hadrons and jets is also important. The importance of hadron calorimetry is expected to increase considerably as the collision energy is further increased.

Calorimeters are highly non-trivial instruments. Many subtle effects conspire to determine their performance. This paper is intended as a compact introduction to and overview of the subject of calorimetry and its applications in detectors for high-energy particle physics. It is subdivided in sections which address the following topics:

1) The physics of shower development

2) The calorimeter response function

3) R&D to further improve (our understanding of) calorimetry

For more complete and extensive coverage of the material contained in this paper, the reader is referred to ref. [1].

2. – The physics of shower development

Although calorimeters are intended to measure energy deposits at the level of 10^9 eV and up, their performance is in practice determined by what happens at the MeV, keV and sometimes eV levels. Since showers initiated by hadrons, such as protons and pions, are distinctly different (and in particular more complicated) than the electromagnetic (em) ones initiated by electrons of photons, we will start with the latter.

2˙1. *Electromagnetic showers*. – The processes that play a role in em shower development are few and well understood. Electrons and positrons lose energy by *ionization* and by *radiation*. The first process dominates at low energy, the second one at high energy. The *critical energy*, at which both processes play equally important roles, is roughly inversely proportional to the Z value of the absorbing medium

$$\epsilon_c = \frac{610\,\mathrm{MeV}}{Z + 1.24}\,. \tag{1}$$

Photons interact either through the *photoelectric effect*, *Compton scattering* or *pair production*. The photoelectric effect dominates at low energies, pair production at high

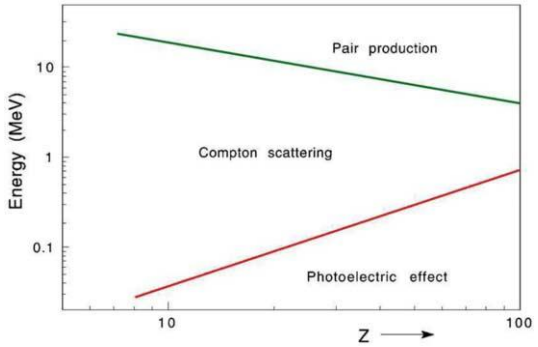

Fig. 1. – The energy domains in which photoelectric effect, Compton scattering and pair production are the most likely processes to occur, as a function of the Z of the absorber material.

energies (fig. 1). The relative cross-sections are also Z-dependent. For example, the cross-section for photoelectron production is proportional to Z^5 and E^{-3}, while the cross-section for pair production gradually increases, both with Z and with E, to reach an asymptotic value near $\sim 1\,\mathrm{GeV}$. The *angular distribution* is more or less isotropic for the photo- and Compton electrons, but highly directional for the e^+e^- pairs produced in pair production.

At energies of 1 GeV and higher, electrons and photons initiate *em showers* in the materials in which they penetrate. Electrons lose their energy predominantly by radiation, the most energetic photons produced in this process convert into e^+e^- pairs, which radiate more γ's, etc. The number of shower particles produced in this particle multiplication process reaches a maximum (the *shower maximum*) at a certain depth inside the absorber, and gradually decreases beyond that depth (fig. 2a). The depth of the shower maximum increases (logarithmically) with the energy of the incoming electron. Because of the particle multiplication, the total amount of material needed to contain em showers is relatively small. For example, when 100 GeV electrons enter lead, 90% of their energy is deposited in only 4 kg of material.

The lateral development of em showers is governed by two types of processes:

1) Electrons and positrons move away from the shower axis because of multiple scattering.

2) Photons and electrons produced in isotropic processes (Compton scattering, photoelectric effect) move away from the shower axis.

The first process dominates in the early stages of the shower development, the second one beyond the shower maximum. Both processes have their own characteristic, exponential scale. The two components are distinctly visible in fig. 2b, which shows the radial energy density for electron showers developing in copper, at three different depths inside the calorimeter.

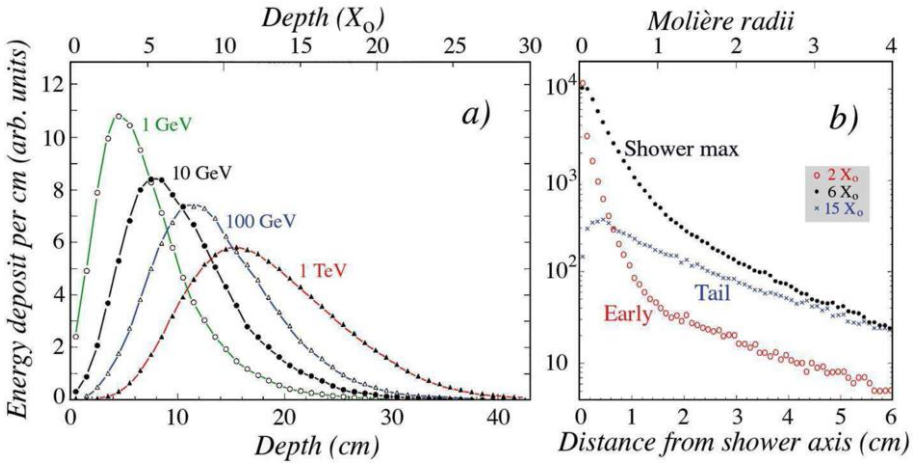

Fig. 2. – The energy deposited as a function of depth for 1, 10, 100 and 1000 GeV electron showers developing in a block of copper. In order to compare the shower profiles, the integrals of these curves have been normalized to the same value (a). The radial distributions of the energy deposited by 10 GeV electron showers in copper, at various depths (b). Results of EGS4 calculations.

The shower development can be described more or less independently of the details of the absorber material in terms of the *radiation length* (for the longitudinal development) and the *Molière radius* (for the lateral development). Both units are defined for the asymptotic energy regime (> 1 GeV). The radiation length (X_0) is the ratio of the electron energy and the specific energy loss by radiation. Therefore, a high-energy electron loses on average 63% $(1 - e^{-1})$ of its energy when it traverses $1X_0$ of material. The mean free path of a high-energy photon equals $9X_0/7$. The Molière radius (ρ_M) is defined through the ratio of the radiation length and the critical energy. When expressed in g/cm^2, X_0 scales as A/Z^2 and ρ_M as A/Z. Therefore, ρ_M is much less material dependent than X_0. For example, copper and lead have approximately the same value for ρ_M, while their radiation lengths differ by a factor of 3.

The radiation length has a fundamentally different meaning for electrons and photons. Showers initiated by high-energy electrons and by photons develop initially quite differently. When they encounter material, high-energy electrons start to radiate immediately. On their way through a few millimeter of material, they may emit thousands of bremsstrahlung photons. On the other hand, high-energy photons may or may not convert in the same amount of material. In the latter case, they do not lose any energy, and when they convert early on, they may lose as much as, or even more than, electrons in the same amount of material. This difference is illustrated in fig. 3. In the same amount of material (in this example $5X_0$), electrons lose on average a larger fraction of their energy than photons, but the spread in the energy losses by photons is larger.

Even though the em shower profiles scale, in first approximation, with X_0 and ρ_M, this scaling is not perfect. This is illustrated in fig. 4. The differences may be understood

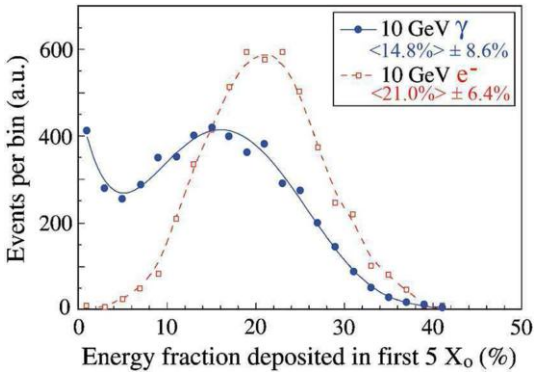

Fig. 3. – Distribution of the energy fraction deposited in the first 5 radiation lengths by 10 GeV electrons and γ's showering in lead. Results of EGS4 calculations [2].

from the fact that the particle multiplication continues down to lower energies in high-Z material and decreases more slowly beyond the shower maximum. For example, a given high-energy electron produces 3 times more positrons when showering in lead than in aluminium. As a result, one needs more X_0 of lead than of aluminium to contain this shower at the 99% level. Also, the shower maximum is located at a greater depth in lead. These features are confirmed by fig. 4.

The material dependence of the calorimeter thickness needed to contain electron showers is shown in fig. 5b. For 99% containment, the difference between high-Z and low-Z absorber materials may be as much as $10X_0$. And for the reasons described above, it takes even more material to contain γ-induced showers. The energy dependence of the calorimeter thickness needed to contain em showers is shown in fig. 5a. For lateral shower containment, material differences are much smaller than for the longitudinal dimension. In addition, there is no energy dependence. A given (sufficiently long) cylinder will thus contain the same fraction of the energy from 1 GeV em showers as from 1 TeV ones.

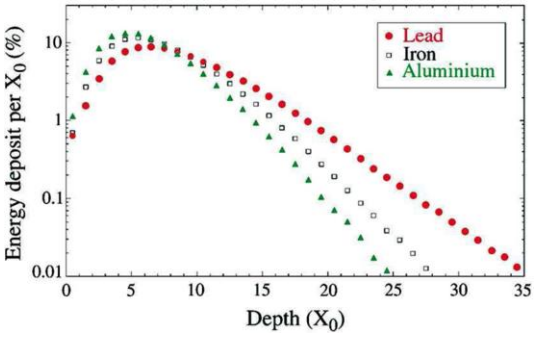

Fig. 4. – Longitudinal profiles of 10 GeV e^- showers developing in aluminium ($Z = 13$), iron ($Z = 26$) and lead ($Z = 82$).

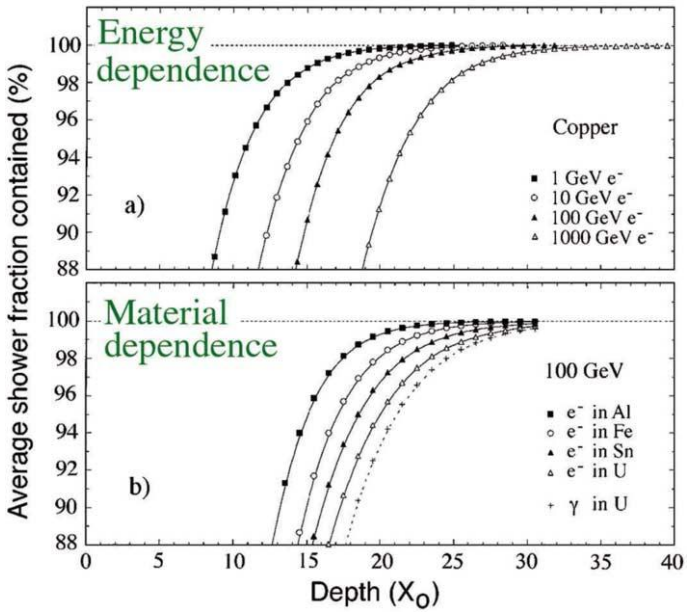

Fig. 5. – Average energy fraction contained in a block of matter with infinite transverse dimensions, as a function of the thickness of the absorber. Shown are results for showers induced by electrons of various energies in a copper absorber (a) and results for 100 GeV electron showers in different absorber materials (b). Results of EGS4 calculations.

Deviations from scaling as observed in figs. 4 and 5 are caused by phenomena that occur at energies below the critical energy. For example, in lead more than 40% of the shower energy is deposited by particles with energies below 1 MeV, while the critical energy is ~ 7 MeV. Only one quarter of the energy is deposited by positrons, the rest by electrons. These facts, which are derived from EGS4 Monte Carlo simulations of em shower development, illustrate that Compton scattering and photoelectron production are very important processes for understanding calorimetry. Both processes dominate at energies far below the critical energy and are therefore not properly described by scaling variables such as X_0 and ρ_M.

2˙2. *Hadronic showers.* – In showers developed by hadrons, an additional complication arises from the role played by the *strong interaction*. This interaction is responsible for:

1) The production of hadronic shower particles. The vast majority of these, $\sim 90\%$, are pions. The neutral pions decay in 2 γ's, which develop em showers.
2) The occurrence of nuclear reactions. In these processes, neutrons and protons are released from atomic nuclei. The nuclear binding energy of these nucleons *has to be provided*. Therefore, the fraction of the shower energy needed for this purpose does not contribute to the calorimeter signals. This is the so-called *invisible-energy* phenomenon.

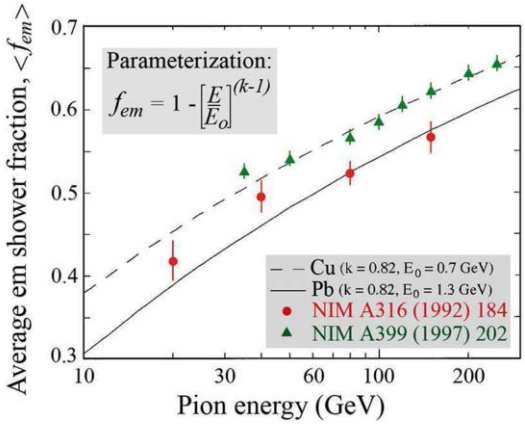

Fig. 6. – Comparison between the experimental results on the em fraction of pion-induced showers in copper-based and lead-based calorimeters [3, 4].

The em showers initiated by π^0's develop in the same way as those initiated by high-energy photons. The fraction of the shower energy carried by this em component (called $f_{\rm em}$ in the following) varies strongly from event to event. On average, this fraction increases with the shower energy, since π^0's may also be (and are, see fig. 7) produced by secondary and higher-order shower particles: the larger the shower energy, the more generations of shower particles, the larger $f_{\rm em}$. Typically, $f_{\rm em}$ increases from $\sim 30\%$ at 10 GeV to $\sim 50\%$ at 100 GeV (fig. 6). In a typical hadron shower developing in lead, the remaining (non-em) energy is deposited in the following way: ionizing particles (56%, two thirds from protons), neutrons (10%), invisible energy (34%). The neutrons are very soft (typically 3 MeV), on average there are 37 neutrons per GeV deposited energy. The protons (which dominate the non-em signals from calorimeters) originate primarily from nuclear spallation processes, they carry typically 50–100 MeV a piece. These numbers illustrate that the large majority of the non-em energy is deposited through *nucleons* and *not* through relativistic particles such as pions.

These characteristics have important consequences for calorimetry:

– As a result of the invisible-energy phenomenon, the calorimeter signals for hadrons are in general smaller than for electrons of the same energy (*non-compensation*).

– Since the em energy fraction is energy dependent, the calorimeter is *non-linear* for hadron detection.

The hadronic shower profiles are governed by the *nuclear interaction length* ($\lambda_{\rm int}$), *i.e.*, the average distance hadrons travel before inducing a nuclear interaction. This interaction length, expressed in g/cm^2, scales with $\sqrt[3]{A}$. On average, hadronic shower profiles look very similar to the em ones displayed in fig. 2, except that the scale factor is usually much larger for the hadronic showers. For example, for copper X_0 amounts to 1.4 cm, while $\lambda_{\rm int} = 15$ cm.

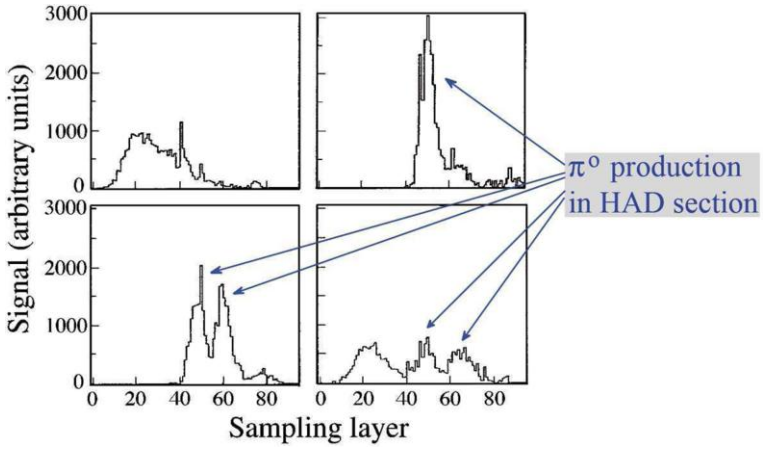

Fig. 7. – Longitudinal profiles for 4 different showers induced by 270 GeV pions in a lead/iron/plastic-scintillator calorimeter [5].

Another important difference between em and hadronic showers is the large variety of profiles for the latter. This is illustrated in fig. 7, which shows 4 different showers induced by 270 GeV pions. The strange shapes result from the production of energetic π^0's in the second or third generation of the shower development.

Just as for em showers, the depth of the calorimeter needed to contain hadronic showers to a certain degree increases logarithmically with energy (fig. 8). However, because of the large longitudinal fluctuations in shower development (fig. 7), leakage effects might still play an important role, even though the calorimeter contains the showers, on average, to 99%. Laterally, it takes *less* material to contain high-energy showers than low-energy ones (fig. 9). This is a consequence of the fact that the em shower fraction increases with energy. The em showers produced by π^0's tend to develop close to the shower axis.

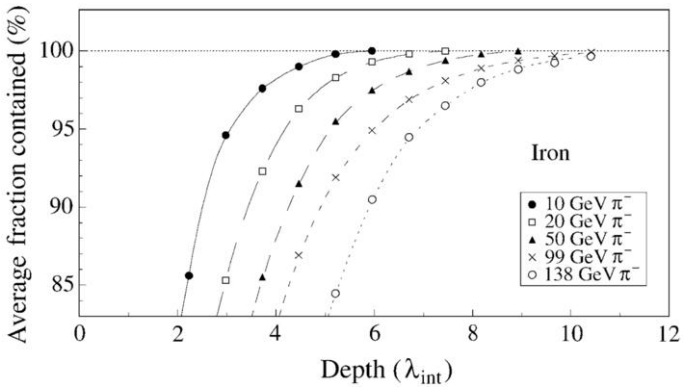

Fig. 8. – Average energy fraction contained in a block of matter with infinite transverse dimensions, as a function of the thickness of the absorber [6].

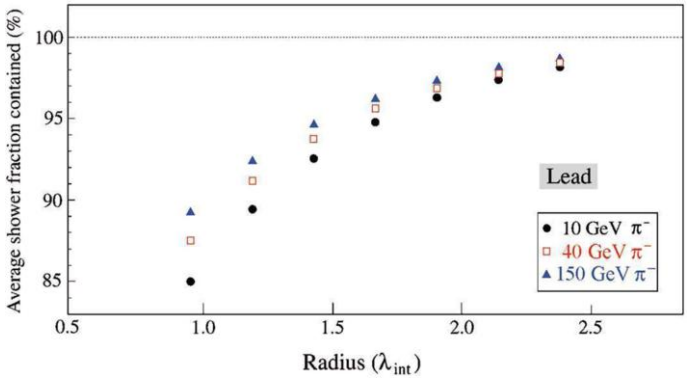

Fig. 9. – Average energy fraction contained in an infinitely long cylinder of absorber material, as a function of the radius of this cylinder, for pions of different energies showering in a lead-based calorimeter [3].

The difference between λ_{int} and X_0, which may be as large as a factor 30 in high-Z materials, is fruitfully used to distinguish between em and hadronic showers. A simple piece of lead (0.5 cm thick) followed by a sheet of scintillating plastic makes a very effective *preshower detector*, as illustrated in fig. 10.

2˙3. *Lessons for calorimetry.* – Based on the shower characteristics discussed above, we can draw some very important conclusions for the design of calorimeters:

– In the absorption processes that play a role in calorimeters, most of the energy is deposited by *very soft shower particles*. In em showers and shower components, photo- and Compton electrons contribute in a major way to the energy deposit

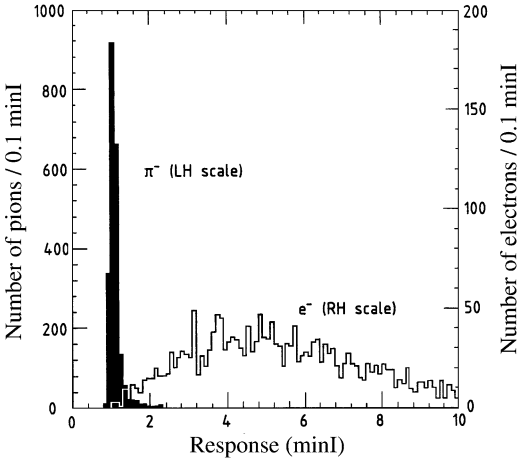

Fig. 10. – Signal distributions for 75 GeV π^- and e^- in a very simple preshower detector.

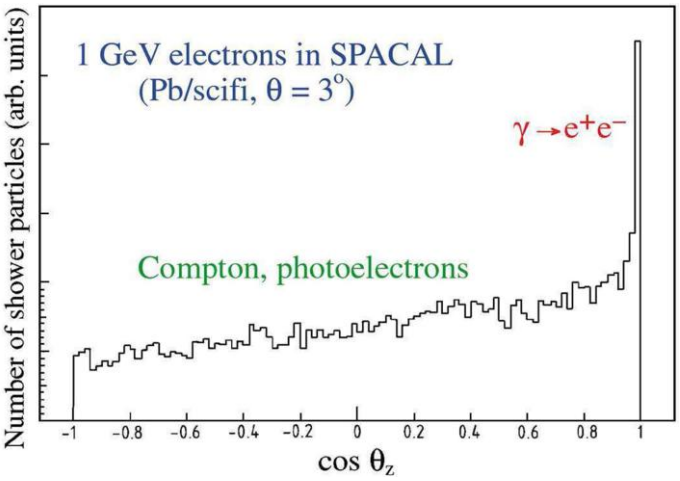

Fig. 11. – Angular distribution of the shower particles (e^+, e^-) through which the energy of a 1 GeV electron is absorbed in a lead-based calorimeter [7].

process and thus to the calorimeter signals. Because of their isotropic angular distribution, these shower particles have "forgotten" the direction of the incoming particle (fig. 11). As a result, it does not matter how one chooses to orient the active layers in a sampling calorimeter. Originally, it was believed that only a "sandwich" calorimeter structure would work. Nowadays, there is a wide variety of geometries in use, including fiber structures with fibers running in the same direction as the showering particles. Such alternative structures may offer considerable advantages, *e.g.*, in terms of hermeticity, signal speed, etc.

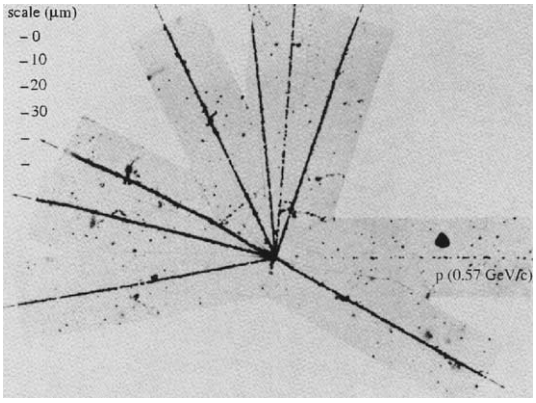

Fig. 12. – A nuclear interaction induced by a proton with a kinetic energy of 160 MeV in a nuclear emulsion stack.

– The typical shower particle in em showers is a 1 MeV electron. The range of such a particle is very short, less than 1 mm in typical absorber materials such as iron or lead. This range, rather than the radiation length, sets the scale for a useful sampling frequency in em calorimeters.

– Typical shower particles in hadron showers are 50–100 MeV spallation protons and 3 MeV neutrons. The range of such protons is typically $\sim$ 1 cm. This sets the scale for a useful sampling frequency in hadron calorimeters. The neutrons travel typically several centimeter between interactions. Neutrons are only important for the signals from sampling calorimeters if they have a sufficiently large probability of interacting in the active material and generate measurable reaction products. Figure 12 shows an example of a type of event that plays a dominant role in hadronic shower development. In such nuclear reactions, large numbers of nucleons are released, and the energy with which they were bound in the struck nucleus ($\sim$ 8 MeV/nucleon) is lost for detection.

As we will see in the next section, very soft shower particles are not only important for the way in which the incoming particle is absorbed, but also for details of the calorimeter response function.

3. – The calorimeter response function

3˙1. *Absolute response and response ratios*. – We define the *calorimeter response* as the average calorimeter signal per unit of deposited energy. The response is thus expressed in terms of photoelectrons per GeV, pico-coulombs per MeV or something similar. When defined like this, a *linear* calorimeter has a *constant response*.

Electromagnetic calorimeters are in general linear, since all the energy carried by the incoming particle is deposited through processes that may generate signals (excitation/ionization of the absorbing medium). Non-linearity is usually an indication of instrumental problems, such as signal saturation or shower leakage. Figure 13 shows an example of a non-linear em calorimeter. In this detector, the wire chambers used to signal the passage of a shower particle operated in the "saturated avalanche" mode, which means that they did not distinguish between 1 and n simultaneous shower particles. As the shower energy, and thus the density of shower particles increased, saturation effects decreased the response. Figure 13b shows that it was the particle *density* and not so much the total energy that was responsible for the effects, since the effects were most prominent early in the shower development (sect. **1**), where the shower was highly collimated. The described effect could be avoided by operating the wire chambers in the proportional regime.

Calorimeters are distinguished according to their composition into two classes:

1) *Homogeneous* calorimeters, in which the absorber and the active (signal producing) medium are one and the same.

2) *Sampling* calorimeters, in which these two roles are played by different media.

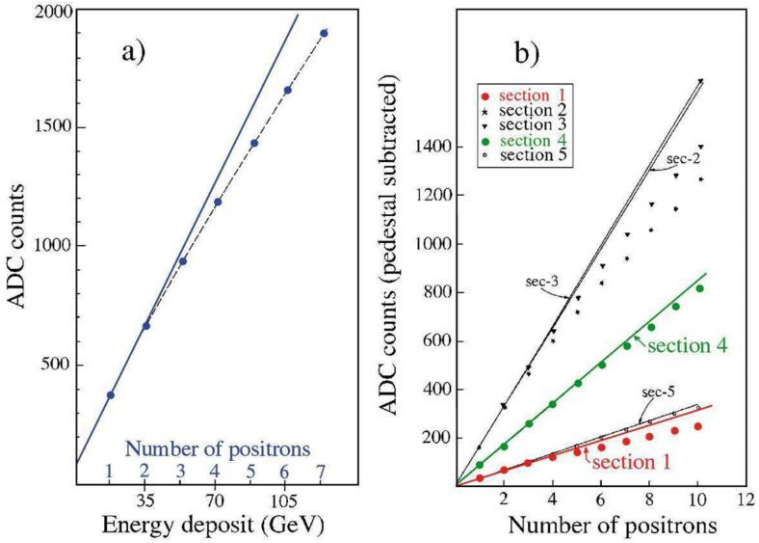

Fig. 13. – Average em shower signal from a calorimeter read out with wire chambers operating in the "saturated avalanche" mode, as a function of energy (a). The calorimeter was longitudinally subdivided. Results for the 5 separate sections are given in (b) [8].

In the latter instruments, only some fraction of the shower energy is sampled by the active material. This sampling fraction is usually defined on the basis of the signals for *minimum ionizing particles* (mip). For example, in the $D0$ calorimeter, which consists of 3 mm thick ^{238}U absorber plates separated by 4.6 mm liquid-argon-filled gaps, the sampling fraction for a mip (derived on the basis of the $\mathrm{d}E/\mathrm{d}x$ values in active and passive material) is 13.7%. However, for em showers, the sampling fraction amounts to only 8.2%.

The reason for this difference (we say that this detector has an e/mip *response ratio* of $8.2/13.7 = 0.6$) is, again, a consequence of the fact that em shower signals are dominated by very soft shower particles. The γ's with energies below 1 MeV are extremely inefficiently sampled in this type of detector, as a result of the overwhelming dominance of the photoelectric effect. Because of the Z^5 cross-section dependence, virtually all these soft shower γ's interact in the absorber layers and contributions to the signal may only be expected if the interaction takes place so close to the boundary with an active layer that the photoelectron (whose range is less than 1 mm) can escape from the absorber into the liquid argon. Because of the crucial role of the photoelectric process, the effect of this phenomenon on the e/mip response ratio depends on the Z values of the passive and active materials (e/mip is smallest for calorimeters with high-Z absorber layers and low-Z active material, as in $D0$), and on the thickness of the absorber plates (fig. 14). If the latter are made sufficiently thin, e/mip will eventually become 1.0.

Signal non-linearity is a very common feature for hadron shower detection. The invisible energy phenomenon and the energy-dependent em shower fraction conspire to this

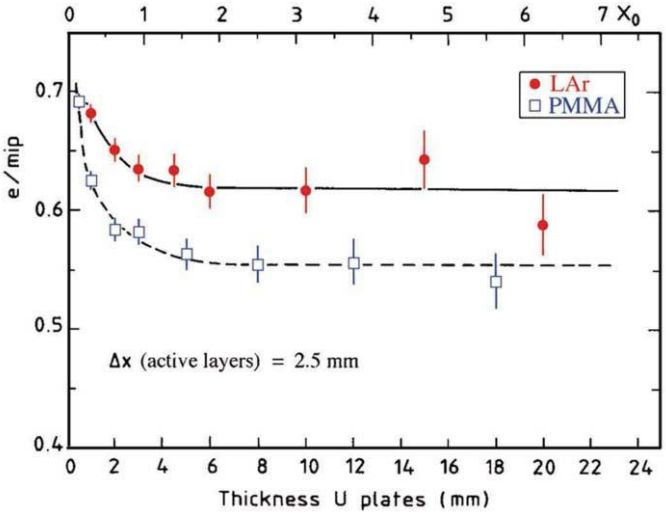

Fig. 14. – The e/mip ratio as a function of the thickness of the absorber layers, for uranium/PMMA and uranium/LAr calorimeters. The thickness of the active layers is 2.5 mm in all cases. Results from EGS4 Monte Carlo simulations.

effect, which may easily lead to a response difference of 10% over one order of magnitude in energy. This is schematically illustrated in fig. 15, which depicts the *response function*, *i.e.*, the distribution of the normalized signals around the mean value, separately for the em and non-em components in a non-compensating calorimeter. The ratio of the mean values of these distributions, *i.e.*, the ratio of the em and non-em responses, is known as the e/h value of the calorimeter. In this example, $e/h = 1.8$. A shower induced by a high-energy pion has both an em and a non-em component. The response function of the calorimeter for such pions thus centers around a mean value in between those for the em (e) and non-em (h) components, at a value determined by the average energy sharing between these components at that energy ($\langle f_{\rm em}\rangle$). And since $\langle f_{\rm em}\rangle$ increases with energy (fig. 6), the response to pions increases as well. This calorimeter is thus non-linear for pion detection, its response increases with energy.

The e/h value cannot be directly measured. However, it can be derived from the e/π signal ratios, measured at various energies. The relationship between e/π and e/h is as follows:

$$\frac{e}{\pi} = \frac{e/h}{1 - \langle f_{\rm em}\rangle(1 - e/h)}\,, \tag{2}$$

where $\langle f_{\rm em}\rangle$ represents the (energy-dependent) average em shower fraction. This relationship is graphically illustrated in fig. 16. Even though invisible-energy losses in the non-em component are naturally leading to e/h values larger than 1, it turns out to be possible to construct calorimeters with $e/h \leq 1$. Calorimeters with $e/h > 1$, $e/h = 1$

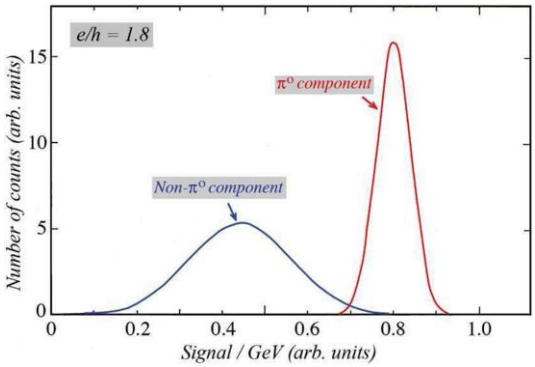

Fig. 15. – Schematic representation of the response functions of a non-compensating calorimeter to the em and non-em components of hadronic showers. The ratio of the mean values of these distributions is the e/h value of this calorimeter (1.8).

and $e/h < 1$ are called *undercompensating, compensating* and *overcompensating*, respectively. Most calorimeters used in practice are undercompensating, with typical e/h values between 1.5 and 2.0.

Equation (2) also quantifies the hadronic signal non-linearity. Since $\langle f_{\rm em} \rangle$ increases with energy, the pion response increases for undercompensating calorimeters, and decreases for overcompensating calorimeters. This is clearly observed in practice (fig. 17). Only compensating calorimeters are linear. This is one of many advantages of compensation.

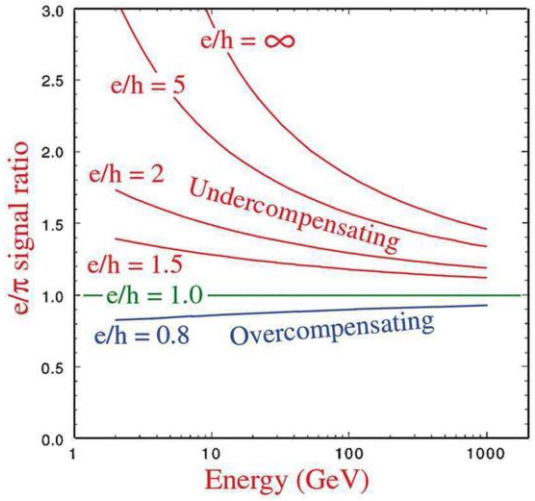

Fig. 16. – Relation between the calorimeter response ratio to em and non-em energy deposits, e/h, and the measured e/π signal ratios.

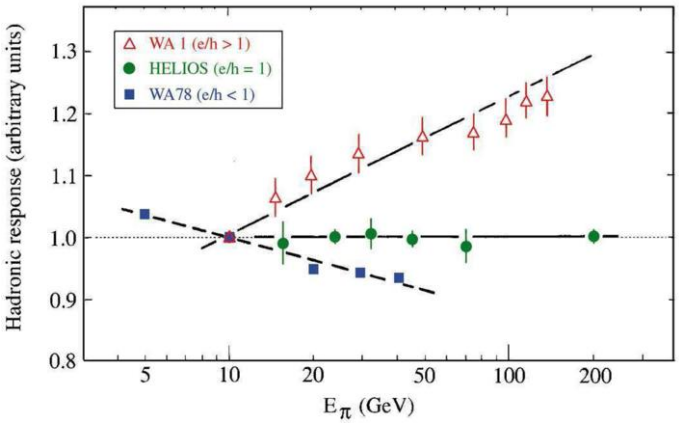

Fig. 17. – The response to pions as a function of energy for three calorimeters with different e/h values. All data are normalized to the response for 10 GeV π^-.

3˙2. *Compensation.* – In order to understand how compensation can be achieved, one should understand in detail the response to the various types of particles that contribute to the calorimeter signals. Most important in this context are the neutrons. Neutrons carry typically not more than $\sim 10\%$ of the non-em shower energy. However, their contribution to the calorimeter signals may be much larger than that. This is because neutrons only lose their energy through the products of the nuclear reactions they undergo. Most prominent at the low energies typical for hadronic shower neutrons is *elastic scattering*. In this process, the transferred energy fraction is on average

$$f_{\text{elastic}} = \frac{2A}{(A+1)^2}\,, \tag{3}$$

where A is the atomic number of the target nucleus. In hydrogen, this fraction is 50%, in lead it is 100 times smaller. Therefore, MeV-type neutrons sent into a Pb/H_2 structure (50/50 in terms of numbers of nuclei), transfer 98% of their kinetic energy to hydrogen nuclei, and only 2% to lead. Since the sampling fraction for charged particles (mips) amounts to 2.2% in this structure, the potential for *signal amplification through neutron detection* (SAND) is enormous, especially also because the recoil protons produced in the active material may directly contribute to the calorimeter signal.

Hydrogenous active material is an extremely efficient medium for SAND in calorimeters. Nowhere has the role of hydrogen been demonstrated more dramatically than in the L3 uranium/gas calorimeter [10]. Figure 18a shows the signals of this calorimeter for pions and for electrons, as a function of energy, for two different gas mixtures: argon/CO_2 and isobutane. For the electron signals, the choice of gas made no significant difference. However, the pion response doubled when isobutane (C_4H_{10}) was used instead of argon/CO_2. The L3 group also tested other gas mixtures. It turned out that by changing

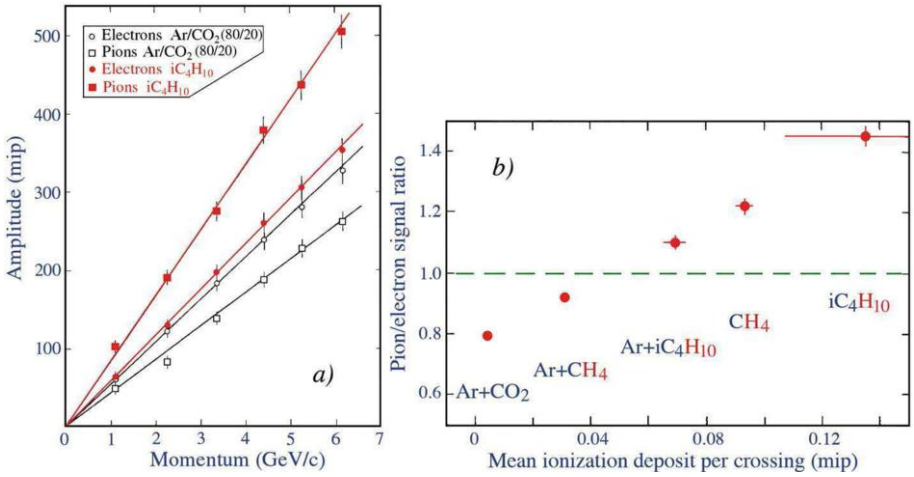

Fig. 18. – Signals for pion and electron showers in the L3 uranium/gas calorimeter, for 2 different gas mixtures in the readout chambers (a). Pion/electron response ratio as a function of the hydrogen content of the gas mixture (b).

the hydrogen content of the gas mixture used in the wire chambers that produced the calorimeter signals, the π/e response ratio could be changed by as much as a factor of two. By choosing the proper mixture, the responses to em and hadronic showers could be equalized (fig. 18b).

Compensation can also be achieved in other types of calorimeters, provided that the active material contains hydrogen. By carefully choosing the relative amount of hydrogen in the calorimeter structure, one can achieve compensation. This has been demonstrated experimentally for plastic-scintillator structures with Pb or ^{238}U as absorber material.

All compensating calorimeters rely on the contribution of neutrons to the hadronic signals. This is also illustrated by fig. 19, which shows typical time structures of signals recorded with the compensating SPACAL (lead/scintillating plastic fibers) calorimeter [11]. The hadronic signals from this calorimeter (fig. 19b) exhibit a tail which is not seen in the electron signals (fig. 19a). This tail is well described by an exponential with a slope of 10 ns, the characteristic time between subsequent elastic scattering processes of neutrons in this material combination (fig. 19c).

By properly amplifying the neutron signals (with respect to those from charged shower particles depositing the same amount of energy), one can *compensate* for the invisible-energy losses. Therefore, the essential ingredients for a compensating calorimeter are:

– One needs to have a *sampling* calorimeter. Compensation can never be achieved in a homogeneous one.

– The active material needs to contain *hydrogen* and be sensitive to the signals from recoil protons produced by elastic neutron scattering.

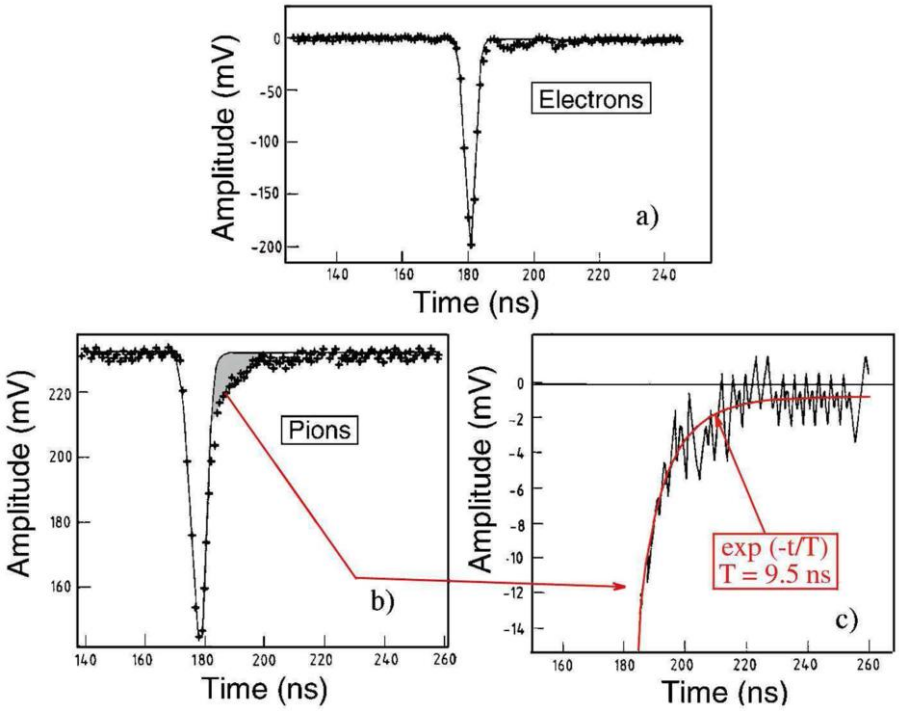

Fig. 19. – Typical signals for 150 GeV electrons (a) and pions (b) measured with the SPACAL calorimeter. The pion signal exhibits an exponential tail with a time constant of ~ 10 ns (c).

– The calorimeter needs to have a precisely tuned *sampling fraction*, in order to amplify the neutron signals by the proper factor. This optimal sampling fraction is $\sim$ 10% for U/plastic-scintillator (fig. 20) and $\sim$ 3% for Pb/plastic-scintillator devices.

The use of uranium absorber, for a long time believed to be a key ingredient for compensation, is helpful, but neither essential nor sufficient.

3˙3. *Fluctuations*. – Since calorimeters are based on physical processes that are inherently statistical in nature, the precision of calorimetric measurements is determined and limited by *fluctuations*. Usually, a variety of fluctuations play a role. In electromagnetic (em) calorimeters, fluctuations that may affect the energy resolution include:

– Signal quantum fluctuations, *e.g.*, photoelectron statistics

– Shower leakage fluctuations

– Fluctuations resulting from instrumental effects, such as electronic noise, light attenuation and structural non-uniformities

– Sampling fluctuations

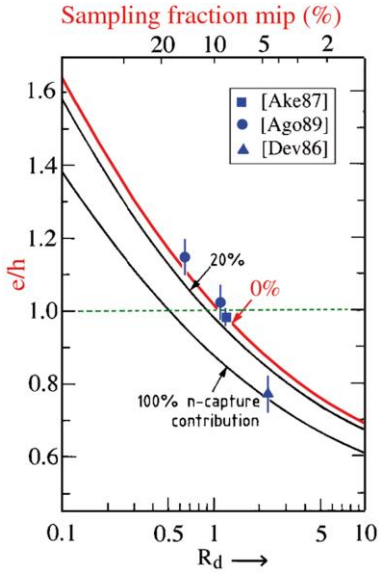

Fig. 20. – The e/h ratio of uranium/plastic-scintillator calorimeters as a function of the sampling fraction for mips (top axis) or the volume ratio of passive and active material (R_d, bottom axis). The 3 curves were calculated for different assumptions concerning the contribution of γ's released in thermal neutron capture to the calorimeter signals [9].

Only the latter ones are characteristic for sampling calorimeters. In a well designed sampling calorimeter, these fluctuations dominate the others, if that is not the case, then money may have been wasted. Unlike some other fluctuations, *e.g.*, those caused by shower leakage and instrumental effects, sampling fluctuations are governed by the rules of Poisson statistics. Therefore, they contribute to the energy and position resolutions through a term that scales with $1/\sqrt{E}$: $\sigma/E \sim E^{-1/2}$.

Sampling fluctuations are determined both by the sampling fraction (*i.e.*, the relative amount of active material) and the sampling frequency (thickness of the layers). In em calorimeters with non-gaseous active media, they are well described by the following general expression:

$$\frac{\sigma}{E} = 2.7\%\sqrt{d/f_{\text{samp}}} \cdot E^{-1/2}, \tag{4}$$

in which d represents the thickness of the active layers (in mm) and f_{samp} is the sampling fraction for mips. For example, in the KLOE lead/scintillating-fiber calorimeter [12], the plastic fibers have a thickness $d = 1.0\,\text{mm}$. The plastic represents 48% of the detector volume, which otherwise consists of 42% lead and 10% glue. Therefore, the sampling fraction for mips is 15%. Equation (4) thus gives $6.9\%/\sqrt{E}$ as the contribution of sampling fluctuations, in reasonable agreement with the experimental resolution ($5.7\%/\sqrt{E}$).

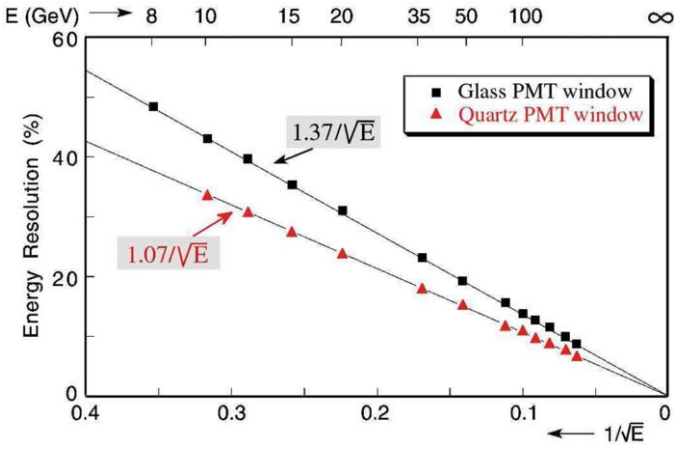

Fig. 21. – The energy resolution for electron detection with a CMS/HF prototype detector, as a function of energy. Results are given for measurements in which photomultiplier tubes with a glass window were used and for measurements in which the same type of PMTs were equipped with a quartz window [4].

Among the calorimeters whose resolution is dominated by *signal quantum fluctuations* we mention the Ge detectors used for nuclear γ-ray spectroscopy and quartz fiber calorimeters such as the CMS/HF. The amount of energy needed for 1 signal quantum differs by 9 orders of magnitude in these two examples. Whereas it takes only 1 eV to produce an electron-hole pair in germanium, the light yield in quartz fiber calorimeters is typically ~ 1 photoelectron per GeV deposited energy. Signal quantum fluctuations thus limit the resolution of Ge detectors to 0.1% at 1 MeV and of quartz fiber calorimeters to 10% at 100 GeV. Figure 21 shows the em energy resolution of a CMS/HF prototype as a function of energy. The dominant role of signal quantum fluctuations is illustrated by the fact that by replacing the PMTs which detected the light from this calorimeter by similar PMTs with a quartz window, the resolution improved. This was a direct result of the fact that these quartz windows transmitted a larger fraction of the Čerenkov light that constitutes the signal from this detector.

The effects of (fluctuations in) shower leakage on the em energy resolution of a calorimeter are illustrated in fig. 22. These fluctuations are non-Poissonian and, therefore, their contribution to the energy resolution does not scale with $E^{-1/2}$. It also turns out that, for a given level of shower containment, the effects of longitudinal fluctuations are larger than the effects of lateral fluctuations. These differences are related to the differences in the *number* of different shower particles responsible for the leakage. For example, fluctuations in the starting point of a photon-induced shower translate into leakage fluctuations for which only one particle (the initial photon) is responsible. Side leakage is a collective phenomenon to which typically a large number of shower particles contribute. Unlike longitudinal and lateral leakage, the third type of leakage, albedo, *i.e.*, backward leakage through the front face of the detector, cannot be affected by the design

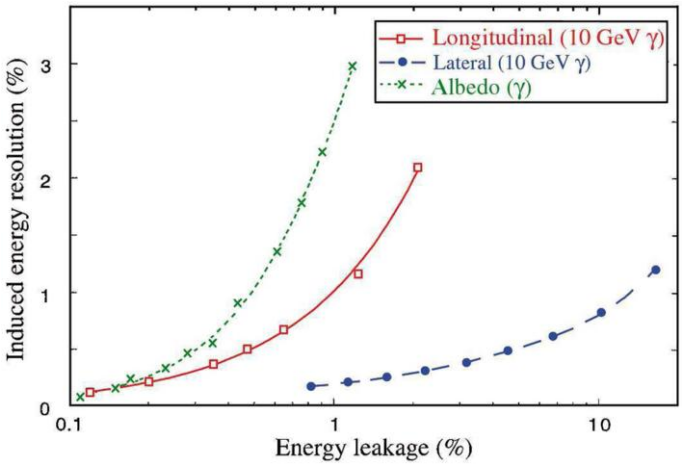

Fig. 22. – A comparison of the effects caused by different types of shower leakage. Shown are the induced energy resolutions resulting from albedo, longitudinal and lateral leakage as a function of the energy fraction carried by the particles escaping from the detector. Results from EGS4 Monte Carlo calculations.

of the detector. Fortunately, the effects of this type of leakage are usually very small, except at very low energy. The results shown in fig. 22 concern Monte Carlo simulations, but have been confimed by a number of experiments. They hold important lessons for the design of calorimeters (*e.g.*, containment requirements).

In practice, the resolution of a given calorimeter is affected by different types of fluctuations, each with its own characteristic energy dependence. Typically, these effects are uncorrelated and therefore have to be added in quadrature. Because of the different energy dependencies, the total resolution of the calorimeter may be dominated by different effects in different energy regimes. This is illustrated in fig. 23 for the EM calorimeter of the ATLAS experiment. For energies below $\sim 10\,\text{GeV}$, electronic noise is the dominating contributor to the resolution, between 10 and 100 GeV sampling fluctuations and other stochastic terms dominate, while at energies above 100 GeV energy-independent effects (such as the impact-point–dependent response) determine the resolution.

The same factors listed above also affect the resolution for hadron detection. Sampling fluctuations are larger for hadron showers than for em ones, typically by a factor of two. This is due to the fact that the hadronic shower signals are dominated by the contributions from spallation protons, which typically carry a few hundred MeV of energy. Unlike the Compton and photo-electrons that dominate the signals from em showers, these spallation protons may traverse several active calorimeter layers. Also, their specific ionization is larger than for mips. Therefore, the number of *different* shower particles that contribute to the calorimeter signals is smaller for hadron showers. Fluctuations in this number, which are the dominating source of sampling fluctuations, are thus larger for hadron showers than for em showers developing in the same detector.

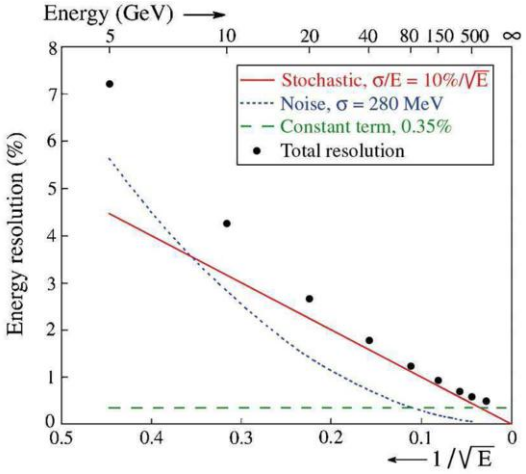

Fig. 23. – The em energy resolution and the separate contributions to it, for the ATLAS EM calorimeter [13].

However, there are some additional effects that tend to dominate the performance of hadron calorimeters. In the nuclear reactions through which many hadrons are absorbed, some fraction of the energy is used to release nucleons from nuclei. This binding energy is *invisible*, it does not contribute to the calorimeter signals. Fluctuations in visible energy play a role in *all* hadron calorimeters and form the ultimate limit to the achievable hadronic energy resolution. Figure 24 gives an impression of these fluctuations [9].

In *non-compensating* calorimeters, which respond differently to the em and non-em shower components ($e/h \neq 1$), the *non-Poissonian* fluctuations in the em shower fraction

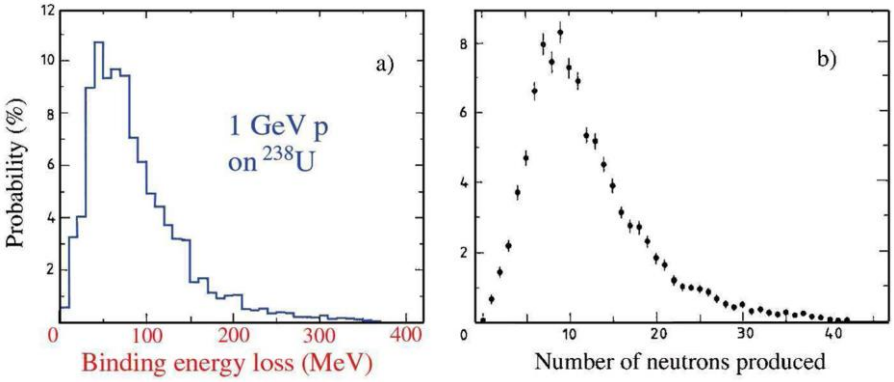

Fig. 24. – The nuclear binding energy lost in spallation reactions induced by 1 GeV protons on ^{238}U nuclei (a), and the number of neutrons produced in such reactions (b).

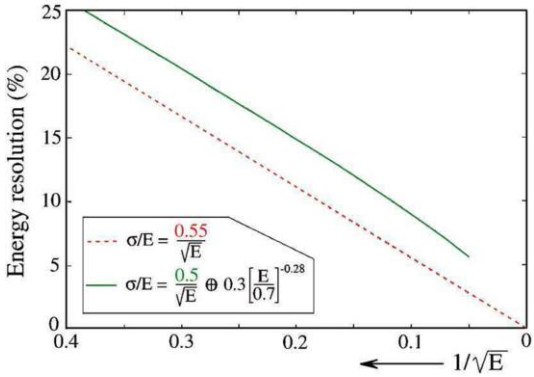

Fig. 25. – The hadronic energy resolution calculated for a typical non-compensating calorimeter in the energy regime up to 400 GeV (the solid line), and calculated with a sole stochastic term with a slightly larger scaling constant [1].

($f_{\rm em}$) tend to dominate the hadronic performance. These fluctuations contribute to the energy resolution *not* through a constant term as is often thought, but rather through an energy-dependent term, $cE^{-0.28}$, which has to be added in quadrature to the other contributing terms, with the parameter c determined by the e/h value ($0 < c < 1$). The result resembles the solid line in fig. 25 which, in the energy range accessible to measurements, runs almost parallel to the curve representing the results of a calorimeter in which only a stochastic term (scaling with $E^{-1/2}$) plays a role. For this reason, one sees the hadronic energy resolution of non-compensating calorimeters sometimes expressed as

$$\frac{\sigma}{E} = \frac{a_1}{\sqrt{E}} + b, \tag{5}$$

instead of

$$\frac{\sigma}{E} = \frac{a_2}{\sqrt{E}} \oplus cE^{-0.28}. \tag{6}$$

Note that the values of a_1 and a_2 in this comparison are different (fig. 25).

The resolution of compensating calorimeters is ultimately limited by fluctuations in (in)visible energy. The importance of these fluctuations depends on the details of how compensation is achieved. In plastic-scintillator calorimeters, the signal from neutrons is correlated with the nuclear binding energy losses, especially for high-Z absorber material. Therefore, the intrinsic fluctuations are reduced. However, this effect is stronger in lead than in uranium, where many neutrons come from fission processes and thus are unrelated to the nuclear binding energy losses. As a result, the ultimate energy resolution achievable with Pb-based calorimeters is better than for uranium ones: $13\%/\sqrt{E}$ *vs.* $20\%/\sqrt{E}$ [14].

3˙4. *The shape of the response function.* – Not all types of fluctuation give rise to response variations that are symmetric around the average value. Examples of effects that

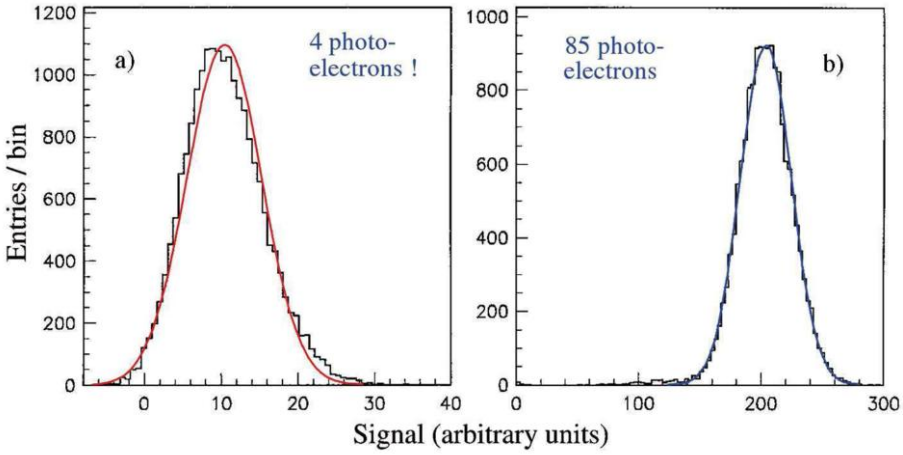

Fig. 26. – Signal distributions for 10 GeV (a) and 200 GeV (b) electrons showering in the CMS quartz-fiber calorimeter. The curves represent Gaussian fits to the experimental data [4].

lead to an asymmetric response function include, but are not limited to, the following:

– If the signal is constituted by a very small number of signal quanta (*e.g.*, photo-electrons), then the Poisson distribution becomes asymmetric. Effects of this type have been observed in the signals from quartz-fiber calorimeters (fig. 26).

– Effects of shower leakage lead to tails in the signal distributions. Usually, these tails occur on the low-energy side of the signal distribution, since energy is escaping from the active detector volume. However, there are examples of detectors where leakage leads to signal amplification, for example in scintillating calorimeters read out by silicon diodes, where an escaping shower electron may produce a signal in the diode that is orders of magnitude larger than the one produced by a scintillation photon (fig. 27a).

– An interesting effect occurs in non-compensating hadron calorimeters. As we saw earlier, fluctuations in the energy fraction spent on π^0 production ($f_{\rm em}$) dominate the resolution of such devices. However, these fluctuations are not necessarily symmetric. For example, in showers induced by pions, the probability of an anomalously large $f_{\rm em}$ value is not equal to that of an equivalently small value. The reason for that is the *leading-particle effect*. A large $f_{\rm em}$ value occurs when in the first nuclear interaction a large fraction of the energy carried by the incoming pion is transferred to a π^0. However, when a similarly large fraction is transferred to another type of particle, the result is not necessarily a small $f_{\rm em}$ value, since this other particle may produce energetic π^0's in subsequent reactions. This effect leads to significant differences in the signal distributions for showers induced by high-energy

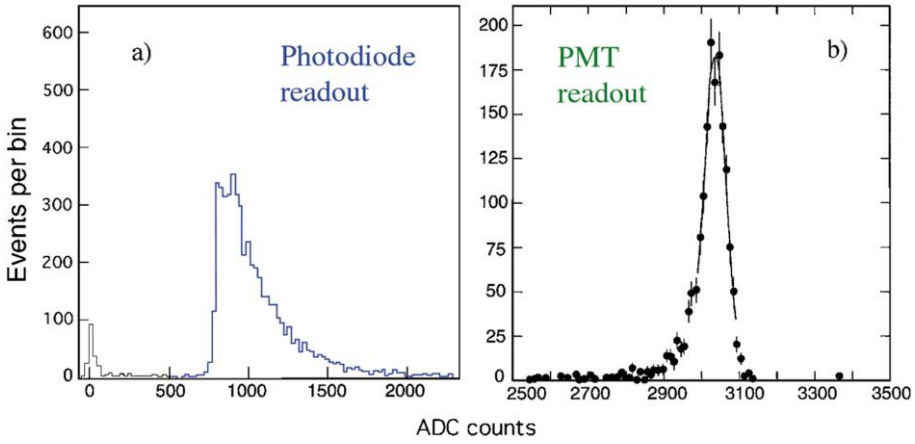

Fig. 27. – Signal distributions for high-energy electron showers measured with a $PbWO_4$ crystal calorimeter [15]. The calorimeter was read out either with silicon photodiodes (a) or with PMTs (b).

pions and protons (fig. 28). In proton-induced showers, the leading particle has to be a baryon and asymmetries such as the ones discussed above are absent.

It is important to note that the response function observed for pion-induced showers is not only determined by the asymmetric fluctuations in $f_{\rm em}$, but also by the e/h value of the calorimeter. For example, in compensating calorimeters, the response function for pions is perfectly Gaussian, despite the asymmetric fluctuations in $f_{\rm em}$. On the other hand, in overcompensating calorimeters, the asymmetry in the

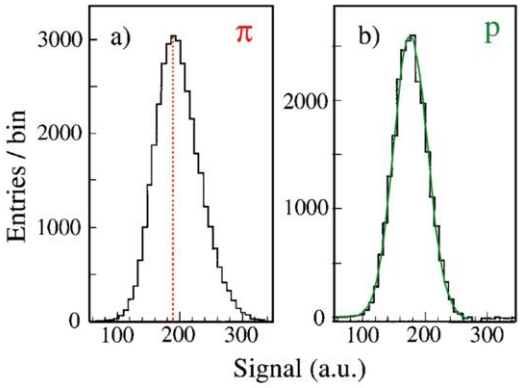

Fig. 28. – Signal distributions for 300 GeV pions and protons detected with a quartz-fiber calorimeter. The curve in (b) represents the result of a Gaussian fit to the proton distribution [16].

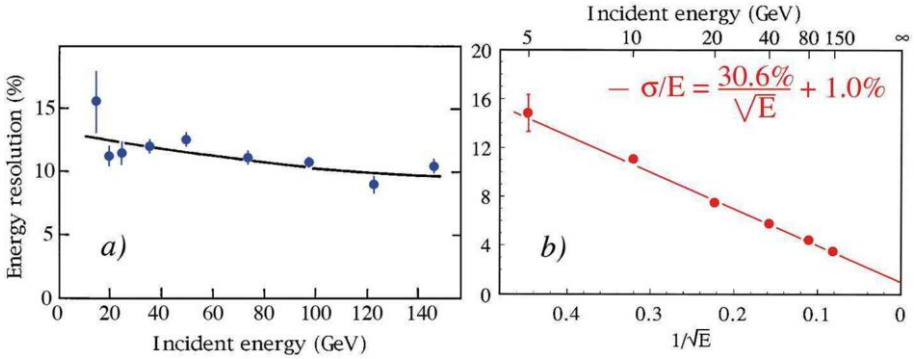

Fig. 29. – The hadronic energy resolution as a function of energy, for a homogeneous calorimeter consisting of 60 tonnes of liquid scintillator (a), and for the compensating SPACAL calorimeter, which has a sampling fraction of only 2% (b). From ref. [17].

response function is reversed (*i.e.*, a low-side tail is observed). These features can be understood from the schematic representation shown in fig. 15. If $h > e$, then an excess of events with an anomalously large $f_{\rm em}$ value will manifest itself as an excess of events with an anomalously *small* total signal.

3˙5. *Lessons for calorimeter design.* – There are some important lessons to be drawn from the characteristics discussed on the previous pages:

– Usually, a variety of different types of fluctuations contribute to the energy resolution of a calorimeter. However, one of these sources of fluctuations dominates. If one wants to improve the calorimeter's energy resolution, one has to work on the fluctuations that *dominate*. As an example, we mention the fact that one has built at some point a *homogeneous* calorimeter for hadron detection, consisting of 60 tons of liquid scintillator. In this device, all sources of fluctuation were eliminated (by design), except for the effects of non-compensation. The resolution of this device was limited to 10% (fig. 29a). On the other hand, the SPACAL detector, a sampling calorimeter designed to eliminate the effects of non-compensation, achieved hadronic energy resolutions of $\sim 2\%$ at high energy (fig. 29b).

In the design of a calorimeter, one should not waste money reducing fluctuations that do not dominate the performance. Unfortunately, this lesson is not always followed in practice. A few examples may illustrate this:

– A thin ($< 2\lambda_{\rm int}$ deep) calorimeter intended for detecting high-energy ($> 10^{11}$ eV) cosmic rays (mainly protons) outside the Earth's atmosphere is subject to severe effects of shower leakage. These effects completely dominate the energy resolution. Therefore, a high-quality crystal (BGO) is as good as a crudely sampling device in this respect, if neither is capable of measuring the effects of shower leakage event-by-event [25].

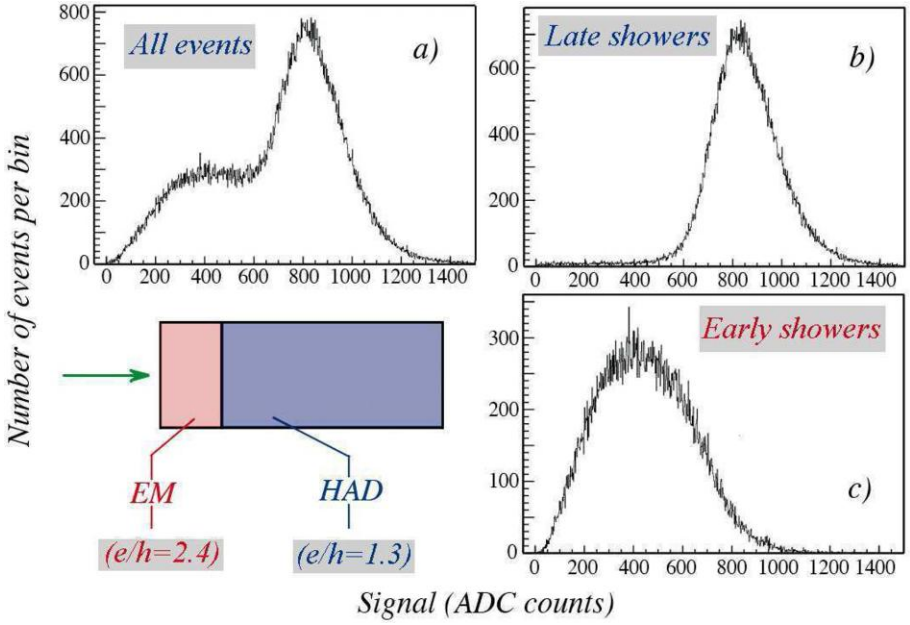

Fig. 30. – Signal distributions for 10 GeV pions showering in the CMS calorimeter system. Events in which the pions penetrate the crystal em section and deposit all their energy in the hadronic section (b) have a very different signal distribution than events in which the shower starts in the em section (c). The total signal distribution (a) is a superposition of the two.

– A calorimeter system with a crystal em section, chosen for ultimate performance in detecting em showers, will have poor performance for hadron detection, *no matter what* one chooses for the hadronic section. The large e/h value of the em section, combined with the large event-to-event fluctuations in the energy sharing between both sections spoils the hadronic performance of the detector. An example of this is shown in fig. 30, and concerns the CMS experiment at CERN's Large Hadron Collider. The CMS calorimeter system is optimized for em shower detection, with a $PbWO_4$ crystal em section. The large e/h value of this section (2.4) has spectacular effects for hadrons. The figure shows very different signal distributions for 10 GeV pions, depending on the starting point of the showers. In practice, this starting point cannot always be determined, especially if these pions are part of a collimated jet. If that is the case, the response function is given by fig. 30a.

– The light yield of quartz-fiber detectors is typically so small that signal quantum fluctuations (photoelectron statistics) are a major contributing factor to the energy resolution. If that is the case, there is nothing to be gained from increasing the sampling frequency, *i.e.*, by using more, thinner fibers instead of fewer, thick ones.

4. – The future of calorimetry

The energy resolution achievable with crystal calorimeters, based on materials such as CsI(Tl) or BGO, is unrivaled at em shower energies below $\sim 20\,\text{GeV}$. However, one should realize that below 1% the resolution is determined by factors other than the intrinsic stochastic term of the detector. Instrumental effects tend to dominate at that point. For this reason, excellent resolution is not a unique feature of crystals at energies above 20 GeV. Sampling calorimeters such as those used in the KLOE [12] and NA48 [18] experiments offer comparable performance. At energies above 50 GeV, crystals offer no specific advantage over other, much cheaper types of detectors. Crystals are substantially less ideal in calorimeter systems with which one also wants to detect hadrons or jets. The latter are collections of photons and hadrons, the result of fragmenting quarks, diquarks or gluons. The effects of the large e/h values of crystal calorimeters were discussed before and illustrated in fig. 30.

In general, factors other than the calorimeter resolution also play an important role in jet detection, in particular the jet algorithm and contributions of underlying events to the signals. However, as the energy increases and jets become more collimated, these effects become relatively less important. Especially at a high-energy linear e^+e^- collider, there is no reason why one should not aim to measure the fourvectors of *all* elementary constituents of matter (including quarks and gluons) with a precision of $\sim 1\%$.

It has become customary to express the energy resolution of calorimeters as the quadratic sum of a scaling term and an energy independent ("constant") term:

$$\frac{\sigma}{E} = \frac{c_1}{\sqrt{E}} \oplus c_2, \tag{7}$$

and often the performance of actual devices is referred to in terms of the value of c_1. As we have seen in subsect. **3**˙3, this parameterization is *fundamentally incorrect*, especially for hadronic showers in non-compensating calorimeters. Therefore, we propose to quote the resolution in terms of a fraction at a given energy, or in terms of the value of σ at that energy. And, of course, σ should represent the rms value of the signal distribution, not the result of a Gaussian fit that ignores the non-Gaussian tails characteristic of the signals from non-compensating calorimeters.

An often quoted design criterion for calorimeters at a future high-energy linear e^+e^- collider is the need to distinguish between hadronically decaying W and Z bosons, and it is claimed that c_1 has to be smaller than 0.3 (30%) to achieve that. This means that one should be able to detect 80–90 GeV jets with a resolution of 3–3.5 GeV. This goal can be achieved with compensating calorimeters. However, because of the small sampling fraction required for compensation, the em energy resolution is limited in such devices (*e.g.*, $15\%/\sqrt{E}$ [19]). Also, because of the crucial role of neutrons produced in the shower development, the signals would have to be integrated over relatively large volumes and time intervals to achieve this resolution, which is not always possible in practice. In the following, we discuss some other methods that are currently being pursued to circumvent these limitations.

4·1. *The energy flow method.* – One method that has been proposed in this context, the so-called *Energy Flow Method*, is based on the combined use of a precision tracker and a highly granular calorimeter. The idea is that charged jet fragments can be precisely measured with the tracker, while the energy of the neutral particles is measured with the calorimeter. Such methods have indeed successfully been used to improve the resolution of jets from Z^0 decay at LEP, to $\sim 7\,\mathrm{GeV}$ [20].

The problem that limits the success of this method is of course that the calorimeter does not know or care whether the particles it absorbs are electrically charged. Therefore, one will have to correct the calorimeter signals for the contributions of the charged jet fragments.

Proponents of this method have advocated a fine granualarity as the key to the solution of this "double-counting" problem [21]. However, it has been argued that, for practical geometries, this is an illusion [22]. Especially in jets with leading charged fragments, the overlap between the showers from individual jet fragments makes the fine granularity largely irrelevant. In the absence of energy constraints, such as the ones used at LEP, the proposed method may improve the performance of a poor calorimeter system by $\sim 30\%$, but the resolution gets nowhere near the performance one may expect from a dedicated stand-alone calorimeter system [22].

Of course, in the absence of any reliable Monte Carlo simulations, the only way to prove or disprove the advocated merits of the proposed method is by means of dedicated experiments in realistic prototype detectors. To that end, the CALICE Collaboration has built an impressive instrument [23], containing ~ 14000 electronic readout channels. However, experimental results from several years of testbeam operations have not (yet) provided any evidence that the mentioned performance requirements can be met with this approach.

4·2. *Off-line compensation.* – The energy resolution of a calorimeter is determined by *fluctuations*, not by mean values. This means that one should not expect any beneficial effect from methods in which the signals from different calorimeter sections are weighted by different factors in an attempt to equalize the response to electromagnetic and hadronic showers. Such methods are known as "offline compensation techniques".

This statement may be illustrated by an example taken from practice. Figure 31 shows test results obtained with a non-compensating calorimeter that was preceded by various amounts of "dead" material (iron). This iron had a larger absorbing effect on electron showers than on hadronic ones. As a result, the e/π signal ratio measured with the calorimeter decreased as the amount of iron was increased (fig. 31a). For an absorber thickness of $8X_0$ (13 cm Fe), the compensation condition $e/\pi = 1$ was achieved. Yet, the hadronic energy resolution was significantly worse than without the "dummy" iron section (fig. 31b). This is of course no surprise, since the signals were collected from only part of the block of matter in which the shower develops. Fluctuations in the fraction of the energy deposited in the part from which the signals were collected added to the ones that determined the resolution in the absence of the dummy section and thus deteriorated the resolution.

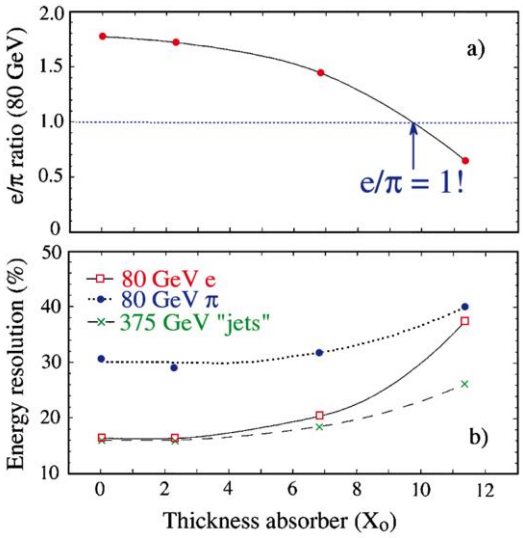

Fig. 31. – The e/π signal ratio at 80 GeV (a) and the energy resolution (b) of a non-compensating calorimeter preceded by dead material (iron), as a function of the thickness of this material. The energy resolution is given for 80 GeV electrons and pions, as well as for 375 GeV multiparticle "jets" generated by 375 GeV pions in an upstream target [24].

Although this is maybe a somewhat extreme example, it does illustrate the fact that there is no magic in the e/π signal ratio. The resolution of a non-compensating calorimeter is determined by the event-to-event fluctuations in the em shower content and as long as nothing is done to reduce (the effect of) these fluctuations *event by event*, no improvement in the hadronic energy resolution may be expected. The key for possible success of such weighting methods lies thus in the *event-by-event* aspect. There are some examples in the literature of more or less successful attempts to improve the hadronic energy resolution through a determination of the em shower content event by event (*e.g.*, fig. 32). These methods were all based on the different spatial dimensions of the em and non-em shower components. The em showers develop in a much smaller detector volume and thus lead to local areas of high energy deposit density (see also fig. 7). Such methods work reasonably well in a clean testbeam environment for single particles carrying a precisely known energy. However, when confronted with a collection of particles of unknown composition and energies (jets), their benefit is much less clear.

4˙3. *Dual-readout calorimetry.* – An alternative approach to measuring the em shower fraction (f_{em}) event by event, which does not rely upon the spatial shower characteristics, exploits the fact that the production of Čerenkov light in hadron showers is almost exclusively due to the em shower component. This is a result of the fact that the electrons and positrons through which the em shower energy is deposited are relativistic down to ~ 0.2 MeV, while the spallation protons that dominate the non-em calorimeter signals

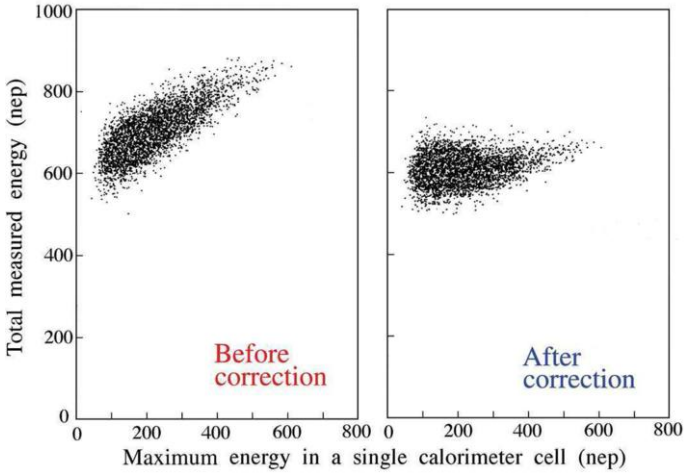

Fig. 32. – WA1 results on off-line compensation, showing the correlation between the total measured signal and the maximum signal observed in one individual calorimeter segment. Results are given for 140 GeV pions before and after applying a weighting factor, based on the signals observed in the individual calorimeter segments [6].

are typically non-relativistic (see sect. **2**). Therefore, by comparing the amounts of Čerenkov light and scintillation light produced by a hadron shower, one can determine the em shower fraction event by event. A description of the dual-readout project is reported in the following section as an example of recent developments in calorimetry.

5. – The DREAM project

The value of this method was first demonstrated with an instrument intended to measure high-energy (PeV) cosmic hadrons. This 1.4 λ_{int} deep calorimeter was equipped with 2 types of optical fibers, plastic-scintillator and quartz, which measured the scintillation and Čerenkov light, respectively [25]. The ratio of the quartz and scintillator signals turned out to be a good event-to-event measure for the fraction of the shower energy carried by π^0's produced in the first interaction, and thus for the shower leakage, which dominated the resolution of this thin detector. Inspired by this success, a fully containing (10 λ_{int} deep) calorimeter was built and tested. This instrument and the Collaboration that operates it became known as DREAM (Dual-REAdout Method). Some results are shown below [26, 27].

The basic element of the detector (fig. 33) is a hollow, extruded copper tube, 200 cm long and $4 \times 4\,\text{mm}^2$ in cross-section. Seven optical fibers are inserted in the 2.5 mm wide hole, 3 scintillating fibers and 4 clear ones for detecting Čerenkov light. The detector consists of about 6000 such tubes and contains in total $\sim$ 90 km of fibers. The fibers are split as they exit at the rear into bunches of the two types of fibers. In this way, a hexagonal readout structure is created. Each hexagonal cell is read out by 2 PMTs, one

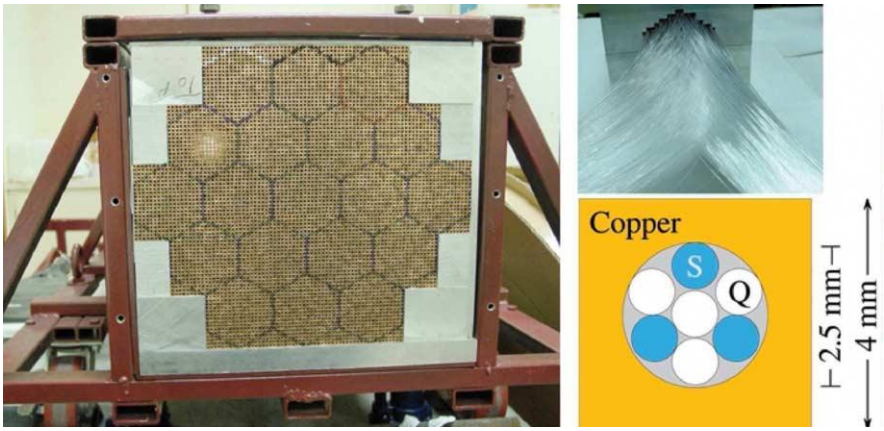

Fig. 33. – Layout of the DREAM calorimeter. The basic element is a 200 cm long extruded copper tube (cross-section $4 \times 4\,\mathrm{mm}^2$), with a central hole of 2.5 mm diameter. Three scintillating fibers and 4 undoped Čerenkov fibers are inserted in this hole. The calorimeter consists of about 6000 such tubes. The fibers are split as they exit at the rear into bunches of the two types of fibers.

for each type of light. Figure 34 shows the signal distributions for 100 GeV π^- recorded in this device. The signal distributions are asymmetric, reflecting the characteristics of the f_{em} fluctuations. The central value is also considerably smaller than that for the electrons that were used to calibrate the detector, by 18% and 36% for the scintillator and Čerenkov signals, respectively.

Using the ratio of the two signals, the value of f_{em} could be determined *event by event* in a straightforward way. The value of this ratio (Q/S) is represented by a straight line in the scatter plot of the two signals (fig. 35). This ratio is related to the em shower fraction as

$$\frac{Q}{S} = \frac{f_{\mathrm{em}} + 0.21\ (1 - f_{\mathrm{em}})}{f_{\mathrm{em}} + 0.77\ (1 - f_{\mathrm{em}})}\,, \tag{8}$$

where 0.21 and 0.77 represent the h/e ratios of the Čerenkov and scintillator calorimeter structures, respectively. The merits of this method are clearly illustrated by fig. 36, which shows the overall Čerenkov signal distribution for 100 GeV π^- (a), as well as distributions for subsamples selected on the basis of their f_{em} value (b), determined by eq. (8). Each f_{em} bin probes a certain region of the overall signal distribution, and the average value of the subsample distribution increases with f_{em}.

Once the value of f_{em} was determined, the signals could be corrected in a straightforward way for the effects of non-compensation. In this process, the energy resolution improved, the signal distribution became much more Gaussian and, most importantly, the hadronic energy was correctly reproduced. This was true both for single pions as well as for jets, an important difference with the methods based on the energy deposit profile, which do not work for jets.

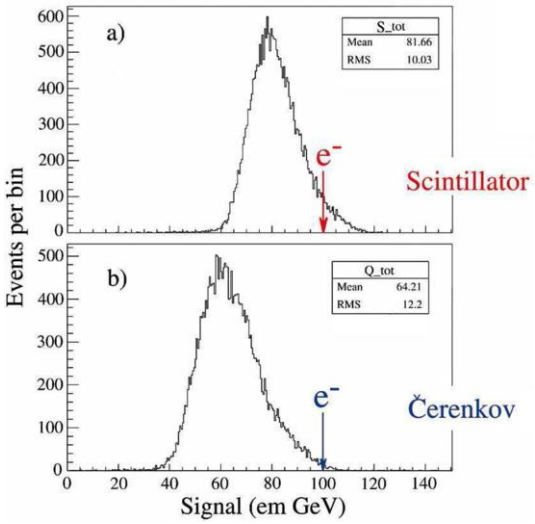

Fig. 34. – Signal distributions for 100 GeV π^- recorded by the scintillating (a) and the Čerenkov (b) fibers. The signals are expressed in the same units as those for em showers, which were used to calibrate the detector.

The results for 200 GeV "jets" are shown in fig. 36c-e. These "jets" were in fact not fragmenting quarks or gluons, but multiparticle events created by pions interacting in a target placed upstream of the calorimeter. Using only the *ratio* of the two signals

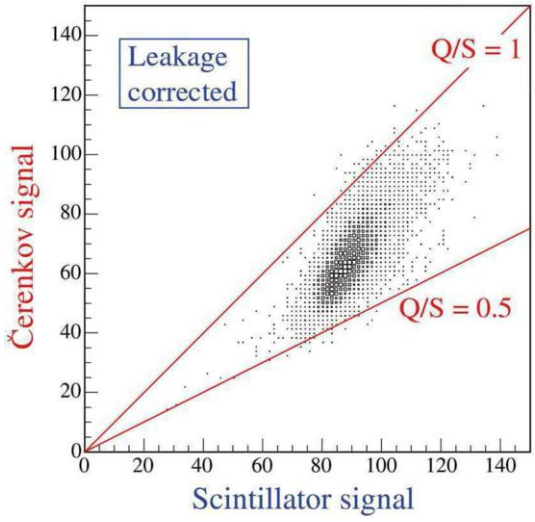

Fig. 35. – Čerenkov signals *versus* scintillator signals, for 100 GeV π^- in DREAM.

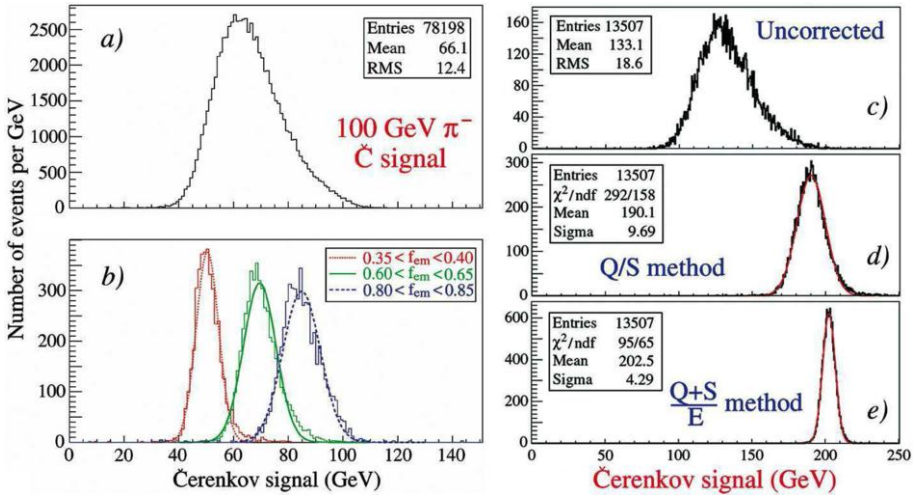

Fig. 36. – Čerenkov signal distribution for 100 GeV π^- (a) and distributions for subsamples of events selected on the basis of the measured $f_{\rm em}$ value, using the Q/S method (b). Signal distributions for high-multiplicity "jets" in the DREAM before (c) and after (d) corrections on the basis of the observed Čerenkov/scintillator signal ratio were applied. In diagram (e), energy constraints were used, which eliminated the effects of lateral shower fluctuations that dominate the resolution in (d).

produced by this calorimeter, the resolution for these "jets" was improved from 14% to 5%, in the Čerenkov channel. It was shown that this 5% resolution was in fact dominated by fluctuations in side leakage in this (small, only 1200 kg instrumented volume) detector. Eliminating such fluctuations led to a further considerable improvement (fig. 36e).

Also the jet energy was well reconstructed as a result of this procedure (fig. 37). Whereas the raw data gave a mean value of 133.1 GeV for these 200 GeV jets, the described procedure led to hadronic energies that were within a few percent correct, *in an instrument calibrated with electrons*. In the process, hadronic signal linearity (a notorious problem for non-compensating calorimeters) was more or less restored as well. Any remaining effects can be ascribed to side leakage and would most likely be eliminated in a larger detector of this type. Simultaneous detection of the scintillation and Čerenkov light produced in the shower development turned out to have other, unforeseen beneficial aspects as well. One such effect is illustrated in fig. 38, which shows the signals from muons traversing the DREAM calorimeter along the fiber direction. The gradual increase of the response with the muon energy is a result of the increased contribution of radiative energy loss (Bremsstrahlung) to the signals. The Čerenkov fibers are *only* sensitive to this energy loss component, since the primary Čerenkov radiation emitted by the muons falls outside the numerical aperture of the fibers. The constant (energy-independent) difference between the total signals observed in the scintillating and Čerenkov fibers represents the non-radiative component of the muon's energy loss. Since both types of fibers

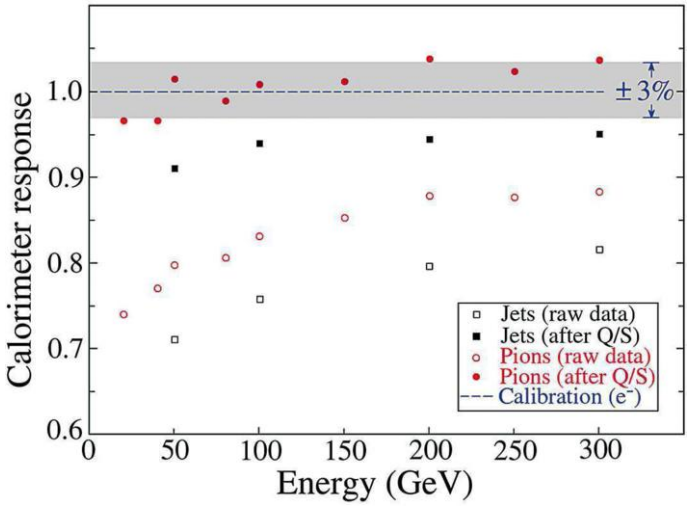

Fig. 37. – The DREAM response to single pions and high-multiplicity jets, before and after corrections made on the basis of the measured Čerenkov/scintillator signal ratio.

were calibrated with em showers, their response to the radiative component is equal. This is the only example we know of a detector that separates the energy loss by muons into radiative and non-radiative components.

5˙1. *Measurement of the neutron fraction.* – The resolution of a sufficiently large detector would then become dominated by nuclear breakup effects. Fluctuations in the fraction of the total energy needed to release protons, neutrons and heavier nuclear fragments in the nuclear reactions initiated by the shower particles lead to fluctuations of the visible energy, and thus to fluctuations in the calorimeter response. It has been demonstrated previously [14] that a measurement of the total kinetic energy carried by neutrons generated in the shower development is a powerful tool for reducing the effects of these fluctuations, especially in high-Z absorber materials where most of the nucleons released in the nuclear reactions are indeed neutrons.

The contributions of neutrons to the signals are responsible for the fact that the energy resolution of compensating calorimeters based on plastic-scintillator readout is considerably better than in those that use liquid-argon or silicon as active components. Neutron contributions also explain why the energy resolution of compensating calorimeters using uranium as absorber material is not as good as in lead/plastic-scintillator devices, since a large fraction of the neutrons in uranium come from fission, instead of nuclear spallation [1]. Measuring the signal contributions from shower neutrons event by event has always been another important objective of the DREAM Collaboration.

Test beam results demonstrated that this can be achieved by measuring the time structure of the scintillator signals [28, 32]. The neutron contribution manifests itself as a tail with a characteristic time constant ($\sim$ 20 ns in the fiber calorimeter). As illustrated in fig. 39, this tail was absent in the Čerenkov signals and also in scintillator

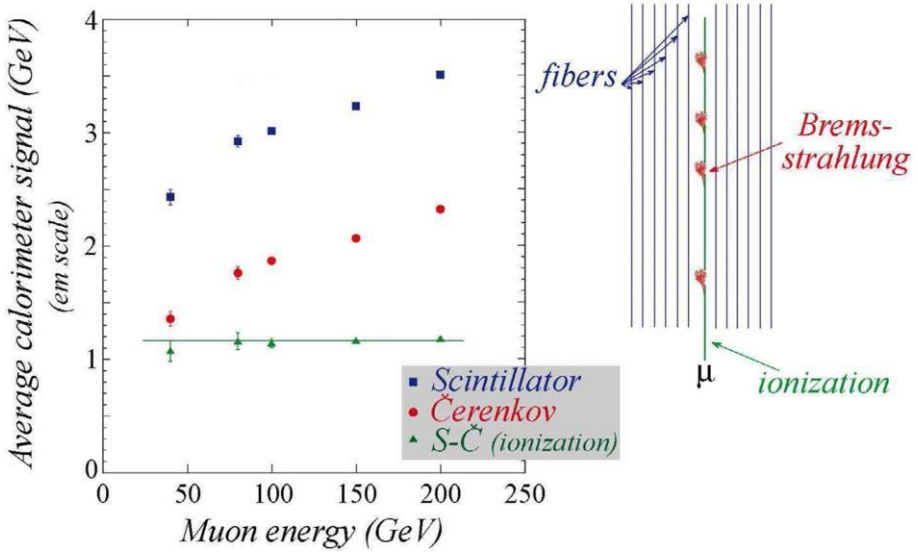

Fig. 38. – Average values of the scintillator and Čerenkov signals from muons traversing the DREAM calorimeter, as a function of the muon energy. Also shown is the difference between these signals. All values are expressed in units of GeV, as determined by the electron calibration of the calorimeter [26].

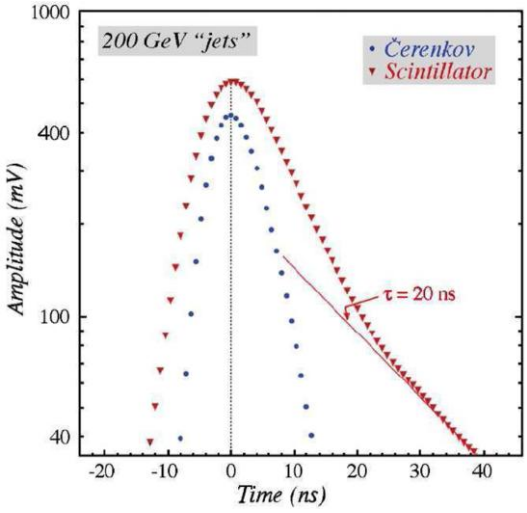

Fig. 39. – Average time structure of the Čerenkov and scintillation signals recorded for 200 GeV "jets" developing in the DREAM calorimeter. The scintillation signals exhibit a tail with a time constant of about 20 ns, which is absent in the Čerenkov signal [32].

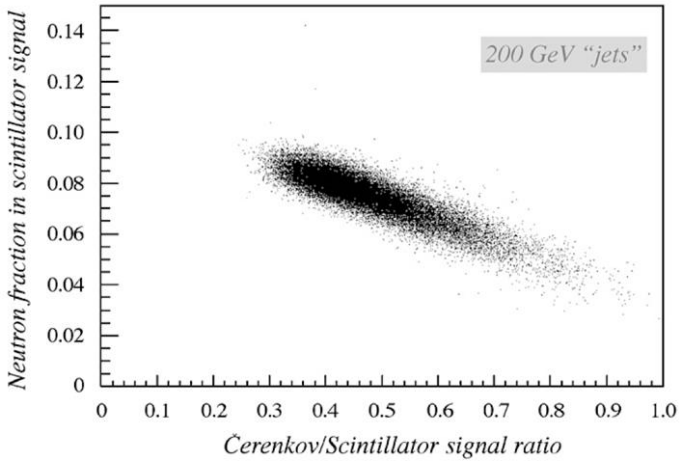

Fig. 40. – Scatter plot for 200 GeV "jets". For each event, the combination of the total Čerenkov/scintillation signal ratio and the fractional contribution of the neutrons to the total scintillation signal is represented by a dot [32].

signals generated by em showers. The time structure measurements made it possible to determine the relative contribution of this tail to the scintillation signals event by event. The fact that this fraction was anti-correlated with the Čerenkov/scintilation signal ratio (fig. 40), and thus with the relative strength of the em shower component, underscores

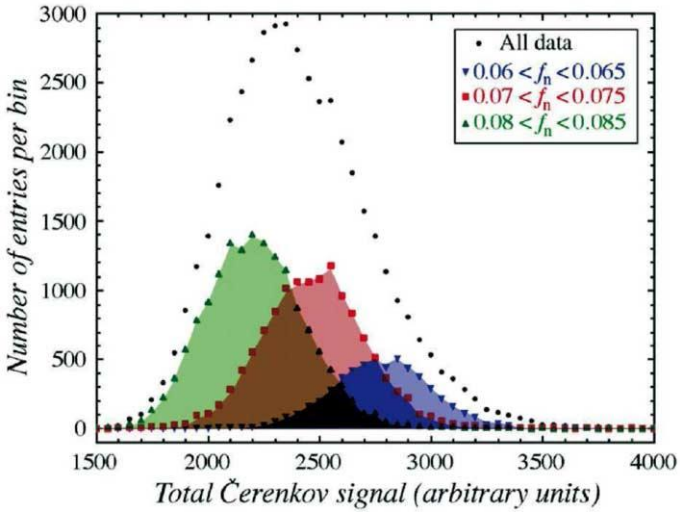

Fig. 41. – Distribution of the total Čerenkov signal for 200 GeV "jets" and the distributions for three subsets of events selected on the basis of the fractional contribution of neutrons to the scintillator signal [32].

TABLE I. – *Different properties of Čerenkov and scintillation light.*

	Čerenkov	Scintillation
Time structure	Prompt	Exponential decay
Light spectrum	$1/\lambda^2$	Characteristic peaks
Directionality	Cone: $\cos\theta_C = 1/\beta n$	Isotropic

that this tail indeed represents the neutrons produced in the shower development [32].

To further check the validity of the above statement, an analysis very similar to the one that was originally used to study the merits of the dual readout method has been carried out. Event samples selected with different neutron fractions (f_n) are selected and their signal distributions are compared with the entire event sample (fig. 41). The figure contains the total Čerenkov signal distributions for all 200 GeV "jet" events, as well as the distributions for subsamples of events with $0.06 < f_n < 0.065$, $0.07 < f_n < 0.075$ and $0.08 < f_n < 0.085$. Clearly, each subsample probes a different region of the total signal distribution for all the events. This total Čerenkov signal distribution for all events is thus a superposition of many distributions such as the ones shown in this figure. Each of these distributions for the subsamples has a different mean value, and a resolution that is substantially better than that of the overall signal distribution. The signal distibutions for the subsamples are also much more Gaussian than the overall signal distribution, whose shape is simply determined by the extent to which different f_n values occurred in practice.

If the techniques described above were fully exploited for eliminating the effects of the fluctuations that limit the performance of hadron calorimeters, then the theoretical resolution limit of $\sim 15\%\sqrt{E}$ should be within reach. Dual-readout detectors thus hold the promise of high-quality calorimetry for all types of particles, with an instrument that can be calibrated with electrons.

5˙2. *Dual-readout with crystals.* – Once the effects of the dominant source of fluctuations are eliminated, the resolution is determined and limited by other types of fluctuations. In the case of the DREAM detector, these fluctuations include, apart from fluctuations in side leakage which can be eliminated by making the detector larger (see fig. 36e), *sampling fluctuations* and fluctuations in the *Čerenkov light yield*. The latter effect alone (8 Čerenkov p.e. per GeV) contributed with $35\%/\sqrt{E}$ to the measured resolution. The DREAM Collaboration is currently exploring the possibility to use crystals for dual-readout purposes. Certain dense high-Z crystals ($PbWO_4$, BGO) produce significant amounts of Čerenkov light, which can in principle be separated from the scintillation light by exploiting differences in time structure, spectral properties and directionality, as summarized here below and in table I.

– *Differences in directionality.* Contrary to scintillation light, which is emitted isotropically, Čerenkov light is emitted at a characteristic angle by the relativistic (shower) particles that traverse the detector. We measured the signals for different orientations (*i.e.*, θ angles) of the crystal with respect to the beam.

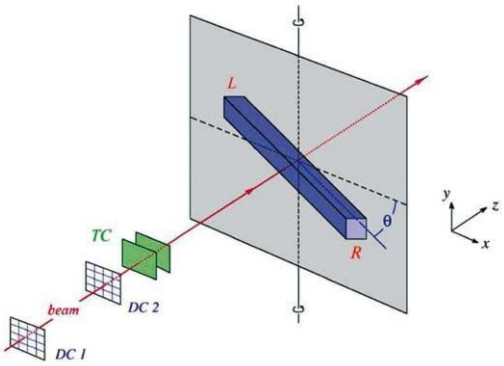

Fig. 42. – Experimental setup in which the beam tests of the crystals were performed. The angle θ is negative when the crystal is oriented as drawn here [30].

– *Differences in time structure.* Čerenkov light is prompt, while the scintillation mechanism is characterized by one or several time constants, which determine the pulse shape. Detailed measurements of the time structure were performed (at different θ angles) to study the properties of the prompt component of the signals from the crystals.

– *Differences in the spectral properties.* Čerenkov light exhibits a λ^{-2} spectrum, while the scintillation spectrum is specific to each type of crystal. Of course, the extent to which these differences may be observed in the measured signals depends also on the optical filters which can be positioned between the crystal and the PMT and on the wavelength dependence of the quantum efficiency of the light detector.

The use of crystals offers the possibility to obtain further significant improvements of the DREAM results, which are determined by the precision with which the relative contributions to the total signal of these two types of light can be measured. Studies on homogeneous media for dual readout have been carried on in testbeams performed in the H4 beam line of the Super Proton Synchrotron at CERN with a 50 GeV electron beam.

The setup for single-crystal tests was common to all measurements. The light produced by particles traversing the crystal under test was read out by two photomultiplier tubes (PMTs) located at opposite ends. The crystal under study was mounted on a platform able to rotate around a vertical axis (fig. 42). Crystal were oriented in the horizontal plane and the rotation axis went through their geometrical center. The particle beam was also steered through this center. The angle θ, which is frequently used in the following, represents the angle between the crystal axis and a plane perpendicular to the beam line. The angle increases when the crystal is rotated in such a way that the crystal axis Left-Right (L-R) approaches the direction of the traveling beam particles. We call as "Čerenkov" angle the angle at which the Čerenkov light has a maximum in one of the two PMTs: $\theta = 30$ for the Right PMT and $\theta = -30$ for the Left one. We also

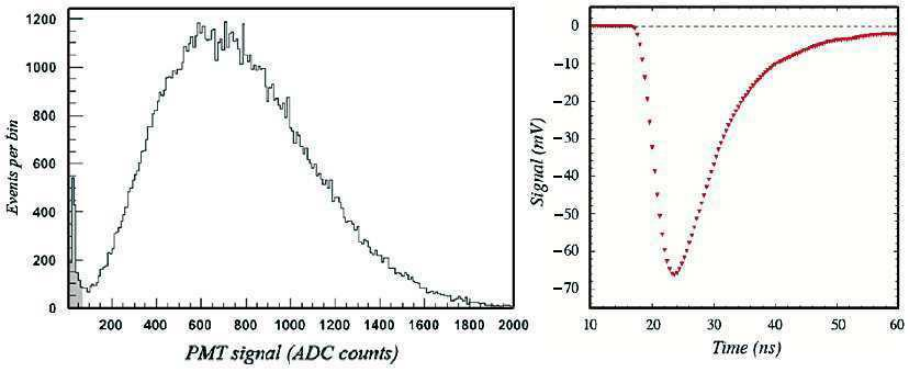

Fig. 43. – Distribution of the energy deposited and average time structure of the signals from 50 GeV electrons in a $PbWO_4$ crystal [31].

call as "anti-Čerenkov" the opposite angle: the angle at which a given PMT collects only scintillation light, but not Čerenkov. The crystal orientation shown in fig. 42 corresponds to $\theta = -30$.

The quality of the information obtained in this way is illustrated in fig. 43, which shows a typical ADC signal distribution (left) and the average time structure of the signals (right) from one PMT, generated by 50 GeV electrons traversing the crystal.

5˙2.1. Lead tungstate crystals. Lead tungstate crystals ($PbWO_4$) are attractive as detectors for electromagnetic showers because of their high density, which implies a short radiation length and Moliere radius, their fast signals and their relative insensitivity to the effects of radiation damage.

A $PbWO_4$ crystal with cross-section of $2.2 \times 2.2\,\mathrm{cm}^2$, corresponding to 2.5 radiation lengths, and 18 cm long, was tested in order to demonstrate that a significant fraction of the signals from those crystals is due to Čerenkov radiation [29]. This was concluded from the measurements of the time structure of the signals and the non-isotropic nature of the light generated by high-energy electrons and muons traversing a $PbWO_4$ crystal. In the crystal used for these studies, Čerenkov light contributed up to 15% of the signals measured by a PMT. This was very promising and further tests were done about the feasibility to use $PbWO_4$ for the Dual Readout technique. In particular, quantitative measurements of the Čerenkov fraction have been carried out through temperature dependence measurements [30].

Two important figures of merit, which show the possibility of using crystals for the dual readout calorimetry, are described here. Figure 44 shows the average time structure of the signals from 50 GeV electrons, for angles $\theta = 30$ and -30, respectively. The trailing edges of these two signals are in great detail identical. However, the leading edge of the signal recorded at the "Cherenov" angle ($\theta = -30$ in the figure) is considerably steeper, and its amplitude larger than for the signal recorded with the same PMT at the "anti-Cherenov" angle. Of course, this behavior is reversed for the PMT on the opposite side.

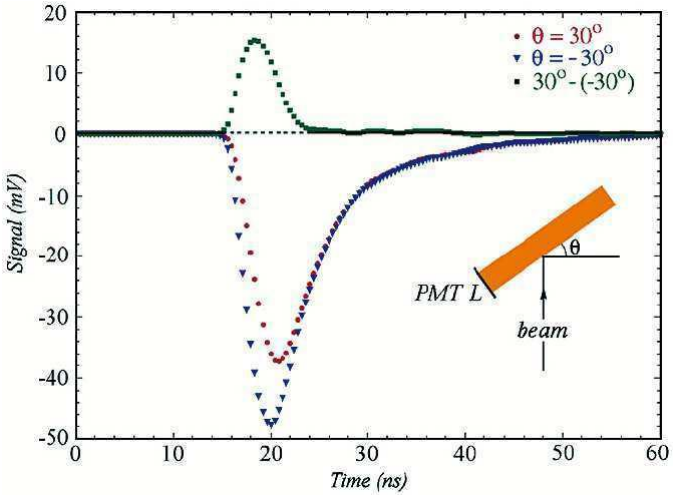

Fig. 44. – Time structures of the PMT signal from 50 GeV electrons traversing a $PbWO_4$ crystal at angles $\theta = 30$ and -30, respectively, and the difference between these two time distributions [31].

The figure also shows the result of subtracting the signal observed at $\theta = -30$ from that at $\theta = 30$. The resulting pulse represents the (inverted) calorimeter response function to the (prompt) Čerenkov component generated by showering electrons in the $PbWO_4$ crystals.

Another useful figure of merit is the response asymmetry defined as the ratio $(R - L)/(R + L)$, where R and L represent the average signals measured in the two PMTs, respectively, for the same events. Any non-zero value in this ratio is indicative for a non-isotropic component in the light generated in the crystals, *i.e.* Čerenkov light. Figure 45 shows the asymmetry response as a function of the rotation angle. The circles in the figure represent the asymmetry as measured in the normal configuration, *i.e.* with beam particles showering in the crystal. The triangles, instead, show the asymmetry as measured in the configuration called "late" in fig. 45: beam particles start showering in a block of lead positioned in front of the crystal. In this case the effect of the asymmetry response is highly reduced, since the light produced in the crystal is generated by particles in the late part of the shower, where their directions is almost isotropic.

These two techniques have been used extensively in the test beam data analysis.

In order to use crystals in dual-readout calorimeters, and to have a better separation between the Čerenkov and the scintillation components, a "perfect" crystal should have an emission wavelength far from the bulk of Čerenkov radiation, a scintillation decay time of tenths of nanoseconds. Using those guidelines, the DREAM Collaboration has tested $PbWO_4$ crystals doped with different ions and BGO crystals.

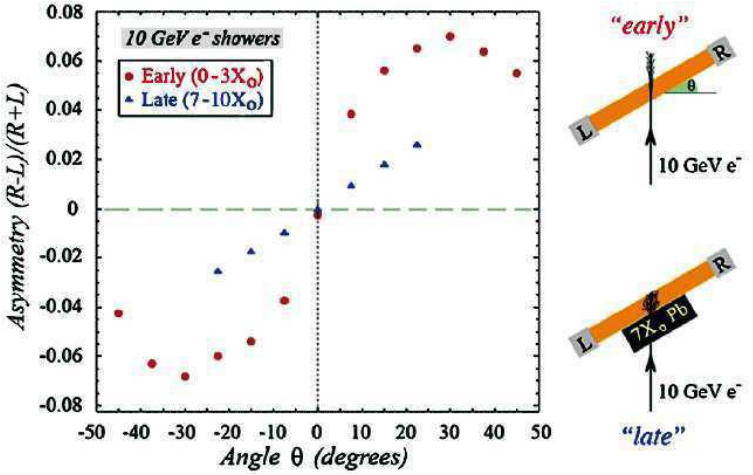

Fig. 45. – Left-right response asymmetry measured for 10 GeV electrons showering in a $2.5X_0$ thick $PbWO_4$ crystal, as a function of the orientation of the crystal (the angle θ). Results are shown for the early and late components of the showers. The latter measurements were obtained by placing 4 cm of lead upstream of the crystal [31].

5˙2.2. Doped $PbWO_4$ crystals. From the literature the DREAM Collaboration has found that some doping elements, if added to the $PbWO_4$ crystals, can achieve a shift of the scintillation spectrum to longer wavelengths, and a longer decay time.

Based on the studies published in [37], the DREAM collaboration tested praseodymium (Pr) as a dopant with three concentration levels (0.5%, 1%, 1.5%). Similar to other trivalent dopants, Pr^{+3} suppresses scintillation in the host crystal altogether. On the other hand, it introduces new scintillation components with long time constants (in the μs range), based on Pr^{3+} $4f$-$4f$ transitions in the green-red part of the spectrum. While spectral separation became optimal, the temporal response made this dopant not suitable for Dual Readout Calorimetry.

Molybdenum dopant [35, 36] resulted to be more promising for the Dual Readout technique. The DREAM collaboration have extensively tested $PbWO_4$ crystals with different amount (0.1% to 5%) of molybdenum [33]. In particular the DREAM collaboration studied the time structure of the signals, the C/S ratio, the effect of light attenuation, and the Čerenkov light yield. The maximum of the emission is shifted from ~ 420 nm to ~ 500 nm. There is a little difference between the effects of the 0.1% and 5% Mo concentration in this measurement, as far as the emission wavelength is concerned.

The doped crystals had a length of 20 cm and a cross-section of $2.0 \times 2.0\,\mathrm{cm}^2$ ($2.25X_0$). In order to select the wavelength region that contributed to the signal, and to study the C/S signal for each of them, different optical filters were used. In particular, long-pass filter (yellow) have been chosen to select the scintillation light and short-pass filter (UV) for the Čerenkov light. Figure 46 shows the time structure measured on both ends of the crystal. The solid line represents the signal from the UV filter side, while the dotted line

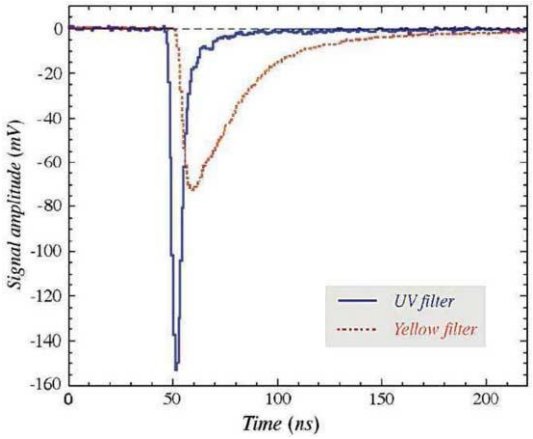

Fig. 46. – Average time structure of the signals from a $PbWO_4$ crystal doped with 1% Mo, generated by 50 GeV electrons. The angle θ was 30 in these measurements. Shown are the results obtained with UV and yellow filters, respectively [33].

represents the time structure measured on the yellow filter one. The shape of the two signals strongly indicates that the light passing the UV filter produced an almost pure Čerenkov signal, while the light passing the yellow filter generated a signal that had all the characteristics of a scintillation light.

Since the signal passing trough the UV filter is completely dominated by Čerenkov radiation, as shown, its dependence on the angle of incidence of the beam particles is expected to be completely different from that of the yellow filter with scintillation light. This is demonstrated in fig. 47 which shows the ratio of the signals read at the two ends, as a function of the angle of incidence of the beam particles. Since Čerenkov light is emitted at the characteristic angle, $\theta_C = \arccos 1/n \sim 63$ (in this case), the signal on the side equipped with the UV filter is expected to show a maximum when the crystal is rotated, with respect to the beam, of an angle: $\theta = 90 - \theta_C \sim 27°$. The signals, and thus their ratio, were determined in two different ways for this analysis, as described in caption of fig. 47.

A measurement of the attenuation length of the two light components shows that the scintillation is almost independent of the impact point, while the signals on the UV-filter side decreased strongly as the distance to the point where the light was produced increased ($\lambda_{att} \sim 10$ cm to 20 cm) using different filters and dopant concentration. This effect is due to the extremely narrow gap between he trasmission windows of the UV filter and the absorption cut-off of the crystal.

The Čerenkov light yield was measured to range from 7.7 p.e./GeV to 60 p.e./GeV, increasing with wider window for the UV filter and with lower Mo concentration.

5˙2.3. BGO crystals. BGO crystals have properties useful for Dual Readout Calorimetry: a scintillation spectrum peaking at 480 nm which allows to use filters to separate the

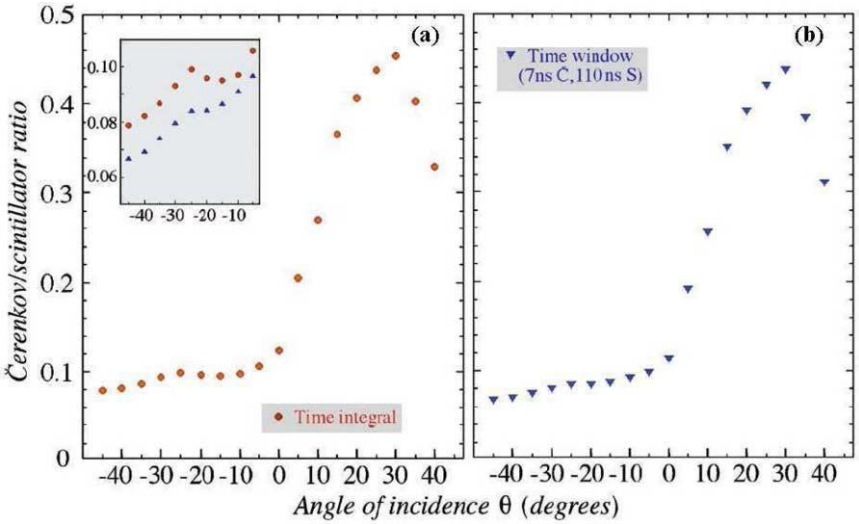

Fig. 47. – Ratio of the signals from the light transmitted by the UV and the yellow filters, as a function of the angle of incidence of the beam particles. The signals were obtained either by integrating over the full time structure (a), or over limited time interval chosen such as to purify their Čerenkov or scintillation content (b). One may notice a very small bump near the anti-Čerenkov angle ($\theta = -27$) in panel (a) and illustrated by its insert. This bump is the result of Čerenkov light that was reflected from the side where the yellow filter was mounted, and detected at the opposite side of the crystal. However, since this light has to make a roundtrip in the crystal before being detected, it arrives somewhat later at the PMT than the direct Čerenkov light seen for $\theta > 0$. Therefore, the effect is less pronounced in panel (b), where a very narrow time interval was used to define the Čerenkov signals [33].

bulk of the Čerenkov light, peaking at short wavelength from the scintillation light, and a decay time around 300 ns. This time constant is suitable for separating the prompt Čerenkov signal from the scintillation emission, while allowing for signals fast enough for high-energy physics. Also in this case, yellow and UV filters were used for the measurements. The time structure of the PMT signals is shown in fig. 48. The (prompt) Čerenkov component is represented by a sharp peak, whereas the long tail has the same characteristic time structure as the pure scintillation signals generated by the light transmitted through the yellow filter. Therefore the signals transmitted through the UV filter contains the event-by-event information about the relative contributions of Čerenkov and scintillation photons. Those contributions can be disentangled by integrating on two different time windows, as shown in fig. 49. Gate 1 was used to digitize the part of the signals that contained the Čerenkov peak, while gate 2 probed the scintillation component. Of course, some fraction of the scintillation light contributed to the signals from gate1 as well. However, the pure scintillation signals from the yellow filter side made it possible to determine this fraction with great precision and allows to correct for this contribution event by event on the basis of the gate 2 signals. In this way, pure digitized Čerenkov

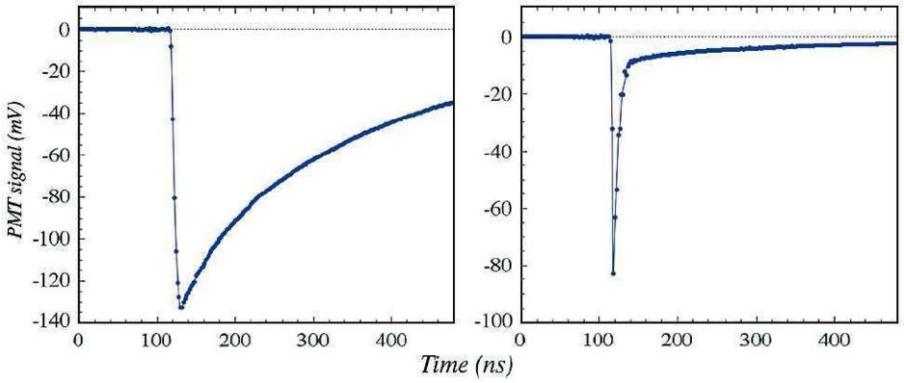

Fig. 48. – The time structure of a typical 50 GeV electron signal measured in the BGO crystal equipped with a yellow filter (a), and with a UV filter (b). These signals were measured with the sampling oscilloscope, with a time resolution of 2.0 ns. The crystal was oriented perpendicular to the beam line ($\theta = 0$) [31].

and scintillation signals were obtained from the crystal signals observed in the UV PMT. The DREAM collaboration measured in fact, the C/S ratio in individual events with a relatively accuracy of $\sim$ 20–30% for an energy deposit of 1 GeV.

5˙3. *Combined calorimetry.* – The Dream collaboration also tested a hybrid dual readout calorimeter. The electromagnetic section (ECAL) of this instrument consists of 100 BGO crystals and the hadronic section is the DREAM fiber prototype. Because of

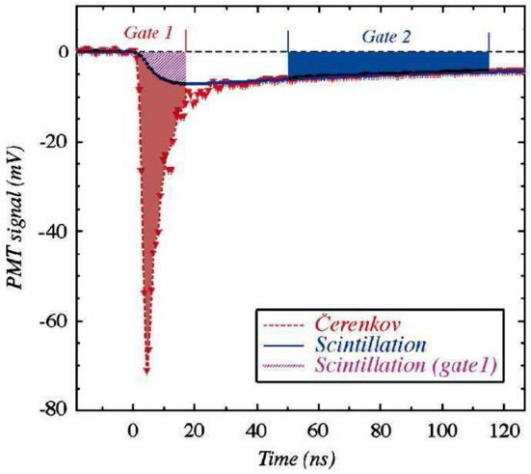

Fig. 49. – The UV BGO signals were used to measure the relative contributions of scintillation light (gate 2) and Čerenkov light (gate 1). The oscilloscope sampled the time structure at intervals of 0.8 ns in this case [34].

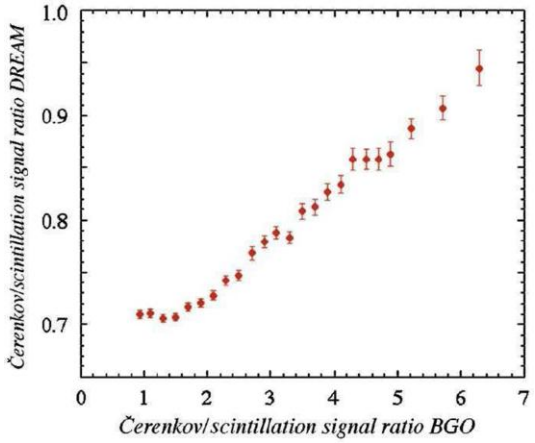

Fig. 50. – The Čerenkov/scintillation signal ratio of the DREAM calorimeter, for 200 GeV π^+ starting a shower in the BGO crystal, as a function of the Čerenkov/scintillation signal ratio of the BGO signal [34].

the small size of the ECAL section (less than 80% of the shower energy deposited by an electron was contained), large hadronic signals in the ECAL were likely to be caused by energetic π^0's produced in the early stages of the shower development. Therefore, it is reasonable to expect that hadronic events in which a considerable fraction of the energy was deposited in the BGO also exhibit substantial Čerenkov signals in the HCAL. In other words, one should expect a correlation between the C/S signal ratios in both sections of the calorimeter system. Figure 50 shows that this correlation was indeed very strong, except for events that had relatively small C/S signal ratios.

The analysis of the DREAM stand-alone data showed a strong correlation between the total hadronic calorimeter signal and the C/S signal ratio. This correlation formed the essence of the elimination of the effects of fluctuations in the em shower component, f_{em}, on the hadronic calorimeter performance [34]. Given the correlation observed in fig. 50, it is therefore no surprise that with this hybrid calorimeter the HCAL signal was strongly correlated with the C/S signal ratio measured in the BGO ECAL.

The crucial aspect of the DREAM procedure is the comparison of the scintillation and Čerenkov signals produced in hadronic shower development. The ratio between these two signals is a measure for the em shower fraction. In the case of the fiber detector in stand-alone mode, there is a simple one-to-one correspondence between this signal ratio and fem. For the combined BGO + fiber system, such a simple relationship does not exist, since the e/h values of the BGO crystal are different from those of the fiber detector, and the energy sharing between these two calorimeter systems varied from event to event. However, also in this case, the ratio of the Čerenkov and scintillator signals itself should be a good measure for the em shower content. This is illustrated in fig. 51. Figure 51a shows the distribution of the total Čerenkov signal. This signal is broad,

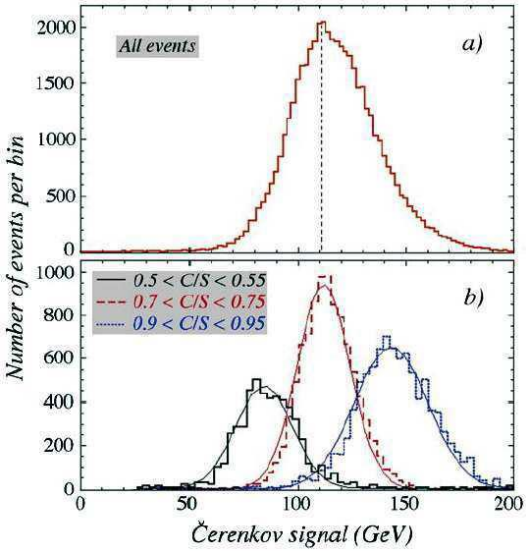

Fig. 51. – The Čerenkov signal distribution for 200 GeV jet events detected in the BGO + fiber calorimeter system (a) together with the distributions for subsets of events selected on the basis of the ratio of the total Čerenkov and scintillation signals in this detector combination (b) [34].

asymmetric (non-Gaussian) and centered around a value of only 110 GeV, whereas the total jet energy was 200 GeV. Figure 51b shows three different subsets of events, selected on the basis of the measured C/S signal ratio. These three distributions are considerably narrower, well described by Gaussian fits and centered at a value that increases roughly proportionally with the C/S value of the selected events. This is precisely what was observed for the fiber calorimeter in stand-alone mode, and what allowed us to eliminate the effects of fluctuations in fem in that calorimeter. The overall signal distribution (fig. 51a) is simply a superposition of many (Gaussian) distributions such as the ones shown in fig. 51b, and the asymmetric shape just represents the extent to which jets with different C/S values occurred in the event sample.

6. – Outlook

We have come a long way in improving calorimeters from rather crude instrumented absorbers to precision detectors. The key to these improvements has always come from a better understanding of the shower development process and its translation into calorimeter signals. Monte Carlo simulations have provided little or no guidance, especially in hadron calorimetry. Trial and error has been and remains the method of choice. Therefore, the only way to further this process is generic detector R&D. We have certainly not yet reached the end of the road in that respect. We believe this field is potentially full of interesting projects for graduate students and postdocs. Moreover, time and effort

invested in this field is likely to pay off, since a better understanding of the detectors is the key to a full exploitation of the physics potential of the experiment in which the detectors are to be used.

REFERENCES

[1] WIGMANS R., *Calorimetry, Energy Measurement in Particle Physics*, *International Series of Monographs on Physics*, Vol. **107** (Oxford University Press) 2000.
[2] WIGMANS R. and ZEYREK M., *Nucl. Instrum. Methods A*, **485** (2002) 385.
[3] ACOSTA D. *et al.*, *Nucl. Instrum. Methods A*, **316** (1992) 184.
[4] AKCHURIN N. *et al.*, *Nucl. Instrum. Methods A*, **399** (1997) 202.
[5] GREEN D., *Proceedings of the 4th International Conference on Calorimetry in High-Energy Physics*, *La Biodola, Italy*, edited by MENZIONE A. and SCRIBANO A. (World Scientific, Singapore) 1994, p. 1.
[6] ABRAMOWICZ H. *et al.*, *Nucl. Instrum. Methods*, **180** (1981) 429.
[7] ACOSTA D. *et al.*, *Nucl. Instrum. Methods A*, **294** (1990) 193.
[8] ATAČ M. *et al.*, *Nucl. Instrum. Methods*, **205** (1983) 113.
[9] WIGMANS R., *Nucl. Instrum. Methods A*, **259** (1987) 389.
[10] GALAKTIONOV Y. *et al.*, *Nucl. Instrum. Methods A*, **251** (1986) 258.
[11] ACOSTA D. *et al.*, *Nucl. Instrum. Methods A*, **302** (1991) 36.
[12] ANTONELLI A. *et al.*, *Nucl. Instrum. Methods A*, **354** (1995) 352.
[13] GINGRICH D. *et al.*, *Nucl. Instrum. Methods A*, **364** (1995) 290.
[14] DREWS G. *et al.*, *Nucl. Instrum. Methods A*, **290** (1990) 335.
[15] PEIGNEUX J. P. *et al.*, *Nucl. Instrum. Methods A*, **378** (1996) 410.
[16] AKCHURIN N. *et al.*, *Nucl. Instrum. Methods A*, **408** (1998) 380.
[17] WIGMANS R., *Rev. Sci. Instrum.*, **69** (1998) 3723.
[18] CONSTANTINI F. *et al.*, *Nucl. Instrum. Methods A*, **409** (1998) 570.
[19] ACOSTA D. *et al.*, *Nucl. Instrum. Methods A*, **308** (1991) 481.
[20] BUSKULIC D. *et al.*, *Nucl. Instrum. Methods A*, **360** (1995) 481.
[21] *TESLA Technical Design Report 2001*, report DESY 2001-011, DESY, Hamburg, Germany.
[22] LOBBAN O., SRIHARAN A. and WIGMANS R., *Nucl. Instrum. Methods A*, **495** (2002) 107.
[23] CALICE COLLABORATION, *Report to the Calorimeter R&D Review Panel*, ILC Report ILC-DET-2007-024 (2007).
[24] FERRANDO A. *et al.*, *Nucl. Instrum. Methods A*, **390** (1997) 63.
[25] NAGASLAEV V., SILL A. and WIGMANS R., *Nucl. Instrum. Methods A*, **462** (2000) 411.
[26] AKCHURIN N. *et al.*, *Nucl. Instrum. Methods A*, **533** (2004) 305.
[27] AKCHURIN N. *et al.*, *Nucl. Instrum. Methods A*, **536** (2005) 29; **537** (2005) 537; **548** (2005) 336; **550** (2005) 185.
[28] AKCHURIN N. *et al.*, *Nucl. Instrum. Methods A*, **581** (2007) 643.
[29] AKCHURIN N. *et al.*, *Nucl. Instrum. Methods A*, **582** (2007) 474.
[30] AKCHURIN N. *et al.*, *Nucl. Instrum. Methods A*, **593** (2008) 530.
[31] AKCHURIN N. *et al.*, *Nucl. Instrum. Methods A*, **595** (2008) 359.
[32] AKCHURIN N. *et al.*, *Nucl. Instrum. Methods A*, **598** (2007) 422.
[33] AKCHURIN N. *et al.*, *Nucl. Instrum. Methods A*, **604** (2007) 512.
[34] AKCHURIN N. *et al.*, *Nucl. Instrum. Methods A*, **610** (2007) 488.
[35] NIKL M. *et al.*, *Nucl. Instrum. Methods A*, **540** (2005) 381.
[36] NIKL M. *et al.*, *J. Appl. Phys.*, **91** (2002) 2791.
[37] NIKL M. *et al.*, *J. Appl. Phys.*, **104** (2008) 093514.

This page intentionally left blank

Proceedings of the International School of Physics "Enrico Fermi"
Course CLXXV "Radiation and Particle Detectors", edited by S. Bertolucci, U. Bottigli and P. Oliva
(IOS, Amsterdam; SIF, Bologna)
DOI 10.3254/978-1-60750-630-0-79

The CMS detector

M. Mulders

CERN, European Organization for Nuclear Research - Geneva, Switzerland

Summary. — This lecture gives an overview of the design and current status of the Compact Muon Solenoid (CMS) detector at the Large Hadron Collider (LHC). After a short introduction of the physics goals and design of the detector, the modular building of the detector is discussed as well as its commissioning using cosmic rays and beam induced muons from the first circulating LHC beams in September 2008. While eagerly anticipating the upcoming restart of the LHC, the CMS collaboration has invested a serious effort in studying the performance of the CMS detector as a scientific instrument using cosmic-ray data from a sustained run with full detector in readout and magnet switched on: the Cosmic Run At Four Tesla (CRAFT), recorded during a month-long campaign in October and November 2008. This was a crucial step towards the commissioning of CMS and understanding of the detector performance, improving the level of preparedness of CMS for physics analysis. The precise mapping of the CMS magnetic field using cosmics rays is highlighted as an example of a successful improvement that resulted from the analysis of the CRAFT data.

1. – Introduction

The LHC accelerator [1] and its experiments are magnificent scientific instruments. In size and complexity they exceed existing facilities by almost an order of magnitude in many of the key parameters. The Compact Muon Solenoid (CMS) [2] is one of four experiments at the LHC, designed as a general purpose detector capable of exploring the full physics program at the energy frontier made accessible by LHC collisions.

After many years of construction, and a final sprint in the beginning of 2008, the CMS detector was completed in time for the start-up of the LHC on September 10, 2008. All major detector components of CMS were installed in time and operational, except for the pre-shower detector, installed during the subsequent winter shutdown. The only other major element that had not been tested *in situ* (under ground) before the 2008 start-up of the LHC was the powering of the 4 T solenoid to its nominal field strength.

On the morning of September 19, 2008, a serious incident in sector 3-4 of the LHC brought an end to the otherwise brilliant start-up phase that began 9 days earlier. This unfortunate event has postponed first proton-proton collisions by more than a year.

As a positive consequence, however, the experiments were given more time to fully prepare the detectors, trigger and software for the physics data taking. The CMS Collaboration has used this time well. Before opening the detector for maintenance work, approximately 300 million cosmic muon events were recorded during a sustained 5-week-long cosmic data taking campaign, the Cosmic Run at Four Tesla (CRAFT), with the full detector operational and the 4 Tesla solenoid switched on. Detailed analysis of this data-set has proven to be extremely helpful to improve the understanding of the overall performance of the CMS detector and in particular its response to muon particles.

In order to reach the maximum physics potential of the LHC detectors, these preparatory studies using cosmic data and other commissioning tests play a crucial role. The experiments are so complex that a subtle detector effect could potentially fake the signal of an elusive new physics process. To maximize the sensitivity in the search for new physics for which the detectors are built, it is therefore mandatory to first reach an excellent understanding of the characteristics of the detector performance.

This lecture starts with a short overview of the design of the CMS detector in sect. **2** before shifting the focus to the commissioning of the CMS detector as a scientific instrument with a selection of striking examples of detailed analysis of CMS detector data. Even before collisions the CMS detector has shown that it is able to perform physics measurements, and physics measurements in turn have contributed to the commissioning of the detector. First an example of the latter category is presented, namely the measurement and detailed analysis of the CMS magnetic field using probes (sect. **3**) and cosmic rays (sect. **4**) important for simulation, triggering and track reconstruction in CMS. Measurements with cosmic muons (sects. **6** and **5**) and LHC beam induced muons (sect. **7**) fall in both categories. After these highlights of physics before collisions, sect. **8** briefly addresses plans for physics analysis after the first LHC collisions are delivered, followed by a conclusion.

2. – The CMS detector

The Compact Muon Solenoid (CMS) experiment has been built as a general purpose detector with excellent tracking and particle identification capabilities [3] designed to fully explore the physics potential of the LHC. The main priorities guiding the design were the following:

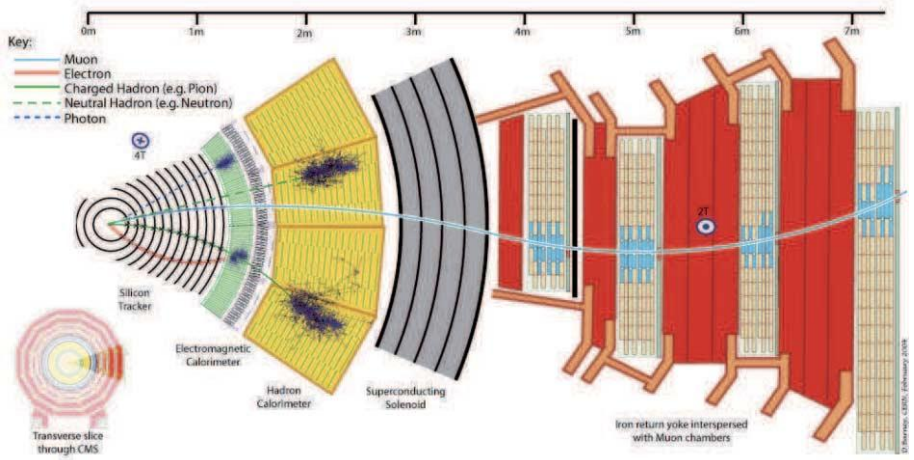

Fig. 1. – A cross-section through the center of CMS, perpendicular to the LHC beam line, showing particles traversing the different subdetectors.

1) A highly robust and redundant muon system.

2) The best possible electromagnetic calorimeter consistent with point 1).

3) A high quality central tracking consistent with points 1) and 2).

4) A hermetic calorimeter system.

5) A financially affordable detector.

In the resulting design, the central feature of the CMS apparatus is a large superconducting solenoid of 6 m internal diameter and a length of 12.5 m. With the exception of the muon chambers, all subdetectors are located inside the solenoid: the silicon pixel and strip tracker, the crystal electromagnetic calorimeter (ECAL) and the brass-scintillator hadronic calorimeter (HCAL). Muons are measured in gas chambers embedded in the iron return yoke. Besides the barrel and endcap detectors, the CMS design includes extensive forward calorimetry.

A cross-section of the detector depicting all layers of the barrel CMS detector is shown in fig. 1, and an overview including endcap components in fig. 2.

The ECAL consists of lead-tungstate crystals with a thickness (in radiation length) of $25.8X_0$ in the barrel and $24.7X_0$ in the endcaps. It has an energy resolution of better than 0.5% for electrons and photons with an energy above 100 GeV.

The HCAL, when combined with the ECAL, measures jets with a resolution $\Delta E/E \approx 100\%/\sqrt{E} \oplus 5\%$. The calorimeter cells are grouped in projective towers, of granularity $\Delta\eta \times \Delta\phi = 0.087 \times 0.087$ at central rapidities and 0.175×0.175 at forward rapidities. By combining calorimeter information with tracking on a particle-by-particle basis, it is expected that the jet resolution can be significantly improved [4].

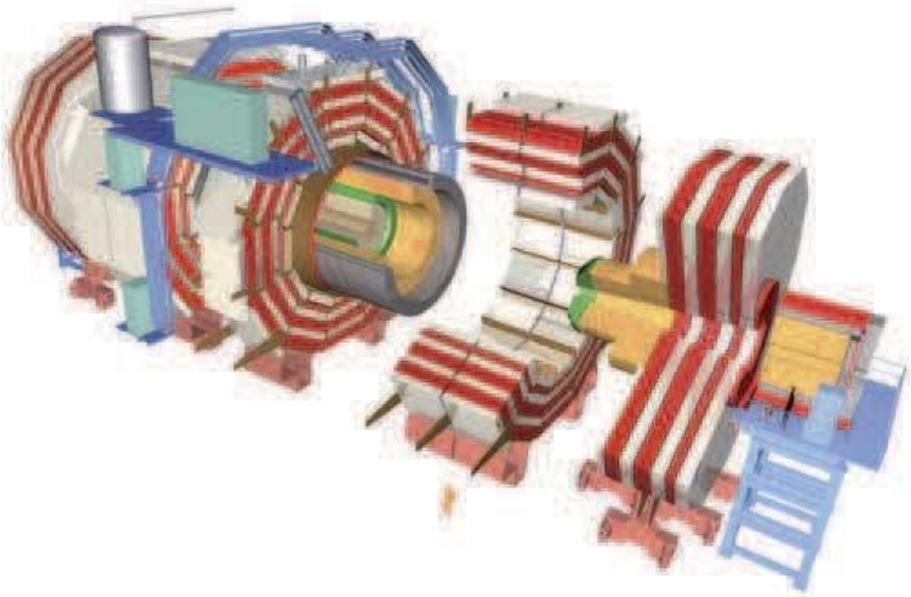

Fig. 2. – Overview of CMS components, illustrating the modular construction of CMS in barrel wheels and endcap disks that can be moved individually.

Muons are measured in the pseudorapidity window $|\eta| < 2.4$, with detection planes made of three technologies: Drift Tubes, Cathode Strip Chambers, and Resistive Plate Chambers. Matching the muons to the tracks measured in the silicon tracker results in a transverse momentum resolution between 1 and 5%, for p_{T} values up to $1\,\mathrm{TeV}/c$. The muon detection system has nearly 1 million electronic channels.

Mid-rapidity charged particles are tracked by three layers of silicon pixel detectors, made of 66 million $100 \times 150\,\mu\mathrm{m}^2$ pixels, followed by ten microstrip layers, with strips of pitch between 80 and $180\,\mu\mathrm{m}$. The silicon tracker is designed to provide the vertex position with $\sim 15\,\mu\mathrm{m}$ accuracy.

The first level (L1) of the CMS trigger system, composed of custom hardware processors, uses information from the calorimeters and muon detectors to select (in less than $1\,\mu\mathrm{s}$) the most interesting events (only one bunch crossing in 1000). The High Level Trigger (HLT) processor farm further decreases the event rate from 100 kHz to 100 Hz before data storage.

The very forward angles are covered by the CASTOR ($5.3 < |\eta| < 6.6$) and Zero Degree ($|\eta| > 8.3$) calorimeters. The ZDC and CASTOR calorimeters are made of quartz fibers/plates embedded in tungsten absorbers. The design includes two extra tracking stations, built by the TOTEM experiment, to be placed at forward rapidities ($3.1 < |\eta| < 4.7$ and $5.5 < |\eta| < 6.6$).

The CMS apparatus has an overall length of 22 m, a diameter of 15 m, and weighs 12500 tons. In total, $\sim 10^8$ data channels are checked in each bunch crossing.

Fig. 3. – The lowering of two disks of the endcap from the surface to the underground cavern.

A more detailed description of the Compact Muon Solenoid (CMS) experiment is given in the CMS detector paper [2] and its physics goals and expected performance are described in the Physics Technical Design Reports [3].

One unique feature of CMS is the modularity of the design. As indicated in fig. 2, CMS is made of 11 large modules: five barrel rings and two times three endcap disks. Each of these modules can be moved individually using air pads to minimize friction with the floor. This modular design was chosen to allow assembly of large components of the CMS detector in the assembly hall on the surface while the underground cavern was being commissioned. As soon as the cavern and essential underground services were ready, the barrel rings and endcap disks were lowered into the underground cavern one by one. Two photographs of the lowering of two of the endcaps are shown in fig. 3.

The modular design also allows CMS to be opened and closed in a matter of days, which will allow access to parts of the detector that cannot normally be reached in the closed position. This ability was first tested during the Magnet Test and Cosmic Challenge (MTCC) in 2006 [5]. This was the first time the full CMS yoke with detector components was closed, while still in the surface assembly hall. The main goal was to test the operation of the magnet and to measure precisely the central field, before lowering the detector. Results from the MTCC are discussed in more detail in the next section. After successful completion of the MTCC, the CMS modules were lowered one by one, starting November 2006, and ending in January 2008.

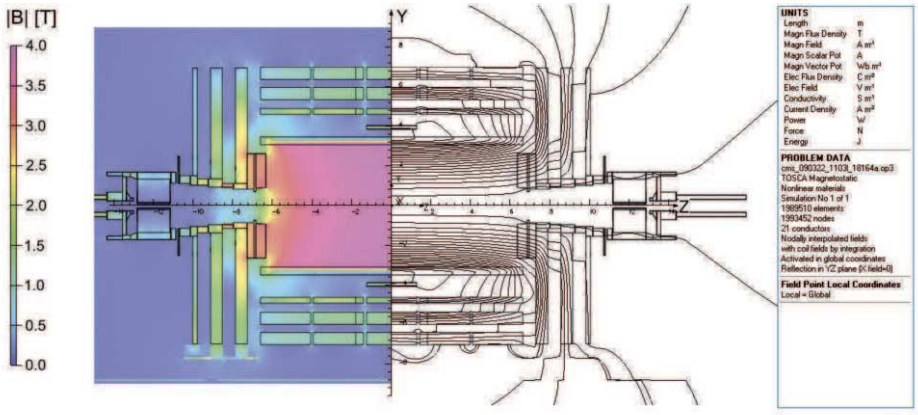

Fig. 4. – The calculated magnetic field strength $|B|$ (left) and field lines (right) in CMS for a central field of 3.8 T. The field is plotted for a cross-section of the CMS detector in the vertical plane, parallel to the beam line. Each field line represents a B flux of 6 Wb.

3. – Precise mapping of the central CMS magnetic field using probes

Central in the CMS design is a high-field (4 T) superconducting solenoid, with a 6 m diameter and a length of 12.5 m. In this section the precise measurement of the central magnetic field is described, as an example of the type of detailed analysis that is needed to prepare CMS for physics data taking.

A detailed map of the field in CMS (fig. 4) is required for simulation, trigger, and track parameter reconstruction in CMS. The map that is provided is based on a three-dimensional model of the magnetic field in the whole CMS detector calculated using the TOSCA finite element program [8]. The model includes a description of the solenoid and the many iron volumes in the return yoke, reflected in the intricate structure of the field seen in fig. 4.

During the Magnet Test and Cosmic Challenge (MTCC) in the fall of 2006 [5], the CMS detector was closed for the first time, and the magnet was ramped to its design value of $B = 4$ T. One of the goals of the MTCC was to perform accurate measurements of the magnetic field in CMS, at different settings of the field strength (2.0, 3.0, 3.5, 3.8 and 4.0 T). A field mapper was installed inside the solenoid, with the ability to perform precise measurements in a cylindrical volume with a radius of 1.724 m and a 7 m length [6]. The measurements were performed using 3D Hall probes mounted on two rotating arms of the remote-controlled field mapper robot. Both arms rotate around a common axis, aligned with and centered along the central axis of symmetry of the cylindrical magnet coil. Five probes on each arm were mounted at radii varying between 92 and 1724 mm. The 3D Hall probes were pre-calibrated to a relative precision of $5 \cdot 10^{-4}$ for a 4 T field.

The TOSCA model agrees well with the field mapper results in the central region, as

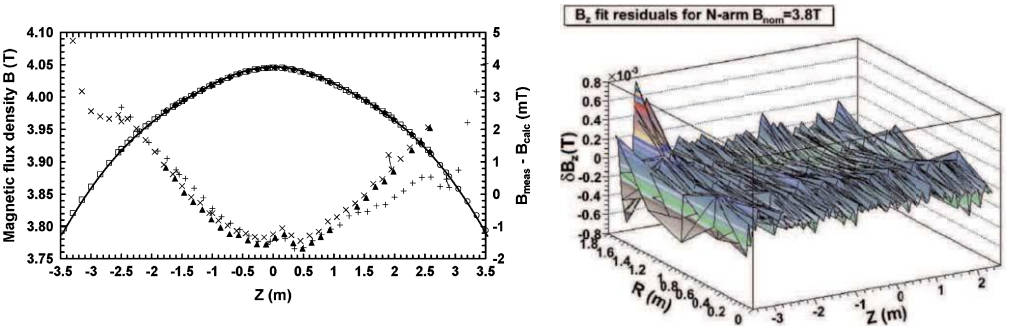

Fig. 5. – Left: magnetic flux density (left scale) measured parallel to the coil axis at a radius of 1.724 m using an NMR probe, and two B-sensors located on the negative (open squares) and positive (open circles) field mapper arm. The smooth curve represents calculations done with the CMS TOSCA model. Triangles show the difference (right scale) between the NMR measurements and calculations, while the right and slanted crosses present the difference between B-sensors and the calculations. The model is normalized to get the measured B_0 (on-axis) value of 4.0124 T. The right plot shows the difference in B_z between the analytical field model and the measured values of the field, including post-calibration (see text), for the whole region inside the solenoid covered by one of the field mapper arms, at a field of 3.8 T.

illustrated in fig. 5 (left plot). The agreement between calculations and measurements is better than 4 mT in the whole range. The agreement between the Nuclear Magnetic Resonance (NMR) and Hall probes is even better, suggesting that the measurements are more accurate than the TOSCA model.

A better fit to the measurements was obtained using a scalar potential approach. The scalar potential is formed as a linear combination of scalar basis functions (polynomials), where each basis function satisfies the Laplace equation and the gradient of the linear combination approximates well the field measurements. Using this analytical fit it was possible to post-calibrate the B-sensors to a level of $5 \cdot 10^{-5}$ at 4 T. Comparing the result of the fit with the measurements of B_z at each point (r, z) in the mapping volume, an agreement better than 0.2 mT is found for the tracker region ($r < 1.2$ m), as shown in fig. 5 (right plot). More details are given in ref. [9]. Thus we have obtained a parametrization of the central field that satisfies Maxwell's equations, and agrees with the MTCC magnetic-field measurements with a relative precision of $5 \cdot 10^{-5}$, which confirms the outstanding quality of the field mapper measurements and our understanding of the data. The resulting parametrization is available in the standard CMS software and can be used for simulation and tracking in the central region.

For the more complex field outside the solenoid, it is impossible to provide an analytical parametrization of the magnetic field. Outside the solenoid the TOSCA finite-element model is therefore the only option. It turns out that the prediction for the field in the yoke depends on the boundary conditions used in the TOSCA model. Figure 6 shows the prediction of the integrated magnetic flux through a disk of radius R in the transverse plane at $z = 0$, for different sizes of the enclosing region used in the TOSCA model.

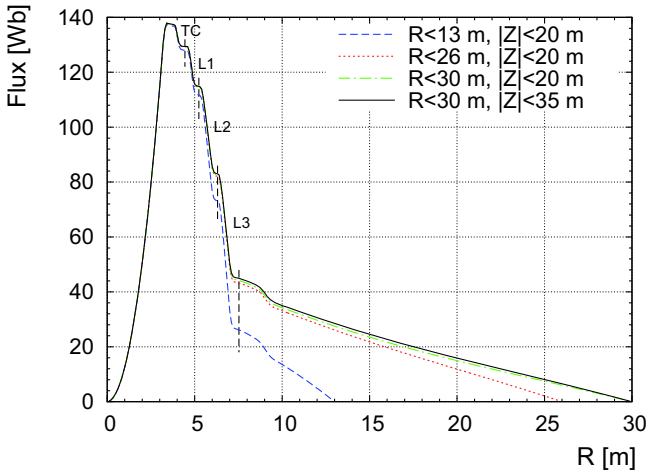

Fig. 6. – Magnetic flux through a disk of radius R in the central ($z = 0$) transverse plane, as predicted by the TOSCA model for 4 T field, computed within different enclosing regions of the model. The vertical dashed lines indicate the location of the four layers of barrel muon chambers, interleaved with the steel absorber plates (TC, L1, L2 and L3). The structure at $R = 9$ is caused by the steel floor plate.

Outside the solenoid ($R > 3$ m) variations can be seen in the predicted return of the flux through the steel in the different yoke layers (the "Tail Catcher" (TC), and three barrel layers L1, L2, and L3). The amount of flux returning outside the barrel yoke ($R > 7$ m) varies by as much as a factor 2 depending on the size of the enclosing region. This indicates a significant modeling uncertainty for the field strength in the return yoke.

Comparisons of the TOSCA field model with flux loop measurements [7] indicate possible differences between the model and the real field in the iron of the return yoke of the order of 10%, but as these measurements are only available in a limited number of locations the results are not conclusive. The only way to obtain a detailed picture of the magnetic field in the iron of the return yoke, is by using the many millions of tracks from cosmic muons that were recorded. The CRAFT data taken in the fall of 2008 allow for the first time to compare the TOSCA field with the B values estimated from the bending of cosmic muons traversing the real CMS detector with the B field turned on. This study is presented in the next section.

4. – Precise mapping of the CMS magnetic field in the yoke using cosmic muons

This section summarizes the detailed analysis of the magnetic field in the barrel yoke, using muons extrapolated from the well-known field inside the silicon tracker [10].

As described in the previous section, the magnetic field in the central tracker region was measured with great precision when the CMS detector was closed for the first time,

TABLE I. – *Comparison of the magnetic flux measured by an NMR probe mounted close to the XY middle plane, close to the inner wall of the coil cryostat, for different currents on the surface and underground. The prediction of the underground TOSCA model at a magnet current of* 18160 A *(*$B = 3.8$ T*) for this location is* 3.9181 T.

Current (A)	Surface (T)	Underground (T)	Δ (T)
7000	1.5218	1.5224	−0.0006
9500	2.0616	2.0643	−0.0027
18160	3.9176	3.9206	−0.0030

still in the assembly hall on the surface. But in order to allow the magnetic-field measurements, everything inside HCAL had to be empty in order to allow space for the magnetic-field mapper robot.

Thus there are some differences between the CMS configuration in 2006 (on the surface) and in 2008 (in the underground cavern). One difference is the amount of iron shielding in the forward region surrounding the beampipe. Simulation has shown that the differences in iron shielding have an effect on the magnetic field in the yoke, but hardly on the field in the tracker region inside the solenoid. Another difference is the silicon tracker, which was not installed at the time of the MTCC measurements. The claim is that the presence of the tracker should not have any sizable effect on the magnetic field either.

To compare the scale of the central solenoid field between 2006 and 2008, measurements with fixed NMR probes installed near the inner wall of the superconducting coil cryostat taken at the same coil current on surface and underground are listed in table I. They show that the field inside the solenoid with full detector installed in the underground cavern for a given magnet current is identical within 0.08%. This means that the measurements of the field on the surface are applicable also for operation in the cavern.

As an additional cross-check, fig. 7 shows the position residuals at the inner muon station between the predicted and measured position in the bending coordinate, for muons extrapolated from the tracker. To suppress the effect of chamber misalignment, the difference between μ^+ and μ^- is plotted, as a function of the transverse momentum measured in the tracker. This difference should be sensitive to discrepancies in the magnetic field. For comparison, the expected effect is shown of a 0.1% discrepancy in scale between the field inside the tracker, and the field between tracker and muon station. These results show that the shape and the scale of the central field (up to the first muon station) are known very well, to an accuracy of better than 0.1%.

This means that the field in the inner tracker region can serve as a reference to probe the field in the yoke with cosmic tracks. In the 270 million cosmic-ray–triggered events recorded by CMS in October-November 2008 during the month-long CRAFT campaign, about three million muons crossed the tracker volume, and can thus be used for this purpose.

In the barrel yoke, four stations of Drift Tube chambers are interleaved with the three steel yoke layers. Each DT chamber can measure the direction of the track in

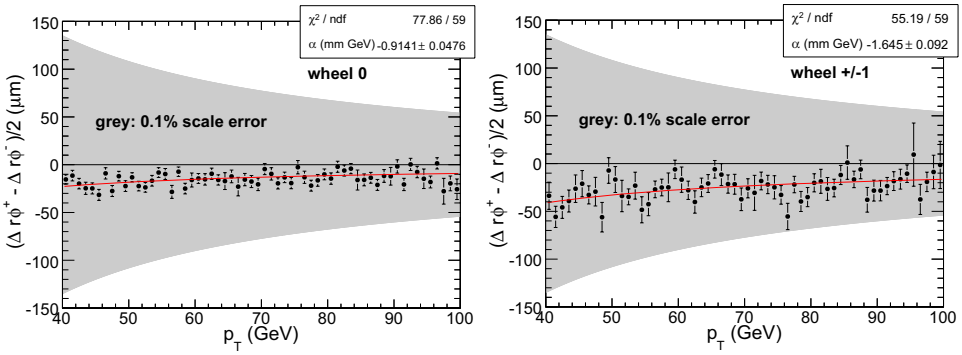

Fig. 7. – Difference of the extrapolation residual in the first muon station between μ^+ and μ^-, propagated from the tracker to the first layer of the muon system, as a function of the transverse momentum measured in the tracker. Left: the central barrel wheel. Right: neighboring barrel wheels, on both sides. The shaded area shows the expected effect of a 0.1% discrepancy of the field map between tracker and muon system. The solid line represents a fit to the function α/p_T.

the transverse plane (ϕ) with a resolution of about 1.8 mrad. The track bending in the transverse plane between two consecutive stations, i and $i+1$, is an ideal quantity to probe the field in the yoke plates, as it is directly related to the integral of the field along the track path:

$$(\phi_{i+1} - \phi_i)p_T = -0.3\ q \int_i^{i+1} \overrightarrow{u_\phi} \cdot \overrightarrow{B} \times \mathrm{d}\overrightarrow{l}\,, \tag{1}$$

where p_T is the muon transverse momentum in units of GeV/c, $\overrightarrow{B}$ is expressed in Tesla, and l in meters.

The transverse bending is dominated by the axial component of the field, B_z. The azimuthal component of the field B_ϕ is small given the cylindrical symmetry of the barrel yoke, and does not contribute to the bending in the transverse plane. Although the radial component, B_r, contributes to eq. (1), its effect is small and can be neglected, both because $B_r \ll B_z$ in the barrel steel plates given the geometry of the yoke (see fig. 4), and because tracks selected in this analysis have small angles in the longitudinal plane.

Also, in order to relate the path integral in eq. (1) to the average field inside the yoke plate, the stray field in the short path between the chambers and the steel plate can be neglected, and the track path length in the transverse plane can be approximated with the thickness L of the steel plate. With this approximation:

$$\int_i^{i+1} \overrightarrow{u_\phi} \cdot \overrightarrow{B} \times \mathrm{d}\overrightarrow{l} \simeq \langle B_z \rangle L, \tag{2}$$

where $\langle B_z \rangle$ is effectively averaged along the trajectory of the particle crossing the layer

between stations i and $i+1$.

The goal of the study presented here is not to obtain directly the value of $\langle B_z \rangle$ from eq. (2), but to compare it with the same quantity predicted by the magnetic-field map, to highlight and possibly correct for average discrepancies. For this purpose, track parameters reconstructed in the CMS inner tracking system are extrapolated to the muon spectrometer, where they are compared with the measurements of the muon chambers, for each muon separately. The extrapolation of track parameters and of their error matrices is performed taking into account multiple scattering and energy loss. These were tuned to reproduce statistically the results of the detailed GEANT4 simulation of CMS.

The magnetic-field map is used both for the measurement of the track momentum in the inner tracker and to predict the track bending in the extrapolation. Given the good accuracy of the magnetic-field map in the region inside the solenoid, the momentum measured by the inner tracker can be taken as a reference. A systematic difference between the track direction measured in the DT chambers and the direction of the extrapolated tracks can therefore be attributed to a difference between the true magnetic-field integral along the extrapolation path and the corresponding integral in the field map used for the extrapolation. Considering two consecutive DT stations and using eq. (1), it is therefore possible to measure the discrepancy of the field integral in the steel layer in between:

$$\begin{aligned} \Delta &= [(\phi_{i+1}^{\mathrm{prop}} - \phi_{i+1}^{\mathrm{data}}) - (\phi_i^{\mathrm{prop}} - \phi_i^{\mathrm{data}})] \cdot p_T \\ &\propto \int_i^{i+1} \overrightarrow{u_\phi} \cdot \overrightarrow{B}^{\mathrm{map}} \times \mathrm{d}\,\overrightarrow{l} - \int_i^{i+1} \overrightarrow{u_\phi} \cdot \overrightarrow{B}^{\mathrm{true}} \times \mathrm{d}\,\overrightarrow{l}, \end{aligned} \tag{3}$$

where ϕ_i^{prop} and ϕ_i^{data} are the bending angles at the i-th DT station for the propagated track and for the measured segment, respectively; p_T is the muon momentum, assumed constant along the path between the two stations and obtained from the extrapolation of the inner tracker track to the middle plane between the stations accounting for energy loss; and $\int_i^{i+1} \overrightarrow{u_\phi} \cdot \overrightarrow{B}^{\mathrm{true}} \times \mathrm{d}\,\overrightarrow{l}$ and $\int_i^{i+1} \overrightarrow{u_\phi} \cdot \overrightarrow{B}^{\mathrm{map}} \times \mathrm{d}\,\overrightarrow{l}$ are the true field path integral between the i-th and the $i+1$st DT station and the one estimated using the field map, respectively.

Measured bending angles are potentially affected by residual misalignment. However, misalignment affects the measured angles of positive and negative muons in the same direction, while a distortion of the field map has opposite effect on the propagated direction of tracks of opposite charge. The charge-antisymmetric combination of the mean values of the distributions of Δ for positive and negative muons crossing a given sector, in the form $(\langle\Delta\rangle_{\mu^+} - \langle\Delta\rangle_{\mu^-})/2$, is not influenced by the misalignment effects, under the assumption that positive and negative muons have the same momentum spectrum.

Equation (2) can be used to relate the right side of eq. (3) with the average flux density in the yoke plate. Also, the systematic effects of the assumptions used in writing these two expressions can be suppressed normalizing eq. (3) to the bending expected

TABLE II. – *Relative difference in B strength, between the latest TOSCA map and B observed in data, averaged between opposite wheels.*

	Wheel ±2	Wheel ±1	Wheel 0
L1	0.994 ± 0.04	1.004 ± 0.004	1.005 ± 0.005
L2	0.956 ± 0.02	0.958 ± 0.003	0.953 ± 0.003
L3	0.918 ± 0.08	0.924 ± 0.003	0.906 ± 0.003

from the field map:

$$\frac{[(\phi_{i+1}^{\mathrm{prop}} - \phi_{i+1}^{\mathrm{data}}) - (\phi_i^{\mathrm{prop}} - \phi_i^{\mathrm{data}})] \cdot p_T}{(\phi_{i+1}^{\mathrm{prop}} - \phi_i^{\mathrm{prop}}) \cdot p_T} = \frac{\langle B_z^{\mathrm{map}} \rangle - \langle B_z^{\mathrm{true}} \rangle}{\langle B_z^{\mathrm{map}} \rangle}|_{i \to i+1}. \tag{4}$$

Charge-antisymmetric combinations are computed separately for the numerator and the denominator of the expression on the left side. Each yoke plate is treated separately. The expression on the right side represents the relative discrepancy of the flux density averaged over a single yoke plate.

The ratio $\langle B_z^{\mathrm{true}} \rangle / \langle B_z^{\mathrm{map}} \rangle$ is computed using eq. (4). It can be interpreted as the corrective scaling factor that has to be applied to the $\overrightarrow{B}$ vector given by the magnetic-field map in each point within the considered steel yoke plate in order to obtain the best estimate of B_z^{true} that reproduces the track bending observed in that plate on data.

The scaling factors obtained with this technique are shown in fig. 8 (blue open circles), separately for each sector and yoke layer. These results were obtained with about 1.0 million selected good-quality muon tracks with a transverse momentum $15 < p_T < 100\,\mathrm{GeV}/c$ measured by the tracker.

The analysis was then repeated on top of this map, with a tighter selection including pointing requirements on the transverse and longitudinal impact parameter, $|d_x y| < 0.4\,\mathrm{m}$ and $|d_z < 1\,\mathrm{m}$, respectively. This ensures good-quality track reconstruction in the tracker, at the cost of reduced statistics especially for the outside barrel wheels ±2.

Results with the tight selection for all sectors in each layer and wheel, as well as results for opposite wheels, have been found to be compatible within statistical errors, and were therefore averaged together. The resulting factors, listed in table II, are adopted as correction factors for the magnetic-flux density in the ϕ-asymmetric map used in the CMS software for reconstruction and simulation.

To verify the consistency of the method, the scaling factors were recomputed on top of the corrected map, for events passing the preselection cuts only. This corrected map also has special field tables for the regions close to the chimneys in the barrel yoke (holes to allow passage of electric wires and cryogenic pipes from the solenoid) in sector 3 and 4 in the gaps between the central barrel wheel and the neighboring wheels.

The resulting factors, shown in fig. 8 (red solid squares), are compatible with unity within the statistical error.

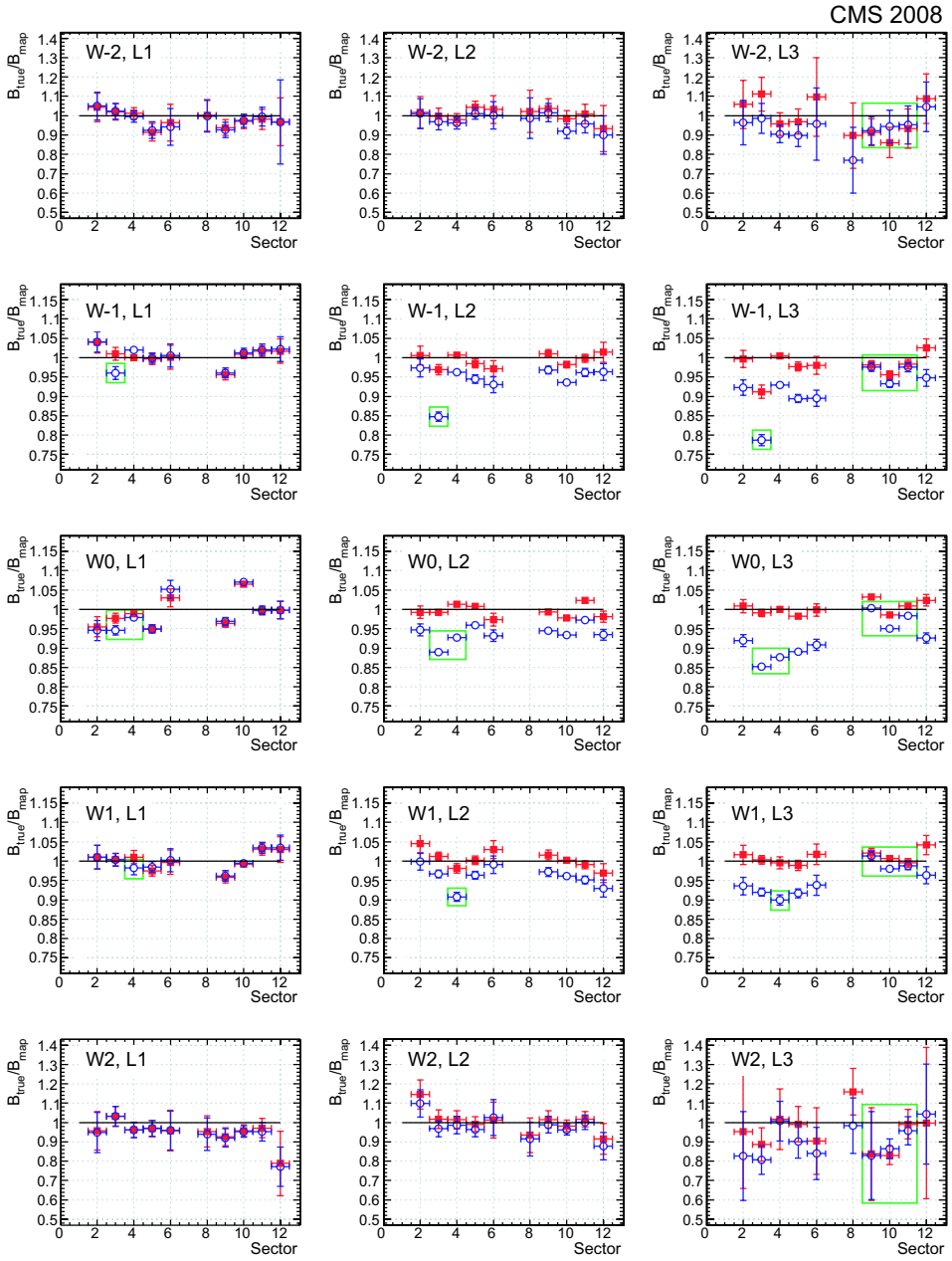

Fig. 8. – (Colour on-line) Solid squares: residual discrepancies found for the new baseline field map including the scaling corrections listed in table II. Open circles: same, for a 12-fold ϕ-symmetric map without scaling corrections and without the special treatment for chimneys and feet. The sectors affected by these features are highlighted with open boxes. Data points are only reported in sectors probed with sufficient numbers of muons. The error bars include only the statistical uncertainty.

TABLE III. – *Closure test of scaling factors for data, and cross-check of the method with Monte Carlo simulation.*

	CRAFT data	Cosmic MC
All sectors/layer/wheels	1.000 ± 0.001	0.993 ± 0.004
All top sectors	0.997 ± 0.002	0.995 ± 0.005
All bottom sectors	1.002 ± 0.002	0.994 ± 0.006
All inner iron layers	0.999 ± 0.003	0.998 ± 0.007
All middle iron layers	1.001 ± 0.002	0.992 ± 0.005
All outer iron layers	0.999 ± 0.002	0.991 ± 0.006
All in wheel 0	1.001 ± 0.002	0.993 ± 0.005
All in wheel $+/-1$	0.999 ± 0.002	0.994 ± 0.005
All in wheel $+/-2$	1.00 ± 0.02	0.98 ± 0.02

The residual discrepancies have been averaged grouping sectors in different ways in order to search for possible biases. The results are listed in table III. No bias is found at the level of the statistical errors (a few per mille). In particular upper and lower sectors agree well inside the statistical error showing that the material budget description is under control with sufficient precision, corresponding to an effect on reconstructed momentum of less than a percent.

Also, the analysis was cross-checked on a simulated Monte Carlo sample where measured scaling factors have been verified to be compatible with one in all sectors. Averaging them in sectors as for data, the results are listed in the right-hand column in table III. Since in Monte Carlo the magnetic field in simulation and reconstruction is identical by definition, any deviation in the measured scaling factor from one would be an indication that the method is biased. As shown in table III, no significant bias is observed, which means that any bias in the method must be smaller than the statistical uncertainty ($< 1\%$).

The resulting CMS magnetic-field map, with vastly improved accuracy compared to the map used during CRAFT 2008, is now included in the CMS software for use in simulation, triggering and offline track reconstruction. The new map is accurate enough to guarantee that systematic effects on track reconstruction from the uncertainty in the magnetic field are negligible compared to other uncertainties such as alignment, hit resolution and multiple scattering.

This measurement of the magnetic field in the barrel yoke of CMS is one of the main results of CRAFT. It is a great advantage for CMS to have reached this level of understanding of the magnetic field before the start of physics data taking.

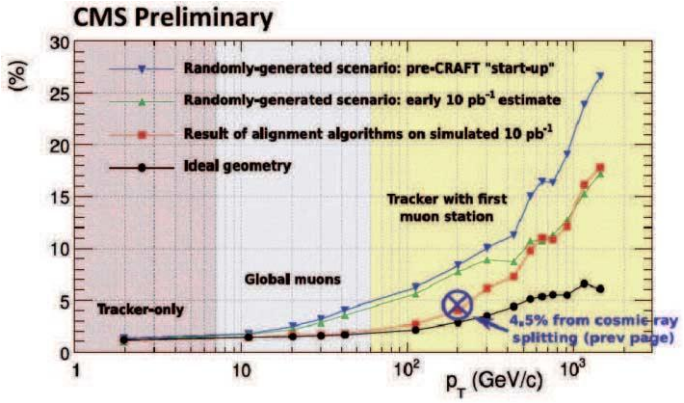

Fig. 9. – Relative resolution on the transverse muon momentum p_T as a function of p_T, obtained with Monte Carlo simulation with different misalignment scenarios. The cross indicates the resolution obtained with cosmic muons with $p_T > 200\,\mathrm{GeV}/c$ in the CRAFT cosmics data sample.

5. – Other commissioning results with cosmic muons from CRAFT

The cosmic muons recorded during the CRAFT campaign were used in many other ways to improve the understanding of the response and characteristics of the CMS detector *in situ*, in the underground experimental cavern with the magnet switched on.

One of the other main results, besides the improved understanding of the magnetic field, was the successful application of alignment procedures, and demonstration that track-based alignment results are in agreement with results obtained with (laser-based) hardware systems, and photo-grammetric surveys. Based on 3 million muon tracks crossing the silicon tracker, the positions of most of the 1440 silicon pixel and 15148 silicon strip detector modules were determined with respect to cosmic-ray trajectories to a precision of 3–4 microns RMS in the barrel and 3–14 microns RMS in the endcap in the most sensitive coordinate and it was shown that the track parameter resolutions obtained with this alignment are close to the design performance [11].

In addition to the alignment of the silicon tracker, methods were tested and improved to derive the relative "internal" alignment of muon chambers in the muon system, as well as the "global" alignment of the muon system in relation to the silicon tracker. The latter is very important to obtain the best possible momentum resolution for high-momentum muons, from a global track fit combining hits in the silicon tracker with hits in the muon system and profiting from the full bending arm in the high-B field provided by the CMS solenoid. Figure 9 shows the expected relative resolution on the transverse muon momentum p_T as a function of p_T, obtained with Monte Carlo simulation with different misalignment scenarios. In this plot different muon track fits are used in different momentum ranges. In the high-p_T region the global fit combines hits from the silicon tracker and the innermost muon station, profiting from the bending arm between the

tracker and muon system while reducing complications in the pattern recognition in the muon spectrometer due to particle showers created by high-energy muons traversing the steel of the yoke.

By selecting cosmic muons pointing close enough to the center of the CMS detector so that they pass through the volume of the pixel detector, splitting them in the middle, and comparing the reconstructed p_T in top half and bottom half, it was possible to test the momentum resolution in the real detector, to be expected for muons in LHC events. Using an alignment derived with muons in the $100 < p_T < 200\,\mathrm{GeV}/c$ range, the p_T resolution for muons in the independent $p_T > 200\,\mathrm{GeV}/c$ bin was estimated to be 4.5% with the latest alignment and magnetic-field map (compared to 8% before track-based alignment). As can be seen in fig. 9, this corresponds to the level of alignment that was believed to be possible only after collecting $10\,\mathrm{pb}^{-1}$ of LHC collision data. This result is already close to the design performance expected from Monte Carlo simulation with perfect alignment.

Using the fact that cosmic muons of sufficient energy ($> 10\,\mathrm{GeV}/c$ at the entrance point) can traverse the whole CMS detector (see fig. 10), the CRAFT data allowed to study also the response of other subdetectors, including the energy calibration, efficiency, (trigger) timing and noise characteristics. One example is the energy deposited in the electromagnetic and hadronic calorimeters. Using the triggers provided by the muon system, and the momentum measured in the tracking systems, it was possible to study the response of the ECAL and HCAL to muons. In fig. 11 the muon energy deposited in ECAL is plotted as a function of the muon momentum, normalized according to the path length through the ECAL crystals and compared to the known curve of the specific energy loss for muons in lead tungstate. An excellent agreement is seen between the expected and observed energy deposits. Comparison of absolute measured values of energy loss with expectations verifies the calibration of the detector, set with $120\,\mathrm{GeV}/c$ electrons, for energy deposits below 1 GeV.

At low momentum the muons behave like minimum ionizing particles and collisions with atomic electrons are the dominant cause of energy loss. Radiative processes, bremsstrahlung and direct pair production dominate at the highest energies. Analysis of data in the full momentum range allows a comparison of collision loss with radiative losses, permitting a determination of the muon critical energy in $PbWO_4$. The muon critical energy was measured to be $169 \pm 13 \pm 10\,\mathrm{GeV}$, in agreement with expectations [12].

6. – First CMS physics measurement with cosmic muons

During the Magnet Test and Cosmics Challenge (MTCC) in 2006, a slice of the detector including a fraction of all subdetectors was integrated including the hardware, trigger, DAQ and offline analysis. More than 200 million cosmic muon events were recorded, with B field settings ranging from 0 to 4 Tesla.

This made it possible to measure the ratio of positively and negatively charged cosmic muons [13]. For the reconstruction of cosmic muons not pointing at the interaction region and crossing the whole detector, a dedicated muon reconstruction algorithm was

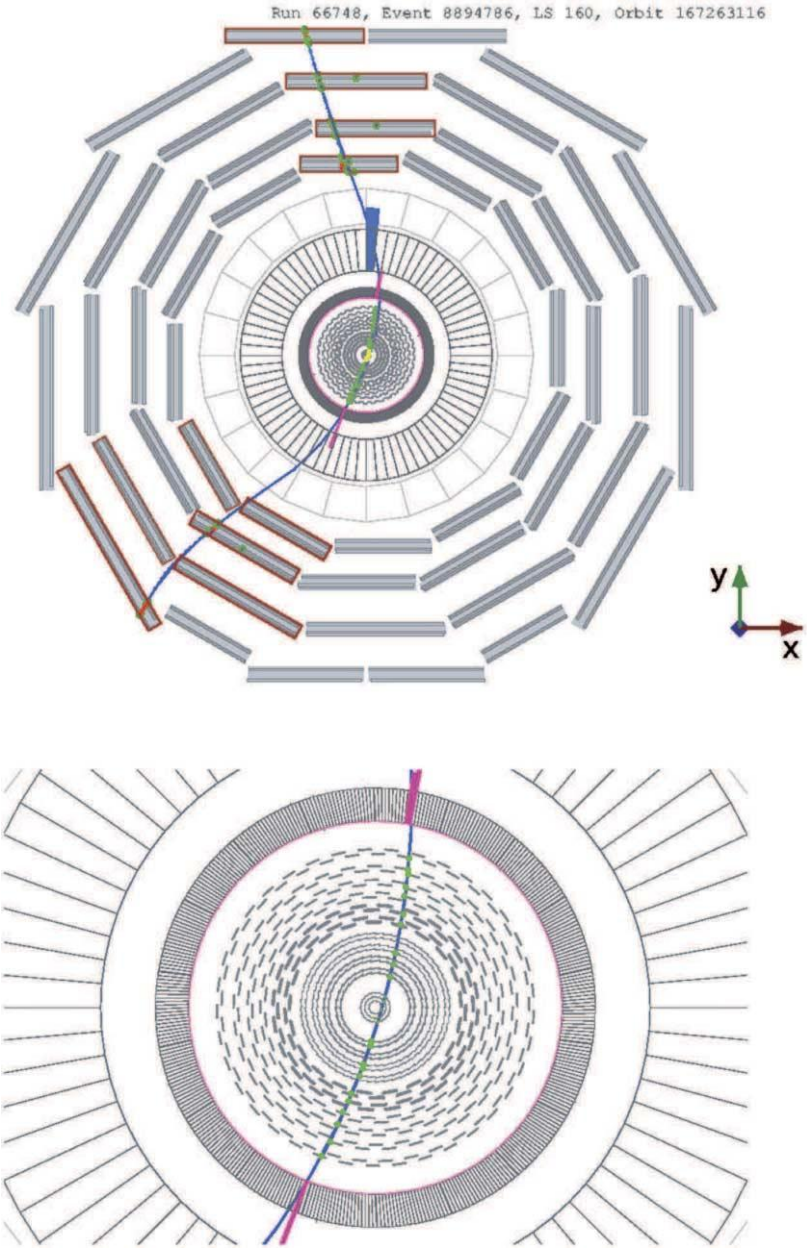

Fig. 10. – An event display of a cosmic muon crossing CMS: the full detector (top) and a detail of the central region. ECAL hits are displayed in magenta, HCAL in blue, tracker and muon hits in green. The views represent a section of CMS in a plane at right angles to the beam direction, the x-axis pointing inwards to the center of the LHC ring and the y-axis pointing vertically upwards.

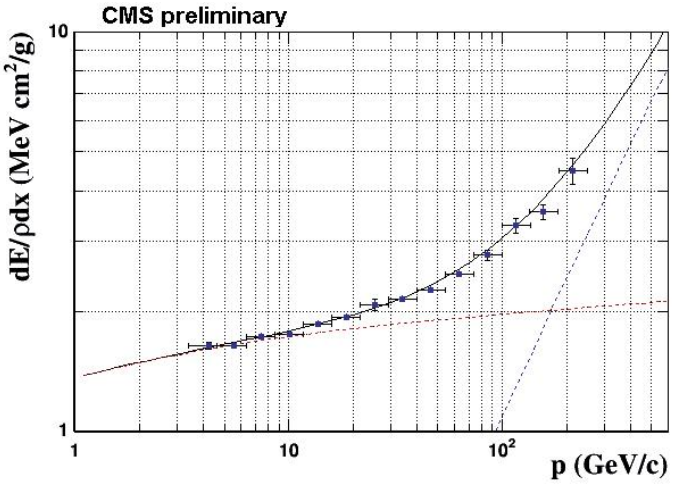

Fig. 11. – (Colour on-line) Stopping power of muons in the electromagnetic calorimeter, as a function of the muon momentum. The data points are compared to a theoretical prediction including the effect of collision losses important at low momentum (red dashed curve), and radiative processes (blue dashed curve) which become the dominant effect above the critical energy.

used [14]. While based on the default track fitting algorithms, it uses a special seeding and navigation for muons not pointing at the (pp) collision region, and it is able to fit tracks crossing the whole CMS detector in a single track. A few examples of muon tracks fitted with this dedicated algorithm are shown in fig. 12, recorded in 2008 during the first global run with a 3 T field.

To measure the ratio of the flux of positively charged muons over negatively charged muons, it is crucial to control the charge asymmetry in the detector acceptance, trigger and reconstruction, and resolution and misalignment leading to charge misreconstruction.

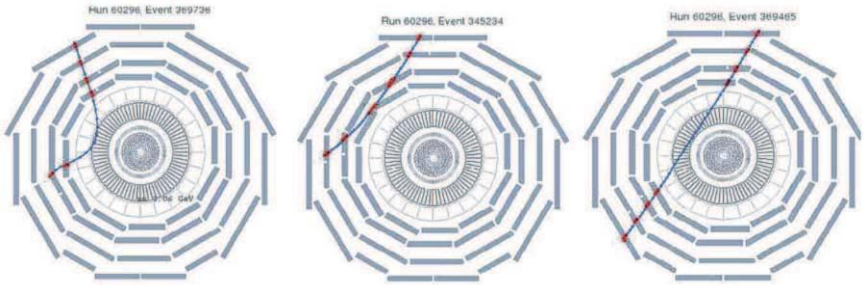

Fig. 12. – Three cosmic muon trajectories fitted with a dedicated muon tracking algorithm, for a 3 T magnetic field. The reconstructed transverse momentum at closest approach to the beampipe is 3.1, 6.2 and 86 GeV/c, respectively.

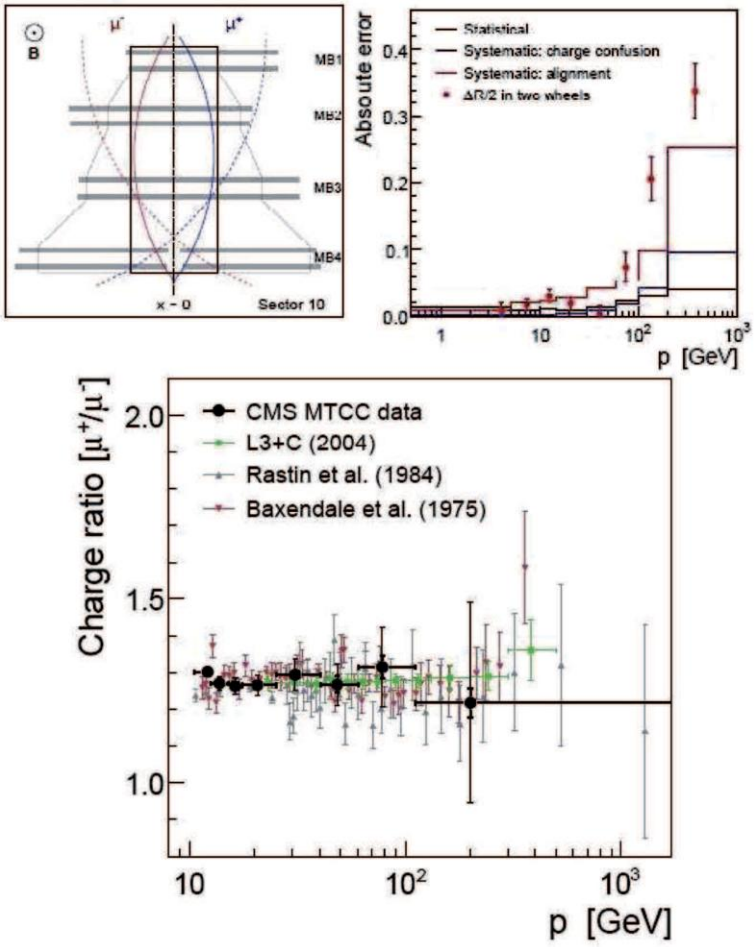

Fig. 13. – Main sources of systematic uncertainty for the muon charge ratio measurement as a function of momentum (top right), and the CMS result compared to existing measurements (bottom). A charge-symmetric fiducial volume (top left) was defined to ensure an unbiased measurement.

To ensure charge symmetry in the acceptance, only muons passing through a "charge"-symmetric fiducial volume of the detector were selected (see fig. 13, top left plot). Monte Carlo simulation was used to correct for the effect of charge confusion due to detector resolution, and to correct the measured momentum spectrum for the average momentum loss passing through the CMS detector before reaching the bottom muon chambers ($\approx 7\,\mathrm{GeV}/c$). Alignment corrections (from survey data and from the measurements of the internal alignment of superlayers within a chamber) were applied to the hit positions before track reconstruction. The main remaining systematic uncertainties are due to charge confusion and alignment. As shown in fig. 13 (top right) the alignment error

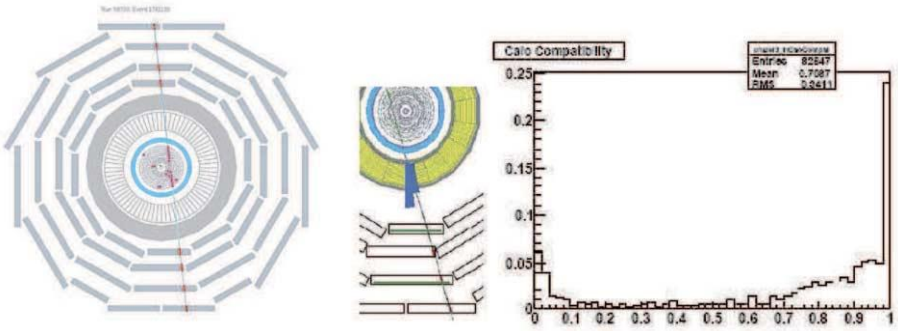

Fig. 14. – Example of a cosmic muon reconstructed as a di-muon event by the high-level trigger (left), a cosmic track matching an energy deposit in the hadronic calorimeter (middle), and a distribution of the muon compatibility (right), based on calorimeter deposits only.

dominates for momenta above 100 GeV/c. The measured ratio,

$$R = 1.282 \pm 0.004(\text{statistical}) \pm 0.007(\text{systematic}),$$

agrees well with previous measurements of the most precise experiments, shown in fig. 13 (bottom).

With the CRAFT data recorded using the complete CMS detector in the fall of 2008, we plan to repeat the cosmics charge ratio measurement. The main goal is to improve the measurement at high muon momentum extending the range to 1 TeV.

The cosmics data also allow to test other aspects of muon reconstruction and identification. As an example in fig. 14 results are shown from one of the first global runs in 2008 including the silicon tracker (with $B = 0\,\text{T}$). This allowed testing of the high level trigger algorithms, matching of muon tracks to ECAL clusters and energy deposits in the HCAL, and the muon identification algorithm which determines a muon compatibility (between 0 and 1), based on the compatibility of matched calorimeter deposits with a muon hypothesis. Even though the algorithm was designed and tuned for pp collisions, the majority of cosmic muons is correctly assigned a high muon compatibility.

A small fraction (0.005%) of the cosmic events are multi-muon events with more than 100 reconstructed muon segments. A muon segment can be reconstructed in each of the 4 layers of muon barrel stations, leading to a typical maximum of 8 segments per muon. With the magnetic field switched off, the precision with which the muon segments are parallel serves as an independent cross-check of the angular resolution of muon segment reconstruction. Conversely, the preliminary analysis of $2 \cdot 10^3$ multi-muon events showed that the origin of the showers had to be at least 0.5 km away from CMS, thus confirming their atmospheric origin. An example of a multi-muon event with ≈ 50 muons is shown in fig. 15.

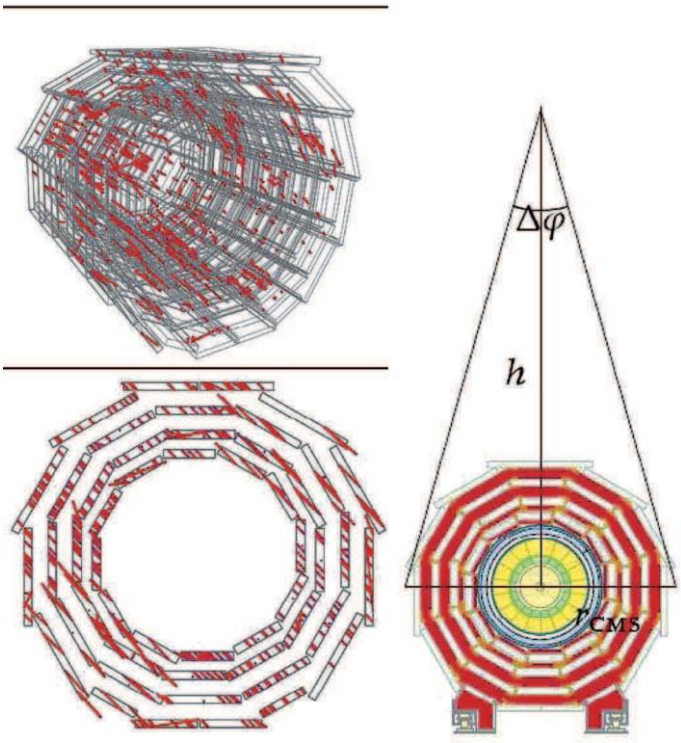

Fig. 15. – Example of a multi-muon event from a cosmic muon shower. The reconstructed segments contain information about the direction and distance of the shower origin.

7. – Observation of the first beam-induced muons

At start-up in September 2008 the LHC machine provided single shots of LHC beam 1 onto a collimator placed 150 m upstream of CMS. These shots were used to synchronize the CMS beam monitoring system to the beam timing. Using the beam monitoring system as trigger, CMS recorded events in all subdetectors except the silicon pixel and strip tracker which were left out of the run. In these shot events an estimated 10^5 muons cross the volume of CMS, firing a large fraction of all channels in the central CMS detector. An example of a beam shot event is shown in fig. 16. This allowed to time in the channels of several subdetectors with a precision of about 1 ns. Within hours after recording the first set of 17 beam shot events, the first analysis results were available, showing clear correlations between subdetectors in the energy recorded, as well as the angular distribution of the energy deposits. In some of the events the energy recorded in ECAL and HCAL exceeded 1000 TeV.

With a circulating LHC beam reaching more and more stable conditions, over a million beam halo muon events were recorded and reconstructed crossing the CMS detector from one Cathode Strip Chamber (CSC) endcap to the other. These events are used to study

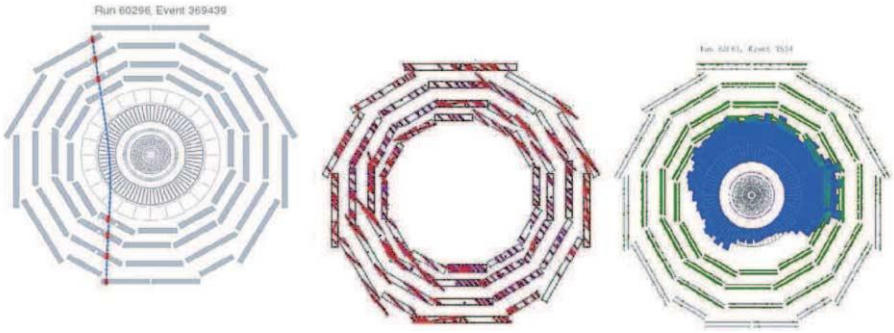

Fig. 16. – From left to right: a single cosmic event, a multi-muon cosmic event, and a beam shot event. These events, spanning a vast range of muon multiplicities (1–10^5), were successfully analyzed using full track reconstruction (left), local segments (middle) or reconstructed muon hits and energy deposits (right).

CSC chamber alignment. In fig. 17 the hit pattern of muon hits in the CSC chambers is shown, from a run dominated by cosmics to a stable run with circulating beam where most of the hits are from beam halo muons, and the shape of the tunnel becomes clearly visible in the hit pattern.

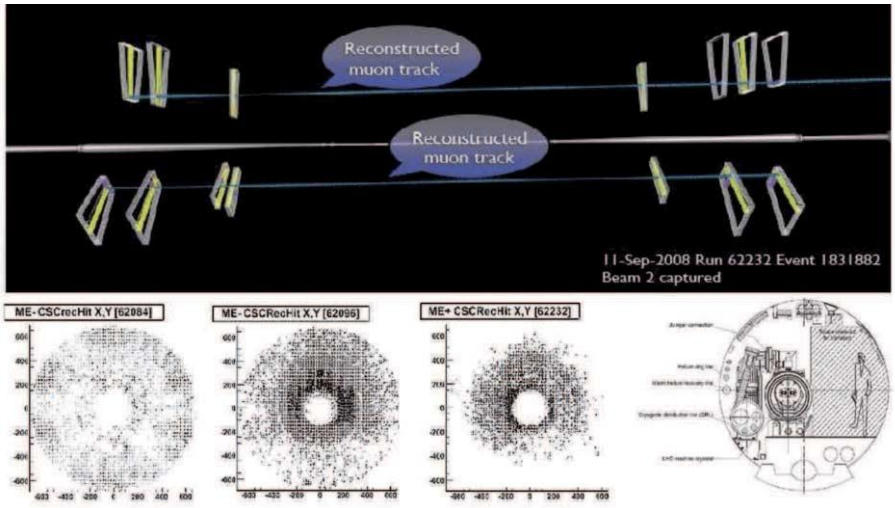

Fig. 17. – The pattern of hits in the endcap muon detectors, for a run with 50 passes of the beam (left), 100 s of passes (middle) and circulating beam (right). The emerging pattern resembles the shape of the LHC tunnel (far right).

8. – Prospects for first physics with collisions

The measurements during commissioning with or without cosmic muons described in this lecture are only preparations for the real physics goals for which the CMS detector has been designed and built.

The next step toward LHC physics will happen when the first proton-proton collisions are delivered by the LHC. This will provide events with particles originating from the collision vertex in the center of the detector, providing a new event topology offering many new challenges to be addressed. This will be a very useful step forward in the commissioning of the LHC detectors, regardless of the collision energy at which the first sizable set of collisions will be delivered by the LHC. The highest priority with the very first data from pp collisions will be to understand the reconstruction performance of physics objects other than muons: electrons, photons, jets, and eventually taus and missing transverse energy (MET).

The early data from LHC collisions will allow the first look at minimum-bias pp collisions, and already with the first few pb^{-1} of integrated luminosity CMS plans to measure cross-sections and differential yields of charged particles and neutrals, as well as their multiplicity distributions. Another important goal will be to tune simulation of the underlying event by looking at the topology of pp collision events with respect to the leading charged jet. Low mass resonances should be visible as well, first in the di-muon channel.

At an integrated luminosity of about $10\,\mathrm{pb}^{-1}$ it should be possible to re-discover well-known standard model processes like W, Z and $t\bar{t}$ production, and measure their production cross-section at the energy scale of LHC collisions. At this point it will become possible to study the lepton, jet and MET reconstruction in detail, and verify that the detector performance is accurately described in the Monte Carlo simulation.

Most searches for new physics will start in earnest at integrated luminosities approaching $100\,\mathrm{pb}^{-1}$ and beyond. A key factor will be to refine data-driven methods to estimate and control with confidence the backgrounds from Standard Model processes.

A comprehensive overview of studies of CMS physics potential and plans for first physics can be found in the CMS Physics TDR [3]. More recent physics analysis summaries are available on the CMS physics web page [15].

9. – Summary and conclusion

After almost 20 years of design and construction, CMS has started taking data with cosmic muons and (single) LHC beams and recorded its first beam events in 2008. The commissioning of the CMS detector already involved several detailed physics analyses before the first LHC collisions. At these occasions the CMS detector and collaboration succeeded in quickly performing varied and meaningful analyses of a wide range of events, from single muon events to events with 10^5 muons crossing the detector (see fig. 16).

Including the latest global runs (in summer 2009), a total of more than a billion cosmic rays has been recorded by the CMS detector, of which more than half with the solenoid

at nominal 3.8 T field and all of the subdetectors included in data taking. Analysis of this data has led to improved understanding of detector response in terms of efficiency, resolution and energy scale calibration, and allowed commissioning of alignment procedures, as well as the precise mapping of the magnetic field. CMS is ready for the first physics analysis with LHC collisions.

* * *

I would like to thank the scientific secretary P. OLIVA and the directors S. BERTOLUCCI and U. BOTTIGLI for inviting me to this wonderful school, organized under the auspices of the Italian Physical Society. All results on the Compact Muon Solenoid detector presented in this report were made possible thanks to the technical and administrative staff at CERN and other CMS Institutes, and with the support from: FMSR (Austria); FNRS and FWO (Belgium); CNPq, CAPES, FAPERJ, and FAPESP (Brazil); MES (Bulgaria); CERN; CAS, MoST, and NSFC (China); COLCIENCIAS (Colombia); MSES (Croatia); RPF (Cyprus); Academy of Sciences and NICPB (Estonia); Academy of Finland, ME, and HIP (Finland); CEA and CNRS/IN2P3 (France); BMBF, DFG, and HGF (Germany); GSRT (Greece); OTKA and NKTH (Hungary); DAE and DST (India); IPM (Iran); SFI (Ireland); INFN (Italy); NRF (Korea); LAS (Lithuania); CINVESTAV, CONACYT, SEP, and UASLP-FAI (Mexico); PAEC (Pakistan); SCSR (Poland); FCT (Portugal); JINR (Armenia, Belarus, Georgia, Ukraine, Uzbekistan); MST and MAE (Russia); MSTDS (Serbia); MICINN and CPAN (Spain); Swiss Funding Agencies (Switzerland); NSC (Taipei); TUBITAK and TAEK (Turkey); STFC (United Kingdom); DOE and NSF (USA). Individuals have received support from the Marie-Curie IEF program (European Union); the Leventis Foundation; the A. P. Sloan Foundation; and the Alexander von Humboldt Foundation.

REFERENCES

[1] EVANS L. and BRYANT P. (Editors), *LHC Machine*, *JINST*, **3** (2008) S08001.

[2] THE CMS COLLABORATION (CHATRCHYAN S. *et al.*), *JINST*, **3** (2008) S08004.

[3] THE CMS COLLABORATION, *CMS Physics Technical Design Report, Volume 1: Detector Performance and Software*, CERN/LHCC 2006-001; THE CMS COLLABORATION, *J. Phys. G: Nucl. Part. Phys.*, **34** (2007) 995.

[4] THE CMS COLLABORATION, *Particle-Flow Event Reconstruction in CMS and Performance for Jets, Taus, and missing Transverse Energy*, CMS PAS PFT-09/001, `http://cdsweb.cern.ch/record/1194487`.

[5] THE CMS COLLABORATION, *The CMS Magnet Test and Cosmic Challenge, Operational Experience and Lessons Learnt*, CMS NOTE 2007/005.

[6] KLYUKHIN V. I. *et al.*, *IEEE Trans. Appl. Supercond.*, **18** (2008) 395.

[7] KLYUKHIN V. I. *et al.*, *Measuring the Magnetic Field Inside the CMS Steel Yoke Elements, Proceedings of the IEEE NSS 2008 Conference.*

[8] *TOSCA/OPERA-3d Software*, Vector Fields Ltd., Oxford, U.K., `http://www.vectorfields.com`

[9] MAROUSSOV V., *An Analytic Fit of the Measured Magnetic Field of the CMS Detector*, PhD Thesis, Purdue University (2008), CMS TS-2009/018, http://cms.cern.ch/iCMS/jsp/openfile.jsp?type=TS&year=2009&files=TS2009_018.pdf.
[10] THE CMS COLLABORATION, *JINST*, **5** (2010) T03021.
[11] THE CMS COLLABORATION, *JINST*, **5** (2010) T03009.
[12] THE CMS COLLABORATION, *JINST*, **5** (2010) P03007.
[13] ALDAYA M. and GARCIA-ABIA P., *Measurement of the Charge Ratio of Cosmic Muons using CMS data*, CMS NOTE 2008/0016.
[14] LIU C. and NEUMEISTER N., *Reconstruction of Cosmic and Beam-Halo Muons*, CMS NOTE 2008/001.
[15] *CMS Physics Results*: https://twiki.cern.ch/twiki/bin/view/CMS/PublicPhysicsResults.

This page intentionally left blank

Proceedings of the International School of Physics "Enrico Fermi"
Course CLXXV "Radiation and Particle Detectors", edited by S. Bertolucci, U. Bottigli and P. Oliva
(IOS, Amsterdam; SIF, Bologna)
DOI 10.3254/978-1-60750-630-0-105

A gravitational wave detector: The Virgo interferometer

J. Marque for the Virgo Collaboration

EGO-European Gravitational Observatory - Via E. Amaldi, 56021 Cascina (PI), Italy

Summary. — Gravitational waves were predicted in 1916 by Einstein as a consequence of the theory of General Relativity: accelerated masses can produce ripples propagating at the speed of light, which perturb the space-time metric. Thanks to the extremely weak coupling with matter, gravitational waves can cross the universe undisturbed and, hence, are a probe of the regions where they are produced which is not accessible by the eventual electromagnetic counterpart. The gravitational waves sources of detectable amplitudes are expected to be compact astrophysical sources such as the coalescence of binaries formed by black holes and neutron stars, the collapses of stellar cores, or the rotation of non–axis-symmetric neutron stars. For more than 40 years the search for gravitational waves has been pursued with resonant detectors made of metallic bars. The development of gravitational wave detectors based on laser interferometers started in the early seventies. After more than two decades of development, the construction of the first interferometers with kilometer scale arms started in the nineties. The sensitivity of such detectors is fundamentally proportional to its length, and with its 3 kilometer long arms Virgo is the largest gravitational wave detector in Europe, and the third largest in the world. It is located at the European Gravitational Observatory (EGO), close to Pisa, and it is designed to detect gravitational waves emitted by astrophysical sources in the frequency range between 10 Hz and a few kHz. Among the other current ground-based gravitational wave detectors, Virgo is the one having the best sensitivity at low frequency, thanks to the particular seismic attenuators, from which the mirrors are suspended. Construction started in 1996 and ended in July 2003. After a very intense commissioning phase, the performances of the detector are now very close to the design ones, and the detector is entering the operation phase. In parallel, the design phase of the second generation of interferometers should be finalized this year with a construction planned to start in 2011. Also, the conceptual design is under study for a third generation. The corresponding European project is called the "Einstein Telescope".

1. – Gravitational waves (GWs)

Newtonian conception of gravity had been in place for 250 years before general relativity. Einstein's special theory of relativity revolutionized physics: space and time are not separate entities. The first observation of gravitational bending was carried out in 1919 during an eclipse in Brazil. One could measure the deviation of the light from a star by the mass of the sun. But, space-time is not just a stage on which dynamics takes place, it is a participant: the field equation of general relativity connects matter dynamics to the curvature of space-time. This leads to the idea that there must exist some notion of "gravitational radiation". Gravitational waves were predicted in 1916 by Eisntein, ten years after his paper on special relativity, as a consequence of the theory of General Relativity: accelerated masses can produce ripples propagating at the speed of light, which perturb the space-time metric. He made the space-time dynamical! Gravitational waves arise from accelerated masses exactly as electromagnetic waves arise from accelerated charges. Due to the extremely weak coupling with matter, gravitational waves can cross the Universe undisturbed and, hence, are a probe of the regions where they are produced which is not accessible by the eventual electromagnetic counterpart.

1˙1. *First evidence.* – GWs are difficult to produce: very large masses moving at relativistic speeds are needed. This follows from the weakness of the gravitational interaction. It is extremely unlikely there will ever be GWs generated in a laboratory. The only objects massive and relativistic enough to generate detectable GWs are astrophysical. Indeed, the first experimental confirmation of the existence of GWs has come from the study of binary neutron star systems. GW emission changes the system's characteristics on a timescale short enough to be observed: the "Hulse-Taylor" pulsar, B1913+16, in 1975 [1]. Thirty years of observation have shown that the orbit is decaying; the results match with extraordinary precision general relativity's prediction for such a decay due to the loss of orbital energy and angular momentum by GWs. Hulse and Taylor were awarded the Nobel Prize for this discovery in 1993. Since this pioneering system was discovered, several other double neutron star systems "tight" enough to exhibit strong GW emission have been discovered.

1˙2. *Sources of gravitational waves.* – Gravitational waves are produced when matter is accelerated in an asymmetrical way, but due to the nature of the gravitational interaction, detectable levels of radiation are produced only when very large masses are accelerated in very strong gravitational fields. Such a situation cannot be found on Earth but is found in a variety of astrophysical systems. Gravitational wave signals are expected over a wide range of frequencies; from 10^{-17} Hz in the case of ripples in the cosmological background to 10^3 Hz from the formation of neutron stars in supernova explosions. Hereafter, we will focus on sources that are in the detection bandwidth of ground-based detectors: 10 Hz to 10 kHz (lower frequency is very challenging to detect on Earth because of ground vibration).

1·3. *Compact binaries.* – Compact binaries are binary systems in which each member is a neutron star (NS) or a black hole (BH). They are currently the best understood sources of GWs. Double neutron stars have been studied observationally since the mid 1970s. The number of events has been estimated per Milky Way Equivalent Galaxy per year with an uncertainty of ± 1 order of magnitude: it is 10^{-4} for NSNS and 10^{-6} for BHBH. Extrapolation to the Universe indicates that ground-based interferometer GW detectors should measure at least several binary neutron star mergers each year (following detector upgrades, the expected rate for current detectors is of the order of one event per several years, so that the detection of an event is plausible but of fairly low probability).

1·4. *Supernovae.* – Core collapse in massive stars (type-II supernova explosions) exhibits the necessary conditions for strong GW generation: large amounts of mass, flow in a compact region (100–1000 km) at relativistic speeds. But the generation of GWs requires also some degree of non-axisymmetry. The degree of asymmetry in collapse is not particularly well understood. If the core of a star is very rapidly rotating during collapse, then instabilities may develop which lead to strong GW emission. If such instabilities develop, core collapse GWs could be detected from events as far away as 10 Mpc, so that several events per year would be likely. Most models of massive stars, however, indicate that such rapid rotation is not likely. Even without the growth of instabilities, the asymmetric dynamics of core collapse is likely to lead to wave emission which would be detectable within the Local Group of galaxies, with perhaps an event every few years detectable by advanced interferometers.

1·5. *Pulsar.* – Continuous GW are expected from rotating neutron star, or GW pulsar. A non-axisymmetry in a neutron star crust will radiate GWs. The amplitude depends on the crucial parameter that characterizes the degree to which the star is distorted; it is rather poorly understood. Measuring these waves requires coherently tracking their signal for a large number of wave cycles. Coherently tracking N cycles boosts the signal-to-noise ratio by a factor $\sqrt{N}$. The Vela and Crab pulsars are one of the main targets of Virgo.

1·6. *Stochastic background.* – Stochastic backgrounds are "random" GWs, arising from a large number of independent, uncorrelated sources that are not individually resolvable. A particularly interesting source of stochastic waves is the dynamics of the early Universe, which could produce an all-sky GW background, similar to the cosmic microwave background. Stochastic waves can be generated in the early Universe through various mechanisms: amplification of primordial fluctuations in the Universe's geometry via inflation, a network of vibrating cosmic strings, the condensation of a brane from a higher-dimensional space. These waves can actually extend over a wide range of frequency bands; waves from inflation in particular span all bands, from ultra-low frequency to high frequency. A recent paper [2] set up an upper limit for the amplitude of such GWs based on the past observation done with LIGO detectors.

1˙7. *Using gravitational waves to study the universe.* – The gravitational wave spectrum is completely distinct from, and complementary to, the electromagnetic spectrum. Electromagnetic radiation is typically emitted in small regions, with short wavelengths, and gives direct information about the physical conditions of small portions of the astronomical sources. Moreover, electromagnetic waves couple strongly to charges and so are easy to detect but are also easily scattered or absorbed by materials between us and the source. On the other hand, gravitational radiation is emitted by the cumulative mass and momentum of entire systems, so they have long wavelengths, and provides direct information about large-scale regions. Besides, gravitational waves couple extremely weakly to matter, making them very hard to detect but also allowing them to travel to us substantially unaffected by matter, even from the earliest moments of the Big Bang. Given that 96% of the mass energy of the Universe carries no charge, gravitational waves provide us with our first opportunity to observe directly a major part of the Universe. Intuitively, it is clear that measuring these waves is very difficult: the weakness of the gravitational interaction ensures that the response of any detector to gravitational waves is very small. However, technology has brought us to the point where detectors are now beginning to set interesting upper limits on GWs from some sources. First direct detection is now hopefully not too far in the future.

2. – The Virgo experiment

2˙1. *The Virgo project.* – Virgo [3, 4] is the Italian-French project of a 3 km long detector located in Cascina, Tuscany. Virgo is the largest gravitational wave detector in Europe, and the third largest in the world. Among the other current ground-based gravitational wave detectors, Virgo is the one having the best sensitivity at low frequency, thanks to the particular seismic attenuators, from which the mirrors are suspended. Virgo has been founded by the Italian "Istituto Nazionale di Fisica Nucleare" (INFN) and the French "Centre National de la Recherche Scientifique" (CNRS). The feasibility studies started independently in Pisa and in Orsay around 1982. The proposal for the construction of Virgo was presented in 1989 by a group of 40 experimentalists and theoreticians. The construction started in Spring 1996 and ended in 2003. The first run of data taking took place in 2007. The design sensitivity has been reached in 2009 and the second run started in July. The project, now, involves 18 research teams (more than 150 physicists and engineers) scattered over France, Italy, Holland, Hungary and Poland.

2˙2. *Gravitational-waves strength and polarization.* – Gravitational waves are most simply thought of as ripples in the curvature of space-time. They change the separation of adjacent masses. Gravitational-wave strength is characterised by the gravitational wave amplitude h which can be interpreted as a physical strain in space: $h = 2\mathrm{d}L/L$ ($\mathrm{d}L$ is the variation of distance between 2 masses separated by a length L). The sensitivity of detectors is fundamentally proportional to their length. Only quadrupole radiation is possible. The magnitude of h produced at a distance r from a source is proportional to the second time derivative of the quadrupole moment of the source and inversely

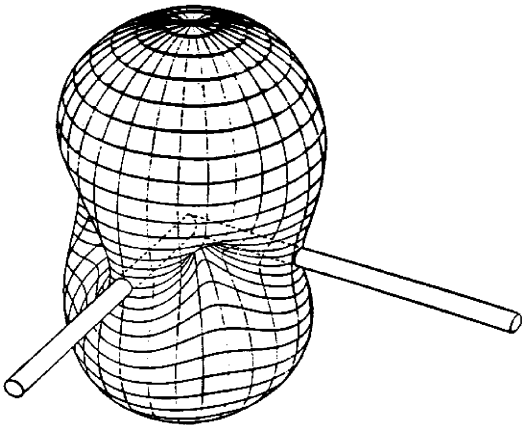

Fig. 1. – Antenna pattern of the Michelson interferometer.

proportional to r. For quadrupole radiation there are two orthogonal polarizations of the wave at 45 degrees to each other, of amplitude h_+ and h_x, and each of these is equal in magnitude to twice the strain in space in the relevant direction. The effect of the two polarizations on a ring of particles is so that the natural principle of most gravitational wave detectors is based on Michelson interferometers.

2˙3. *The Michelson interferometer.* – Because of its quadrupole nature, waves propagating perpendicular to the plane of the interferometer will result in one arm of the interferometer being increased in length while the other arm is decreased and vice versa. The induced change in the length of the interferometer arms results in a small change in the intensity of the light observed at the interferometer output. Gravitational wave antennas are essentially omnidirectional, with linearly polarized quadrupolar antenna patterns (fig. 1) that typically have a response better than 50% of its average over 75% of the sky [5]. Their nearly all-sky sensitivity is an important difference from telescopes.

2˙4. *Sensitivity requirement.* – The problem for the experimental physicist is that the predicted magnitudes of the amplitudes or strains in space in the vicinity of the Earth caused by gravitational waves even from the most violent astrophysical events are extremely small, of the order of 10^{-21} or lower. Indeed current theoretical models on the event rate and strength of such events suggest that in order to detect a few events per year (from coalescing neutron star binary systems for example) an amplitude sensitivity close to 10^{-22} is required over a large bandwidth. For a kilometer scale interferometer, this sensitivity can be translated in terms of differential length measurement target: 10^{-19} m over a large bandwidth, typically 10–10000 Hz.

2˙5. *Ground vibrations.* – Seismic noise at a reasonably quiet site on the Earth follows a spectrum in all three dimensions close to $10^{-7}\,\mathrm{m}/\sqrt{\mathrm{Hz}}$. Thus, the reduction of seismic

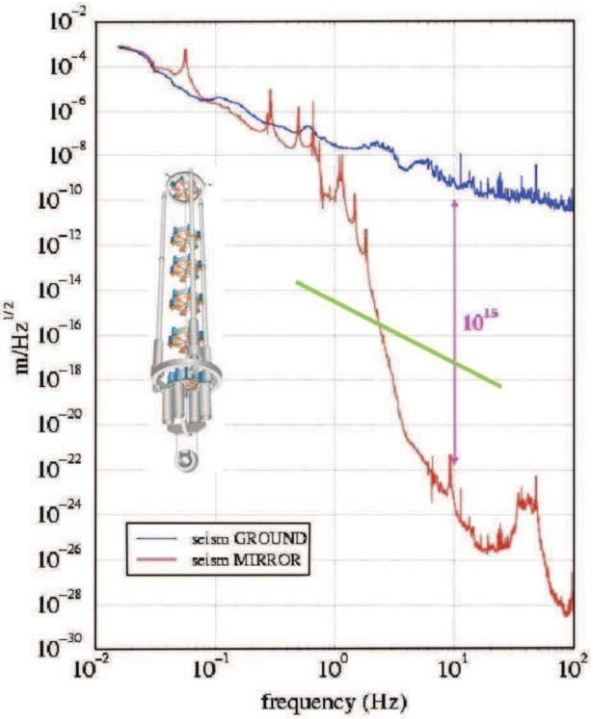

Fig. 2. – Seismic attenuation provided by the Virgo Superattenuator with respect to ground seismic activity.

noise required at that frequency in the horizontal direction is greater than 10^{12} (a similar significant attenuation has to be obtained in vertical also because of couplings). The isolation can be provided in a relatively simple way by making use of the fact that, for a simple pendulum system, the transfer function to the pendulum mass of the horizontal motion of the suspension point falls off as $1/f^2$ above the pendulum resonance. In a similar way, isolation can be achieved in the vertical direction by suspending a mass on a spring.

2˙6. *Superattenuator*. – In Virgo, a seven-stages pendulum arrangement [6] was adopted with six of the upper stages being suspended with cantilever springs to provide vertical isolation. The pendulum is a good mechanical filter for frequencies above its natural frequency. By hanging the mirrors on pendulums of around 1 m length, one achieves filtering above a few Hertz (fig. 2). The whole suspension is 8 m long, equiped with 18 coil-magnet pairs distributed in 3 actuation points (top stage, marionette, mirror). Various position sensors are distributed in different locations: 5 accelerometers on top stage, 14 position sensors, one payload coarse local position readout via CCD camera, marionette and mirrors fine local position readout via optical levers. The marionette and mirror actuators are used to control angular and longitudinal degrees of freedom.

The top stage actuators are used to control the suspension point to cancel the Earth tide effect.

2˙7. *The laser*. – The photon-noise–limited sensitivity of an interferometer is proportional to $1/\sqrt{P}$, where P is the laser power incident on the interferometer, and $\sqrt{\lambda}$, where λ is the wavelength of the laser light. Thus single-frequency lasers of high output power and short wavelength are desirable. Laser development has concentrated on Nd:YAG lasers (1064 nm): more power available, less absorption, low noise and good controllability. The Virgo master laser is a 1 W Nd:YAG Non Planar Ring Oscillator (from Innolight). A higher power laser (slave laser, from Laser Zentrum Hannover) is locked to the frequency of the light from the master laser to increase the power up to 20 W and copy the laser frequency stability properties (the pump energy is delivered from fiber coupled laser diodes).

2˙8. *The amplifier and Pre-Mode Cleaner*. – The light from the slave laser is sent to the amplifier: it is based on 4 Nd:YVO4 laser crystals. Each crystal is longitudinally pumped by a fiber-coupled laser diode with a maximum output power of 50 W at 1064 nm. To obtain high performance from the modulation techniques, at the modulation frequency, the power fluctuations of the laser light must be shot-noise–limited in the amount of light detected at the interferometer output (typically up to a few hundreds of mW). These high-frequency power fluctuations are reduced by passing through a Pre-Mode Cleaner cavity (a resonant triangular cavity). Above the corner frequency f_c (equal to $FSR/2F$) of the cavity, power and frequency fluctuations of the laser light are reduced by a factor f/f_c.

2˙9. *Electro-optic modulators*. – Four frequencies of modulation have to be applied to the laser light in order to control all the degrees of freedom of the optical cavities and of the interferometer using the Pound-Drever-Hall technique. These frequencies of modulation are applied through 3 electro-optic modulators: one LiNbO3 crystal ($f = 14$ MHz for slave laser and Pre Mode Cleaner control), one KTP crystal ($f = 22$ MHz for Input Mode Cleaner control) and one KTP crystal ($f = 6$ MHz and 8 MHz for interferometer control).

2˙10. *Beam geometry fluctuations*. – Fluctuations in the lateral or angular position of the input laser beam, changes of the size and variations in its phasefront curvature may all couple into the output signal of the interferometer and reduce its sensitivity. These fluctuations may be due to intrinsic laser mechanical noise or from seismic motion of the laser with respect to the isolated test masses. The beam positional fluctuations of the laser need to be suppressed by several orders of magnitude either through a filtering by fibers or by optical cavities. A cavity called Input Mode Cleaner is used to reduce beam geometry fluctuations and adjusted to be resonant only for the fundamental mode of the input light. Any higher-order modes are suppressed. The use of a resonant cavity is the only way right now to handle high laser powers and has the additional benefit of acting as a filter for fast fluctuations in laser frequency and power.

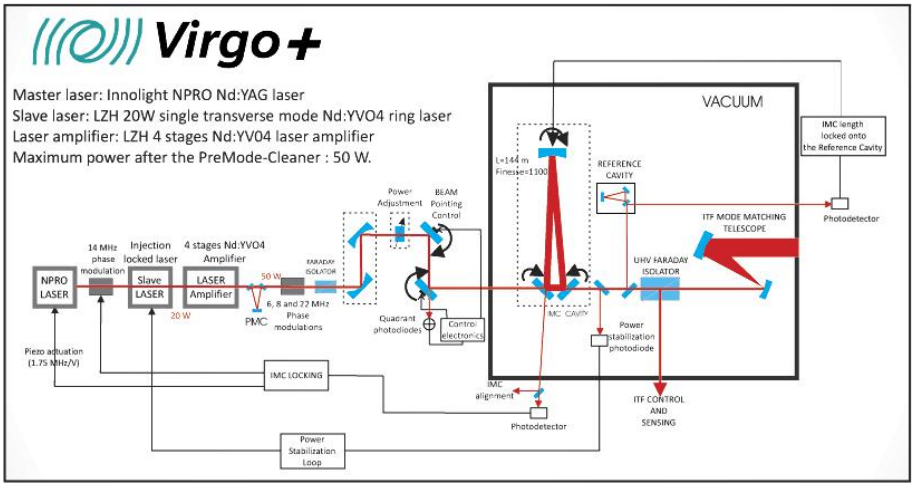

Fig. 3. – Optical scheme of the Virgo input optics system.

2˙11. *Input Mode Cleaner cavity.* – The Input Mode Cleaner cavity is a 143.5 m long triangular cavity of finesse 1200, suspended under vacuum. The cavity has various filtering properties: spatial filtering at all frequencies (so filtering of beam jitter by suppression of high-order modes), laser frequency and amplitude fluctuations filtering above the cut-off frequency f_0 ($f_0 = c/2LF = 500\,\mathrm{Hz}$).

2˙12. *Frequency noise.* – A change in the differential path length of the interferometer arms causes a phase change in the light at the interferometer output which depends directly on the change in the laser frequency. Hence, to achieve the target sensitivity, the fluctuations in frequency must be lower than $10^{-22}/\sqrt{\mathrm{Hz}}$. This level of frequency noise is achieved by using an appropriate laser frequency stabilization system involving high-finesse reference cavities (the Reference Cavity, the Input Mode Cleaner cavity and the 3 km cavities) and acting directly on the master laser.

2˙13. *The Faraday isolator.* – The light reflected by the interferometer is passing through the Input Mode Cleaner in the inverse direction with respect to the light going towards the interferometer. Unfortunately, some light is scattered at very little angle on the end mirror of this cavity, and part of this light becomes resonant in the cavity as the light entering the interferometer. This light adds spurious information on the sensors used to control the Input Mode Cleaner cavity. So, there is the need to isolate the "Input Optics System" from the interferometer. That's the role of the Faraday isolator (polarization-dependent isolator) which provides an isolation as high as 40–50 dB. As a high power is circulating inside the Faraday, the system needs to deal with several issues: thermal lensing, thermal isolation change with temperature and thermal depolarisation.

The optical scheme of the Virgo input optics is summarized in fig. 3.

2˙14. *Residual gas.* – The refractive index of the remaining gas on the path of the beam can fluctuate and produce a background noise: all the interferometer is in a high vacuum to avoid this effect: 7000 m^3 at 10^{-9} mBar, the largest ultra-high-vacuum system in Europe.

2˙15. *The mirrors.* – The mirrors are made of very pure substrate of fused silica of 35 cm diameter and 10 cm thickness (Suprasil from Heraeus). Their main characteristics are: very low absorption (0.25 ppm/cm), very low number of bubbles and inclusions, very good homogeneity and low birefringence. They have been polished with the best performance available on the market: roughness RMS is a few nm over 10 cm diameter. The infrastructure is equipped with clean rooms of class 1 to provide the best cleanliness during the assembling and integration of the payloads.

2˙16. *The coatings.* – The LMA laboratory (Laboratoire des Matériaux Avancés) in Lyon was created to be able to make the very demanding coatings of the Virgo mirrors and measure their performances. The performances achieved are: high reflective coatings with $R > 0.99995$, antireflective coating with $R < 10$ ppm, coating absorption below 1ppm, and scattering of a few ppm.

2˙17. *Thermal noise.* – The thermal noise associated with the mirror masses, the coating and the last stage of the suspensions is the most significant noise source at low frequency for long-baseline gravitational wave detectors. For any simple harmonic oscillator such as a pendulum, the spectral density of the thermal motion of the mass depends essentially on the mass, the temperature and the loss angle or loss factor of the oscillator. The substrate thermal noise will not be a limiting factor as long as one can hang massive enough mirrors. The coating thermal noise will be a limiting factor in the next generation and extensive research programs are ongoing to improve the understanding and techniques to decrease this noise. The thermal noise of the suspensions is currently limiting Virgo at low sensitivity. Next year, the detector will be upgraded with new monolithic payloads (in particular, the wires hanging the mirror will be made of fused silica fibers [7]).

2˙18. *Thermal lensing compensation.* – A small amount of light power is absorbed during transmission, which raises the temperature of the mirror and changes its index of refraction ($dn/dT = 9$ ppm). The resulting "thermal lensing" can ruin the optical properties of the system (a 10 km extra focal lensing is enough). This effect actually limits the amount of laser power that can be used in the current detectors. Thermal compensation systems have been set up to balance the temperature distribution over the mirror (by heating the mirror with a ring-shaped CO_2 laser).

2˙19. *Shot noise.* – The photons that are used to do interferometry are quantized, and so they arrive at random and make random fluctuations in the light intensity. As a random process, the error improves with the square root of the number of photons. To reach the design sensitivity, a few kW have to circulate into the arms. But only a few

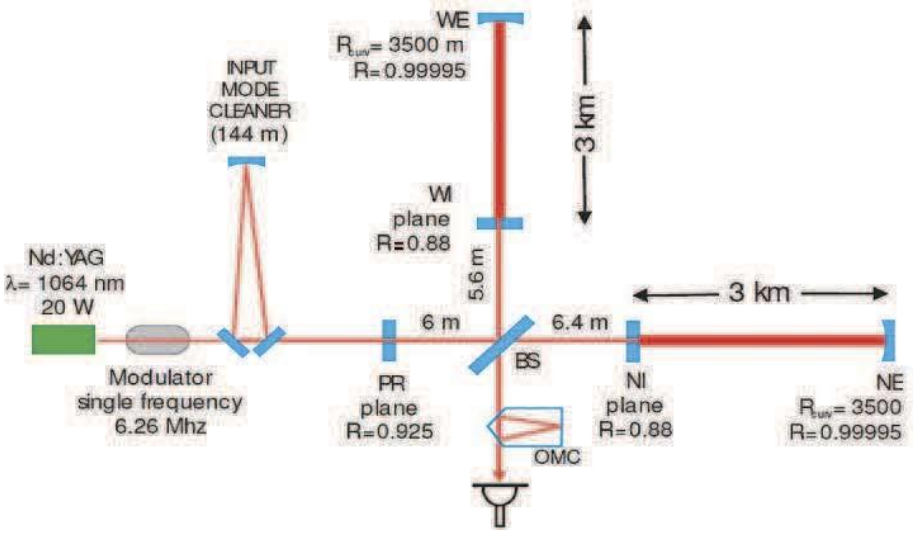

Fig. 4. – Optical scheme of the Virgo interferometer.

tens of Watts are available at the input of the interferometer. Two techniques are used to increase the power: a Fabry-Perot cavity of finesse 50 is installed in each arm, and a power recycling mirror is put at the input of the interferometer. An interferometer actually has two places where light leaves. One is where the interference is measured, the difference port. The other is the sum of the two return beams on the beam splitter, which goes back towards the input laser. This means that all the light normally returns towards the laser input, apart from the round trip losses inside the Fabry-Perot cavities of the arms. By placing a power-recycling mirror in front of the laser, one can reflect this wasted light back in, allowing power to build up in the arms. This can dramatically reduce the power requirement for the laser.

2˙20. *Optical scheme*. – The optical scheme of the Virgo interferometer is summarized in fig. 4.

2˙21. *Controls*. – As already stated, an electro-optic phase modulator is placed in front of the interferometer and used to phase modulate the input laser light at 6 MHz. If the arms of the interferometer are arranged to have a slight mismatch in length this results in a detected signal which, when demodulated, is zero with the cavity exactly on a null fringe and changes sign on different sides providing a perfect error signal. This can be fed back to the actuators controlling the interferometer mirror to hold the interferometer locked near to a null fringe (Pound-Drever-Hall technique [8,9]). It is used to control the main 4 longitudinal degrees of freedom: common length of both arms, the differential length, the recycling length and the differential length of the central interferometer. Also, all angular degrees of freedom need to be controlled: 14 more loops (see fig. 5).

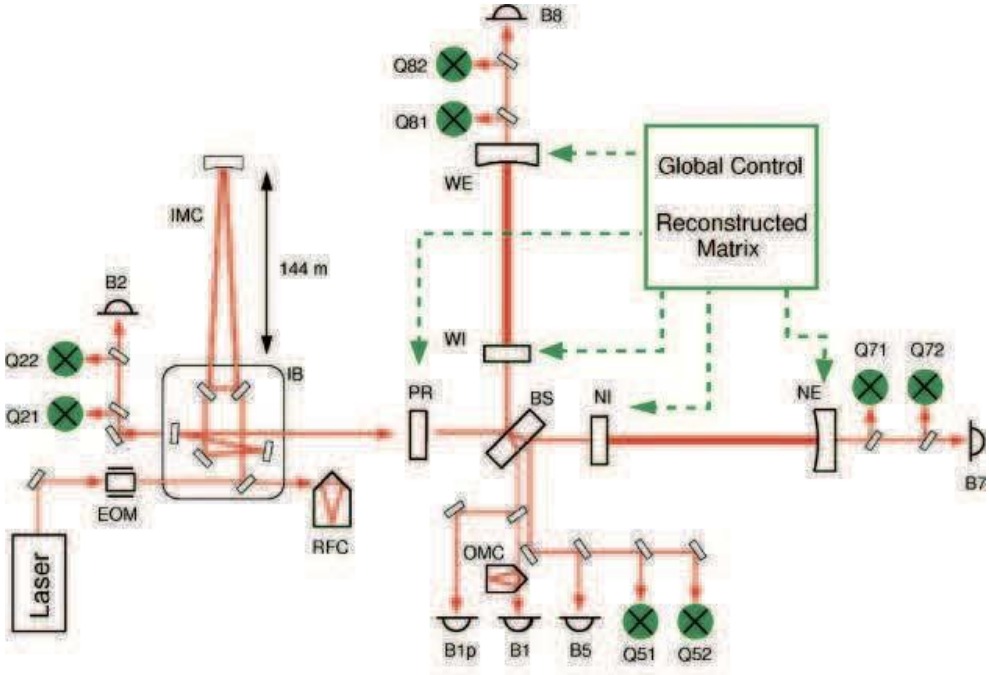

Fig. 5. – Control scheme of the Virgo interferometer.

3. – Other gravitational waves detectors

3˙1. *Resonant-mass detectors*. – A resonant-mass antenna consists of a solid body that "rings like a bell" when a gravitational wave hits it. Resonant-mass detectors were the first kind of detector built in a laboratory to detect gravitational waves: Joseph Weber (University of Maryland) built two cylindrical aluminum bar detectors and attempted to find correlated disturbances that might have been caused by a passing impulsive gravitational wave. His claimed detections led to the construction of many other bar detectors of comparable or better sensitivity, which never verified his claims. Some of those detectors were not developed further, but others had their sensitivities improved by making them cryogenic, and today there are two ultra-cryogenic detectors in operation. A typical "bar" detector consists of a cylinder of aluminum with a length of 3 m, a very narrow resonant frequency between 500 Hz and 1.5 kHz, and a mass of 1000 kg. A short gravitational wave burst with $h = 10^{-21}$ will make the bar vibrate with an amplitude of 10^{-21} m. Currently there are still 3 bar detectors in operation around the world. They are working in cooperation since 1993. The experiments are AURIGA [10] (Padova), EXPLORER [11] (CERN) and NAUTILUS [12] (Frascati).

3˙2. *The LIGO detectors.* – There are 2 American ground-based interferometers: one in the Hanford Nuclear Reservation and one in Livingston [13]. They are pretty similar to the Virgo interferometer. There are mainly 2 differences: the suspension system of the mirrors is less performant (the sensitivity is limited by the suspension below 40 Hz), the arms are longer (4 km) and the Fabry-Perot finesse is higher (200) allowing better performances above 100 Hz.

3˙3. *The GEO detector.* – The GEO600 [14] ground-based interferometer is located near Hannover and is a German-British collaboration. There are many different features with respect to LIGO/Virgo: triple suspension with monolithic ultimate stage, signal recycling (possibility to shape the detector response), folded arms 2×600 m (but no Fabry-Perot cavity in the arms), mirror electrostatic actuation (instead of magnetic actuation). The detector will be upgraded in the next future with squeezed light to reduce the shot noise and the radiation pressure noise.

3˙4. *Space interferometers.* – Gravity gradient noise on the Earth is much larger than the amplitude of any expected waves from astronomical sources at frequencies below 1 Hz, but this noise is very weak far from the Earth. The Laser Interferometer Space Antenna [15] (LISA) project developed in collaboration by ESA and NASA (launch in 2020), would open the frequency window between 0.1 mHz and 0.1 Hz. Many exciting sources are expected in this wave band, for example the coalescences of giant black holes in the centers of galaxies. LISA will have 5000000 km long arms and consists of three free-flying spacecraft, arranged in an array that orbits the Sun, about 20 degrees behind the Earth in its orbit. They form an approximately equilateral triangle. By passing light along each of the arms, one can construct three different Michelson-type interferometers. ESA is planning to launch a satellite called LISA Pathfinder to test all of these technologies end of 2009. The DECIGO proposal is a more ambitious design, positioned at a higher frequency to fill the gap between LISA and ground-based detectors. Even more ambitious is the Big Bang Observer, a NASA concept study to examine what technology would be needed for detecting a gravitational wave background from inflation at these low frequencies.

3˙5. *Pulsar timing.* – Many pulsars are extraordinarily regular clocks when averaged over timescales of a few years. By observing simultaneously two or more pulsars, comparing the delays between signals offers a means of actually detecting strong gravitational waves with periods of several years. Observations are currently underway at various observatories. The most stringent limits to date are from the Parkes Pulsar Timing [16] Array, which sets an upper limit on the stochastic background. Two further collaborations for timing have been formed: the European Pulsar Timing Array (EPTA) and NanoGrav. Future timing experiments will be even more powerful, using new phased arrays of radio telescopes that can observe many pulsars simultaneously, such as the Low Frequency Array (LOFAR) and the Square Kilometer Array.

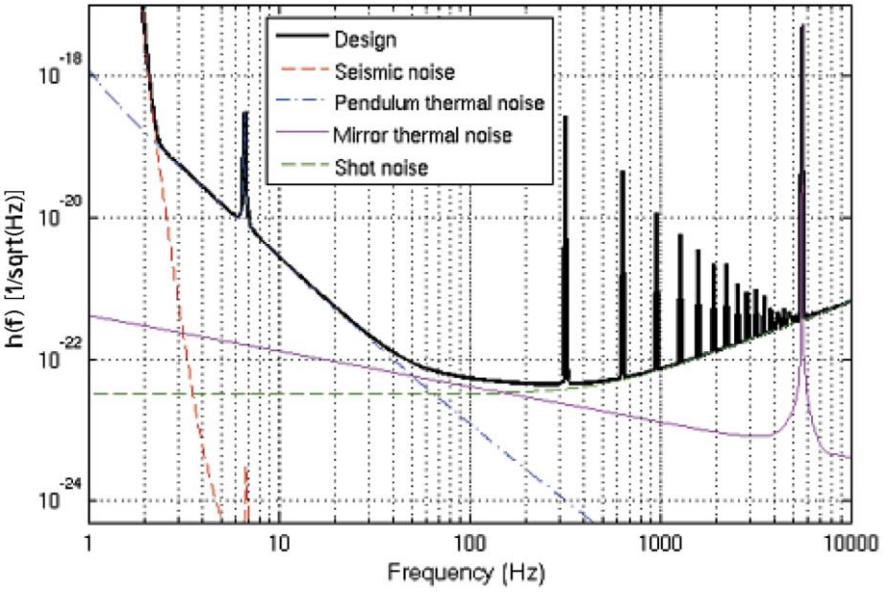

Fig. 6. – Virgo design sensitivity and fundamental noise limitations.

4. – Performances of gravitational waves detectors

The performance of a gravitational wave detector is characterized by the power spectral density of its noise background. A gravitational wave detector outputs a dimensionless data train, which in the case of an interferometer is the relative strain in the two arms, scaled to represent the value of h that would produce that strain if the wave is optimally oriented with respect to the detector. The design sensitivity is shown in fig. 6, the measured sensitivity in fig. 7, and a comparison between LIGO and Virgo sensitivity in fig. 8.

4˙1. *Resonant-mass detectors.* – Novel and imaginative designs for resonant-mass detectors continue to be proposed. Large spheres of a similar size (1 to 3 m in diameter) to existing cylinders have been proposed. This increases the mass of the detector and also improves its direction sensing. A spherical prototype called MiniGRAIL has been operated in the Netherlands. A similar prototype called the Schenberg detector is being built in Brazil. Bar detectors have a disadvantage, however, in that they are sensitive only to signals that have significant spectral energy in a narrow band around their resonant frequency. An alternative design of gravitational wave detector based on a laser interferometer, overcomes this limitation. The remaining bar detectors are likely to be shut down in the near future.

4˙2. *Horizon.* – The horizon (fig. 9) is the inspiral ranges for a standard NSNS coalescence. It is simply the integral of the power spectrum density over a certain band.

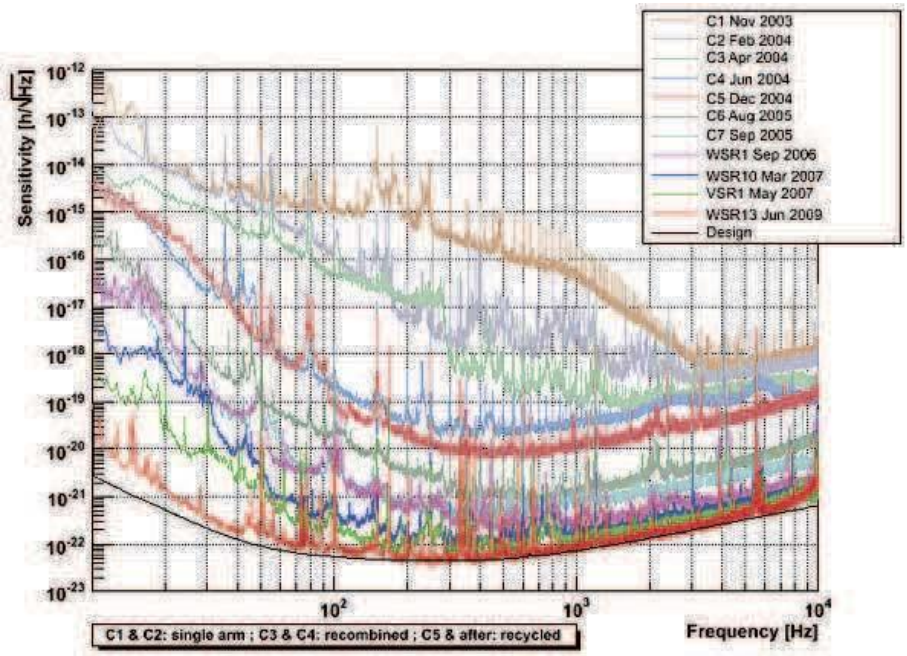

Fig. 7. – Virgo sensitivity as measured during the last 6 years.

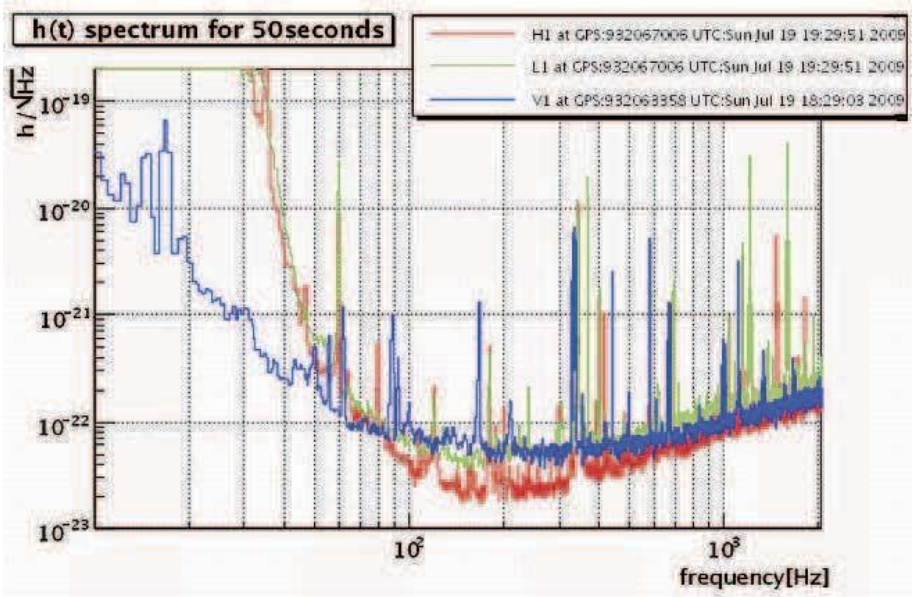

Fig. 8. – Recent LIGO and Virgo sensitivity as measured during the data taking period.

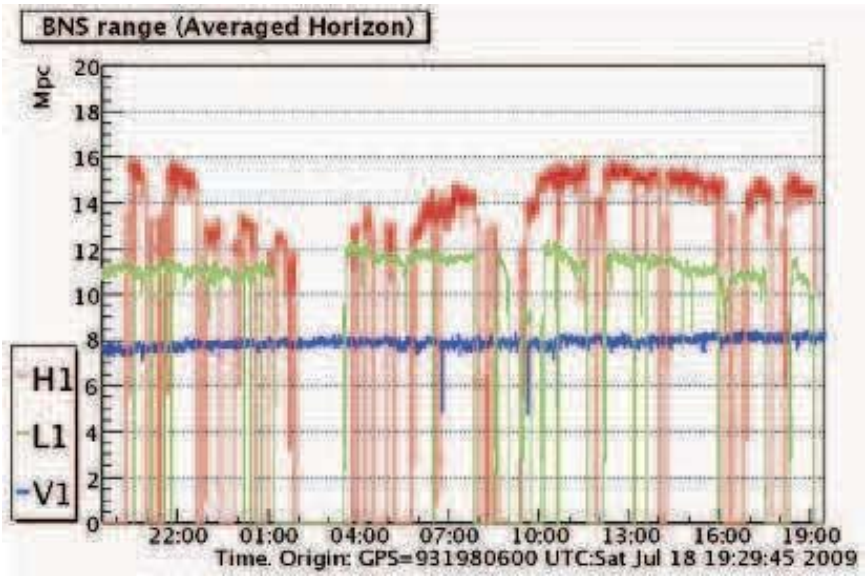

Fig. 9. – Recent LIGO and Virgo horizon evolution as measured during the data taking period.

It provides the limit distance to detect this kind of event with SNR=8 (averaged sky location).

4˙3. *Duty cycle.* – Since July, Virgo is taking data continuously and its duty cycle is around 90%. The remaining time is used to carry out maintenance operation and small improvements. Only 2–3% of duty cycle is lost because of problems. For instance, earthquakes of magnitude higher than 6–7 around the world prevent from controlling the interferometer because of the very large induced oscillations of the suspensions.

5. – Future challenges

5˙1. *Future of ground-based interferometers.* – The first generation of ground-based interferometers has now successfully reached their design sensitivity. Long duration observations of around one year are taking place now with both LIGO and Virgo interferometers in parallel to try to make coincident detections. The second generation of ground-based interferometers is in the end of the design phase. The construction phase of some parts has already started. LIGO and Virgo will re-use the same infrastructure as the first generation. Integration of the new parts will start in 2010-2011. This generation of interferometers, called Advanced Interferometers, has been designed to be 10 times more sensitive than the first generation, being able to observe in a volume of the Universe 1000 times larger. The third generation of ground-based interferometers is in a design study phase. Their design sensitivity target is a factor 100 better than the first generation.

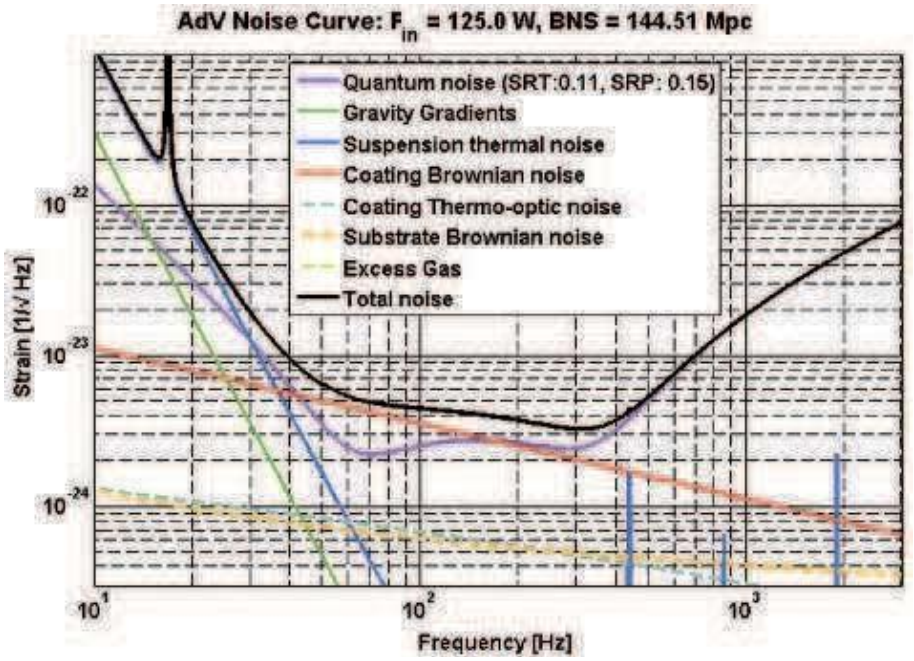

Fig. 10. – Design sensitivity of Advanced Virgo with fundamental noises limitations.

5˙2. *Advanced Virgo*. – The Advanced Virgo project, to reach the design sensitivity (fig. 10), will consist in the following main new feature: 125 W input power (instead of 20 W currently), arm cavity finesse of 900 (instead of 50 currently), signal recycling [17] (a signal recycling cavity is added to enhance the gravitational wave signal), mirrors 20 cm thick (42 kg, instead of 10 cm thick currently). The assembly and integration is planned for 2011-2013.

5˙3. *Some limitations*. – Coating Brownian noise will be a limiting noise for advanced detectors. The reduction of coating mechanical losses is investigated by using different materials for the high/low-refractive-index layers and different doping (tantala doped with titania). A trade-off with the coating absorption is mandatory. Moreover, the mirror flatness has to be improved to decrease the optical losses in the Fabry-Perot cavities. Corrective coatings are under development to decrease the roughness RMS over 120 mm down to 1 nm.

5˙4. *Future beams*. – In order to get a more uniform distribution of power onto the mirror (which means less thermal noise and less lensing effect), people are thinking to use more exotic beams with respect to Gaussian beams. A Laguerre-Gauss55 beam shape would reduce thermal noise by a factor 2 to 3 for the same mirror size, a factor 4 for the same beam size (Laguerre-Gauss beams require larger optics than Gaussian beams to get the same clipping losses). A huge advantage of Laguerre-Gauss beams is that they have a

spherical wavefront, so that there is no need to produce mirrors with very peculiar shape (as it is required for flat beams/"Mexican" wavefront). Some research and development programs are ongoing to generate these beams in an efficient way and to understand how to control the cavities (sensitivity to shift and tilt completely different).

5˙5. *Quantum noise.* – Quantum noise consists of photon shot noise at high frequencies and photon radiation pressure noise at low frequencies. The first one goes as $1/\sqrt{P}$, the second as $\sqrt{P}$. As laser power is increased to reduce shot noise, the position sensing accuracy improves, and one eventually comes up against the Heisenberg uncertainty principle: the momentum transferred to the mirror by the measurement leads to a disturbance. A trade-off is mandatory to get good sensitivity in all the band. This will probably force the third generation to build several instruments to cover the all bandwidth with best sensitivity (interferometers one upon the other with different characteristics): "xylophone" configuration. However, there is a way to partially overcome the problem: in order to reduce the quantum noise, scientists are experimenting new interferometer configurations that modify the quantum state of the light by "squeezing" the Heisenberg uncertainty ellipse, to reduce the effect of this uncertainty on the variable being measured.

5˙6. *Gravity gradient noise.* – Changes in the local Newtonian gravitational field cannot be screened out. A gravitational wave detector will respond to tidal forces from local sources just as well as to gravitational waves. Environmental noise comes not only from man-made sources, but even more importantly from natural ones: seismic waves are accompanied by changes in the gravitational field, and changes in air pressure are accompanied by changes in air density. The spectrum falls steeply with increasing frequency, so that it is not a problem for first-generation interferometers, but it will limit the performance of more advanced detectors. The solution may be to go underground: the seismic noise is expected to reduce with the depth, far from dominant waves at the surface of the ground, far from the atmosphere and far from local noise sources.

5˙7. *Einstein Telescope.* – The European project for third generation of interferometers, currently in a design study phase, is called the Einstein Telescope. Different topologies are under investigation: a triangle configuration, for instance, would fully resolve the polarizations, provide redundancy and minimize tunnel length. The target sensitivity may require the following new feature: 10 km arm length, 500 W input power, larger and heavier mirrors (120 kg), non-Gaussian beams, cryogenics (to cool down the mirrors), suspensions 50 m long, squeezing, underground infrastructure, xylophone topology.

6. – Conclusion

Gravitational waves observation should contribute to Astrophysics by bringing new information about not well-known astronomical systems. It should also contribute to Cosmology by studying the structure and kinematics of the Universe. A direct observation of a stochastic background of GWs of cosmological origin would be of first interest. Finally, GWs observation should contribute to Physics in the sense that they would pro-

vide a unique opportunity to test strongly nonlinear and highly relativistic gravity. It is a fantastic opportunity to compare general relativity with its competitors [18].

One generation of experimental physicists has been necessary to reach current GWs detector sensitivity. But no detection have been done until now at LIGO and Virgo first-design sensitivity. However, the technology is well understood now, and it is an important experience for data analysis people. International collaborations are more and more efficient [19] and the next detectors upgrade between 2011 and 2014 must offer the chance for the first detection. If advanced detectors do not make early detections, then there will inevitably be serious questions about general relativity.

REFERENCES

[1] Hulse R. and Taylor J., *Astrophys. J.*, **195** (1975) L51.
[2] The LIGO scientific collaboration and the Virgo collaboration, *Nature*, **10** (2009) 1038.
[3] Acernese F. *et al.*, *Opt. Lasers Engin.*, **45** (2007) 478.
[4] `http://www.virgo.infn.it/`.
[5] The Virgo Collaboration, `http://wwwcascina.virgo.infn.it/vpb/` (2006).
[6] Braccini S. *et al.*, *Astroparticle Phys.*, **23** (2005) 557.
[7] Amico P. *et al.*, *Rev. Sci. Instrum.*, **73-9** (2002) 9.
[8] Pound R. V., *Rev. Sci. Instrum.*, **17** (1946) 490.
[9] Drever R. W. P., Hall J. L., Kowalski F. V., Hough J., Ford G. M., Munley A. J. and Ward H., *Appl. Phys. B*, **31** (1983) 97.
[10] `http://www.auriga.lnl.infn.it/`.
[11] `http://www.roma1.infn.it/rog/explorer/`.
[12] `http://www.roma1.infn.it/rog/nautilus/`.
[13] `http://www.ligo.caltech.edu/`.
[14] `http://geo600.aei.mpg.de/`.
[15] `http://www.lisa.aei-hannover.de/`.
[16] `http://www.atnf.csiro.au/research/pulsar/ppta/`.
[17] Saulson P. R., *Fundamentals of Interferometric Gravitational Wave Detectors* (World Scientific) 1994.
[18] Sathyaprakash B. S. and Schutz B. F., *Living Rev. Relat.*, **12** (2009) 2.
[19] Gravitational Wave International Committee, `http://gwic.ligo.org/roadmap/`.

Proceedings of the International School of Physics "Enrico Fermi"
Course CLXXV "Radiation and Particle Detectors", edited by S. Bertolucci, U. Bottigli and P. Oliva
(IOS, Amsterdam; SIF, Bologna)
DOI 10.3254/978-1-60750-630-0-123

Underwater/ice high-energy neutrino telescopes

G. Riccobene and P. Sapienza

Laboratori Nazionali del Sud, Istituto Nazionale di Fisica Nucleare
Via S. Sofia 62, I-95123, Catania, Italy

Summary. — Many indications suggest that the observed High Energy Cosmic Rays could be produced in astrophysical sources, namely SuperNova Remants, Gamma Ray Bursters and Active Galactic Nuclei, where Fermi acceleration mechanism of charged particles takes place. In this scenario, accelerated protons undergo photo-meson interaction with the ambient photon field, or hadronic interactions within the source and/or with close molecular clouds, producing high-energy gammas and neutrinos. In the last decade, the operation of air and water Čerenkov gamma ray detectors led to the discovery of about hundred cosmic TeV gamma-ray sources. At least few tens of the identified TeV gamma sources in the Galaxy are expected to be also high-energy neutrinos sources. Many other extragalactic sources, not seen in TeV gamma rays due to gamma ray absorption through interaction with the Cosmic Microwave Background, may also be high-energy neutrino emitters. Neutrinos, light and uncharged, are very promising probes for high-energy astrophysics since they can reach the Earth from cosmic distances and from astrophysical environments obscure to high-energy gammas and nuclei. Theoretical estimates indicate that a detection area of the order of a few km^2 is required for the measurement of HE cosmic ν fluxes. The underwater/ice optical Čerenkov technique is considered the most promising experimental approach to build high-energy neutrino detectors in the TeV-PeV energy range. After the first generation of underwater/ice neutrino telescopes (Baikal, AMANDA and ANTARES), the quest for the construction of km^2 size detectors has already started. At the South Pole the construction of the IceCube neutrino telescope is in an advanced stage, while the ANTARES, NEMO and NESTOR collaborations together with several other European Institutions take part to KM3NeT aiming at the installation of a km^3-scale neutrino telescope in the Mediterranean Sea. Also limits for UHE neutrino detection were strongly improved in the last years, especially with the recent results of ANITA and Pierre Auger Observatory. An intense R&D activities is also ongoing on thermo-acoustic techniques that could provide a viable solution for Ultra High Energy neutrino detection underwater.

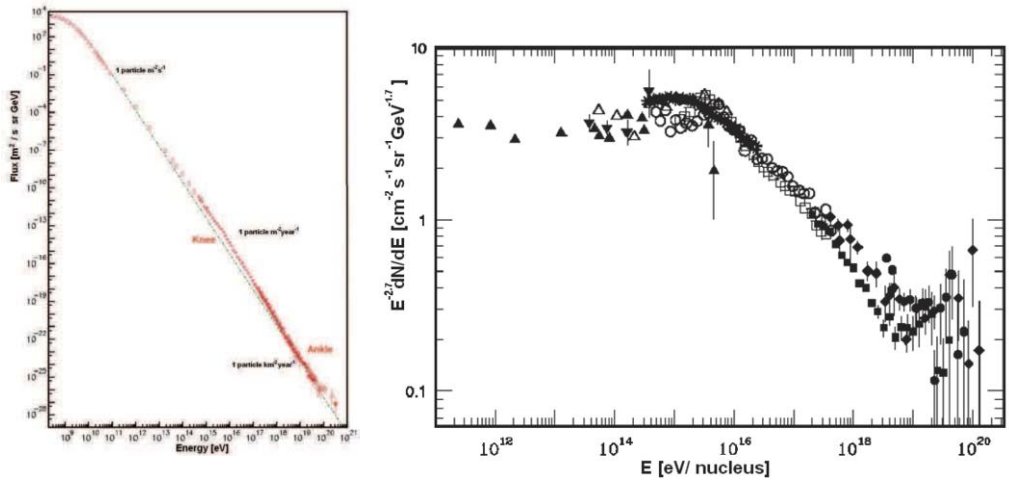

Fig. 1. – Left: the measured cosmic ray spectrum as a function of energy [2]. Right: the CR spectrum multiplied by $E^{2.7}$; two main changes of the spectral index occur at $E \simeq 10^{14.5}$ eV (*knee*) and at $E \simeq 10^{14.5}$ eV (*ankle*), see text [3].

1. – The Cosmic-Ray spectrum

Cosmic Rays, whose first studies date back to the beginning of the XX century [1], are still a puzzling subject for physicists. Up-to-date measurements show that CR flux extends over 10 orders of magnitude in energy, up to $3{\cdot}10^{20}$ eV, and over 28 orders of magnitude in flux, down to few particles per 100 km^2 per century. The measured composition of the bulk of CR is hadron dominated, with about 87% protons, 9% alpha particles and the rest shared among heavier nuclei, photons and electrons [2]. The low-energy region of CR spectrum ($E_{\rm CR} < $ GeV) is well explained by solar activity; above a few GeV the CR energy spectrum follows a power law with spectral index $\alpha \simeq 2.7$ as show in fig. 1 [3]. For the sake of clarity in fig. 1 we also show the CR spectrum multiplied by $E^{2.7}$, that reveals the presence of different trends with increasing energy. At $E < 10^{14.5}$ eV the CR spectral index is $\alpha \simeq 2.7$ and the chemical composition is proton dominated; between $E \simeq 10^{14.5}$ eV and $E \simeq 10^{17.5}$ eV the spectral index becomes softer ($\alpha \simeq 3$) and the chemical composition is heavier; above $E = 10^{18.5}$ the spectral index changes again to $\alpha \simeq 2.7$, the chemical composition in this region is not firmly measured yet. The two breaks in the energy spectrum are usually referred as *knee* and *ankle*, respectively. Above $E \simeq 10^{19}$ eV, the CR flux measured at the Earth is as low as 1 particle/(km^2 year), and above 10^{20} eV the observed CR spectrum is suppressed.

In spite of the fact that CR spectrum has been measured with great accuracy up to 10^{20} eV, a conclusive evidence of connection with sources is still missing, as discussed in the following.

Several astrophysical environments were suggested as candidates sources of the observed Cosmic Ray Spectrum. Among all, Galactic SuperNova Remnants (SNR), Active

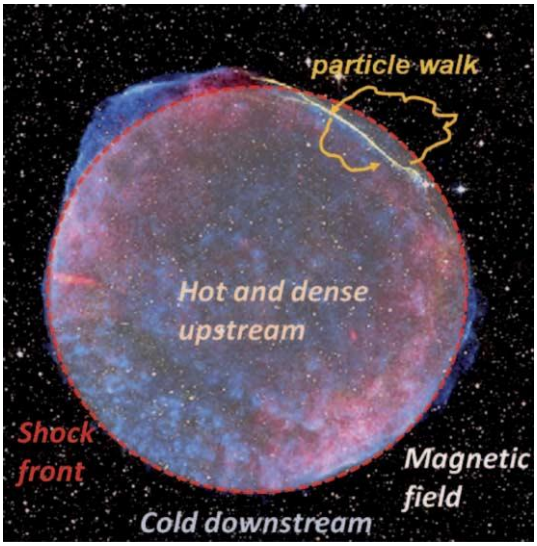

Fig. 2. – The Remnant of SN1006 observed by the Hubble Space Telescope (visible) and by the Chandra satellite (X-Rays). Shocks of SuperNova Remnants are indicated as responsible of CR acceleration in the Galaxy.

Galactic Nuclei (AGN) and Gamma Ray Burst (GRB) seem to play a major role. The bulk of CR spectrum is, in fact, understood in terms of particles accelerated in astrophysical sources through the Fermi acceleration mechanism [4]. This mechanism (whose theoretical description was revised in a more effective version by Bell [5]) takes place in sources where a plasma of charged particles (e^+e^- or/and p^+e^-) is contained by strong magnetic fields and is driven by strong shock waves. Charged particles gain energy, statistically, crossing the shock front from the downstream to the upstream region and viceversa, as shown in fig. 2. The expected spectrum of Fermi accelerated particles follows an $E^{-(2\div 2.2)}$ power law and the maximum energy that a particle can reach is a function of the confinement time within the shock. Since confinement is a function of the object dimensions and strength of the magnetic field, Hillas [6] provided a useful rule of thumb to estimate the maximum energy that a charged particle can reach in a shock:

$$E_{\max} \approx \beta_{\text{shock}} Z B_{\mu\text{G}} R_{\text{kpc}} \quad [\text{eV}], \tag{1}$$

where Z is the particle charge in units of e, $\beta_{\text{shock}} \times c$ is the shock wave velocity, B and R are the source magnetic field and the source linear extension, respectively.

A number of arguments —dealing with energetics, observed chemical composition and spectral shape [7]— indicate that Galactic SNRs are the most probable sources of CR flux below the ankle. In this scenario protons are accelerated in SNR, through Fermi mechanism, and the observed energy spectrum follows the Bell-Fermi $\simeq E^{-2\div -2.1}$

distribution, times a factor $\tau(E) \propto E^{-0.6}$ due to confinement time in the Galaxy, in agreement with the observed $\alpha \simeq 2.7$ spectral index. Nevertheless the question whether only SNRs shocks are responsible for a "local" acceleration of CR, or the statistical acceleration process takes place in a distributed way in the whole Galaxy or in active region such as super-bubbles, is still open [8]. The arrival direction at the Earth of cosmic rays is, in fact, randomized by magnetic fields in the Galaxy ($B \simeq 3\,\mu$G) and in the intergalactic space ($B \simeq$ nG). The Larmor radius of a $E \simeq 10^{18}$ eV proton is comparable with the thickness of the Galactic disk Halo ($\simeq 200$ pc) and much smaller than the Galactic disk radius ($\simeq 15$ kpc). This implies that pinpointing of CR sources is not possible for protons having $E_p < 10^{19}$ eV.

Above the knee energy the total CR flux decreases and the composition increases in metallicity as expected in the scenario of SNR acceleration: protons are not confined any more in the Galaxy, and only nuclei with higher Z remains trapped in the Galaxy. At $E > 10^{18.5}$ eV (the *ankle* region) the CR spectrum features change again. Above this energy the CR flux seems to be similar to the pre-knee region: the spectral index is close to 2.7 and the flux measured by AGASA [9] and HIRES [10, 11] experiments appears to be proton-dominated —though experimental data from the Pierre Auger Observatory (PAO, hereafter Auger) detector seem to favor a mixed composition [12]. Since the known Galactic sources (SNR, Microquasars, Pulsar Wind Nebulae) cannot accelerate particles to extremely high energies, as shown in eq. (1), the detection of cosmic protons with energies up to $E > 10^{19}$ eV suggests the presence of extragalactic accelerators. According to eq. (1), there are only few classes of cosmic objects capable to accelerate protons at $E >$ EeV (10^{18} eV), among these Gamma Ray Bursters (GRB) [13] and powerful Active Galactic Nuclei (AGN) [14] are the most favorable candidates. These sources are respectively the most luminous bursting ($L_{\rm GRB} \simeq 10^{53}$ erg/s) and the most luminous steady ($L_{\rm AGN} \simeq 10^{46}$ erg/s) objects in the Universe ever observed. Protons having $E \geq 10^{19.5}$ eV, likely accelerated in AGNs and GRBs, are considered good astrophysical probes being only slightly bent by cosmic magnetic fields.

Experimental results concerning a possible correlation between UHE proton arrival directions and AGNs are, however, controversial. Results published by the Auger collaboration in 2007 [15] indicated a correlation between the Veron Cetty Veron (VCV) AGN catalog [16] and the arrival direction distribution of events with $E \geq 56$ EeV, with $\phi = 3.1^\circ$ and redshift $z_{\rm max}^{\rm AGN} = 0.018$([1]), while the probability of random correlation is as small as 10^{-5}. However, the correlation claimed by the Auger Collaboration is in contrast with the isotropic distribution measured by HIRES with no evidence of clustering. The most recent analysis of the correlation between the arrival directions of the highest cosmic rays ($E \geq 55$ EeV) for the whole present set of Auger data [17] indicates, for the 58 observed events, a weaker degree of correlation with nearby quasars and active galactic nuclei of the VCV catalogue than previously observed,

([1]) The distance of an object at redshift z corresponds to $4.2 \cdot z$ Gpc, assuming the Hubble constant $H_0 = 71\,{\rm km\,s^{-1}\,Mpc^{-1}}$.

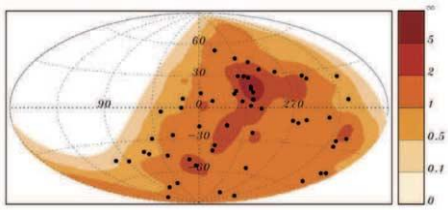

Fig. 3. – The sky map, in Galactic Coordinates, of Auger events up to March 2009. The black dots represent the 58 events with $E > 5.5 \cdot 10^{19}$ eV. Grayish areas represent the distribution of AGN observed by the SWIFT-BAT satellite [18].

while the overlap with the SWIFT-BAT AGN catalogue [18] is stronger, as shown in fig. 3.

Above 10^{20} eV, in an energy region were protons are insensitive to the effect of the Galactic and Extragalactic magnetic fields, the observed CR flux indicates a suppression due the so-called GZK effect [19, 20], named after the scientists Greisen, Zatsepin and Kuzmin. This effect refers to the absorption of extremely high-energy protons in the Universe, through their interaction with the Cosmic Microwave Background Radiation (CMBR): $p\gamma \to \Delta(1232\,\mathrm{MeV})$. The energy threshold of the process is $E_p \simeq 5 \cdot 10^{19}$ eV, that leads to the prediction of the GZK cut-off in the UHECR energy spectrum. In fact, since the cross-section of the proton photo-pion production is $\sigma_{p\gamma}$ is $\simeq 100\,\mu$barn and the average CMBR density is $n_{\mathrm{CMBR}} \simeq 400$ photons $\times\,\mathrm{cm}^{-3}$, the absorption length of EHE protons in the Universe is roughly

$$L_{p,\mathrm{CMBR}} \simeq (\sigma_{p\gamma} \cdot n_{\mathrm{CMBR}})^{-1} < 50\,\mathrm{Mpc}. \tag{2}$$

AGNs and GRBs, the most promising sources of UHECR, are typically located at cosmological distances ($\gg 100$ Mpc), thus $E > 10^{20}$ eV protons and nuclei accelerated in these sources are expected to be absorbed during their journey to the Earth. On the other hand, the presence of the GZK effect would lead to the production of a cosmological flux of "guaranteed" ultra high-energy neutrinos, called GZK or BZ (Berezinsky-Zatsepin) neutrinos [21]. Estimates of the expected BZ neutrino flux are still controversial, as shown in fig. 33, reported below in the text.

Figure 4 shows the absorption length of protons and gamma rays in the Universe as a function of energy: the Very High Energy (VHE, 10^{12} eV $< E < 10^{15}$ eV) photon horizon is limited to few tens Mpc by the interaction on the diffuse cosmic microwave and infrared background ($\gamma\gamma_{\mathrm{CMBR}} \to e^+e^-$); ultra high-energy protons are absorbed within 100 Mpc by their interaction with the CMBR.

In conclusion the proton bending, due to cosmic magnetic fields and the GZK effect, shrinks the energy region accessible to proton astronomy between $\simeq 10^{19.5}$ eV and $\simeq 10^{20.5}$ eV and few hundreds Mpc in distance. As discussed in the following, the observation of gammas and neutrinos is mandatory to unveil the Cosmic Ray sources [22].

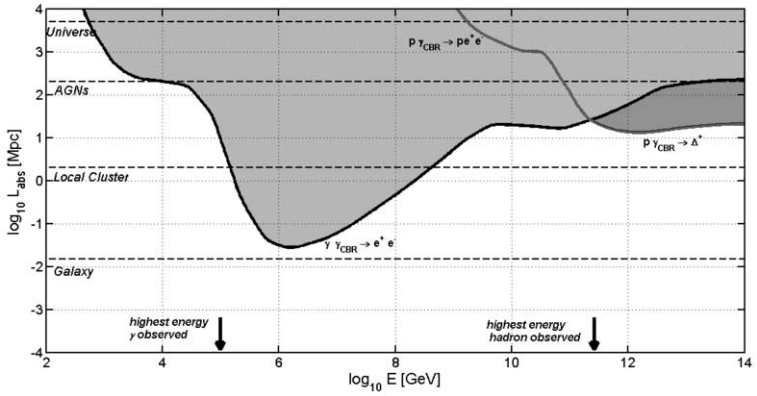

Fig. 4. – Absorption length of protons and gammas in the Universe as a function of particle energy. The gray shaded areas indicate the region not accessible to proton and gamma astronomy.

2. – The high-energy gamma-neutrino connection

After the operation of the first generation IACT (Imaging Air Čerenkov Telescopes) CANGAROO [23], Whipple [24] and HEGRA [25], that detected a few intense VHE sources such as the Crab Nebula and the close AGN Mkn-501, in recent years the TeV gamma ray sky has become "bright". The advent of the second generation IACT such as MAGIC [26], the stereoscopic systems HESS [27] and VERITAS [28], and the operation of MILAGRO [29] and ARGO [30] experiments, allowed a detailed survey of the TeV gamma ray sky and lead to the discovery of about 100 TeV gamma sources [31, 32]. Due both to gamma ray absorption in the Universe and closeness to the Earth, a large part of these sources are harbored in the Milky Way [33] (see fig. 5).

Galactic TeV gamma ray sources are mainly associated with SNR and X-Ray Binaries and with their jetty subclasses: Pulsar Wind Nebulae (PWN), that were found to be the dominant species γ TeV emitters in our Galaxy, and microquasars [31]. In particular SNR and microquasars show peculiar TeV gamma emission that suggests interaction of accelerated protons on dense media or local radiation field, that could also produce TeV neutrino fluxes [34, 35].

Very High Energy gamma ray emission from astrophysical sources is historically interpreted through electromagnetic mechanisms, namely the inverse Compton scattering of Fermi accelerated electrons/positrons on the low-energy radiation field produced by synchrotron emission of charged particles. The latter seems to be the case of Galactic Pulsar Wind Nebulae (PWN) or of the close AGNs Mkn-421 and Mkn-501 [36], whose emissions are studied since several years.

However, hadronic processes seem now to play a major role in several of the observed TeV gamma ray sources. In this scenario, protons accelerated via Fermi mechanism interact with ambient radiation and/or matter, within the source or with nearby gas

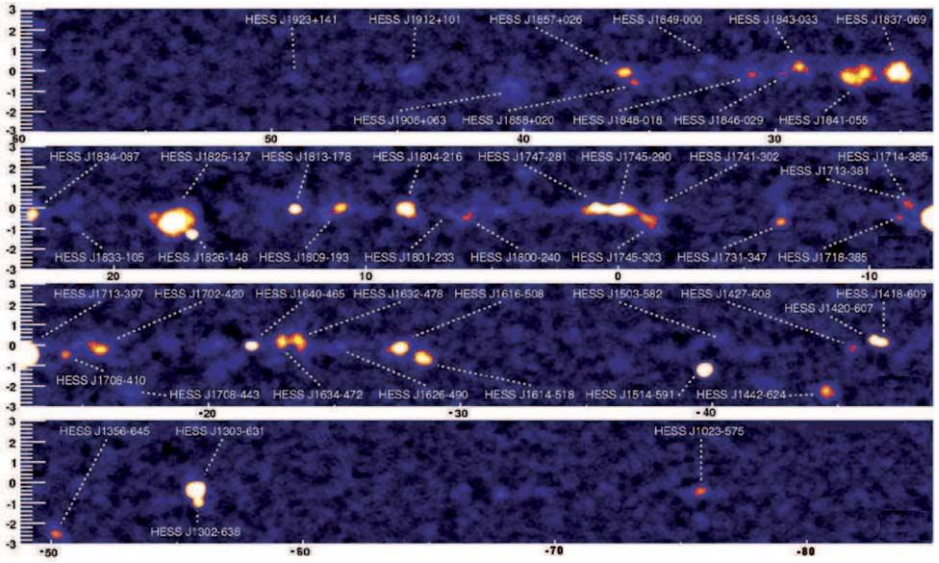

Fig. 5. – Distribution of TeV Gamma rays in the Galactic plane region observed by HESS, Galactic plane survey 2008 [33].

clouds producing pions. Neutral pions then decay into a pair of γ's, while charged pions decay producing neutrinos. In the case of interaction with ambient radiation, the reaction chain is the following:

$$
\begin{array}{rll}
 & & \pi_0 \to \gamma + \gamma \\
 & \nearrow & \\
p + \gamma \to N+ & \pi & \\
 & \searrow & \\
 & & \pi^{\pm} \to \nu_\mu + \mu \\
 & & \qquad\qquad \searrow \\
 & & \qquad\qquad \mu \to e + \nu_\mu + \nu_e .
\end{array}
\tag{3}
$$

Roughly speaking the threshold of the $p\gamma \to N\pi$ reaction is $E_p \simeq 300\,\mathrm{MeV}$ in the center-of-mass reference frame, assuming the main contribution due to the Δ^+ resonant channel, and the pion carries about 20% of the proton energy.

The expected "hadronic" gamma flux (produced in the $\pi^0 \to \gamma\gamma$ channel) therefore follows an E^{-2} power law, as the primary Fermi proton flux, within the energy region constrained, at low energy by the Δ^+ resonance threshold and, at high energy, by $E^p_{\max}$ achievable in the cosmic accelerator. Similarly a muon neutrino flux is produced, with a spectrum E_ν^{-2} and average energy $E_\nu \simeq 5\% E_p$. If the muon cooling time in the source is larger than the muon decay time, high-energy electron neutrinos are also produced with a production ratio of 2 : 1 (see eq. (3)). Taking into account neutrino flavor

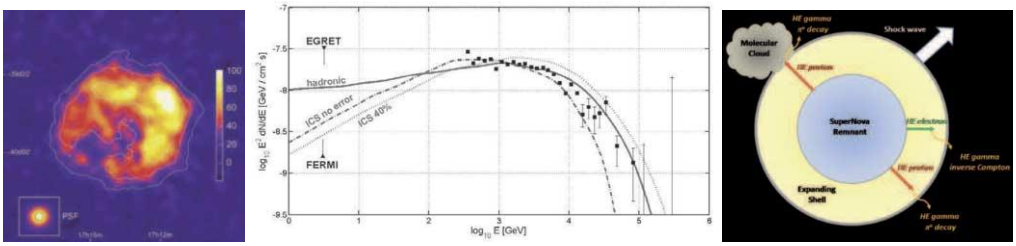

Fig. 6. – Left: contour map of gamma rays counts from SNR RXJ1713.7-394 detected by HESS (threshold $E_\gamma = 800\,\mathrm{GeV}$), the solid lines indicates the X-ray surface brightness as seen by ASCA and ROSAT in the 1–3 keV range. Centre: average spectral index of photons as a function of energy. Right: the HESS observation suggests a scenario in which CRs are accelerated in SNR and subsequently interact in the superposition region between SNR shells and a close-by Molecular Cloud [27].

oscillations during the source-Earth journey, equipartition between the three leptonic flavors $N_{\nu_\mu} : N_{\nu_e} : N_{\nu_\tau} = 1 : 1 : 1$ is expected at the Earth.

The observation by the HESS telescope of TeV gamma rays emitted by the ROSAT and ASCA X-Ray source RXJ1713.7-3946 [27] indicated, for the first time, features suggesting the presence of proton Fermi acceleration. In fig. 6 the gamma spectrum of the source, measured by HESS is reported. The measured spectral index $\alpha \simeq 2.1$ and the morphology of the source favorably indicate a scenario of Fermi accelerated protons interacting on a dense molecular cloud in the NW region close to the source.

Another class of promising hadronic sources is formed by the TeV gamma sources that have no counterpart in other wavelengths, for this reason, called "Dark Accelerators". The number of these sources is, up to date, about 20 [37]. However, also for these sources, purely electromagnetic processes cannot be definitively ruled out and only the detection of high-energy neutrinos will provide the ultimate "smoking gun" to demonstrate the occurrence of hadron acceleration processes.

Moreover, the horizon of $E_\gamma \geq 10\,\mathrm{TeV}$ gamma rays is about 100 Mpc, this limits VHE gamma telescopes to the observation of the Galaxy and of the close Universe (see fig. 4). The observation of astrophysical neutrinos will, therefore, open a window on the far high-energy Universe, where AGN and GRB emissions are expected to play a major role. These extragalactic sources are expected to produce neutrino fluxes extending up to Ultra High Energies, that will emerge above the atmospheric neutrino diffuse flux [38], as shown in fig. 33. The most luminous AGNs and GRBs are also candidate for point-like observation.

Starting from the hypothesis that AGNs and GRBs are the dominant sources of CR observed in the energy range 10^{19}–10^{21} eV, and that the observed particles are protons, Waxman and Bahcall [39] set an upper bound (the so-called Waxman & Bachall limit) for the high-energy neutrino diffuse flux, that can be detected at the Earth. Their limit, obtained assuming that the energy density injection rate of CR, in the mentioned energy region, is $\simeq 10^{44.5}\,\mathrm{erg\,Mpc^{-3}\,year^{-1}}$ and that the AGN and GRB proton spectrum at

the source follows an E^{-2} power law, is

$$E_\nu^2 \Phi_\nu \simeq \frac{c}{4\pi} \frac{f_\pi}{4} E_p^2 \left(\frac{\mathrm{d}N_p}{\mathrm{d}E_p \mathrm{d}t} \right) t_{\mathrm{Hubble}} \simeq 10^{-7.5} \quad [\mathrm{GeV\,cm^{-2}\,s^{-1}\,sr^{-1}}]. \tag{4}$$

Astrophysical objects that do not contribute to CR spectrum at Ultra High Energies are not constrained by the WB limit. Among these, galactic sources such as SuperNova Remnants and microquasars and "optically thick" sources (for which the optical depth is $\tau_{p\gamma} \equiv R_{\mathrm{source}} \cdot (\sigma_{p\gamma} n_\gamma) \gg 1$) where nucleons interact while neutrinos can escape giving rise to a neutrino flux not constrained by eq. (4). This limit does not apply also to a different kind of processes, known as *top-down*, which foresee the production of high-energy CR, gammas and neutrinos by the decay or annihilation of particles with mass $M_X > 10^{21}$ eV, relics of the primordial Universe such as: Topological Defects or GUT-scale mass WIMPS (Weakly Interactive Massive Particles)([2]).

Equation (4) sets, nevertheless, a "reference" value (as shown in fig. 33) for the expected neutrino fluxes and sets the minimum dimension of high-energy neutrino telescopes to km^3 scale, as we will discuss in the next sections.

3. – High-energy neutrino detection

Neutrino astronomy is expected to open a new window on the "violent" Universe. Light and neutral neutrinos are, in fact, optimal probes for high-energy astronomy, *i.e.* for the identification of astrophysical sources of UHE particles. To fulfill this task, neutrino detectors must be designed to reconstruct both the neutrino energy and direction, thus they are commonly referred to as *Neutrino Telescopes* (for a clear review see also [41]). Theoretical estimates of astrophysical neutrino fluxes indicate that masses of target media of the order of few Gton are needed, and up to hundreds of Gton for EHE neutrinos ($E_\nu > 10^{18}$ eV). The use of natural media as ν target is therefore mandatory to build such detectors with affordable budget. In the following the principles of high-energy neutrino detection are described in details.

At energies above few hundreds GeV, neutrinos are detected through deep-inelastic scattering of the ν with a target nucleon N. In the $\nu + N \to l + X$ interaction, the lepton l escapes while the hadronic debris X leads to a hadronic cascade. The initial neutrino energy E_ν is shared among the lepton E_l and the hadronic cascade. The cascade carries $E_h = y \cdot E_\nu$, where y is the Bjorken inelasticity parameter, with a mean value of $\langle y \rangle \simeq 0.25$ at very high energies, and a very broad distribution; the lepton takes the remaining energy [42]. In weak charged-current (CC) interactions the outgoing lepton is charged and it preserves the neutrino flavour (e, μ or τ). In neutral-current (NC) interactions, the outgoing lepton is a neutrino, thus only the hadronic cascade is detectable. The detection of the ν interaction is, therefore, based on the observation of the outgoing charged lepton and/or of the hadronic cascade.

([2]) For a clear review, see [40].

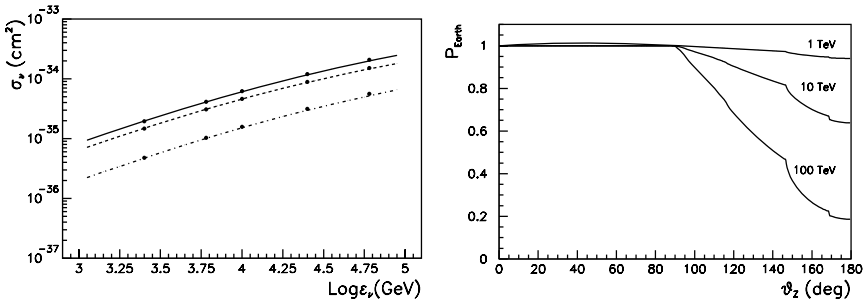

Fig. 7. – Left: the neutrino-nucleon cross-section as a function of energy for charged-current interaction (dashed line), neutral current (dotted line) and total cross-section (solid line). Right: neutrino absorption probability inside the Earth as a function of the zenith angle for $E_\nu = 1\,\mathrm{TeV}$, 10 TeV and 100 TeV, respectively.

The νN cross-section is as low as $\sigma_{\nu N} \simeq 10^{-35}\,\mathrm{cm}^2$, at $\simeq 1\,\mathrm{TeV}$, increasing linearly with the neutrino energy up to 5 TeV energy, above this value its slope changes to $E^{-0.4}$, as shown in fig. 7 [43]. The increase of the neutrino cross-section as a function of energy implies also that at $E > 10\,\mathrm{TeV}$, the Earth is not transparent to neutrinos. Figure 7 shows the probability of absorption of neutrinos as a function of zenith angle for different neutrino energies, taking into account the different densities of the Earth core, mantle and crust [44]. This effect plays an important role for the energy range accessible to different experimental techniques, as described in the following.

Due to the low νN cross-section and to the faint expected astrophysical ν fluxes ($\propto E_\nu^{-2}$), the detectors must have a ν interaction target mass of several Gtons for $E_\nu \simeq 10^{12}$–$10^{17}\,\mathrm{eV}$ and much larger for higher energies. For this reasons Markov, Zheleznykh and Askaryan proposed the use of natural media to detect cosmic neutrinos [45].

Depending on the candidate interaction target medium and on the energy range to explore, different experimental techniques were proposed (see fig. 8):

– In the range $E_\nu \simeq 10^{11}$–$10^{17}\,\mathrm{eV}$, the technique is based on the detection Čerenkov light originated by charged leptons outgoing a CC neutrino interaction in seawater or in the polar ice-cap [45].

– At higher ν energies, the proposed experiments rely on: the detection of radio pulses produced by e.m. showers following a neutrino interaction in polar ice, salt domes or in the Moon Regolith [46, 47]; the detection of acoustic waves produced by deposition of energy in the interaction of ν in seawater, polar ice-cap or salt domes [48]; the detection of air showers initiated by neutrinos interacting with rocks or deep Earth's atmosphere [49].

In the following sections a more detailed description of the different techniques is given together with a closer view on the status of the experiments.

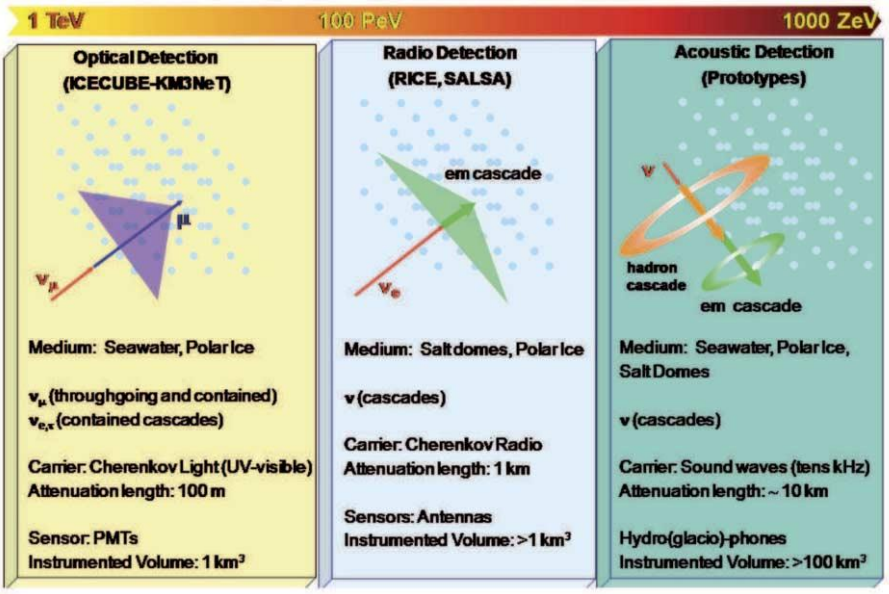

Fig. 8. – Detection techniques for high-energy astrophysical neutrinos as a function of the ν energy range.

4. – Underwater/ice Čerenkov technique

Among all, the underwater/ice Čerenkov technique is, at present, the most promising and advanced. The idea, proposed by Markov [45], is based on instrumentation of large volumes of sea/lake water or polar ice, in order to detect the charged leptons (in particular muons, as we will discuss) emerging from a CC neutrino interaction. Underwater (ice) Čerenkov neutrino detectors are large arrays of optical sensors, typically photomultiplier tubes (PMTs) of about $10''$ diameter, which permit charged-leptons tracking, by timing the Čerenkov light wavefront radiated by these particle.

In water and ice, relativistic particles radiate Čerenkov light mainly in the UV-blue wavelengths. In both media the refractive index in this spectral region is $n \simeq 1.35$, and photons are emitted along the particle track at the angle $\vartheta \simeq 42°$ and symmetrically in ϕ. The time sequence of Čerenkov photons hits on PMTs is thus correlated by the space-time causality relation (see fig. 9):

$$c(t_j - t_0) = l_j + d_j \tan(\vartheta_{\check{C}}). \tag{5}$$

The above relation is used to reconstruct the Čerenkov wavefront, therefore the particle track, from the experimental data. The reconstructed track direction is however affected by experimental indetermination: the error on PMTs position and on absolute photon hit time, due to photon scattering in the medium, PMT transit time spread and

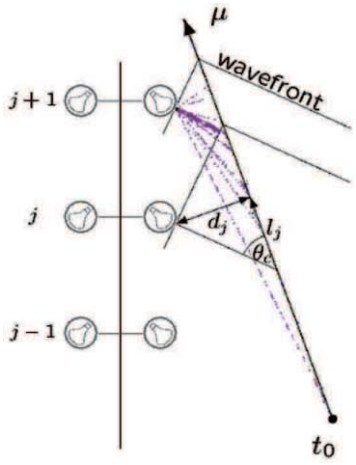

Fig. 9. – The lepton Čerenkov wavefront is reconstructed using the information on photon hit and PMT positions (see eq. (5)).

to detector time calibration. Photon scattering in the medium is an important issue, since scattering deflects Čerenkov photons, affecting track direction reconstruction. In ice the scattering length of light is only few tens of cm, in water is about 100 m [50].

It is worth mentioning that particle energy loss via Čerenkov radiation is only a small fraction of the total one, and the number of Čerenkov photons (UV-blue) is only 300 per cm of track. Given this small amount of light, photons hits PMTs only if the average distance between optical sensors is not larger than the light absorption length in the medium. The medium optical properties, thus, determine the detector granularity (*i.e.* the PMT density) and its size. As shown in fig. 10, water is transparent only to a narrow range of wavelengths ($350\,\text{nm} \leq \lambda \leq 550\,\text{nm}$). In particular, for deep polar ice $L_a(\text{UV-blue nm}) \simeq 100\,\text{m}$ [51], and it is about 70 m for clear ocean waters [50]. This leads to the use of not less than $\simeq 5000$ optical sensors per km^3.

The "golden channel" for astrophysical neutrino detection is the ν_μ CC interaction. The muon range in water is, at $E \simeq$ TeV, of the order of kilometres (see fig. 11), therefore the ν_μ interaction can take place either within the detector or far outside it, providing a flux of high energy muons, either contained or crossing the detector. The muon direction is recovered from the reconstruction of the Čerenkov wavefront, radiated along the muon track, within the detector instrumented volume. The detection of the neutrino-induced muon also allows "neutrino astronomy": the angle between the outgoing muon and the interacting neutrino decreases as a function of neutrino energy (see fig. 11): at $E_\nu > 1\,\text{TeV}$, the muon track is almost co-linear to the ν_μ one and permit pointing back to the ν cosmic source. These detectors are, in fact, also named as *Neutrino Telescopes*.

For the muon neutrino detection, up-going or horizontal muon tracks are preferred. In fact, when an upward going muon is reconstructed this is a unique signature of a neutrino event, being the up-going atmospheric muon background completely filtered

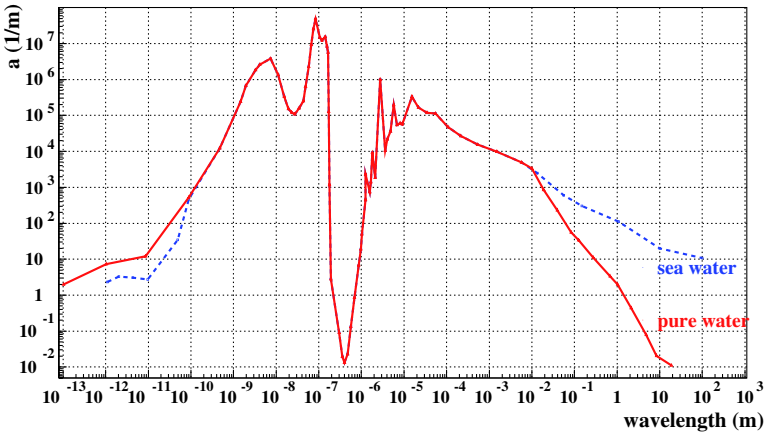

Fig. 10. – Light absorption as a function of wavelength for pure water (solid line) and sea water (dashed line). The absorption length is defined as $L_a(\lambda) = a^{-1}(\lambda)$.

out within few tens of km of water (see fig. 12). The suppression of the intense downgoing atmospheric muon flux is achieved installing the detector at large water(ice) depth: the muon stopping power of 3000 m of water is equivalent to the one of 1 km of rock. Water and ice have, therefore, a threefold function: huge (and inexpensive) neutrino target, Čerenkov light radiator and shield for cosmic muon background.

Neutrino telescopes are also expected to disentangle between neutrino flavours by reconstructing the Čerenkov wavefront shape of the event which depends on the different propagation of e, μ and τ in water (and ice).

In case of ν_e CC interactions, the final state involves high-energy electrons that provide a high-energy electromagnetic shower superimposed on the hadronic one. Both showers extend for few tens of metres from the ν interaction point, thus only interactions that are fully contained into the detector instrumented volume, or very close to it, can be

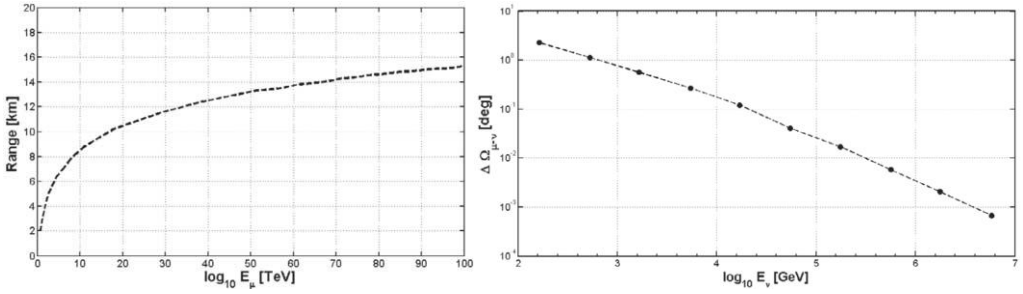

Fig. 11. – Left: average muon range in water as a function of muon energy. Right: median of the distribution $\Delta\Omega_{\nu-\nu_\mu}$ (muon exit angle with respect to the ν_μ direction) as a function of neutrino energy.

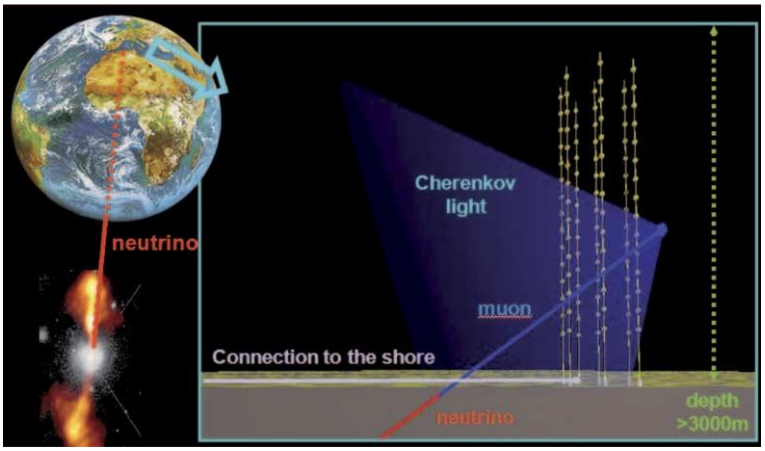

Fig. 12. – Detection principle of an underwater neutrino telescope: Astrophysical neutrinos reach the Earth and interact in water or close to the seabed generating a muon. The array of several thousand optical sensors detect Čerenkov photons generated along the muon track. A water shielding $\geq 3000\,\mathrm{m}$ reduces the atmospheric μ flux by a factor $\simeq 10^6$ with respect to sea surface.

identified. At a distance of few hundred metres from the shower, the shape of the light wavefront is similar to an expanding sphere, thus, the neutrino direction is difficult to reconstruct. On the other hand, showers involve a large number of charged particles ($N \propto E_\nu$) radiating Čerenkov light and, in this case, the lepton energy can be well estimated from the shower light yield. Photon yield is also effectively used to estimate energy in UHE ν_μ detection, for which the muon generates high-energy showers along its path([3]). The charge dynamic range of the PMTs and their readout electronics is therefore an important parameter. The scenario depicted for ν_e is similar to the case of tau neutrino detection: up to $E_\nu \simeq 1\,\mathrm{PeV}$ the τ decay length is too short ($\simeq 50/E_\tau\,\mathrm{mm/TeV}$) to reconstruct the tau decay shower from the hadronic one. When the τ path is about 100 m long, then the two cascades can be separated and the event topology shows the typical signature of a "double light bang".

In order to calculate the number of detectable events expected by cosmic neutrino fluxes, it is important to introduce the quantity $P_{\nu\mu}$, which is the probability to convert neutrinos into detectable muons. $P_{\nu\mu}$ is a function of the neutrino interaction cross-section and of the average muon range $R(E_\mu, E_\mu^{\min})$:

$$P_{\mu\nu}(E_\nu) = N_A \int_{E_\mu^{\min}}^{E_\nu} \mathrm{d}E\mu \frac{\mathrm{d}\sigma_{\nu N}^{\mathrm{CC}}}{\mathrm{d}E\mu} R(E_\mu), \tag{6}$$

([3]) For low-energy "naked muon", the indetermination on the reconstructed energy is large, indeed, since the number of Čerenkov light photons is small.

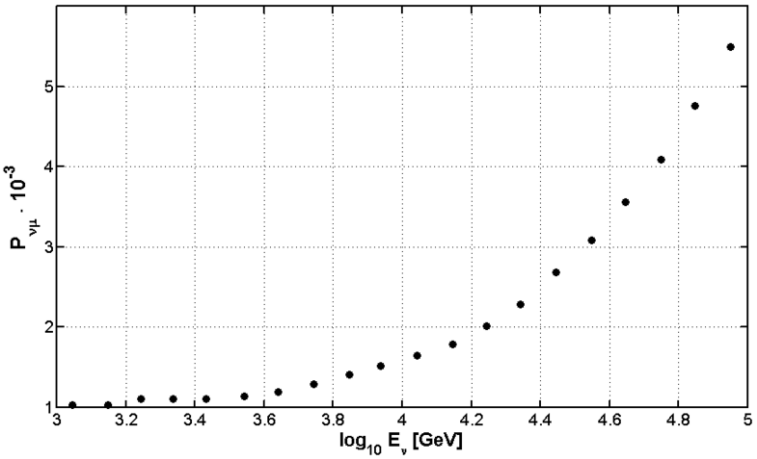

Fig. 13. – P_{ν_μ} as a function of neutrino energy for a detector threshold of 1 TeV.

where N_A is the Avogadro number and $E_\mu^{\min}$ is the minimum detectable muon energy, or detector threshold. For a given detector the value of $P_{\mu\nu}$ has to be calculated via simulations [41]. As a rule of thumb $P_{\mu\nu} \simeq 1.3 \times 10^{-6}$ for TeV neutrinos ($E_\mu^{\min} = 1\,\text{GeV}$) and it increases with energy([4]) as $E^{0.8}$, see fig. 13.

As already mentioned, above 10^{12} eV, the muon range is larger than several kilometres, and detectable muons can be originated far from the detector sensitive volume. The parameter usually quoted to describe detector performance for muon neutrino detection is its *effective area*, A_{eff}, for muons, *i.e.* the surface intersecting the neutrino-induced muon flux folded with the detection efficiency for muons. The rate of events produced by a neutrino flux $\Phi_\nu(E_\nu, \vartheta)$ per unit of detector effective area, is then expressed by

$$\frac{N_\mu(E_\mu^{\min}, \vartheta)}{A_{\text{eff}}\ T} = \int_{E_\mu^{\min}}^{E_\nu} \mathrm{d}E_\nu \Phi_\nu(E_\nu, \vartheta) P_{\nu\mu} e^{-\frac{Z(\vartheta)}{L_{\nu N}(E_\nu)}}, \tag{7}$$

being $L_{\nu N}$ the neutrino absorption length in the Earth and $Z(\vartheta)$ the Earth column depth (see fig. 7).

Plugging the WB bound flux (see formula (4)) into eq. (7) and integrating over solid angle, one gets a rate of about 10^2 up-going events per year for a $1\,\text{km}^2$ effective area detector with $E_\mu \simeq 1\,\text{TeV}$ threshold. This number sets the scale of dimension for astrophysical neutrino detectors.

Due to photon detector and installation costs, the affordable size of these apparatuses is of the order of few km^3. This size is optimal for the exploration of the ν energy range 10^{11}–10^{17} eV.

([4]) For $E_\nu \gg E_\mu^{\min}$ the $P_{\mu\nu}$ the shape is independent of $E_\mu^{\min}$.

The study of detector performance in details requires Monte Carlo simulations that have to take into account the detector layout, the characteristics of the Čerenkov radiator which surrounds the detector (light refraction index, light absorption and scattering coefficients) and the sources of background, that will be discussed in the following section. Simulations show that an underwater detector having an instrumented volume of about $1\,\mathrm{km}^3$ equipped with several thousand optical modules can achieve an affective area of $\simeq 1\,\mathrm{km}^2$ and an angular resolution of $\simeq 0.1^\circ$ for $E_\mu > 10\,\mathrm{TeV}$ [52].

4˙1. *Sources of background*. – There are different kinds of backgrounds with which optical Čerenkov neutrino telescopes have to cope: atmospheric μ and ν background and optical background that affects only underwater telescopes. In neutrino detectors a few of cosmic neutrino events has to be identified and sorted among a huge diffuse atmospheric background. Atmospheric muons (produced by the interaction of primary cosmic rays with the atmosphere), that at sea surface exceed the number of neutrino-induced up-going muons by about 10 orders of magnitude, are attenuated in flux and energy below sea surface as a function of depth and as a function of zenith angle: the atmospheric muon flux falls to zero near the horizon and below where the large slant of water and the Earth shield all the muons (fig. 14). This is the reason why astrophysical neutrino signals are (mainly) searched among upward-going muons. Since at 3000 m depth, an underwater neutrino telescope "sees" a cosmic muon flux still about 10^6 times higher than the up-going atmospheric neutrino signal, accurate reconstruction procedures and quality cuts are needed to get rid of the atmospheric muon tracks mis-reconstructed as "fake" up-going. The atmospheric neutrinos are instead an unavoidable source of background and only energy cuts and statistical arguments allow to discriminate these events from astrophysical ones during data analysis. In fact, atmospheric ν flux is expected to produce diffuse events with a known spectral index ($\alpha \simeq -3.7$ at $E_\nu > 10\,\mathrm{TeV}$) [53] while neutrino fluxes coming from astrophysical point sources are expected to follow E^{-2} and to be concentrated within a narrow angular region, in the direction of their source, whose dimension is essentially given by the detector angular resolution. Diffuse flux searches look for an excess of signals above the atmospheric neutrino flux for a given energy threshold (about $10^5\,\mathrm{GeV}$) and in this case the major concern is the poor knowledge of the component due to the prompt charm decay. Both atmospheric muons and neutrinos are, besides sources of background as discussed above, very useful particles for detector calibration. In particular, atmospheric muons can be used to verify the pointing accuracy of the neutrino telescope and its absolute positioning by detecting the Moon shadow. This method, already exploited by the MACRO [54] and ARGO [55] experiments, is currently used also by the IceCube Collaboration (see subsect. **5**˙3) that presented the first preliminary results on the muon deficit from the Moon direction, shown in fig. 15 [56]. On the other hand, the measurement of the atmospheric neutrino energy spectrum is of crucial importance since it allows to calibrate the detector and in the near future it will provide data in the region of the prompt charm decay where theoretical expectations vary a lot.

A different source of background is the optical noise in seawater that superimposes

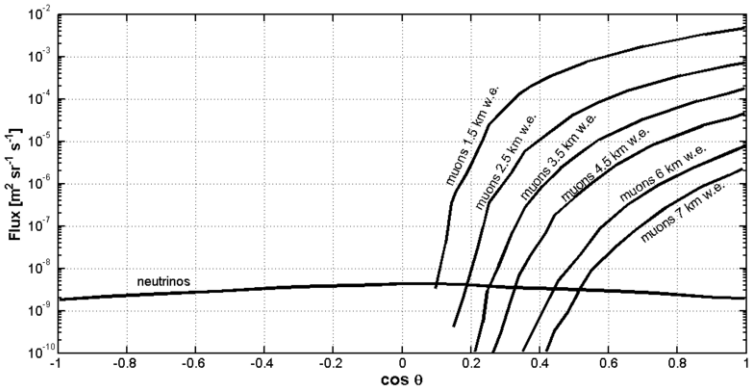

Fig. 14. – Atmospheric muon and neutrino fluxes as a function of zenith angle for different depths of installation of a detector in units of metres of water equivalent (m.w.e.).

random hits that are not correlated to the track to the hits produced from charged leptons. This background is due to the presence of radioactive isotopes and bioluminescent organisms. Radioactive elements in seawater (mainly ^{40}K contained in salt) emit electrons above the Čerenkov threshold. The uncorrelated background produced by ^{40}K decay on PMTs was measured to be about few tens of kHz for 10″ PMT (at 0.5 single photoelectron —s.p.e.— threshold) [52] and does not depend on the site since the salt concentration variations are negligible. Optical noise is also due to bioluminescent organisms living in deep water. These organisms (from small bacteria to fish) produce long lasting ($\simeq 10^{-3}$ s) bursts of light that may saturate PMTs close to the bursts for the period of light emission. In oceanic very deep seawater, bioluminescence signals are rare (few per hour) and do not affect the average optical noise rate on PMTs, as measured at 3000 m depth in the Capo Passero Site, Latitude: 36° 30′, Longitude: 016° 00′, and

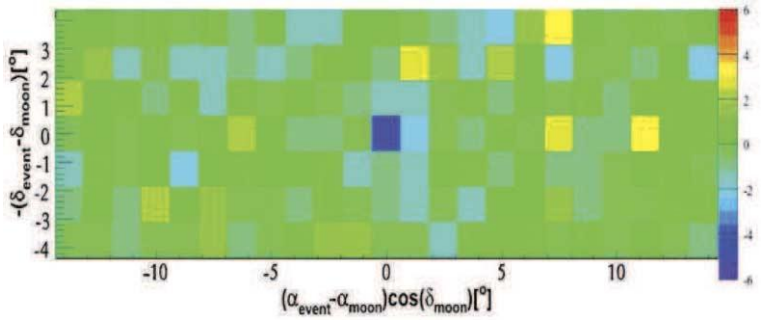

Fig. 15. – Observation of the Moon shadow effect in the cosmic muon flux with IceCube. The gray scale refers to the significance of the atmospheric muon flux deficit in the Moon direction. Data show a 5σ significance.

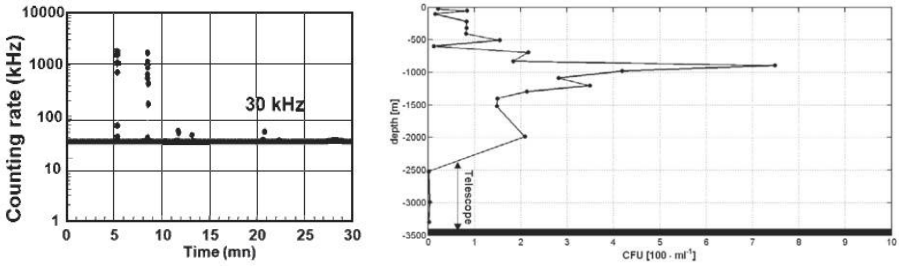

Fig. 16. – Left: optical background rate measured at 3000 m depth in the Capo Passero site, Latitude: 36° 30′, Longitude: 016° 00′, Ionian Sea Plateau. Right: concentration of bioluminescent bacteria as a function of depth measured in the same site.

reported in fig. 16. On the contrary, in biologically active waters, bioluminescence signals may produce an intense background noise up to several hundred kHz (on 10″ PMTs, 0.5 s.p.e) [52]. Background hits have to be filtered by event triggers and reconstruction algorithms. Very high rates of bioluminescence can deteriorate the track reconstruction quality and in the worst cases could affect the data transmission.

5. – Status of neutrino telescope projects

The realization of km^3-scale neutrino Čerenkov detectors both under ice and in deep water requires extended R&D activities in order to cope with the huge technological challenges that working in hostile environments (high pressure, low temperature, corrosion, ...) implies. In the following sections the status of experimental activities in the field is reported.

5˙1. *Baikal.* – After the pioneering experience made by the DUMAND Collaboration off-shore Hawai Island [57], Baikal was the first neutrino telescope operating underwater. The Baikal Neutrino Telescope (NT) is operated in Lake Baikal (Siberia) where the detector is moored between 1000 and 1100 m depth [58]. Deployment and recovery operations are carried out during winter, when a thick ice cap of about 1 meter is formed over the lake. After a first deployment stage, in 1993 (NT36, equipped with 36 PMTs), the Baikal NT200 (fig. 17) was completed in 1998 and it takes data since then. Baikal NT200 is an umbrella-like array with a 72 m height and 43 m diameter. It is made of 8 strings, each with 24 pairs of down-looking Optical Modules (OM). Each OM contains a 37 cm quasar photomultiplier. The two OMs of a pair operate in coincidence in order to suppress the background due to bioluminescence. Baikal NT200 is a high-granularity detector with a threshold $E_\mu \simeq 15$ GeV [59].

A rather low light transmission length in water, 15–20 m, high sedimentation, biofouling rate and a high optical background rate due to bioluminescence limit the NT200 detector performances as HE astrophysical neutrino telescope. Due also to the small lever arm, the angular resolution of NT200 for muon track is only 4°. Nevertheless, for

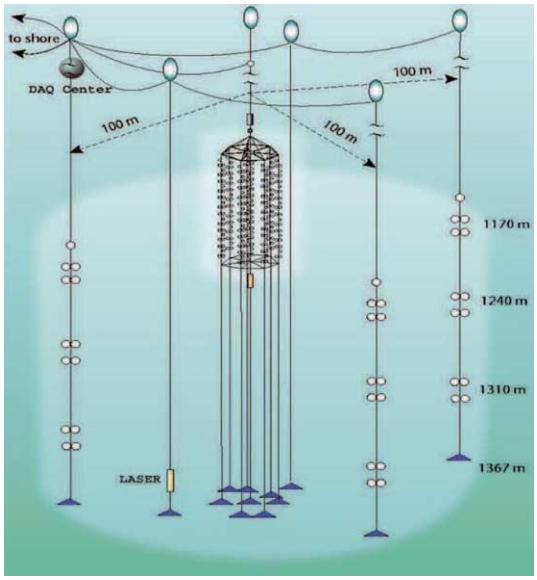

Fig. 17. – Pictorial view of the Baikal telescope NT200+: the compact NT200 detector (center) and the three outer strings are shown.

several years, Baikal has been the largest high-energy neutrino telescope in the world and the only one operating in the Northern Hemisphere thus providing upper limits on several physics items that were the most stringent ones up to the advent of AMANDA (see subsect. **5**˙2). In particular the Baikal Collaboration set first limits on diffuse HE neutrino fluxes. From the analysis of the 5-year sample (1008 days live time) 372 upward going neutrino candidates were selected in good agreement with Monte Carlo simulations of atmospheric neutrinos that give 385 neutrino events to be detected in a corresponding livetime. The collaboration has presented also data analysis of ν_e events, which set an upper limit for diffuse astrophysical neutrino fluxes $E_\nu^2 \Phi_\nu < 8.1 \cdot 10^{-7}\,\mathrm{cm}^{-2}\,\mathrm{s}^{-1}\,\mathrm{sr}^{-1}\,\mathrm{GeV}$ (at 90% Confidence Level, not including systematic uncertainties) [59].

In order to improve the pattern recognition and vertex reconstruction of high-energy cascade events, an upgrading of the NT200 telescope, named NT200+, was realized in 2005 by adding three outer strings (see fig. 17). Each string of NT200+ is made of 12 OM each with a larger spacing. NT200+ has an enclosed detector volume of about 5 Mton and it is expected to increase the sensitivity to diffuse fluxes by almost a factor four. The collaboration also plans the construction of a km^3-size detector in Lake Baikal, the Giant Volume Detector (GVD). The GVD will be made of 90–100 sparsely instrumented strings with 12–16 OMs/string arranged over a 350 m string length. The detector will be made of triangular detection units made of three 200 m spaced strings and a fourth one located in the center of the triangle. GVD configuration will instrument a volume of about $0.7\,\mathrm{km}^3$ for cascade ($E \geq 100\,\mathrm{TeV}$) and will detected muon with an energy threshold of few tens of TeV. NT200+ represents, in this framework, the first step towards GVD.

5˙2. *AMANDA.* – The Antarctic Muon And Neutrino Detector Array (AMANDA), constructed at the Amundsen-Scott South Pole Station was completed in 2001 [60]. AMANDA was a first-generation instrument that served as test bench for technologies and as prototype for the km^3 size detector IceCube. During an exploratory phase of the project in 1993-1994, four strings equipped with 20 OM each (with a 8″ PMT and analogue readout) were deployed between 800 and 1000 m. The strings were connected to surface electronics via coaxial cables. OMs were illuminated by laser light shot into diffusers placed close to the OMs, thus allowing time calibration and, from the arrival times on distant PMT, to derive the optical properties of the ice. These studies showed that at these depths the high residual concentration of air bubbles leads to a light scattering so strong that it does not allow an accurate track reconstruction. For this reason, the next stage of the project AMANDA-B10, made of ten strings, was deployed at depths between 1500 m and 2000 m below the ice sheet surface where the concentration of residual bubbles was expected to be negligible [61].

The final detector configuration, AMANDA II that started in 2000 and run for seven years, consisted of 677 OMs arranged in 19 strings [62]. High voltage power was provided to OMs from surface and PMT signals were amplified and sent to the surface over electro-optical cables. Strings were arranged in concentric circles, the outermost diameter being 200 m, thus giving an instrumented volume of about 15 Mton of ice.

AMANDA II accumulated a total exposure of 3.8 years, taking into account maintenance periods and acquisition system dead time. The average rate of single photo-electron signals on PMTs (mainly dominated by housing and PMT glass impurities) was about 400 Hz per PMT.

The atmospheric neutrino flux, that constitutes the most relevant background to astrophysical ν searches, but also a useful calibration source, has been measured with a statistics of about 1000 events per years.

This allowed to extend the atmospheric muon-neutrino energy spectrum by several orders of magnitude compared with previous data. The neutrino energy spectrum measured by AMANDA is reported in fig. 18 together with the expected neutrino energy spectrum. The observed spectrum is consistent with the predictions, including the contribution of the so-called "prompt" atmospheric neutrinos due to the decay of charmed particles in the atmosphere, as shown in fig. 33 [63].

Despite a quite poor angular resolution (about 2 degrees), the search for astrophysical neutrino point sources was performed with an unbinned method together with a staking analysis on 26 *a priori* point-like sources. No statistically significative excess was found. The sensitivity of AMANDA for point-like sources is reported in fig. 32 [64].

AMANDA was incorporated into IceCube in 2007 and the detector was decommissioned in May 2009.

5˙3. *IceCube.* – The experience accumulated with AMANDA, both in physics and in technological issues, was fundamental for the construction of the ice-base km^3-scale detector IceCube at the South Pole. Several improvements, compared to AMANDA, were anyway necessary to undertake the IceCube construction [68]. Due to hostile South

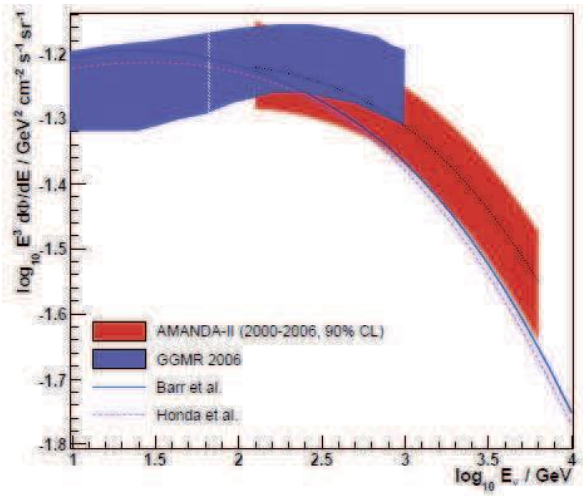

Fig. 18. – Angle-averaged atmospheric neutrino ($\nu_\mu + \bar{\nu_\mu}$) flux, measured with AMANDA, multiplied by E^3 [63]. The solid bands represent 90% Confidence Level from the forward-folding analysis. The dotted line shows the central best-fit curve. Also shown is a previous result by Gonzalez-Garcia *et al.* using Super-Kamiokande data [65], as well as Barr *et al.* [66] and Honda *et al.* [67] predictions. All fluxes are shown prior to oscillations.

Pole environment, which permits line deployment only in a 2-month time window over a year, a major effort of IceCube was addressed to the reduction of the time necessary to install the whole detector. The drilling method pioneered by AMANDA was made more effective by the use of a new very powerful drill with 5 MW of thermal power that allows to strongly reduce the time needed to drill a 2500 m deep, 60 cm diameter hole to about only 40 hours.

In its complete configuration, IceCube, will consists of 80 vertical strings, each equipped with 60 Digital Optical Modules (DOM) [69], deployed between 1450 m and 2450 m depth below the surface, as shown in fig. 19. The DOM spacing along the string is 17 m and the strings are placed on a hexagonal lay-out with 125 m spacing, giving 1 km^3 of instrumented volume. The DOM shown in fig. 20 contain a 10″ PMT and digital readout electronics to permit signal waveform analysis, leading to a relevant improvement of detector performance. The size of IceCube is well matched to the energy scale since a muon with an energy of about 200 GeV travels about 1 km in ice. An improvement of the telescope sensitivity in the low-energy range will be achieved by the addition of six more densely instrumented strings that will be deployed in the bottom center of the telescope to form the so-called DeepCore detector that will lower the IceCube threshold for muons to about 10 GeV, thus allowing to address more effectively low-energy physics issues and especially to increase the sensitivity for the indirect search of Dark Matter [70].

On the ice surface, above the IceCube strings, the IceTop air shower array is installed. IceTop will consist of 180 ice-filled tanks of about 1 m^3 volume, shown in fig. 20, each

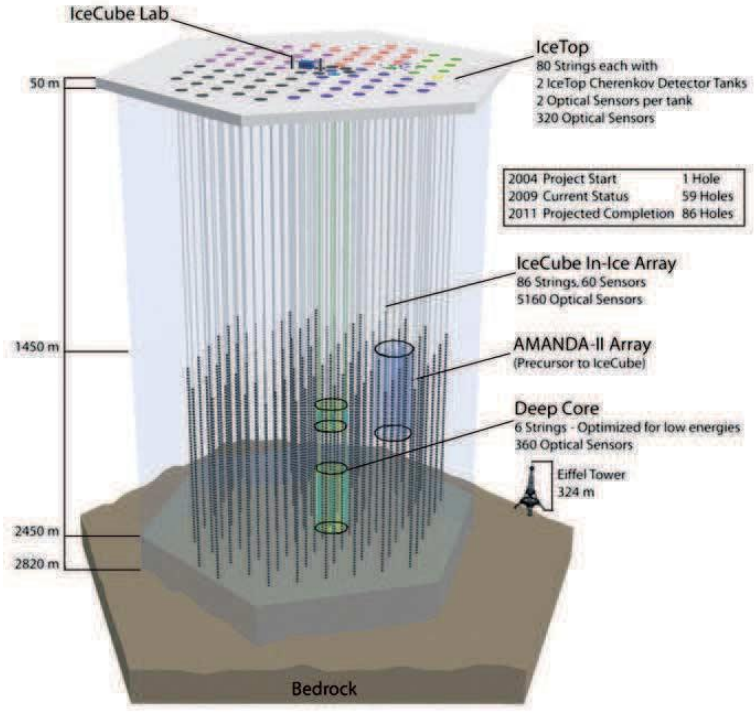

Fig. 19. – Pictorial view of the IceCube detector.

Fig. 20. – Left: deployment of an IceCube string, equipped with DOMs. Right: a tank of IceTop.

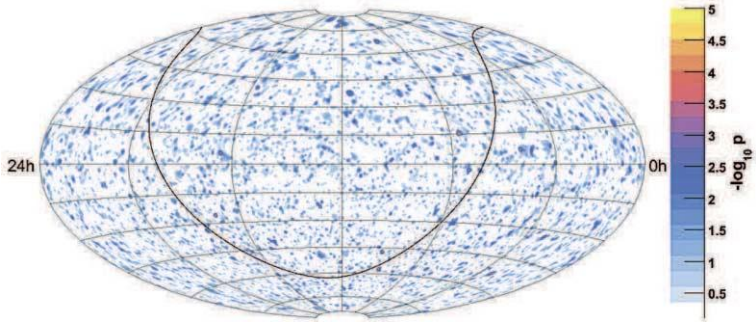

Fig. 21. – The neutrino sky map seen by IceCube.

equipped with two DOMs [71]. IceTop allows to study high-energy cosmic ray showers. With its 59 strings already deployed, 118 IceTop tanks in operation together with the first DeepCore line, IceCube is currently the largest neutrino telescope operating in the world.

The detector is operational since 2006: with 9 lines during 2006 (IC9, 137 days livetime), 22 lines (IC22, 275 days livetime in 2007) and 40 lines (IC40, 365 days livetime in 2008). In the IC40 configuration the single photoelectron rate is 280 Hz per PMT, while atmospheric muon rate and muon-neutrino rate are 1000 Hz and 100 Hz of events per day, respectively. Several triggers, that use the arrival times of the hits on the DOMs, are implemented in the IceCube data acquisition software, thus allowing a first (fast) selection of events that feed a set of software filters performing a variety of simple reconstructions.

An analysis of the 275.5 day 22 string data performed with 4 different muon energy estimators gave a diffuse upper limit for a $E_{\nu_\mu}^{-2}$ spectrum of $2.5 \cdot 10^{-8}$ GeV, that does not show any excess with respect to the expected atmospheric neutrino flux, within systematics errors. Figure 33 reports the limits obtained with IC40 for diffuse muon-neutrino flux and UHE all-flavour neutrino flux, together with expectations for the complete IceCube detector (IC80) [72, 73]. In the near future IceCube will be, thus, able to test the atmospheric neutrino component due to prompt charm decay and to reach a sensitivity for diffuse fluxes lower than the WB limit.

Thanks to angular resolution of less than 1 degree, the sensitivity for neutrino point-like source with IC40 is strongly improved compared to AMANDA. The full neutrino sky map seen by IceCube including both up-going and down-going neutrinos is reported in fig. 21. Down-going events are selected using an energy threshold ($E_\mu \geq 10^5$ GeV) sufficiently high to get rid of atmospheric muons. No significant excess from any sky direction has been observed up to now. In fig. 32 the sensitivity to point-like neutrino sources, as a function of source declination, is reported for different stages of the project [74].

A dedicated analysis was devoted to the search for muon neutrinos from GRBs [75]. The analysis of 41 GRB, mostly detected by the SWIFT satellite [76], and the relative

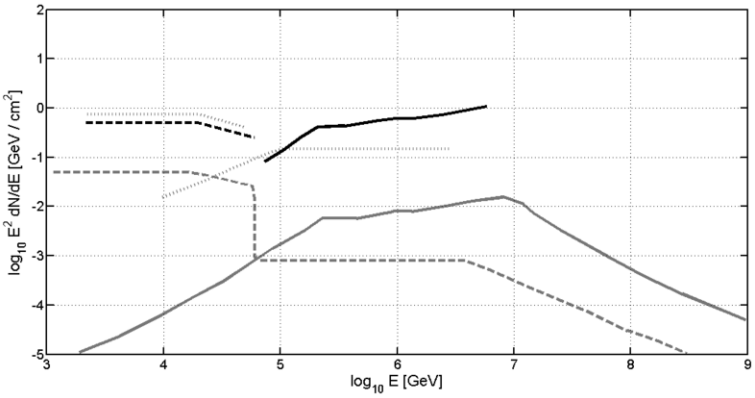

Fig. 22. – Light lines: predicted fluences from the 41 northern hemisphere GRBs for different emission models: prompt (solid, sum of individual spectra) and precursor (dashed). Dark lines: 90% upper limits on the neutrino fluences obtained with the unbinned likelihood analysis [75].

limits obtained with IC22 are reported, for both expected precursor and prompt emission, in fig. 22.

5˙4. *NESTOR.* – The Neutrino Extended Submarine Telescope with Oceanographic Research (NESTOR) was the first Collaboration that operated in the Mediterranean Sea [77]. NESTOR indicated, for the installation of the km^3 telescope, a marine region near the Peloponnese Coast (Greece) where seabed depth ranges between 3800 m and 5000 m. As expected in the Ionian Sea (an oligotrophic environment, compared to the eutrophic Tyrrhenian Sea), recent measurements of optical and oceanographic properties in the deep waters of the site show low optical background and light transmission length close to optically pure seawater (that is salt water without particles) [52]. On the other hand, the presence of a steep shelf break, the so called Hellenic Trench, and of a strong seismic activity, has to be constantly monitored as source of possible changes in the deep-sea environment [78, 79]. A semi-rigid structure (the NESTOR *tower*), 360 m high and 32 m in diameter, equipped with 168 PMTs was designed to be used as "detection unit" for the neutrino telescope [80]. The basic element of the NESTOR tower is a hexagonal floor or star with two optical modules, one up-looking and the other down-looking, at the edge of each arm. The optical modules consists of a 15″ diameter photomultiplier tube enclosed in a spherical glass housing which can withstand the hydrostatic pressure up to 630 bar (fig. 23).

In March 2003 NESTOR deployed one tower floor, with a reduced size of 12 m and equipped with 12 PMTs, DAQ and transmission electronics, and associated environmental sensors. The electronics is placed at the center of the floor, housed in a 1 meter diameter titanium sphere. The cable for connection to shore, previously deployed at 3850 and connected to the off-shore station, was brought to the surface so that the floor was attached, cabled and redeployed to a depth of 3800 m [81]. This array was operational for

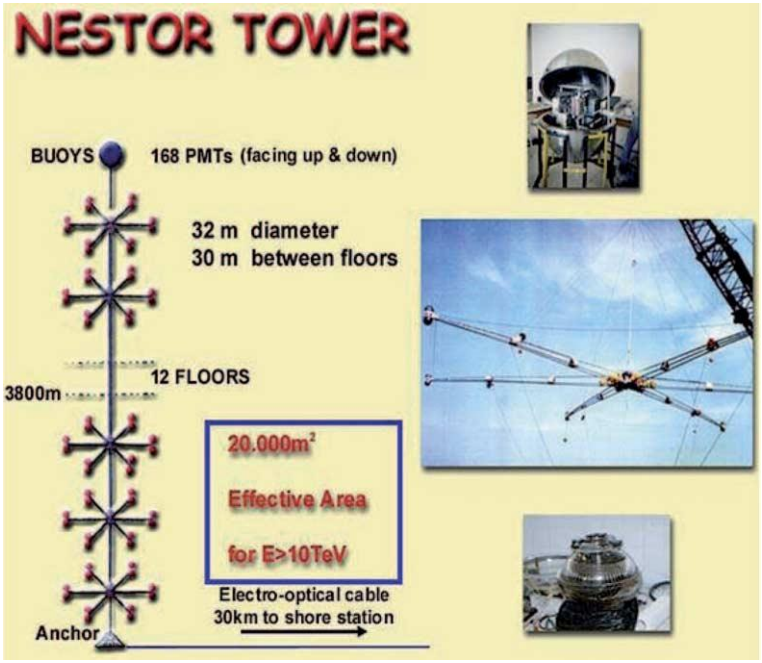

Fig. 23. – Concept of the NESTOR tower.

about one month and the 745 down-going muon reconstructed events allowed to measure cosmic ray muon flux at the installation depth. As shown in fig. 24, good agreement was found between distribution of the zenith angle of reconstructed tracks between data and Monte Carlo event samples [82].

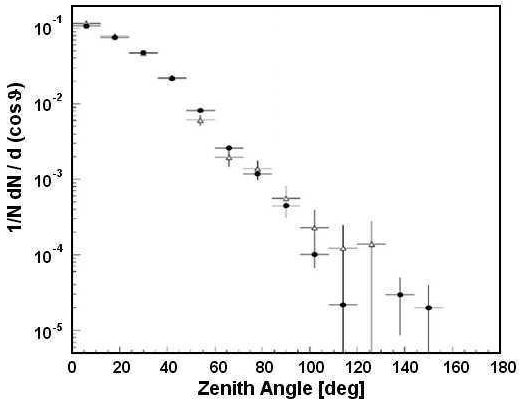

Fig. 24. – Distribution of the zenith angle of reconstructed tracks for the data (open triangles) and Monte Carlo (solid points) event samples [82].

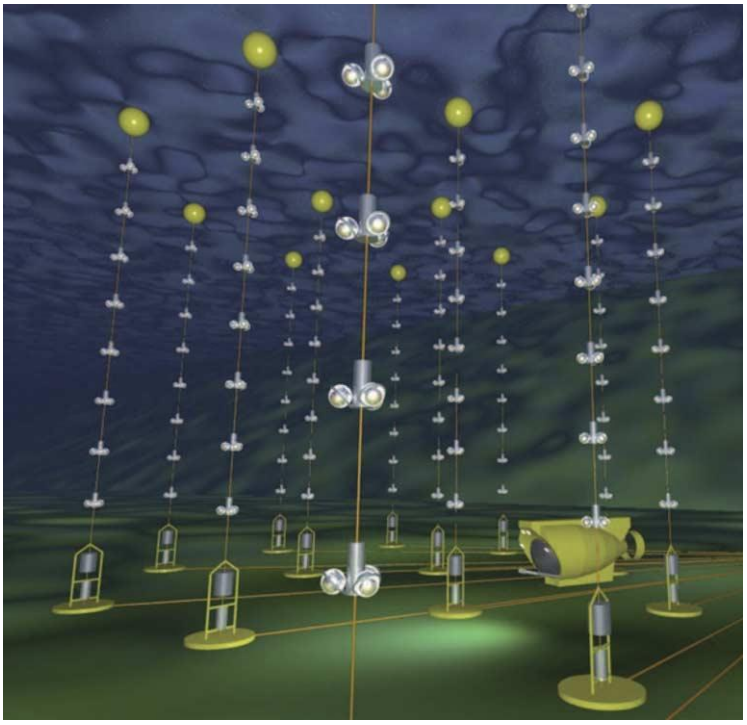

Fig. 25. – Pictorial view of the ANTARES detector.

5˙5. *ANTARES*. – ANTARES (Astronomy with a Neutrino Telescope and Abyss environmental RESearch), with nearly 900 optical modules, is at present the largest neutrino telescope operating in the Northern Hemisphere [83]. The R&D activities towards the construction of a deep-sea neutrino telescope demonstrator of limited size, started in 1996 including site evaluation campaigns and the construction of some prototype lines that allow to test critical components and technologies. ANTARES, see fig. 25 is made of 12 strings, 60 m apart, equipped with 25 storeys consisting of 3 pressure resistent Optical Modules containing each one a $10''$ PMT oriented at 45° down-looking. The spacing between storeys is 14.5 m. The covered footprint is about 0.1 km^2. The detector design was optimized for the detection of up-going tracks. The strings are moored at a depth of 2400 and interlinked in a Junction Box connected with a 45 km long electro-optical cable to the shore station at La Seyne sur Mer (close to Toulon, France). The site shows stable underwater currents, but a largely variable optical background due to bioluminescence activity that can reach values of several hundred kHz [84].

The data transmission is based on the "all data to shore" concept, therefore all PMT signals above a 0.3 photo-electron threshold are sent to shore where a computer farm performs the data filtering. Several different triggers looking for specific neutrino signals are implemented. Thanks to its high PMT granularity, the ANTARES telescope has

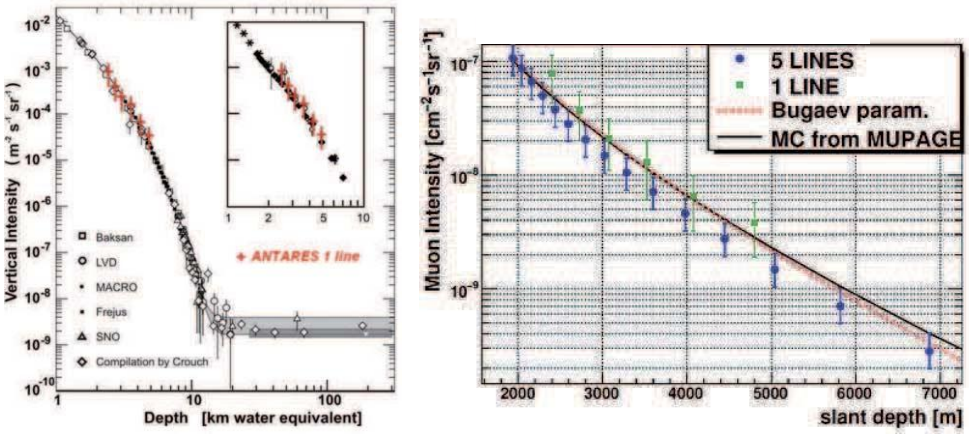

Fig. 26. – Depth *versus* muon flux intensity relation measured with ANTARES for 1 line (left) and 5 lines (right), respectively.

an energy neutrino threshold of about 20 GeV for reconstructed muon events and detector performance dramatically improves with increasing energy reaching at neutrino energy of 10 TeV an angular resolution of 0.3 degrees [85].

Data taking started in March 2006 after the deployment of the first detector line and by January 2007 five lines were deployed while the 12 line telescope was completed in May 2008 [83].

Data with one and five lines have been analysed and results have been presented, while data of the whole telescope are at present under analysis. The comparison of data events with simulated atmospheric neutrinos and muons exhibits a good agreement indicating that the response of the detector is well understood.

In particular the atmospheric muon flux as a function of slant water depth was measured, as shown in fig. 26, indicating good agreement between ANTARES data, other measurements and expectations. A detailed analysis of atmospheric muon events is reported in [86].

The search for cosmic neutrino point-like sources was performed using 140-day five-line data taking, with binned and unbinned analysis. A neutrino signal was searched from 25 possible source candidates including SNRs, microquasars, AGNs and the Galactic Center [87]. A different approach involved a blind search over the whole sky. Although no significant excess was found, the sensitivity obtained, shown in fig. 32, represents the best existing limits for point-like neutrino sources in the Southern Sky, even if compared to the multi-year experiments MACRO [88] and SuperKamiokande [89]. The predicted sensitivity of one year livetime for the whole 12 lines ANTARES detector, also shown in fig. 32, is expected to improve the present limit for the Northern Hemisphere neutrino detectors, by about one order of magnitude.

The successful experience of ANTARES represents an important achievement in the field of deep-underwater high-energy neutrino telescopes.

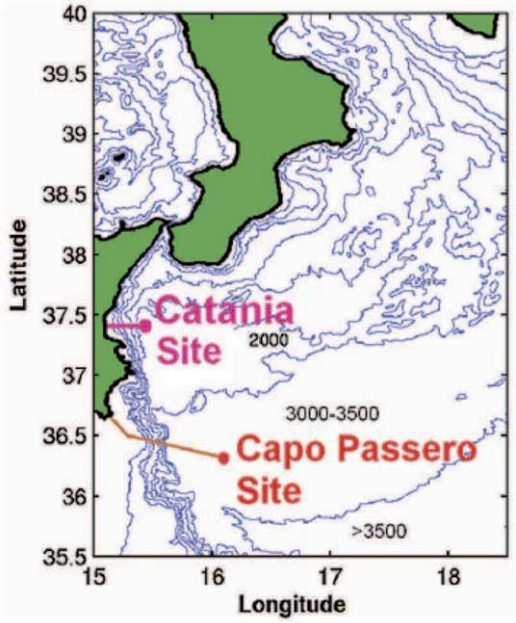

Fig. 27. – Geographic location of the Capo Passero Site: Latitude: 36° 30′, Longitude: 016° 00′, depth 3500 m, and of the NEMO Test Site: Latitude: 37° 30′, Longitude: 015° 30′, depth 2100 m, offshore Catania, Sicily.

5˙6. *NEMO*. – The NEMO (NEutrino Mediterranean Observatory) Collaboration aims at developing and validating key technologies for a cubic-kilometre-scale underwater neutrino telescope [90]. In particular, the project aims at developing technologies that fulfil the requirements of costs and operations even at depths larger than 3000 m for a km^3 underwater telescope. Moreover, more than 30 sea campaigns were performed by the NEMO Collaboration aiming at the search and characterization of a deep-sea site for the installation of the km^3-scale detectors in the Mediterranean Sea. The NEMO collaboration choose the Capo Passero site (fig. 27), located at a depth of 3500 m and 80 km offshore the Sicily coast, that shows optimal features to host the km^3 detector: low optical background (30 kHz on 10″ PMTs at 0.5 s.p.e. threshold), blue light absorption length of 70 m (close to optically pure water), low currents (3 cm/s in average) and low sedimentation rate [91]. The site is located on a wide abyssal plateau, showing very stable environmental conditions and a flat seabed morphology allowing for possible extension of the telescope.

The NEMO detector concept is based on semirigid vertical structures (the NEMO *towers*), see fig. 28, composed of a sequence of horizontal frames (named stories) made of marine grade aluminum. Each storey has two optical modules at either end, one looking vertically downwards and the other horizontally outwards and hosts instrumentation for positioning and environmental parameter monitoring. A tower, which consists of a

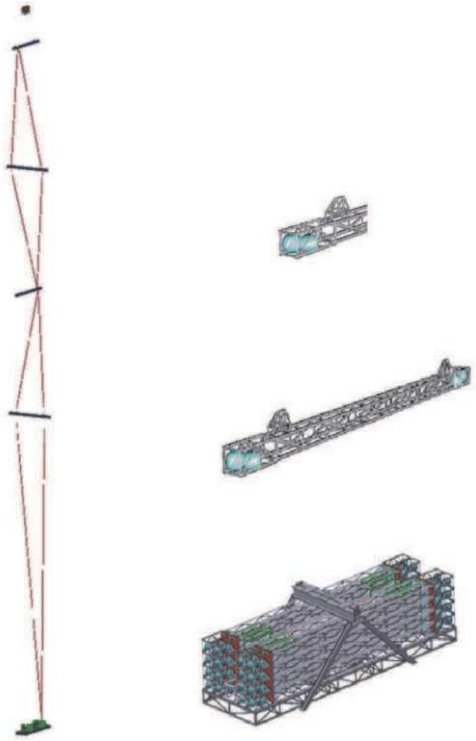

Fig. 28. – The NEMO *tower*. The length of each storey (*floor*) is 12 m and the interstorey distance is 40 m. Thanks to the modular design of the tower, these parameters can be modified.

sequence of stories interlinked by a system of ropes, is anchored to the seabed and kept vertical by appropriate buoyancy on the top. The spacing between storeys is 40 m, while the distance between the anchor and the lowermost storey is 150 m. The structure is designed to be assembled and deployed in a compact configuration, and unfurled on the sea bottom under the pull provided by the buoy. Once unfurled each floor assumes an orthogonal orientation with respect to its vertical neighbors, obtaining a three-dimensional displacement of PMTs. Differently from one-dimensional strings of PMTs, the tower allows disentangling of the muon azimuthal direction reconstruction even with data from only one structure.

In order to validate the prototypes proposed for the km^3 detector, the Collaboration constructed a technological demonstrator at the NEMO Test Site, 2100 m undersea, located 25 km offshore the Port of Catania (Sicily, Italy). The NEMO Phase-1 project started in 2002 and it was completed in December 2006 with the deployment and connection of a submarine Junction Box and a 4-floor prototype NEMO tower (called *mini-tower*) [92].

All key components of an underwater neutrino detector were included: optical and environmental sensors, power supply, front-end electronics and data acquisition, time and

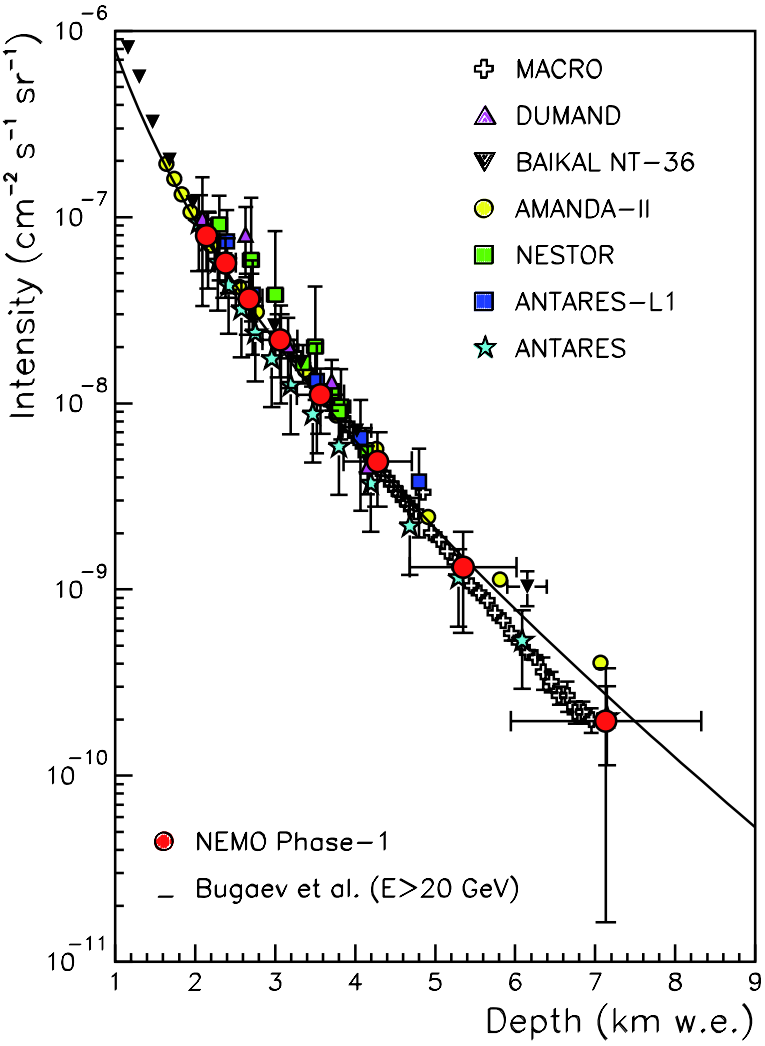

Fig. 29. – Atmospheric muon flux as a function of slant depth measured with the NEMO Phase-1 detector. Data from previous measurements and the parameterization of Bugaev are also reported for comparison.

PMT position calibration systems, slow control systems, on-shore data processing [93]. Five month data were analyzed providing information on the correct behavior of the apparatus, thus providing an important test for the tower design, construction and operation. Data allowed the measurement of the vertical muon intensity as a function of the angular distribution of the muon flux (see fig. 29). Though these data are collected with only one tower and a rather limited number of PMTs, very good agreement was found between data an simulation, confirming the optimal performances of the tower in muon reconstruction [94].

The Collaboration is now undergoing the NEMO Phase-2 project, that is the installation of an infrastructures for an underwater neutrino telescope, at the Capo Passero site. The NEMO Phase-2 infrastructure includes a shore laboratory, located in the harbor area of Portopalo (Capo Passero), a 90 km long electro-optical cable which links a shore station to the underwater infrastructure, consisting of a main Junction Box (JB) used to connect detector prototypes and structures. The JB receives 10 kVDC from shore and distributes 400 VDC power supply to the underwater instrumentation. The total available power for Phase-2 project is 10 kW, to be soon implemented up to 60 kW. The experience gained with the Phase-1 led to a revision of the NEMO tower design aimed at simplifying the tower integration and reducing construction costs. In 2010, a prototypal *tower*, taken in consideration for the KM3NeT telescope as a complete prototype of detection unit, will be constructed and eventually deployed in the Capo Passero site. The *tower* will be equipped with 20 storeys of 6 meters length, optical modules, environmental sensors, hydrophones, data acquisition and transmission electronics, power supply and distribution electronics, and a electro-optical cabling system [90].

5˙7. *KM3NeT: towards a* km^3 *scale detector in the Mediterranean Sea.* – The KM3NeT consortium, funded by the EU, aims at the construction of a cubic-kilometre-scale neutrino telescope in the Northern Hemisphere with an integrated platform for Earth and Deep sea sciences [95]. KM3NeT profits from the experience accumulated within the three pilot neutrino telescope projects operating in the Mediterranean Sea (ANTARES, NEMO, and NESTOR), whose members participate in the consortium together with members from other institutions, including ocean science laboratories. The telescope location in the Mediterranean Sea, due to the Earth rotation, will allow to see upgoing neutrinos from about 3.5π and to survey of a large part of the Galactic Plane, including the Galactic Centre, that has been already identified as a high energy gamma ray source [96, 97]. In particular, the most intense SuperNova Remnants known up to date, RXJ1713.7-3946 and Vela-Jr (RXJ0852.0-4622) that are both in the field of view of KM3NeT with a good visibility. Figure 30 shows the sky coverage of a neutrino telescope located in the Mediterranean Sea compared to the one of IceCube. A major advantage of a deep-sea cubic-kilometre-scale neutrino telescope is its angular resolution, around 0.1° above 30 TeV, indeed, a good point spread function allows to increase the signal-to-background ratio in neutrino point-like source searches, thus improving the sensitivity. The goal of the project is to achieve a sensitivity for point-like sources of about $1 \cdot E_\nu^2 \Phi_\nu \simeq 10^{-9}\,\mathrm{GeV\,cm^{-2}\,s^{-1}}$ in 1 year [52].

In April 2008 the KM3NeT consortium reached an important milestone with the publication of the Conceptual Design Report (CDR) for the telescope. The Design Study phase (KM3NeT-DS) will culminate at the end of 2009 with the KM3NeT Technical Design Report (TDR) proposing technologies and the expected physics performance of the future detector. In parallel, since March 2008, a KM3NeT Preparatory Phase project (KM3NeT-PP, EU FP7) is addressing the political, funding, governance and strategic issues that need to be settled before the start of construction.

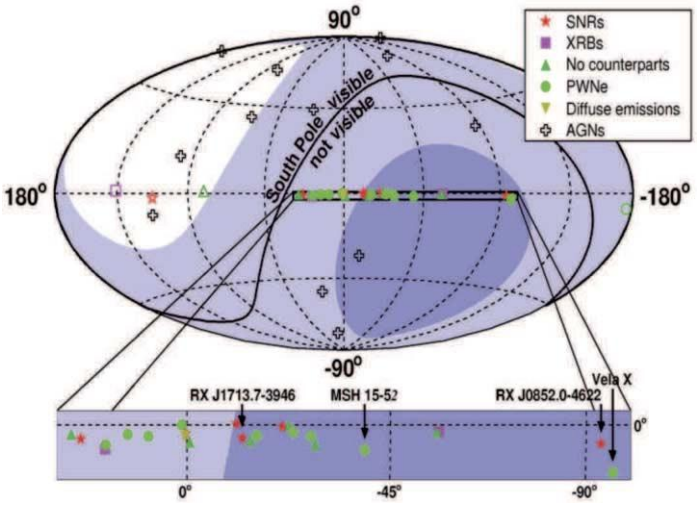

Fig. 30. – Sky visibility to up-going neutrinos for IceCube (solid line) and the one expected for KM3NeT (turquoise $>$ 18 h per day, cyan $>$ 6 hours per day). The position of a sample of identified TeV gamma sources is also shown. The insert represents a portion of the Galactic Plane.

Three candidate sites, shown in fig. 31, were proposed by the ANTARES, NEMO and NESTOR Collaborations. The site choice as well as the possibility of a multi-site option is one of the strategic issues that will be addressed in KM3NeT-PP [98].

The investigation of the possible technical solutions concerning all the aspects of the design, construction, installation and maintenance of the telescope and their impact on physics performance is a major goal of KM3NeT. Several options for photo-sensors housed in pressure-resistant glass spheres have been studied: one or two large PMTs (8″ or 10″), or several 3″ PMTs per OM.

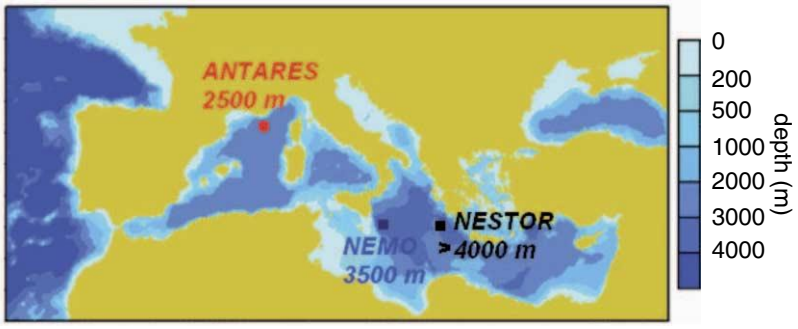

Fig. 31. – Geographic location of the three sites candidate for the installation of the Mediterranean km^3 detector.

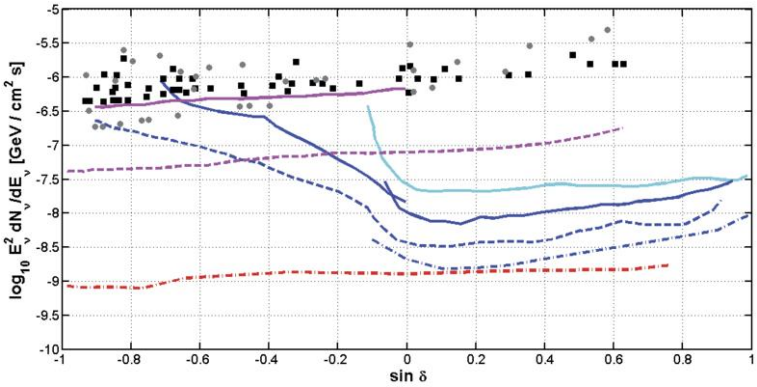

Fig. 32. – Sensitivity to E^{-2} neutrino point sources as a function of source declination for AMANDA (1387 days, cyan solid line), IC22 (276 days, blue dotted line: up-going ν, blue dash-dotted line: down-going ν), ANTARES 5 lines (magenta solid line), SuperKamiokande (dark green squares) and MACRO (light green triangles). The estimated sensitivity for IceCube (unbinned method: IC40 (1 year, blue dashed line), IC80 (1 year, blue solid line)) and the preliminary sensitivity for KM3NeT (1 year, binned method).

Following the concept of "all data to shore", all PMT signals above a given threshold (typically 1/3 of a single photo-electron) will be sent to the shore. The overall data rate will be of the order 100 Gb/s. On shore, a computer farm will perform the online filtering to reduce this rate by about 5 orders of magnitude.

Different options exist for the electronics performing the digitisation of the PMT signals and handling their transport to the shore. Due to the large path and data rates, optical fibers will be mandatory for the communication from the shore to the basis of the detection units, while the data transmission along the detection units themselves could be performed by copper wires as well as by optical fibers.

Concerning the mechanical structures, which are strongly linked to the deployment method, two major options are envisaged: detection units without horizontal extent (*strings*), and detection units with horizontally extended storeys (*towers*). The former solution can carry one multi-PMT OM per storey, or several OMs housing a single large PMT each. The latter solution, based on the principle developed by the NEMO Collaboration, is made of horizontal arms of a few meters length carrying 4 or 6 OMs each. For the deployment of NEMO-like towers, a compact configuration is deposited on the sea bed, and then an acoustic signal triggers the unfolding of the tower, under the buoyancy of a buoy at its top. The wet connections between towers and junction boxes are then performed with a Remotely Operated Vehicle. Monte Carlo simulations indicate that a telescope made of towers allows a better reconstruction of the induced muon tracks. In particular, a three-dimensional disposal of the optical module allows to solve ambiguities in the azimuthal angle [99].

Full Monte Carlo simulation for the optimisation of the telescope has been performed [100-104] and the results will be presented in TDR [98]. The sensitivity to point-like sources with E^{-2} spectrum, for the KM3NeT detector is shown in fig. 32.

The KM3NeT infrastructure will also provide interfaces for Earth and marine science instrumentation. It is foreseen that such devices are installed both in the neutrino telescope volume, if they are compatible and complementary, and in dedicated marine science nodes at some distance to the neutrino telescope to avoid adverse interferences.

6. – Ultra High Energy neutrino detection

The underwater optical Čerenkov technique is at present the most powerful tool for the investigation of astrophysical neutrino fluxes in the energy range between 1 TeV and 10 PeV. At higher energies, instead, the expected neutrino flux is so low that km^3-scale detectors are too small to detect UHE neutrino events. The distance between structures hosting optical sensor is, indeed, of the order of 100 m, due to light absorption length in water and ice. Therefore the cost of sensors, hardware, deployment and installation limits the affordable detector size to about some km^2 effective area for neutrino-induced muons, which is not enough for the detection of the expected neutrino fluxes at $E_\nu > 100$ PeV. For this reason, different, complementary techniques have been investigated with the aim of observing extremely high-energy neutrino events, *e.g.* GZK neutrinos. These techniques rely on the identification of a UHE neutrino interaction through the detection of coherent radiation (Askaryan radiation) —produced by neutrino-induced cascades— that propagates in dense media for very large distances. Hadronic showers, produced at the vertex of the UHE neutrino interaction, or electromagnetic showers, produced by e outgoing a ν_e interaction, radiate coherent radio and acoustic emissions. Radio waves have typical attenuation lengths of few km in the ice and the attenuation length for acoustic waves in the sea is also of the order of several km. Therefore, a sparse array of acoustic or radio sensors can be used to reconstruct the UHE ν interaction vertex. Observation of radio pulses from particle showers has been observed [105, 106] and the RICE [107, 108] and ANITA [109] experiments have already set strong limits on the Extremely High-energy neutrino flux (above 10^{19} eV), as shown in fig. 33.

Another method for looking at UHE neutrinos is the reconstruction of quasi-horizontal extensive atmospheric showers, initiated by CC or NC neutrino interaction in very deep atmosphere (close to ground) or looking at up-going showers in the atmosphere initiated by the decay products of an emerging (Earth-skimming) τ lepton, after the propagation and interaction of a UHE ν_τ inside the Earth [49]. The HIRES [110] and Auger data [111, 112] were also analysed looking at these kind of events and neutrino signatures were excluded. Limits form the above-mentioned experiments are reported in fig. 33.

Among all, the thermo-acoustic technique is the only one that can complement the optical Čerenkov one, in deep-sea experiments.

6˙1. *The thermo-acoustic technique.* – The thermo-acoustic technique is based on the identification of the acoustic signature induced in water by showers initiated by Extremely High Energy ν. Though the studies on this technique are still in an early stage, its potential use to build very large neutrino detectors water is appealing, thanks to the optimal properties of water as sound propagator [113].

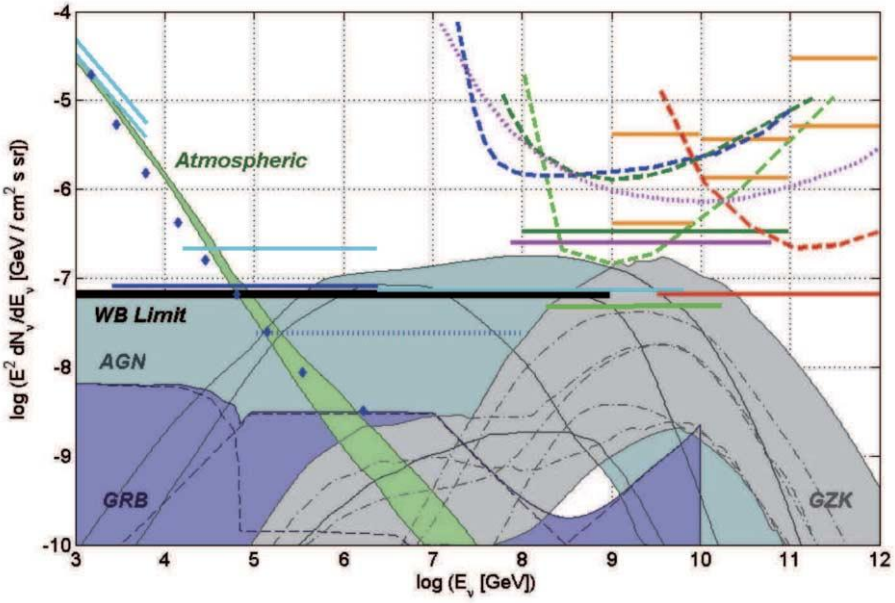

Fig. 33. – Expected HE neutrino fluxes and present limits measured by different experiments. Theoretical atmospheric neutrino flux (light green area): upper line: horizontal ν, lower line: vertical ν. Waxman Bahcall bound (black solid line). Expected cumulative AGN neutrino fluxes: the blueish area corresponds to maximal flux models. Expected GRB neutrino flux for $\Gamma = 300$ and $z = 2$: the violet area is the sum of different contribution reported in dashed lines; precursor ($E < 10^5\,\mathrm{GeV}$), prompt ($10^5\,\mathrm{GeV} < E < 10^{8.5}\,\mathrm{GeV}$), afterglow ($E > 10^{8.5}\,\mathrm{GeV}$). Expected GZK neutrino flux: the greyish area corresponds to maximal flux models. Experimental data from AMANDA-II (solid cyan line): measured ν_μ flux ($E < 10^4\,\mathrm{GeV}$), sensitivity to upgoing astrophysical ν_μ ($10^4\,\mathrm{GeV} < E < 10^{6.5}\,\mathrm{GeV}$), sensitivity to ν induced cascades ($10^{6.5}\,\mathrm{GeV} < E < 10^{10}\,\mathrm{GeV}$). Experimental data from IceCube: IC22 measured ν_μ flux (blue diamonds), sensitivity to upgoing astrophysical ν_μ (solid blue line), sensitivity to ν induced cascades (dashed blue line), expected IC80 sensitivity to astrophysical ν_μ (dotted blue line). Experimental data from RICE: sensitivity to ν-induced cascades (magenta solid line), differential sensitivity to ν-induced cascades (magenta dotted line). Experimental data from ANITA: sensitivity to ν-induced cascades (red solid line), differential sensitivity to ν-induced cascades (red dotted line). Experimental data from Auger: sensitivity to upgoing ν_τ (light green solid line) and downgoing ν (dark green solid line), differential sensitivity to ν_τ induced cascades (light green dashed line) and downgoing ν (dark green dashed line). Experimental data from HIRES: sensitivity to ν_τ (yellow solid line) and ν_e (orange solid line).

The idea of acoustic neutrino detection, first proposed by Askaryan in 1957 [114], is based on the reconstruction of hadronic and electromagnetic showers produced by neutrino interaction in dense media. As discussed above, both in the case of CC or NC interaction, the hadronic cascade carries about 25% of the neutrino's energy. In case of CC interaction of a ν_e, an e.m. shower is also produced close to the neutrino interaction vertex. The deposit of the cascade energy in a small volume of water, cylin-

drical in shape with a length L_c of few tens of metres and a few centimetres in radius r_c turns out in heating of the medium, therefore in its expansion([5]). The typical time of the energy deposition along the shower axis, almost co-linear with the neutrino direction, is of the order of $L_c/c \simeq 10^{-7}$ s, while the expansion time is of the order of $r_c/c_{\rm sound} \simeq 10^{-4}$ s. The net result is the coherent production of a mechanical wave, "pancake-shaped" propagating, in a homogeneous medium, perpendicularly to the shower axis.

Acoustic pulses from particle showers were first observed at Brookaven NL in 1979 [117], using a beam of 200 MeV protons with a total energy deposit in water of about 10^{18} eV. The pulse amplitude as a function of total energy deposition, water temperature and pressure was studied. The acoustic pulse production was recently confirmed by several experiments, using proton beams (in Uppsala and ITEP Moscow) and high-intensity laser beams (in Erlangen).

According to Learned's theoretical work [118], the acoustic pulse is bipolar, following the second time derivative of the temperature of the excited medium. The frequency spectrum of the signal is a function of the transverse spread ($r_{\rm cascade}$) of the shower, with typical maximum amplitude in the range of few tens kHz. The amplitude of the bipolar signal is proportional to the deposited energy and to the medium properties: the thermal expansion coefficient (β), the sound velocity (c_s) and the specific heat capacity (C_p). A rule of thumb to calculate the acoustic pulse amplitude at 1 metre produced by a neutrino of energy E_ν, impinging in a dense medium is

$$P_0 \simeq 0.25\ E_\nu \cdot \Gamma\ E_\nu/V_c \simeq 2\ \Gamma\ E_\nu \cdot 10^{-19} \quad [\text{Pa/eV}], \tag{8}$$

where V_c is the volume of the medium where the shower deposits its energy, the factor 0.25 is the fraction of E_ν (in units of (eV)) transferred to the shower and $\Gamma = c_s^2\beta/C_p$ is the (dimensionless) Gruneisen coefficient of the medium [119]. The Γ coefficient for deep Mediterranean Sea water is about 0.12, about a factor ten larger in polar ice and about 3.2 in compact mineral salt. Since, at frequencies of few tens kHz, acoustic pulses can travel large distances in ice, seawater and salt, these natural media can be used to build large-volume neutrino detectors instrumented with sparsely spaced arrays of acoustic sensors.

Assuming radial propagation of the sound wave and that the sound absorption length in water is $L_a^{\rm sound} \simeq 10$ km at 20 kHz, the pulse amplitude produced by a $E_\nu = 10^{20}$ eV neutrino, recorded at 1 km distance, is expected to be about 15 mPa. Ice, despite the fact that the Gruneisen coefficient is larger, suffers a stronger sound absorption ($L_a^{\rm sound} \simeq$ 300 m, at about 400 m depth) compared to water.

The energy threshold for neutrino acoustic detection is set by the ratio between ambient noise and signal.

([5]) This scenario is valid at energies below the LPM (Landau, Pomeranchuk, Migdal) effect energy regime [115, 116], $E \geq 10^{19}$ eV, that causes a strong reduction of the Bremsstrahlung and pair production cross-sections for e and γ, respectively, and, therefore, a lower energy deposit per unit of volume.

In the frequency range of interest for neutrino detection (10–40 kHz), the acoustic ambient noise amplitude in deep sea adds up about few mPa. This permits, in a first approximation, the discrimination of acoustic signals originated by neutrinos having $E_\nu > 10^{19}$ eV (assuming 1 km distance). The possibility to use time and direction coincidence can help to reduce the abient noise by at least one order of magnitude. The absolute value of noise in deep ice has not been measured yet. Present data indicate a decrease of noise amplitude as a function of depth and a Gaussian distribution of amplitudes in deep ice [120].

In both media, moreover, sound refraction must be taken into account. Sound refraction is originated by change of sound velocity in the medium as a function of depth, due to different pressure and temperature (in ice and water) and salinity (in sea water). The effect of refraction is that the expected pancake-shaped neutrino-induced wavefront becomes a hyperboloid in the real case.

Based on the previous considerations several groups have carried out simulations on future extremely large acoustic neutrino detectors. It is worth mentioning, however, that acoustic detectors can be hardly used as "telescopes", due to the poor angular accuracy of the wavefront reconstruction ($\simeq 10^\circ$).

Calculations performed by the ANTARES [121] and by the AMADEUS [122] groups indicate that a 1500 km^3-detector deployed in deep seawater, made of about 200 sensors per km^3 may reach sensitivity at the level of the WB limit for $E_\nu = 10^{20}$ eV in few years. A different result was recently presented by the ACORNE group, that simulated the response of a dense array of 1100 acoustic modules displaced in a 1 km^3 volume of seawater, anchored to the structures of a km^3 Čerenkov neutrino telescope. Sophisticated acoustic signal identification, based on matched filters, and reconstruction strategy of the acoustic wavefront geometry should allow to reach a sensitivity close to the Waxman-Bahcall limit for UHE neutrinos [123] in 10 years of data taking.

Another intriguing possibility is also to use a very large volume array of acoustic sensors both as independent detector and as a calorimeter for the (few, but almost background free) UHE neutrino events detected by the km^3 telescope. At energies greater than 10 PeV, the majority of neutrino-induced muon tracks, reconstructed by the km^3 optical telescope, are quasi-horizontal. For these events, the $\nu_\mu N \to \mu X$ interaction vertex is located several kilometers outside the telescope. Clusters of acoustic modules, displaced in a large volume around the km^3 telescope, could be able to identify the acoustic signature generated by the hadronic cascade at the ν vertex. Once the ν vertex is located, thus the muon range is reconstructed, the total energy of the muon crossing the km^3 detector can be reconstructed. Despite the fact that, for independent acoustic detection, the neutrino energy threshold is high ($E_\nu > 10^{18}$ eV), the time and arrival direction correlation between optical and acoustic signals would help to strongly lower the acoustic detection energy threshold([6]).

([6]) An improvement of about one order of magnitude is expected using the information of the sound wave arrival direction, provided by the optical detector, to reduce the acoustic signal-to-background ratio.

Thanks to the possibility to use also the optical, radio and acoustic techniques in ice, the SPATS (South Pole Acoustic Test Setup) group -aiming at R&D and tests for the construction of a large acoustic detector at the South Pole- has simulated a hybrid detector made of: 80 IceCube strings plus an external ring of 13 strings deployed in holes at 1 km distance from the centre (2.5 km deep); 91 radio/acoustic strings with a spacing of 1 km, 1.5 km deep. Monte Carlo simulations predict, for optimistic GZK neutrino flux models, 16 events per year could be seen by the acoustic detector, and 8 in coincidence with the radio detectors: that would offer the potential for cross-calibration of signals from the different technologies [124].

On the experimental side, in recent years the possibility of using hydrophones installed on military array and the infrastructures of new underwater/ice Čerenkov telescopes has permitted several experimental groups to start R&D activities on acoustic detection.

The SPATS team installed three acoustic test lines, each equipped with 7 transmitters and 7 receivers, within the IceCube detector. SPATS allowed the first studies of deep-ice acoustic properties, using calibrated pingers deployed at several depths and distances. The operation of SPATS allowed for the first time the experimental measurement of sound attenuation length and velocity in deep polar ice. Present results show that sound attenuation length in ice is about 300 m, a value much less than expected from theoretical estimates [125].

The SAUND (Study of Acoustic Ultra-high energy Neutrino Detection) collaboration uses the AUTEC naval array of wide band hydrophones deployed at $\simeq$ 1500 m depth offshore Bahamas. SAUND recorded 15 days of data reading out 6 hydrophones at the site, displaced in a $\simeq 7\,\mathrm{km}^2$ wide area and obtained the first limit of the UHE neutrino using the acoustic technique [126, 127]. In the second phase of SAUND, data from 56 hydrophones, covering an area of about $1000\,\mathrm{km}^2$ were recorded for 120 days, aiming at reaching 1 year of data acquisition. SAUND phase 2 is currently active and is also permitting a detailed characterisation of deep-sea noise as a function of frequency and direction [128].

In the framework of the activities of the ANTARES neutrino telescope, the AMADEUS (ANTARES Modules for Acoustic Detection Under the Sea) group has deployed few tens hydrophones onboard two strings. Hydrophones are both commercial piezo-ceramic hydrophones (see fig. 34), self-made piezo-ceramic hydrophones and self-made hydrophones hosted in and acoustically coupled with 17 pressure-resistant glass spheres that currently house the ANTARES PMTs. The system permitted the monitoring of deep-sea noise in the site and sound source tracking. AMADEUS could easily identify and locate signal emitted by the beacons used for the ANTARES acoustic positioning system and from biological sources [129].

The NEMO Collaboration is also conducting the first studies for acoustic neutrino detection. In 2005 the Collaboration deployed OνDE (Ocean Noise Detection Experiment) at the NEMO test site, 2000 m depth, 25 km off the coast of Sicily. OνDE, that was successfully recovered on April 2008, comprises four hydrophones arranged on a pyramidal-shaped (see fig. 34) mounting and low-cost electronics for data acquisition

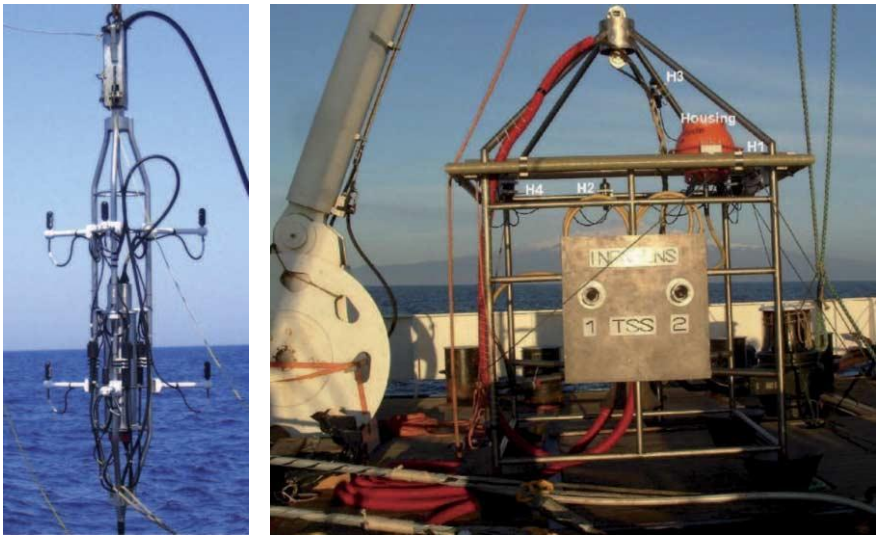

Fig. 34. – Left: an acoustic module of AMADEUS, equipped with 6 hydrophones. Right: OνDE before the deployment.

and transmission. Data (sampled at 96 kHz and with 24 bit resolution) were transmitted in real-time from deep sea and recorder on shore. Acoustic noise was studied as a function of time, weather conditions, presence of ships and biological sources, with important drawbacks in bio-acoustics [130]. Based on the experience of OνDE, the NEMO Collaboration is designing an innovative acoustic position system for the km^3 detector that will be installed on the KM3NeT *tower* prototype to be deployed in Capo Passero. The system, an array about 30 hydrophones, will be able to work both as positioning system and acoustic detector, in coincidence with the optical detector [131].

7. – Conclusions

High energy neutrino telescopes are "discovery" instruments that are expected to expand our knowledge of the High Energy Universe, revealing the source of Cosmic Rays, and the occurrence of hadronic processes in extreme astrophysical environments. An important contribution to the design and optimization of High Energy neutrino detectors comes from the results obtained VHE gamma and UHECR experiments.

In the last decade huge technological progresses have been made in this field. At South Pole, IceCube, with 59 out of 80 deployed strings and the completion expected by 2011, is about to reach the sensitivity region below the Waxman and Bahcall limit where, in the hypothesis of extragalactic proton dominance at $E > 10^{19}$ eV, neutrino signals from cosmic sources are expected to be detected.

On the other hand, after many years of activities focused to prototyping and validation of deep sea technologies, mainly undertaken by the Collaborations operating in the

Mediterranean Sea, the KM3NeT consortium is ready for the start-up of the construction phase of the km^3-scale underwater neutrino telescope in the Mediterranean.

KM3NeT will cover a large fraction (about 3.5π) of the sky, for up-going neutrinos, where RXJ1713.7-3946 and Vela Jr. are visible for more than 18 hours per day.

Great progresses have also been made also towards the detection of UHE neutrinos: an intense R&D activity is undergoing, for example, in the field of acoustic detection, that although has not yet reached the maturity level of the radio Čerenkov technique, is a promising approach that can be exploitable for the UHE neutrino detection underwater.

REFERENCES

[1] Hess V., *Phys. Z.*, **13** (1913) 1084.
[2] Gaisser T. K., *Cosmic Rays and Particle Physics* (Cambrige University Press, Cambrige) 1990.
[3] Cronin J. W., Gaisser T. K. and Swordy S. P., *Cosmic Rays at the Energy Frontier* (Scientific American) 1997.
[4] Fermi E., *Phys. Rev.*, **75** (1949) 1169.
[5] Bell A. R., *Mon. Not. R. Astron. Soc.*, **182** (1978) 147.
[6] Hillas A. M., *Annu. Rev. Astron. Astrophys.*, **22** (1984) 425.
[7] Ginzburg V. L. and Syrovatsky S. I., *Origin of Cosmic Rays* (Moscow) 1964.
[8] Butt Y., *Nature*, **460** (2009) 7256.
[9] Takeda M. *et al.*, *Phys. Rev. Lett.*, **81** (1998) 1163.
[10] Abbasi R. *et al.*, *Astroparticle Phys.*, **32** (2009) 53.
[11] Abbasi R. *et al.*, *Phys. Rev. Lett.*, **104** (2010) 161101.
[12] Abbasi R. *et al.*, *Proceedings of the 31st ICRC, Lodz, Poland* (2009) arXiv:0906.2319.
[13] Waxmann E. and Bahcall J., *Phis. Rev. Lett.*, **78** (1997) 2292.
[14] Biermann P. and Strittmatter P. A., *Astrophys. J.*, **322** (1997) 643.
[15] The Pierre Auger Collaboration, *Science*, **318** (2007) 938.
[16] Véron-Cetty M. P. and Véron P., *Astron. Astrophys.*, **455** (2006) 773.
[17] Hague J. D. for the Pierre Auger Collaboration, *Proceedings of the 31st ICRC, Lodz, Poland* (2009).
[18] Tueller J. *et al.*, *Astrophys. J. Suppl. Ser.*, **681-1** (2008) 113.
[19] Greisen K. *et al.*, *Phys. Rev. Lett.*, **16** (1966) 748.
[20] Zatsepin G. T. and Kuzmin V. A., *JETP Lett.*, **4** (1966) 78.
[21] Berezinsky V. S. and Zatsepin G. T., *Phys. Lett. B*, **28** (1969) 423.
[22] Sapienza P. and Riccobene G., *Riv. Nuovo Cimento*, **32** (2009) 591.
[23] Tanimori T. *et al.*, *Astrophys. J. Lett.*, **429** (1994) L61.
[24] de la Calle Pérez I *et al.*, *Astrophys. J.*, **599-2** (2003) 909.
[25] Aharonian F. *et al.*, *Astrophys. J.*, **539** (2000) 317.
[26] Albert J. *et al.*, *Astroparticle Phys.*, **23** (2005) 493.
[27] Aharonian. F. *et al.*, *Nature*, **432** (2000) 75.
[28] Acciari V. A. *et al.*, *Astrophys. J. Lett.*, **684** (2008) L73.
[29] Abdo A. A. *et al.*, *Phys. Rev. Lett.*, **101** (2008) 221101.
[30] Vernetto S. *et al.*, *Proceedings of the 31st ICRC, Lodz, Poland* (2009) arXiv:0908.0864.
[31] Aharonian. F., *Sceince*, **315** (2007) 70.
[32] De Angelis A. *et al.*, *Nuovo Cimento*, **31** (2008) 131.
[33] Aharonian F. *et al.*, *Astron. Astrophys.*, **477** (2008) 353.

[34] LEVINSON A. and WAXMAN E., *Phys. Rev. Lett.*, **87** (2001) 171101.
[35] DISTEFANO C. *et al.*, *Astrophys. J.*, **575** (2002) 378.
[36] COSTAMANTE L. and GHISELLINI G., *Astron. Astrophys.*, **56** (2002) 384.
[37] TIBOLLA O. for the HESS COLLABORATION, *Proceedings of the 31st ICRC, Lodz, Poland* (2009) arXiv:0907.0574v1.
[38] THE SUPERKAMIOKANDE COLLABORATION, *Phys. Rev. Lett.*, **82** (1992) 2644.
[39] WAXMAN E. and BACHALL J., *Phys. Rev. D*, **59** (1999) 023002.
[40] BATTACHARIJE P. and SIGL G., *Phys. Rep.*, **327** (2000) 109.
[41] GAISSER T. K., HALZEN F. and STANEV T., *Phys. Rep.*, **D258** (1995) 173.
[42] OKUN L., *Leptons and Quarks* (North Holland, Amsterdam) 1982.
[43] GANDHI R. *et al.*, *Phys. Rev. D*, **58** (1998) 93009.
[44] DZIEWONSKI A., *Earth Sructure in The Encyclopedia of Solid Earth Geography* (Van Nosrtand Reinhold, New York) 1989.
[45] MARKOV M. A. and ZHELEZNYKH I. M., *Nucl. Phys.*, **27** (1961) 385.
[46] ASKARYAN G. A., *JETP*, **14** (1962) 441.
[47] ASKARYAN G. A., *JETP*, **21** (1965) 658.
[48] ASKARYAN G. A. *et al.*, *Nucl. Instrum. Methods*, **164** (1979) 267.
[49] FARGION D. *et al.*, *Astrophys. J.*, **613** (2004) 1285.
[50] MOBLEY C. D., *Light and Water: radiative transfer in natural waters* (Academic Press, San Diego) 1994.
[51] ACKERMANN M. *et al.*, *J. Geophys. Res.*, **111** (2006) D13203.
[52] BAGLEY P. *et al.*, *Conceptual Design Report for a Deep-Sea Research Infrastructure Incorporating a Very Large Volume Neutrino Telescope in the Mediterranean Sea* (2008) `http://www.km3net.org/CDR/CDR-KM3NeT.pdf`.
[53] HONDA M. *et al.*, *Phys. Rev. D*, **75** (2007) 043006.
[54] AMBROSIO M. *et al.*, *Astroparticle Phys.*, **20** (2003) 145.
[55] WANG Y. *et al.*, *Nucl. Phys., B Proc. Suppl.*, **175** (2008) 551.
[56] GLADSTON L. for the ICECUBE COLLABORATION, *Proceedings of the 31st ICRC, Lodz, Poland* (2009).
[57] ROBERTS A. *et al.*, *Rev. Mod. Phys.*, **64** (1992) 259.
[58] WISCHNEWSKI R. for the BAIKAL COLLABORATION, *Int. J. Mod. Phys. A*, **20** (2005) 6932.
[59] AYUTDINOV V. for the BAIKAL COLLABORATION, *Nucl. Instrum. Methods A*, **602** (2009) 14.
[60] ANDRES E. *et al.*, *Astroparticle Phys.*, **13** (2000) 1.
[61] AHRENS J. *et al.*, *Phys. Rev. Lett.*, **90** (2003) 251101.
[62] AHRENS J. *et al.*, *Phys. Rev. Lett.*, **92** (2004) 071102.
[63] THE ICECUBE COLLABORATION, *Phys. Rev. D*, **79** (2009) 102005.
[64] SCHUKRAFT A. for the ICECUBE COLLABORATION, *Proceedings of the 31st ICRC, Lodz, Poland* (2009).
[65] GONZALEZ-GARCIA M. C. *et al.*, *JHEP*, **0610** (2006) 075.
[66] BARR G. D. *et al.*, *Phys. Rev. D*, **70** (2004) 023006.
[67] HONDA M. *et al.*, *Phys. Rev. D*, **75** (2007) 043006.
[68] THE ICECUBE COLLABORATION, *IceCube Preliminary Design Document* (2001) `http://www.icecube.wisc.edu/science/publications/pdd/pdd.pdf`.
[69] STOKSTAD R. G. for the ICECUBE COLLABORATION, *Nucl. Phys., B Proc. Suppl.*, **118** (2003) 514.
[70] WIEBUSCHV C. for the ICECUBE COLLABORATION, *Proceedings of the 31st ICRC, Lodz, Poland* (2009).

[71] Gaisser T. K. for the IceCube Collaboration, *Proceedings of the 30th ICRC, Merida, Mexico* (2007) arXiv:0711.0353.
[72] DeYoung T. for the IceCube Collaboration, *Mod. Phys. Lett. A*, **24** (2009) 1543.
[73] Karle A. for the IceCube Collaboration, *Proceedings of the 31st ICRC, Lodz, Poland* (2009).
[74] Abbasi R. for the IceCube Collaboration, *Astrophys. J. Lett.*, **701** (2009) L47.
[75] Kappes A. for the IceCube Collaboration, *Proceedings of the 31st ICRC, Lodz, Poland* (2009).
[76] Sakamoto T. *et al.*, *Astrophys. J. Suppl.*, **175** (2009) 179.
[77] Resvanis L. K. for the NESTOR Collaboration, *Proceedings of NOVE, Venice, Italy* (2006).
[78] Stanley D. J. *et al.*, *Nature*, **273** (1978) 110.
[79] Le Pinchon X. *et al.*, *Geol. Soc., Special Publ.*, **10** (1982) 319.
[80] Anassontis E. G. for the NESTOR Collaboration, *Nucl. Instrum. Methods A*, **479** (2002) 439.
[81] Rapidis P. for the NESTOR Collaboration, *Nucl. Instrum. Methods A*, **602** (2009) 54.
[82] Aggouras G. for the NESTOR Collaboration, *Astroparticle Phys.*, **23** (2005) 377.
[83] Circella M. for the ANTARES Collaboration, *Nucl. Instrum. Methods A*, **602** (2009) 2.
[84] Vallage B. for the ANTARES Collaboration, *Nucl. Phys. B*, **151** (2006) 407.
[85] Montaruli T. for the ANTARES Collaboration, *Int. J. Mod. Phys. A*, **24** (2009) 1656.
[86] Heijboer A. for the ANTARES Collaboration, *Proceedings of the 31st ICRC, Lodz, Poland* (2009) arXiv:0908.0816.
[87] Toscano S. for the ANTARES Collaboration, *Proceedings of the 31st ICRC, Lodz, Poland* (2009) arXiv:0908.0864.
[88] Ambrosio M. *et al.*, *Astrophys. J.*, **564** (2001) 1038.
[89] Abe K. *et al.*, *Astrophys. J.*, **652** (2006) 198.
[90] Migneco E. *et al.*, *Nucl. Instrum. Methods A*, **588** (2008) 111.
[91] Riccobene G. *et al.*, *Astroparticle Phys.*, **27** (2007) 1.
[92] Capone A. *et al.*, *Nucl. Instrum. Methods A*, **602** (2009) 47.
[93] Ameli F. *et al.*, *IEEE Trans. Nucl. Sci.*, **55** (2008) 233.
[94] Aiello S. *et al.*, arXiv:0910.1269 (2009).
[95] Katz U. F. *et al.*, *Nucl. Instrum. Methods A*, **602** (2009) 40.
[96] Aharonian F. *et al.*, *Astron. Astrophys.*, **503** (2009) 817.
[97] Eckart A. *et al.*, *J. Phys.: Conf. Ser.*, **131** (2008) 012002.
[98] `http://www.km3net.org/CDR/CDR-KM3NeT.pdf`.
[99] Coniglione R. *et al.*, *Nucl. Instrum. Methods A*, **602** (2009) 98.
[100] Sapienza P. *et al.*, *Nucl. Instrum. Methods A*, **602** (2009) 101.
[101] Vannoni G. *et al.*, *Proceedings of VLVnT09 Athens, Greece*, to be published in *Nucl. Instrum. Methods A*.
[102] Sapienza P. *et al.*, *Proceedings of VLVnT09 Athens, Greece*, to be published in *Nucl. Instrum. Methods A*.
[103] Kopper C. *et al.*, *Proceedings of VLVnT09 Athens, Greece*, to be published in *Nucl. Instrum. Methods A*.
[104] Coniglione R. *et al.*, *Proceedings of VLVnT09 Athens, Greece*, to be published in *Nucl. Instrum. Methods A*.
[105] Saltzberg D. *et al.*, *Phys. Rev. Lett.*, **86** (2001) 2802.
[106] Gorham P. W. *et al.*, *Phys. Rev. D*, **72** (2004) 023002.

[107] HOGAN D. P. *et al.*, *Phys. Rev. D*, **78** (2008) 075031.
[108] BESSON D. Z., *Astroparticle Phys.*, **19** (2003) 15.
[109] GORHAM P. W. *et al.*, *Phys. Rev. Lett.*, **103** (2009) 051103.
[110] ABBASI R. U. *et al.*, *Astrophys. J*, **684** (2008) 790.
[111] THE P. AUGER COLLABORATION, *Phys. Rev. Lett.*, **100** (2008) 211101.
[112] THE P. AUGER COLLABORATION, *Proceedings of the 31st ICRC, Lodz, Poland* (2009).
[113] RICCOBENE G., *J. Phys.: Conf. Ser.*, **136** (2008) 022053.
[114] ASKARYAN G. A., *Atom. Ener.*, **3** (1957) 153.
[115] LANDAU L. D. and POMERANCHUK I. J., *Dokl. Akad. Nauk. SSSR*, **92** (1953) 535.
[116] MIGDAL A. B., *Phys. Rev.*, **103** (1956) 1811.
[117] SULAK L. *et al.*, *Nucl. Instrum. Methods*, **161** (1979) 203.
[118] LEARNED J. G., *Phys. Rev. D*, **19** (1979) 3293.
[119] URICK R. J., *Sound Propagation in the Sea* (Peninsula Publishing) 1982.
[120] DESCAMPS F. *et al.*, *Proceedings of the 31st ICRC, Lodz, Poland* (2009) arXiv:0908.3251.
[121] NIESS V. and BERTIN V., *Astroparticle Phys.*, **28** (2007) 366.
[122] KARG T. *et al.*, *J. Mod. Phys. Int.*, **A1S1** (2006) 212.
[123] PERKIN J. *et al.*, *Nucl. Instrum. Methods A*, **604-1S** (2009) S193.
[124] VANDENBROUCKE J. *et al.*, *Nucl. Instrum. Methods A*, **604-1S** (2009) S164.
[125] DESCAMPS F. *et al.*, *Nucl. Instrum. Methods A*, **604-1S** (2009) S175.
[126] LETHINEN N. G. *et al.*, *Astroparticle Phys.*, **17** (2002) 279.
[127] VANDENBROUCKE J. *et al.*, *Astrophys. J.*, **612** (2005) 301.
[128] KURAHASHI N. *et al.*, *Nucl. Instrum. Methods A*, **604-1S** (2009) S127.
[129] LAHMAN R. *et al.*, *Nucl. Instrum. Methods A*, **604-1S** (2009) S158.
[130] NOSENGO N., *Nature*, **462** (2009) 560.
[131] RICCOBENE G. *et al.*, *Nucl. Instrum. Methods A*, **604-1S** (2009) S149.

This page intentionally left blank

International School of Physics "Enrico Fermi"

Villa Monastero, Varenna

Course CLXXV

20–25 July 2009

"Radiation and Particle Detectors"

Directors

Sergio BERTOLUCCI
CERN
CH-1211 Genève 23
Switzerland
tel.: ++41-22-7671440
fax: ++41-22-7676555
Sergio.Bertolucci@lnf.infn.it

Ubaldo BOTTIGLI
Dipartimento di Fisica
Università di Siena
Via Roma 56
53100 Siena
Italy
tel.: ++39-0577-234670
fax: ++390577-234689
bottigli@unisi.it

Scientific Secretary

Piernicola OLIVA
Struttura Dipartimentale
di Matematica e Fisica
Università di Sassari
Via Vienna 2
07100 Sassari
Italy
tel.: ++39-079-229484
fax: ++39-079-229482
oliva@df.unipi.it

Lecturers

M. Giuseppina BISOGNI
Dipartimento di Fisica
Università di Pisa
Largo B. Pontecorvo 3
56127 Pisa
Italy
tel.: ++39-050-2214240
fax: ++39-050-2214317
bisogni@pi.infn.it

Pablo CIRRONE
INFN, Laboratori Nazionali del Sud
Via Santa Sofia 46
95123 Catania
Italy
tel.: ++39-095-542294
fax: ++39-095-542294
cirrone@lns.infn.it

Gabriella GAUDIO
INFN, Sezione di Pavia
Via Bassi 6
27100 Pavia
tel.: ++39-0382-987324
fax: ++39-0382-423241
gabriella.gaudio@pv.infn.it

Julien MARQUE
European Gravitational Observatory
Via E. Amaldi
56021 S. Stefano a Macerata-Cascina (PI)
Italy
tel.: ++39-050-752543
fax: ++39-050-752550
julien.marque@ego-gw.it

PierAndrea MANDÒ
Dipartimento di Fisica
Università di Firenze
Via Sansone 1
50019 Sesto Fiorentino (FI)
Italy
tel.: ++39-055-4572707
fax: ++39-055-4572121
mando@fi.infn.it

Giorgio RICCOBENE
INFN, Laboratori Nazionali del Sud
Via S. Sofia 62
95123 Catania
Italy
tel.: ++39-095-3785404
riccobene@lns.infn.it

Martijn MULDERS
CERN
CH-1211 Genève 23
Switzerland
tel.: ++41-22-7673635
fax: ++41-22-7678940
mulders@mail.cern.ch

Arnaldo STEFANINI
Dipartimento di Fisica
Università di Pisa
Largo B. Pontecorvo 3
I-56127 Pisa
Italy
tel.: ++39-050-2214879
fax: ++39-050-2214317
stefanini@df.unipi.it

Andrea VACCHI
INFN, Sezione di Trieste
Via Valerio 2
34127 Trieste
Italy
tel.: ++39-040-3756229
fax: ++39-040-5583350
Andrea.Vacchi@ts.infn.it

Students

Andrea AGOSTINELLI
Dipartimento di Fisica
Università di Bologna
Via Irnerio 46
40126 Bologna
Italy
andrea.agostinelli@hotmail.it

Fauzia ALBERTIN
Dipartimento di Fisica
Università di Ferrara
Via Saragat 1
44100 Ferrara
Italy
tel.: ++39-0532-974637
fax: ++39-0532-974210
albertin@fe.infn.it

Paolo ALLEGRINI
Dipartimento di Ingegneria Elettronica
Università di Roma Tre
Via Della Vasca Navale 84
00146 Roma
Italy
tel.: ++39-06-57337201
fax: ++39-06-57337101
pallegrini@uniroma3.it

Francesca BELLINI
Dipartimento di Fisica
Università di Bologna
Via Irnerio 46
40126 Bologna
Italy
tel.: ++39-051-2091152
francesca.bellini09@gmail.com

Paolo BENNATI
Edemom Phd School
Università di Roma Tre
Via Della Vasca Navale 84
00146 Roma
Italy
tel.: ++39-06-57337261
fax: ++39-06-57337059
paolo.bennati@uniroma3.it

Davide CAFFARRI
Università di Padova
Via Marzolo 8
35131 Padova
Italy
tel.: ++39-049-8277106
caffarri@pd.infn.it

Lucia CAFORIO
Labec - INFN, Sezione di Firenze
Via B. Rossi
50019 Sesto Fiorentino (FI)
Italy
tel.: ++39-055-4572647
fax: ++39-055-4572641
caforio@fi.infn.it

Viviana CAVALIERE
INFN, Sezione di Pisa
Largo B. Pontecorvo 3
56127 Pisa
Italy
viviana.cavaliere@pi.infn.it

Angelo DI CANTO
INFN, Sezione di Pisa
Largo B. Pontecorvo 3
56127 Pisa
Italy
angelo.dicanto@pi.infn.it

Marco ENDRIZZI
INFN, Sezione di Pisa
Largo B. Pontecorvo 3
56127 Pisa
Italy
tel.: 0502214000
fax: 0502214317
endrizzi@pi.infn.it

Daniele FASANELLA
INFN, Sezione di Bologna
Viale Berti Pichat 6/2
40127 Bologna
Italy
tel.: ++39-051-2095227
daniele.fasanella@bo.infn.it

Paola GAROSI
INFN, Sezione di Pisa
Largo B. Pontecorvo 3
56127 Pisa
Italy
paola.garosi@pi.infn.it

Barbara GUERZONI
INFN, Sezione di Bologna
Viale Berti Pichat 6/2
40127 Bologna
Italy
tel.: ++39-051-2091103
barbara.guerzoni@bo.infn.it

Emine GURPINAR
Faculty of Sciences and Letters
Department of Physics
Cukurova University
Balcal Kampüsü
TR-01330 Sarçam, Adana
Turkey
tel.: ++90-3223386084
fax: ++90-3223386070
emine.gurpinar@cern.ch

Alexandra JUNKES
Institut für Experimentalphysik
Universität Hamburg
Luruper Chaussee 149
Desy Bldg 67 B
D-22761 Hamburg
Germany
tel.: ++49-4089984728
fax: ++49-4089982959
alexandra.junkes@desy.de

Jörn LANGE
Institut für Experimentalphysik
Universität Hamburg
Luruper Chaussee 149
D-22761 Hamburg
Germany
tel.: ++49-4089984725
joern.lange@desy.de

Massimo NOCENTE
Dipartimento di Fisica "G. Occhialini"
Università di Milano-Bicocca
Piazza Della Scienza 3
20126 Milano
Italy
tel.: ++39-02-64482326
fax: ++39-02-64482367
massimo.nocente@mib.infn.it

Giovanni SABATINO
INFN, Laboratori Nazionali di Frascati
Via E. Fermi 40
00044 Frascati (RM)
Italy
giovanni.sabatino@roma2.infn.it

Federico SFORZA
INFN, Sezione di Pisa
Largo B. Pontecorvo 3
56127 Pisa
Italy
sforza@pi.infn.it

Maria Vittoria SICILIANO
Dipartimento di Scienze dei Materiali
Università del Salento
Via Per Arnesano
73100 Lecce
Italy
tel.: ++39-083-2297554
fax: ++39-083-2297482
maria.vittoria.siciliano@le.infn.it

Melinda SICILIANO
Università di Torino
Via Pietro Giuria 1
10125 Torino
Italy
tel.: ++39-011-6707046
melinda.siciliano@unito.it

Alessandro SILENZI
Dipartimento di Fisica
Università di Bologna
Via Irnerio 46
40126 Bologna
Italy
tel.: ++39-051-2091009
silenzi@bo.infn.it

Lawrence SOUNG YEE
Center For Particle Physics
and Phenomenology (Cp3)
Chemin Du Cyclotron 2
B-1348 Louvain-La-Neuve
Belgium
tel.: ++32-10472994
fax: ++32-10452183
lawrence.soungyee@uclouvain.be

Luciano VELARDI
Dipartimento di Fisica
Università di Bari
Via Amendola 173
70126 Bari
Italy
tel.: ++39-080-5443190/2450
luciano.velardi@le.infn.it

Giacomo VOLPE
Università di Bari
INFN, Sezione di Bari
Via Orabona 4
70126 Bari
Italy
tel.: ++39-080-5442531
giacomo.volpe@ba.infn.it

Observers

Matteo BETTUZZI
Dipartimento di Fisica
Università di Bologna
Viale Berti Pichat 6/2
40127 Bologna
Italy
tel.: ++39-051-2095098
fax: ++39-051-2094057
matteo.bettuzzi@unibo.it

Daniele LATTANZI
ENEA–FNP/FUSTEC
Centro Ricerche Frascati
Via E. Fermi 45
00044 Frascati (RM)
Italy
tel.: ++39-06-94005150
daniele.lattanzi@frascati.enea.it

Sonia TANGARO
INFN, Sezione di Bari
Via Amendola 173
70126 Bari
Italy
tel.: ++39-080-5442370
sonia.tangaro@ba.infn.it

This page intentionally left blank

PROCEEDINGS OF THE INTERNATIONAL SCHOOL OF PHYSICS "ENRICO FERMI"

Course I (1953)
Questioni relative alla rivelazione delle particelle elementari, con particolare riguardo alla radiazione cosmica
edited by G. Puppi

Course II (1954)
Questioni relative alla rivelazione delle particelle elementari, e alle loro interazioni con particolare riguardo alle particelle artificialmente prodotte ed accelerate
edited by G. Puppi

Course III (1955)
Questioni di struttura nucleare e dei processi nucleari alle basse energie
edited by C. Salvetti

Course IV (1956)
Proprietà magnetiche della materia
edited by L. Giulotto

Course V (1957)
Fisica dello stato solido
edited by F. Fumi

Course VI (1958)
Fisica del plasma e relative applicazioni astrofisiche
edited by G. Righini

Course VII (1958)
Teoria della informazione
edited by E. R. Caianiello

Course VIII (1958)
Problemi matematici della teoria quantistica delle particelle e dei campi
edited by A. Borsellino

Course IX (1958)
Fisica dei pioni
edited by B. Touschek

Course X (1959)
Thermodynamics of Irreversible Processes
edited by S. R. de Groot

Course XI (1959)
Weak Interactions
edited by L. A. Radicati

Course XII (1959)
Solar Radioastronomy
edited by G. Righini

Course XIII (1959)
Physics of Plasma: Experiments and Techniques
edited by H. Alfvén

Course XIV (1960)
Ergodic Theories
edited by P. Caldirola

Course XV (1960)
Nuclear Spectroscopy
edited by G. Racah

Course XVI (1960)
Physicomathematical Aspects of Biology
edited by N. Rashevsky

Course XVII (1960)
Topics of Radiofrequency Spectroscopy
edited by A. Gozzini

Course XVIII (1960)
Physics of Solids (Radiation Damage in Solids)
edited by D. S. Billington

Course XIX (1961)
Cosmic Rays, Solar Particles and Space Research
edited by B. Peters

Course XX (1961)
Evidence for Gravitational Theories
edited by C. Møller

Course XXI (1961)
Liquid Helium
edited by G. Careri

Course XXII (1961)
Semiconductors
edited by R. A. Smith

Course XXIII (1961)
Nuclear Physics
edited by V. F. Weisskopf

Course XXIV (1962)
Space Exploration and the Solar System
edited by B. Rossi

Course XXV (1962)
Advanced Plasma Theory
edited by M. N. Rosenbluth

Course XXVI (1962)
Selected Topics on Elementary Particle Physics
edited by M. Conversi

Course XXVII (1962)
Dispersion and Absorption of Sound by Molecular Processes
edited by D. Sette

Course XXVIII (1962)
Star Evolution
edited by L. Gratton

Course XXIX (1963)
Dispersion Relations and their Connection with Casuality
edited by E. P. Wigner

Course XXX (1963)
Radiation Dosimetry
edited by F. W. Spiers and G. W. Reed

Course XXXI (1963)
Quantum Electronics and Coherent Light
edited by C. H. Townes and P. A. Miles

Course XXXII (1964)
Weak Interactions and High-Energy Neutrino Physics
edited by T. D. Lee

Course XXXIII (1964)
Strong Interactions
edited by L. W. Alvarez

Course XXXIV (1965)
The Optical Properties of Solids
edited by J. Tauc

Course XXXV (1965)
High-Energy Astrophysics
edited by L. Gratton

Course XXXVI (1965)
Many-body Description of Nuclear Structure and Reactions
edited by C. L. Bloch

Course XXXVII (1966)
Theory of Magnetism in Transition Metals
edited by W. Marshall

Course XXXVIII (1966)
Interaction of High-Energy Particles with Nuclei
edited by T. E. O. Ericson

Course XXXIX (1966)
Plasma Astrophysics
edited by P. A. Sturrock

Course XL (1967)
Nuclear Structure and Nuclear Reactions
edited by M. Jean and R. A. Ricci

Course XLI (1967)
Selected Topics in Particle Physics
edited by J. Steinberger

Course XLII (1967)
Quantum Optics
edited by R. J. Glauber

Course XLIII (1968)
Processing of Optical Data by Organisms and by Machines
edited by W. Reichardt

Course XLIV (1968)
Molecular Beams and Reaction Kinetics
edited by Ch. Schlier

Course XLV (1968)
Local Quantum Theory
edited by R. Jost

Course XLVI (1969)
Physics with Intersecting Storage Rings
edited by B. Touschek

Course XLVII (1969)
General Relativity and Cosmology
edited by R. K. Sachs

Course XLVIII (1969)
Physics of High Energy Density
edited by P. Caldirola and H. Knoepfel

Course IL (1970)
Foundations of Quantum Mechanics
edited by B. d'Espagnat

Course L (1970)
Mantle and Core in Planetary Physics
edited by J. Coulomb and M. Caputo

Course LI (1970)
Critical Phenomena
edited by M. S. Green

Course LII (1971)
Atomic Structure and Properties of Solids
edited by E. Burstein

Course LIII (1971)
Developments and Borderlines of Nuclear Physics
edited by H. Morinaga

Course LIV (1971)
Developments in High-Energy Physics
edited by R. R. Gatto

Course LV (1972)
Lattice Dynamics and Intermolecular Forces
edited by S. Califano

Course LVI (1972)
Experimental Gravitation
edited by B. Bertotti

Course LVII (1972)
History of 20th Century Physics
edited by C. Weiner

Course LVIII (1973)
Dynamics Aspects of Surface Physics
edited by F. O. Goodman

Course LIX (1973)
Local Properties at Phase Transitions
edited by K. A. Müller and A. Rigamonti

Course LX (1973)
C*-Algebras and their Applications to Statistical Mechanics and Quantum Field Theory
edited by D. Kastler

Course LXI (1974)
Atomic Structure and Mechanical Properties of Metals
edited by G. Caglioti

Course LXII (1974)
Nuclear Spectroscopy and Nuclear Reactions with Heavy Ions
edited by H. Faraggi and R. A. Ricci

Course LXIII (1974)
New Directions in Physical Acoustics
edited by D. Sette

Course LXIV (1975)
Nonlinear Spectroscopy
edited by N. Bloembergen

Course LXV (1975)
Physics and Astrophysics of Neutron Stars and Black Hole
edited by R. Giacconi and R. Ruffini

Course LXVI (1975)
Health and Medical Physics
edited by J. Baarli

Course LXVII (1976)
Isolated Gravitating Systems in General Relativity
edited by J. Ehlers

Course LXVIII (1976)
Metrology and Fundamental Constants
edited by A. Ferro Milone, P. Giacomo and S. Leschiutta

Course LXIX (1976)
Elementary Modes of Excitation in Nuclei
edited by A. Bohr and R. A. Broglia

Course LXX (1977)
Physics of Magnetic Garnets
edited by A. Paoletti

Course LXXI (1977)
Weak Interactions
edited by M. Baldo Ceolin

Course LXXII (1977)
Problems in the Foundations of Physics
edited by G. Toraldo di Francia

Course LXXIII (1978)
Early Solar System Processes and the Present Solar System
edited by D. Lal

Course LXXIV (1978)
Development of High-Power Lasers and their Applications
edited by C. Pellegrini

Course LXXV (1978)
Intermolecular Spectroscopy and Dynamical Properties of Dense Systems
edited by J. Van Kranendonk

Course LXXVI (1979)
Medical Physics
edited by J. R. Greening

Course LXXVII (1979)
Nuclear Structure and Heavy-Ion Collisions
edited by R. A. Broglia, R. A. Ricci and C. H. Dasso

Course LXXVIII (1979)
Physics of the Earth's Interior
edited by A. M. Dziewonski and E. Boschi

Course LXXIX (1980)
From Nuclei to Particles
edited by A. Molinari

Course LXXX (1980)
Topics in Ocean Physics
edited by A. R. Osborne and P. Malanotte Rizzoli

Course LXXXI (1980)
Theory of Fundamental Interactions
edited by G. Costa and R. R. Gatto

Course LXXXII (1981)
Mechanical and Thermal Behaviour of Metallic Materials
edited by G. Caglioti and A. Ferro Milone

Course LXXXIII (1981)
Positrons in Solids
edited by W. Brandt and A. Dupasquier

Course LXXXIV (1981)
Data Acquisition in High-Energy Physics
edited by G. Bologna and M. Vincelli

Course LXXXV (1982)
Earthquakes: Observation, Theory and Interpretation
edited by H. Kanamori and E. Boschi

Course LXXXVI (1982)
Gamow Cosmology
edited by F. Melchiorri and R. Ruffini

Course LXXXVII (1982)
Nuclear Structure and Heavy-Ion Dynamics
edited by L. Moretto and R. A. Ricci

Course LXXXVIII (1983)
Turbulence and Predictability in Geophysical Fluid Dynamics and Climate Dynamics
edited by M. Ghil, R. Benzi and G. Parisi

Course LXXXIX (1983)
Highlights of Condensed Matter Theory
edited by F. Bassani, F. Fumi and M. P. Tosi

Course XC (1983)
Physics of Amphiphiles: Micelles, Vesicles and Microemulsions
edited by V. Degiorgio and M. Corti

Course XCI (1984)
From Nuclei to Stars
edited by A. Molinari and R. A. Ricci

Course XCII (1984)
Elementary Particles
edited by N. Cabibbo

Course XCIII (1984)
Frontiers in Physical Acoustics
edited by D. Sette

Course XCIV (1984)
Theory of Reliability
edited by A. Serra and R. E. Barlow

Course XCV (1985)
Solar-Terrestrial Relationship and the Earth Environment in the Last Millennia
edited by G. Cini Castagnoli

Course XCVI (1985)
Excited-State Spectroscopy in Solids
edited by U. M. Grassano and N. Terzi

Course XCVII (1985)
Molecular-Dynamics Simulations of Statistical-Mechanical Systems
edited by G. Ciccotti and W. G. Hoover

Course XCVIII (1985)
The Evolution of Small Bodies in the Solar System
edited by M. Fulchignoni and Ľ. Kresàk

Course XCIX (1986)
Synergetics and Dynamic Instabilities
edited by G. Caglioti and H. Haken

Course C (1986)
The Physics of NMR Spectroscopy in Biology and Medicine
edited by B. Maraviglia

Course CI (1986)
Evolution of Interstellar Dust and Related Topics
edited by A. Bonetti and J. M. Greenberg

Course CII (1986)
Accelerated Life Testing and Experts' Opinions in Reliability
edited by C. A. Clarotti and D. V. Lindley

Course CIII (1987)
Trends in Nuclear Physics
edited by P. Kienle, R. A. Ricci and A. Rubbino

Course CIV (1987)
Frontiers and Borderlines in Many-Particle Physics
edited by R. A. Broglia and J. R. Schrieffer

Course CV (1987)
Confrontation between Theories and Observations in Cosmology: Present Status and Future Programmes
edited by J. Audouze and F. Melchiorri

Course CVI (1988)
Current Trends in the Physics of Materials
edited by G. F. Chiarotti, F. Fumi and M. Tosi

Course CVII (1988)
The Chemical Physics of Atomic and Molecular Clusters
edited by G. Scoles

Course CVIII (1988)
Photoemission and Absorption Spectroscopy of Solids and Interfaces with Synchrotron Radiation
edited by M. Campagna and R. Rosei

Course CIX (1988)
Nonlinear Topics in Ocean Physics
edited by A. R. Osborne

Course CX (1989)
Metrology at the Frontiers of Physics and Technology
edited by L. Crovini and T. J. Quinn

Course CXI (1989)
Solid-State Astrophysics
edited by E. Bussoletti and G. Strazzulla

Course CXII (1989)
Nuclear Collisions from the Mean-Field into the Fragmentation Regime
edited by C. Detraz and P. Kienle

Course CXIII (1989)
High-Pressure Equation of State: Theory and Applications
edited by S. Eliezer and R. A. Ricci

Course CXIV (1990)
Industrial and Technological Applications of Neutrons
edited by M. Fontana and F. Rustichelli

Course CXV (1990)
The Use of EOS for Studies of Atmospheric Physics
edited by J. C. Gille and G. Visconti

Course CXVI (1990)
Status and Perspectives of Nuclear Energy: Fission and Fusion
edited by R. A. Ricci, C. Salvetti and E. Sindoni

Course CXVII (1991)
Semiconductor Superlattices and Interfaces
edited by A. Stella

Course CXVIII (1991)
Laser Manipulation of Atoms and Ions
edited by E. Arimondo, W. D. Phillips and F. Strumia

Course CXIX (1991)
Quantum Chaos
edited by G. Casati, I. Guarneri and U. Smilansky

Course CXX (1992)
Frontiers in Laser Spectroscopy
edited by T. W. Hänsch and M. Inguscio

Course CXXI (1992)
Perspectives in Many-Particle Physics
edited by R. A. Broglia, J. R. Schrieffer and P. F. Bortignon

Course CXXII (1992)
Galaxy Formation
edited by J. Silk and N. Vittorio

Course CXXIII (1992)
Nuclear Magnetic Double Resonsonance
edited by B. Maraviglia

Course CXXIV (1993)
Diagnostic Tools in Atmospheric Physics
edited by G. Fiocco and G. Visconti

Course CXXV (1993)
Positron Spectroscopy of Solids
edited by A. Dupasquier and A. P. Mills jr.

Course CXXVI (1993)
Nonlinear Optical Materials: Principles and Applications
edited by V. Degiorgio and C. Flytzanis

Course CXXVII (1994)
Quantum Groups and their Applications in Physics
edited by L. Castellani and J. Wess

Course CXXVIII (1994)
Biomedical Applications of Synchrotron Radiation
edited by E. Burattini and A. Balerna

Course CXXIX[1] (1994)
Observation, Prediction and Simulation of Phase Transitions in Complex Fluids
edited by M. Baus, L. F. Rull and J. P. Ryckaert

Course CXXX (1995)
Selected Topics in Nonperturbative QCD
edited by A. Di Giacomo and D. Diakonov

Course CXXXI (1995)
Coherent and Collective Interactions of Particles and Radiation Beams
edited by A. Aspect, W. Barletta and R. Bonifacio

Course CXXXII (1995)
Dark Matter in the Universe
edited by S. Bonometto and J. Primack

Course CXXXIII (1996)
Past and Present Variability of the Solar-Terrestrial System: Measurement, Data Analysis and Theoretical Models
edited by G. Cini Castagnoli and A. Provenzale

Course CXXXIV (1996)
The Physics of Complex Systems
edited by F. Mallamace and H. E. Stanley

Course CXXXV (1996)
The Physics of Diamond
edited by A. Paoletti and A. Tucciarone

Course CXXXVI (1997)
Models and Phenomenology for Conventional and High-Temperature Superconductivity
edited by G. Iadonisi, J. R. Schrieffer and M. L. Chiofalo

Course CXXXVII (1997)
Heavy Flavour Physics: a Probe of Nature's Grand Design
edited by I. Bigi and L. Moroni

Course CXXXVIII (1997)
Unfolding the Matter of Nuclei
edited by A. Molinari and R. A. Ricci

Course CXXXIX (1998)
Magnetic Resonance and Brain Function: Approaches from Physics
edited by B. Maraviglia

Course CXL (1998)
Bose-Einstein Condensation in Atomic Gases
edited by M. Inguscio, S. Stringari and C. E. Wieman

Course CXLI (1998)
Silicon-Based Microphotonics: from Basics to Applications
edited by O. Bisi, S. U. Campisano, L. Pavesi and F. Priolo

[1] This course belongs to the NATO ASI Series C, Vol. 460 (Kluwer Academic Publishers).

Course CXLII (1999)
Plasmas in the Universe
edited by B. Coppi, A. Ferrari and E. Sindoni

Course CXLIII (1999)
New Directions in Quantum Chaos
edited by G. Casati, I. Guarneri and U. Smilansky

Course CXLIV (2000)
Nanometer Scale Science and Technology
edited by M. Allegrini, N. García and O. Marti

Course CXLV (2000)
Protein Folding, Evolution and Design
edited by R. A. Broglia, E. I. Shakhnovich and G. Tiana

Course CXLVI (2000)
Recent Advances in Metrology and Fundamental Constants
edited by T. J. Quinn, S. Leschiutta and P. Tavella

Course CXLVII (2001)
High Pressure Phenomena
edited by R. J. Hemley, G. L. Chiarotti, M. Bernasconi and L. Ulivi

Course CXLVIII (2001)
Experimental Quantum Computation and Information
edited by F. De Martini and C. Monroe

Course CXLIX (2001)
Organic Nanostructures: Science and Applications
edited by V. M. Agranovich and G. C. La Rocca

Course CL (2002)
Electron and Photon Confinement in Semiconductor Nanostructures
edited by B. Deveaud-Plédran, A. Quattropani and P. Schwendimann

Course CLI (2002)
Quantum Phenomena in Mesoscopic Systems
edited by B. Altshuler, A. Tagliacozzo and V. Tognetti

Course CLII (2002)
Neutrino Physics
edited by E. Bellotti, Y. Declais and P. Strolin

Course CLIII (2002)
From Nuclei and their Constituents to Stars
edited by A. Molinari, L. Riccati, W. M. Alberico and M. Morando

Course CLIV (2003)
Physics Methods in Archaeometry
edited by M. Martini, M. Milazzo and M. Piacentini

Course CLV (2003)
The Physics of Complex Systems (New Advances and Perspectives)
edited by F. Mallamace and H. E. Stanley

Course CLVI (2003)
Research on Physics Education
edited by E.F. Redish and M. Vicentini

Course CLVII (2003)
The Electron Liquid Model in Condensed Matter Physics
edited by G. F. Giuliani and G. Vignale

Course CLVIII (2004)
Hadron Physics
edited by T. Bressani, U. Wiedner and A. Filippi

Course CLIX (2004)
Background Microwave Radiation and Intracluster Cosmology
edited by F. Melchiorri and Y. Rephaeli

Course CLX (2004)
From Nanostructures to Nanosensing Applications
edited by A. D'Amico, G. Balestrino and A. Paoletti

Course CLXI (2005)
Polarons in Bulk Materials and Systems with Reduced Dimensionality
edited by G. Iadonisi, J. Ranninger and G. De Filippis

Course CLXII (2005)
Quantum Computers, Algorithms and Chaos
edited by G. Casati, D. L. Shepelyansky, P. Zoller and G. Benenti

Course CLXIII (2005)
CP Violation: From Quarks to Leptons
edited by M. Giorgi, I. Mannelli, A. I. Sanda, F. Costantini and M. S. Sozzi

Course CLXIV (2006)
Ultra-Cold Fermi Gases
edited by M. Inguscio, W. Ketterle and C. Salomon

Course CLXV (2006)
Protein Folding and Drug Design
edited by R. A. Broglia, L. Serrano and G. Tiana

Course CLXVI (2006)
Metrology and Fundamental Constants
edited by T. W. Hänsch, S. Leschiutta, A. J. Wallard and M. L. Rastello

Course CLXVII (2007)
Strangeness and Spin in Fundamental Physics
edited by M. Anselmino, T. Bressani, A. Feliciello and Ph. G. Ratcliffe

Course CLXVIII (2007)
Atom Optics and Space Physics
edited by E. Arimondo, W. Ertmer, W. P. Schleich and E. M. Rasel

Course CLXIX (2007)
Nuclear Structure far from Stability: New Physics and New Technology
edited by A. Covello, F. Iachello, R. A. Ricci and G. Maino

Course CLXX (2008)
Measurements of Neutrino Mass
edited by F. Ferroni, F. Vissani and C. Brofferio

Course CLXXI (2008)
Quantum Coherence in Solid State Physics
edited by B. Deveaud-Plédran, A. Quattropani and P. Schwendimann